Search for New Heavy Charged Bosons and Singly Produced Leptoquarks with the ATLAS Experiment

Dissertation

zur Erlangung des Grades

Doktor der Naturwissenschaften

am Fachbereich Physik, Mathematik und Informatik

der Johannes Gutenberg - Universität

in Mainz

Holger Herr

geboren in Mainz

Mainz, 26.10.2020

Kurzfassung

In dem Zeitraum von 2015 bis 2018 wurden mithilfe des Large Hadron Collider (LHC) am CERN Protonen bei sehr hoher instantanen Luminosität mit einer Schwerpunktsenergie von $\sqrt{s} = 13$ TeV zur Kollision gebracht. Kein Teilchenbeschleuniger hat jemals zuvor solch hohe Energien erreicht. Deshalb bieten die Datensätze der an Kollisionspunkten befindlichen Experimenten eine beispiellose Chance, Vorhersagen des Standardmodells (SM) der Teilchenphysik präzise zu testen und Phänomene neuer Physik auf der TeV Skala zu erkunden. Zwei direkte Suchen nach neuen Teilchen werden unter Zuhilfenahme des von dem ATLAS Experiment aufgenommenen Datensatzes in dieser Arbeit präsentiert. Mögliche Signale in den untersuchten Endzuständen werden von einer Vielzahl von SM-Erweiterungen vorhergesagt. Diese werden postuliert, um konzeptionelle Probleme zu lösen und um von den SM-Vorhersagen abweichende Messungen zu erklären. In beiden Analysen wird die sensitive Variable so gewählt, dass diese eine hohe Korrelation zu der invarianten Masse der Zerfallsprodukte des neu eingeführten Teilchens aufweist. Der Untergrundbeitrag wird jeweils mithilfe von Monte Carlo Simulationen und auf Daten basierten Methoden abgeschätzt.

In der ersten Analyse wird nach einem resonanten Signal in Endzuständen mit einem geladenen (Anti-)Lepton (Lepton entspricht hier Elektron oder Myon) und hoher fehlender transversaler Energie gesucht, welche von dem zugehörigen (Anti)-Neutrino erzeugt wird. Diese Signalcharakteristen werden von einer Vielzahl an Erweiterungen postuliert, weshalb die Suche so weit wie möglich Signalmodell unabhängig konzipiert wurde. Signaturen dieser Art werden beispielsweise vorhergesagt von Theorien, die neue schwere geladene Eichbosonen - sogenannte W' Bosonen - einführen. Für diese Suche wurden die in 2015 und 2016 von ATLAS aufgenommen Daten untersucht. Dieser Datensatz entspricht einer integrierten Luminosität von $36\,\mathrm{fb}^{-1}$.

In der zweiten Suche liegt der Fokus auf hypothetischen Teilchen, die sowohl eine Lepton als auch eine Baryon Quantenzahl tragen - sogenannte Leptoquarks (LQ). Speziell wurde deren einzelne Produktion untersucht. Im Unterschied zu der paarweisen Produktion können in diesem Kanal höhere LQ-Massenhypothesen erforscht werden, auf Kosten von engeren Signalmodellannahmen. Dieser Signalprozess besitzt einen Endzustand, der aus einem Paar aus einem geladenen Lepton und einem geladenen Anti-Lepton (Lepton entspricht hier Elektron oder Myon) und mindestens einem hochenergetischen Jet besteht. Für diese Analyse wurde der gesamte Run 2 Datensatz mit einer integrierten Luminosität von $139\,\mathrm{fb}^{-1}$ mit einbezogen.

In beiden Suchen wurde keine signifikante Abweichung von der SM-Vorhersage festgestellt. Diese Beobachtung wurde mithilfe von Liklihood-Quotienten-Tests quantifiziert. Abschließend wurden jeweils obere Ausschlussgrenzen mit 95% Vertrauensniveau (CL) auf die Produkte von dem Signalwirkungsquerschnitt und dem Verzweigungsverhältnis gesetzt. Aus diesen wurden untere Ausschlussgrenzen für die Massen der postulierten Teilchen bestimmt. Die Existenz von neuen geladenen Eichbosonen, die im Rahmen des sequentiellen Standardmodells eingeführt wurden, wurde für Massen unterhalb von 5,43 TeV ausgeschlossen. Dies entspricht einer Verbesserung der Ausschlussgrenzen um mehr als 2 TeV im Vergleich zu Suchergebnissen, die mithilfe des $\sqrt{s} = 8$ TeV Datensatzes von ATLAS und CMS erzielt wurden. Für die Bestimmung von LQ-Massenausschlussgrenzen wurde die Annahme gemacht, dass die LQ-Lepton-Quark-Kopplung eins entspricht. Diese Grenzen liegen im Bereich von 1,2 TeV bis 2,8 TeV. Unter diesen modellspezifischen Annahmen sind die unteren Ausschlussgrenzen, die für LQ-Zerfälle mit Up Quarks in den Endzuständen bestimmt wurden, die derzeit höchsten - mit 2,3 TeV im Elektronenkanal und 2,8 TeV im Myonenkanal.

Abstract

In the years 2015 to 2018 the Large Hadron Collider (LHC) at CERN collided protons at a center of mass energy of $\sqrt{s} = 13$ TeV while operating at a very high instantaneous luminosity. This energy range has never been reached by accelerator experiments before. This is the reason why the data set, collected by each of the four big experiments which are located at an interaction point of the LHC, gives a great opportunity to precisely test Standard Model (SM) predictions and explore new physics phenomena on the TeV scale. Two direct searches for new particles in the data, which was collected by the ATLAS experiment during this period, are presented in this thesis. A signal in each probed final state can be created by a variety of SM extensions. These are postulated to address its conceptual problems and explain observations, which are inconsistent with SM predictions. The sensitive variable is designed with the aim to be highly correlated to the invariant mass of the new particles' decay products in both analyses. Background contributions are estimated with Monte Carlo simulations and data driven techniques.

Resonant signals in final states with a charged (anti-)lepton (lepton meaning electron or muon) and large missing transverse energy, that is created by the corresponding (anti-)neutrino, are probed in the first analysis. The considered signal characteristic is introduced by a variety of new theories, which is the reason why this search is designed with the aim to make no strong model assumptions. For example the existence of a new heavy charged gauge boson - a so-called W' - creates this signature. The analysis is conducted on the data set recorded in 2015 and 2016 by ATLAS, which corresponds to an integrated luminosity of $36\,\mathrm{fb}^{-1}$.

In the second search the existence of new particles, which carry a lepton and a baryon number simultaneously - the so-called Leptoquarks (LQ) - is investigated. Specifically their single production is explored, which allows to probe higher LQ mass hypotheses at the cost of making stronger model assumptions compared to their pair production process. This leads to final states with a particle anti-particle pair of charged leptons (lepton meaning electron or muon) and at least one high energy jet. For this the full Run 2 data set of proton-proton collisions, which corresponds to $139\,\mathrm{fb}^{-1}$, is probed.

No significant deviations from the SM prediction are found in either of the searches. This observation is quantified by likelihood ratio tests. In the end 95% confidence level (CL) upper limits on the signal cross-section times branching ratio are determined. These are then interpreted as lower limits on the new particles' mass. When probing the Sequential Standard Model, new heavy charged gauge bosons are excluded up to masses of 5.43 TeV at 95% CL, which is an improvement by more than 2 TeV compared to Run 1 results published by ATLAS and CMS. For the determination of the 95% CL lower mass exclusion limits, the LQ-lepton-quark coupling is assumed to be one. Results are in the range of 1.2 TeV to 2.8 TeV. Under these model specific assumptions, mass limits determined for the LQ decay into up quarks are the strongest to date - with 2.3 TeV in the electron and 2.8 TeV in the muon channel.

Contents

Chapter 1

Introduction

Today's state of scientific knowledge describes matter as point like components interacting via particle exchange. The idea of elementary particles as building blocks of the surrounding environment reaches back to the ancient Greeks. First constituents of atoms were discovered at the end of the 19th and the beginning of the 20th century [1][2][3]. Observations of numerous new particles in the 1960s lead to the introduction of the quark model [4][5] attempting to classify and structure the large ensemble of discoveries made. In the end of this decade first investigations into the proton structure by deep inelastic electron-proton scattering [6][7] and the discovery of the weak bosons Z and $W^{\pm}$ at LEP [8][9] in the 1980s paved the way for the formulation of the Standard Model (SM) of particle physics [10]. The SM is very successfully describing a large variety of precise particle physics measurements to this day. However, there are some observations and conceptual problems which hint at the fact that the SM might be an effective theory within a more fundamental one.

Various extension of the SM are postulated to address and solve shortcomings. For example one of the open questions is the hierarchy problem. It refers to the large differences between the coupling strength of different forces and the high amount of parameter fine tuning necessary. This could be assessed for example by introducing additional dimensions or symmetries which motivate the values observed for fundamental constants [11]. Furthermore, every theory aspires to be as simplistic as possible, which is the reason why multiple Grand Unified Theories (GUT) [12] are postulated. These unify all forces described in the SM and can be obtained by a single gauge group.

Many of these extensions postulate the existence of new heavy particles, which can serve as evidence for physics beyond the SM. Experiments which examine particle scatterings at very high center of mass energies allow to search for signatures of new heavy particle decays. During the years 2015 to 2018 the Large Hadron Collider (LHC) [13] at CERN collided two proton beams at $\sqrt{s} = 13$ TeV giving the opportunity to explore new phase space regimes, which have

never been reached by earth based experiments before. ATLAS [14] is one of the detectors located directly at an interaction point of the accelerator. Two direct searches for new particles are presented in this thesis, both of them use data collected during this time period. The fraction of the data set collected in 2015 and 2016 is used to search for new phenomena which introduce a resonant shape at high invariant masses in events with a charged lepton and large missing transverse energy. Processes with this signature are predicted for example by models introducing super-symmetry [15] or extra-dimensions [11]. The full data set is utilized to probe the existence of particles which carry lepton and baryon quantum numbers - so-called Leptoquarks [16]. The existence of these particles are commonly postulated by GUTs and serve as possible explanation of observations, which are inconsistent with SM predictions.

This thesis starts with theoretical foundations in Ch. 2. This includes the content and mathematical description of the SM, phenomenology of inelastic proton-proton scattering as well as conceptual problems of these theories. The chapter closes with a description of SM extensions, which are relevant for the presented searches, and a general discussion of the strategy utilized to probe the existence of new particles. Afterwards the ATLAS experiments, its components as well as the coordinate system used for data analysis are detailed in Ch. 3. Algorithms which reconstruct tracks and particles, as well as the calibration procedures applied, are introduced in Ch. 4. In Ch. 5 the basics of simulating particle physics processes and expected detector responses with Monte Carlo methods are laid out. This is followed by the two main parts. First the search for a new heavy charged gauge boson decaying into a charged lepton and a neutrino is presented in Part I. Afterwards the existence of singly produced Leptoquarks is probed in Part II. Each of these analysis starts with a motivation and a discussion of general aspects of the search. The interpretations and results of each analysis are described in separate chapters. Finally, this thesis closes with a summary and short outlook in Ch. 14.

Chapter 2

Theoretical Foundations

This chapter will briefly discuss the Standard Model of Particle Physics (SM), as well as its conceptual problems and hypothetical extensions addressing those. Sec. 2.1 starts with an overview of the particles and their interactions included in the SM, followed by a more detailed description of the mathematical structure for the electroweak interaction in Sec. 2.1.2 and strong interaction in Sec. 2.1.3. Then parton density functions will be introduced in Sec. 2.2, which describe the structure of the protons. Sec. 2.3 gives an overview of Proton-Proton Scattering phenomenology and how predictions can be obtained for the collision of composite objects. Finally, in Sec. 2.4 problems of the SM, measurements deviating from predictions and some hypothetical model extensions incorporating those observations are discussed. Sec. 2.5 gives a short overview of the procedure conducted to search for a heavy particles. In this entire thesis natural units are used ($\hbar = c = 1$).

The first sections of this chapter follow closely chapter 2 of my master thesis [17].

2.1 The Standard Model of Particle Physics

In the Standard Model of Particle Physics (SM) [10] all matter directly observed in the environment consists of fermions. These kinds of particles are specified by their characteristic half-integer spin. In nature four different types of interactions can be observed: the electromagnetic, the weak and the strong force as well as gravitation. The latter is not described by the SM. Due to their relative strengths, gravitation is not relevant considering the energy scales in high energy particle physics experiments. The electromagnetic and weak force are combined into a common theory - the electroweak interaction.

The interaction between two fermions is described by the exchange of a mediating particle - so-called bosons. There are different types of bosons, each of them is associated to a specific

interaction and carries integer spin. The electromagnetic interaction is propagated by the exchange of photons γ while the strong force is mediated by eight different types of gluons g. The weak force has three different bosons associated to it - the neutral Z and the electrically charged W^+ and W^- bosons. Each interaction type couples to a different particle property. The exchange of photons is only possible between electrically charged particles. The strong force is only observed between particles carrying color charge, which comes in three states: blue, red and green. Gluons carry color charge themselves - one color and one anti-color charge - each type of gluon carrying another combination. The weak interaction couples to left handed chirality state projections of each particle. The fact that every weak boson carries an invariant mass limits the range of this force. Gluons are massless. However, self-coupling effects lead to a finite range of the strong interaction as well. Only the electromagnetic interaction has infinite range due to the absence of both limiting factors. Tab. 2.1 gives a brief summary of bosons - excluding the higgs - and some of their properties.

boson	shortcut	invariant mass [GeV]	electric charge [e]
photon	γ	0	0
gluon	g	0	0
W boson	$W^{\pm}$	80.379	± 1
Z boson	Z	91.1876	0

TABLE 2.1: View over bosons involved in interactions described by Standard Model of particle physics. [18]

Fermions are separated into two different groups - leptons and quarks. A corresponding anti-fermion exists for each fermion type, which carries equal mass but the opposite charge. Additionally, each type of particle exists in three generations differing in mass and thus in their lifetime. Leptons carry no color and integral electric charge - meaning multiples of the elementary electric charge e - and do not interact strongly. The electron, muon and tau carry negative charge in contrast to the three different types of neutrinos. Quarks and their corresponding anti-particles interact via all three forces included in the SM. They carry color and electromagnetic charge. Due to the nature of the strong interaction only color neutral states exist freely. Therefore quarks create-color neutral bound states - so called hadrons. Two possible combinations achieve this requirement. Baryons consist of three quarks or anti-quarks and mesons of a quark and an anti-quark. Tab. 2.2 gives an overview over all fermions and some of their properties.

Interactions and particle propagation in the SM are described by a gauge quantum field theory [19]. Here, particles are associated with quantum fields which can be used to obtain probability densities of measurable observables. Fermions are characterized by so called spinors $\psi(x)$ and bosons by vector fields A_ν. The evolution of these fields is described by a Lagrangian density $\mathcal{L}$, which will be referred to as Lagrangian in the following. The Lagrangian for the propagation of a free particle with mass m and spinor ψ is shown in Eq. 2.1.

generation	name	shortcut	invariant mass	electric charge $[e]$
quarks				
1	up quark	u	$\approx$ 2 MeV	2/3
	down quark	d	$\approx$ 5 MeV	$-1/3$
2	charm quark	c	1.275 GeV	2/3
	strange quark	s	95 MeV	$-1/3$
3	top quark	t	173.0 GeV	2/3
	bottom quark	b	4.18 GeV	$-1/3$
leptons				
1	electron	e^-	0.511 MeV	-1
	electron-neutrino	ν_e	< 2 eV	0
2	muon	μ^-	105.658 MeV	-1
	muon-neutrino	ν_μ	< 0.17 MeV	0
3	tau	τ^-	1.77686 GeV	-1
	tau-neutrino	ν_τ	< 18.2 MeV	0

TABLE 2.2: All known fermions separated in leptons and quarks for each generation. Their mass, shortcut and electric charge is shown. The top mass value is taken from the direct measurement. [18]

$$\mathcal{L} = \bar{\psi}(i\gamma^\mu \partial_\mu - \mathrm{m})\psi \tag{2.1}$$

$\bar{\psi}$ is defined as $\bar{\psi} = \psi^\dagger \gamma^0$ and γ^μ are the gamma matrices. The postulation of local invariance of the Lagrangian under transformations of symmetry groups introduces interactions between particles.

2.1.1 Feynman Formalism and Fermi's Golden Rule

The interaction rate is the most common observable in high energy particle physics, which is connected to the probability for a given process taking place. This is measured by its cross-section. These measurements verify and test the SM and possible extensions. To obtain theoretical predictions a matrix element amplitude $\mathcal{M}$ for each process in question is calculated as a first step. The Feynman formalism [20] and Feynman diagrams give a visual approach for determining those. For each particle line, vertex and propagator in a Feynman diagram there is a mathematical description. The ingredients needed for those can be obtained using the Lagrangians introduced in the following sections. The matrix element at a given order of a process is calculated by considering all diagrams with the initial and final state in question. The contribution to $\mathcal{M}$ of a diagram with n vertices scales with α to the power of n, where α is the coupling constant of the interaction taking place. The number n is directly connected to the order of a combined matrix element. The ensemble of all diagrams with the lowest number of vertices possible give in combination the leading-order (LO) matrix element amplitude.

$|\mathcal{M}|^2$ is integrated over the phase space in consideration to obtain the measurable cross-section σ. This is done using Fermi's Golden Rule [21] which relates both quantities. The general expression for a process with two initial state particles - with four-momenta p_1 and p_2 - and n final state particles - with four momenta q_i, $i \in [1, n]$ - is shown in Eq. 2.2.

$$\sigma = (2\pi)^4 \int \frac{|\mathcal{M}|^2}{4\sqrt{(p_1 p_2)^2 - (\mathrm{m}_1^2 \mathrm{m}_2^2)}} \frac{\prod_{j=1}^{n} d\tilde{q}_j}{\prod_i N_i} \delta^4 \left(p_1 + p_2 - \sum_{j=1}^{n} q_j \right) \tag{2.2}$$

$$d\tilde{q}_j = \frac{d^3 \vec{q}_j}{(2\pi)^3 2 q_j^0} \Bigg|_{q_j^0 = \sqrt{\vec{q}_j^2 + \mathrm{m}_j^2}} \tag{2.3}$$

Here, m_i are the masses and $\vec{p}_i$ and $\vec{q}_i$ the three-momenta of the particles considered. N_i is the number of identical particles of species i in the final state.

Interference effects are introduced when calculating the absolute square of the matrix element via Eq. 2.4, in case final states of multiple processes - with amplitudes $\mathcal{M}_i$ - are not distinguishable.

$$|\mathcal{M}|^2 = |\sum_i \mathcal{M}_i|^2 \tag{2.4}$$

In perturbation theory [22] the cross-section σ up to the order N can be obtained by the polynomial shown in Eq. 2.5. The relation shown is a series of the coupling strength α.

$$\sigma = \sum_{n=1}^{N} \sigma^{(n)} (\alpha)^n \tag{2.5}$$

Here, $\sigma^{(n)}$ is the cross-section of all possible diagrams of order n. In case the value of α is low the series shown converges quickly giving a precise estimate of the total cross-section at a finite order N. Loop diagrams contribute at higher orders and introduce divergences when integrating over all possible momenta inside the loop, which is done in the computation of $\sigma^{(n)}$. Fig. 2.1 shows two schematic examples of a higher order loop Feynman diagrams.

The divergences cancel in case all higher order corrections are included. However, this is not possible in theoretical calculations. Thus to avoid these singularities, the coupling constant is renormalized by cutting the energy scales considered at μ_R - the so-called renormalization scale. In practice this is done by introducing a cutoff Λ and extrapolating its value to infinity again as the last step in the calculation. The coupling constant obtained at a finite order α_0 is related to the actual physical constant α_{phys} by introducing a correction term $\delta\alpha$. This term absorbs

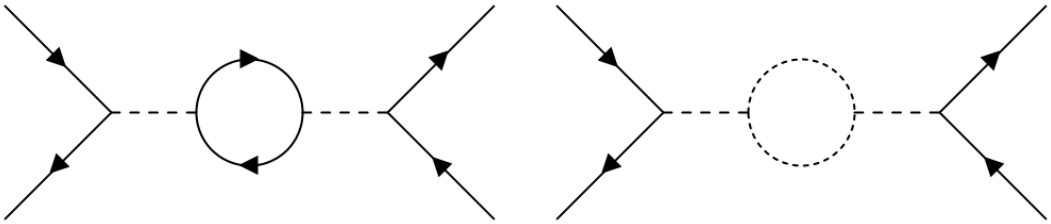

(a) (b)

FIGURE 2.1: Higher order Feynman diagrams with fermion - solid line - (a) and boson - dashed line - loops.

divergences in the calculation as shown in Eq. 2.6. This means that in the limit $\Lambda \to \infty$ the correction term $\delta\alpha$ becomes infinite as well.

$$\alpha_{phys} = \alpha_0 + \delta\alpha \tag{2.6}$$

Consequently, the actual physical coupling constant α_{phys} incorporates these divergences. This can be schematically explained by considering screening effects from vacuum polarizations which lead to a measured finite charge of an infinitely charged object. An additional implication is that the coupling constant is dependent on the scale of the momentum transfer Q^2 and the choice of the renormalization scale μ_r^2. Particle masses are scale dependent as well since they are assessed by their propagator, which contains loop diagrams at higher orders.

The dependence of the μ_r choice on the cross-section is propagated by the coupling constant. Every additional higher order calculation included in the cross-section determination reduces the impact of this dependency.

2.1.2 The Electroweak Interaction

The electromagnetic interaction [19] is introduced by requiring local invariance under transformations of the $U(1)$ symmetry group. Transformations of ψ in this group can be parametrized by Eq. 2.7 with the generator α of the $U(1)$ group.

$$\psi \to \psi' = e^{i\alpha(x)}\psi \tag{2.7}$$

To keep the Lagrangian of a free particle displayed in Eq. 2.1 gauge invariant under local transformations of this kind the covariant derivative $\mathcal{D}_\mu$ with the bosonic gauge field $A_\mu(x)$ are introduced in Eq. 2.8. $A_\mu(x)$ is associated to the field of the photon.

$$\partial_\mu \rightarrow \mathcal{D}_\mu = \partial_\mu + ieA_\mu(x) \tag{2.8}$$

e is conserved under the transformation and can be identified with the electric charge. Due to the fact that photons can exist as free particles an additional kinematic term has to be added to the Lagrangian. The full Lagrangian describing Quantum Electrodynamics (QED) is shown in Eq. 2.9.

$$\mathcal{L}_{\text{QED}} = \bar{\psi}(i\gamma^\mu\partial_\mu - \text{m})\psi - e\bar{\psi}\gamma^\mu A_\mu\psi - \frac{1}{4}F_{\mu\nu}F^{\mu\nu} \tag{2.9}$$

with the electromagnetic field tensor

$$F_{\mu\nu} = \partial_\mu A_\nu - \partial_\nu A_\mu. \tag{2.10}$$

The weak interaction is a consequence of requiring local invariance under $SU(2)_L$ transformations and couples only to the left-handed chirality of a particle. This characteristic is considered by introducing the quantum number weak isospin T. It is constructed in a way that left-handed fermions form doublets with a total value of $T = 1/2$ and third components of $T_3 = \pm 1/2$, while fermions with right-handed chirality are described by singlets with $T = 0$ and $T_3 = 0$. The interaction itself couples to each particle's T_3. All transformations of doublets inside the $SU(2)$ symmetry group are described using the three generators $T_i = \sigma_i/2$ with $i \in [1, 3]$. σ_i are the Pauli matrices and each generator has a vector field assigned to it: W^1_μ, W^2_μ and W^3_μ.

Weinberg [23], Glashow [24] and Salam [25] developed theories which unify the electromagnetic and weak interaction into an electroweak theory. In this combination the weak hypercharge Y_w is introduced combining the electromagnetic charge of a particle Q and its third component of the weak isospin as displayed in Eq. 2.11.

$$Q = T_3 + \frac{Y_w}{2} \tag{2.11}$$

The hypercharge is related to the $U(1)_Y$ group introducing the vector field B_μ. Transformations in the unified electroweak theory are members of the $SU(2)_L \times U(1)_Y$ symmetry group. Analogously to QED the Lagrangian of the electroweak theory can be obtained by requiring local gauge invariance and is shown in Eq. 2.12.

$$\mathcal{L}_{\text{EW}} = \sum_j \bar{\psi}^L_j i\gamma^\mu \mathcal{D}_\mu \psi^L_j + \sum_{j,f} \bar{\psi}^R_{j,f} i\gamma^\mu \mathcal{D}_\mu \psi^R_{j,f} - \frac{1}{4}W^i_{\mu\nu}W^{\mu\nu}_i - \frac{1}{4}B_{\mu\nu}B^{\mu\nu} \tag{2.12}$$

The first term is the sum over each generation j of the left-handed fermion doublets ψ_j^L and the second term the sum over all generations j and particle types f within of the right-handed fermion singlets $\psi_{j,f}^R$. The covariant derivative $\mathcal{D}$ is defined as shown in Eq. 2.13.

$$\mathcal{D}_\mu = \partial_\mu - i\frac{g}{2}\sigma_i W_\mu^i + ig'\frac{Y_w}{2}B_\mu \tag{2.13}$$

g and g' are the coupling constants of the $SU(2)_L$ and $U(1)_Y$ symmetry group. The field strength tensors $W_{\mu\nu}^i$ and $B_{\mu\nu}$ are displayed in Eq. 2.14.

$$\begin{aligned} W_{\mu\nu}^i &= \partial_\mu W_\nu^i - \partial_\nu W_\mu^i + g\epsilon_{ijk}W_\mu^j W_\nu^k \\ B_{\mu\nu} &= \partial_\mu B_\nu - \partial_\nu B_\mu \end{aligned} \tag{2.14}$$

The last term of the field strength tensor $W_{\mu\nu}^i$ represents the self coupling of the W_μ^i fields. This is a direct consequence of the $SU(2)$ symmetry group being non-abelian.

The fields corresponding to the observed mass eigenstates $W_\mu^\pm$ are given by the linear combinations of W_μ^1 and W_μ^2 shown in Eq. 2.15.

$$W_\mu^\pm = \frac{1}{\sqrt{2}}\left(W_\mu^1 \mp iW_\mu^2\right) \tag{2.15}$$

The fields associated to the Z boson (Z_μ) and photon (A_μ) are obtained by combining W_μ^3 and B_μ which can be expressed by a rotation in order of the weak mixing angle θ_W. The corresponding relation is displayed in Eq. 2.16.

$$\begin{pmatrix} A_\mu \\ Z_\mu \end{pmatrix} = \begin{pmatrix} \cos\theta_W & \sin\theta_W \\ -\sin\theta_W & \cos\theta_W \end{pmatrix} \begin{pmatrix} B_\mu \\ W_\mu^3 \end{pmatrix} \tag{2.16}$$

There is a mis-match observed between the quark eigenstates q_m ($q \in \{d, s, b\}$) which are propagated freely and the ones participating in the weak interaction q ($q \in \{d, s, b\}$). Cabibbo [26] introduced a formalism which describes this mis-match for the lightest two particle generations. Kobayashi and Maskawa [27] expanded this to all three generations using a unitary 3×3 matrix, the so-called CKM-Matrix V_CKM. Conventionally the parametrization is done using the down type quarks. The eigenstates which interact weakly are a linear combination of the mass eigenstates as displayed in Eq. 2.17.

$$\begin{pmatrix} d \\ s \\ b \end{pmatrix} = V_\mathrm{CKM} \begin{pmatrix} d_\mathrm{m} \\ s_\mathrm{m} \\ b_\mathrm{m} \end{pmatrix} \tag{2.17}$$

In first order V_{CKM} is an identity matrix. It is required to be unitary in order to keep the amount of particles conserved and can be parametrized with four independent parameters. Typically the Euler parametrization [28] is used which introduces three mixing angles θ_i ($i \in \{1, 2, 3\}$) and a complex phase δ. A non-vanishing phase introduces CP violation. This means that a process is not invariant under the combination of charge-conjugation C - exchanging each particle with its anti-particle - and the parity transformation P.

A similar eigenstate mis-match is observed in the neutrino sector which is described with a similar formalism using the unitary V_{PMNS} matrix, introduced by Pontecorvo [29], Maki, Nakagawa and Sakata [30].

2.1.2.1 Spontaneous Symmetry Breaking

The fields W_μ^1, W_μ^2, W_μ^3 and B_μ must correspond to massless bosons in order to keep local gauge symmetry. This is the reason why an additional mechanism - the spontaneous symmetry breaking [31] - is introduced which assigns the observed masses of W and Z bosons while keeping the photon massless. This is done by introducing the higgs field - a single complex scalar doublet field displayed in Eq. 2.18.

$$\Phi(x) = \begin{pmatrix} \phi^\dagger(x) \\ \phi^0(x) \end{pmatrix} \tag{2.18}$$

The Lagrangian of the the higgs field $\mathcal{L}_{\text{Higgs}}$ and the embedded potential $V(\Phi)$ are shown in Eq. 2.19.

$$\begin{aligned} \mathcal{L}_{\text{Higgs}} &= (\mathcal{D}_\mu \Phi)^\dagger (\mathcal{D}^\mu \Phi) - V(\Phi) \\ V(\Phi) &= -\mu^2 \Phi^\dagger \Phi + \tfrac{\lambda}{4} \left(\Phi^\dagger \Phi\right)^2 \end{aligned} \tag{2.19}$$

Under the assumptions of $\mu^2 > 0$ and $\lambda > 0$ this potential has the degenerate ground state $\Phi^\dagger \Phi = -4\mu^2/\lambda = v^2$ and a non-vanishing vacuum expectation value v. The ground state $\langle \Phi \rangle$ is then chosen to break the $SU(2)_L \times U(1)_Y$ symmetry into the $U(1)_{EM}$ symmetry. By expanding Φ by $H(x)$ around the vacuum expectation value Eq. 2.20 follows.

$$\Phi(x) \approx \frac{1}{\sqrt{2}} \begin{pmatrix} 0 \\ v + H(x) \end{pmatrix} \tag{2.20}$$

A neutral physical scalar $H(x)$ manifesting itself as the higgs boson with mass $\mathrm{m}_H = \mu\sqrt{2}$. The mass terms for the three heavy bosons are introduced by absorbing Φ's three remaining degrees of freedom and can be expressed by:

$$\mathrm{m}_Z = \frac{1}{2}v\sqrt{g^2 + g'^2}, \qquad \mathrm{m}_W = \frac{1}{2}vg. \tag{2.21}$$

Similarly to the W and Z bosons' mass, the masses m_f of fermions f violate local gauge symmetry. This is the reason why they are also introduced by the interaction with the higgs field. Yukawa couplings describe this and are included to the Lagrangian as displayed in Eq. 2.22 - in unitary gauge.

$$\mathcal{L}_{\mathrm{Yuk}} = -\sum_f \mathrm{m}_f \bar{\psi}_f \psi_f - \sum_f \frac{\mathrm{m}_f}{v} \bar{\psi}_f \psi_f H \tag{2.22}$$

2.1.3 The Strong Interaction

The strong interaction is described by Quantum Chromodynamics (QCD) [22]. The symmetry group used to introduce interaction terms to the Lagrangian is the $SU(3)_C$. Transformations can be expressed by eight generators, which are be parametrized by the Gell-Mann matrices λ_i, $i \in [1, 8]$. The Lagrangian of QCD and the corresponding covariant derivative is shown in Eq. 2.23 and Eq. 2.24.

$$\mathcal{L}_{\mathrm{QCD}} = \sum_q \bar{\psi}_{q,a}(i\gamma^\mu \left(\mathcal{D}_\mu\right)_{ab} - \mathrm{m}_q \delta_{ab})\psi_{q,b} - \frac{1}{4} G^A_{\mu\nu} G^{\mu\nu}_A \tag{2.23}$$

$$\left(\mathcal{D}_\mu\right)_{ab} = \partial_\mu \delta_{ab} + i\sqrt{\pi\alpha_s}\lambda^g_{ab} A^g_\mu \tag{2.24}$$

$\psi_{q,a}$ refers to the spinor of color a and quark-flavor q with mass m_q. All possible colors are considered for the indices a and b. The effective fine-structure constant of QCD is given by α_s of QCD and A^g_μ is the gauge field of gluon type g. λ^g_{ab} is the Gell-Mann matrix associated to the gluon type g which is classified by its color (a) anti-color ($\bar{b}$) combination. The sum over all types g is taken in the derivative shown in Eq. 2.24. $G^A_{\mu\nu}$ is the field strength tensor of the gluon and is given by Eq. 2.25.

$$G^A_{\mu\nu} = \partial_\mu A^C_\nu - \partial_\nu A^C_\mu - 2\sqrt{\pi\alpha_s} f_{ABC} A^B_\mu A^C_\nu \qquad [\lambda^A, \lambda^B] = i f_{ABC} \lambda^C \tag{2.25}$$

f_{ABC} are the structure constants of the $SU(3)_C$ group and the last term of the definition of the field strength tensor introduces - similarly to the weak interaction - the self coupling between gluons.

The strong coupling constant and the more commonly used effective fine-structure constant α_s depend on the scale Q^2 of the interaction. The corresponding correlation can be expressed at LO by Eq. 2.26 assuming α_s is known at some reference scale Q^2_{ref}.

$$\alpha_s(Q^2) = \frac{\alpha_s(Q^2_{ref})}{1 + \alpha_s(Q^2_{ref})\beta_0 \ln(Q^2/Q^2_{ref})} \qquad \beta_0 = \frac{33 - 2N_f}{12\pi} \tag{2.26}$$

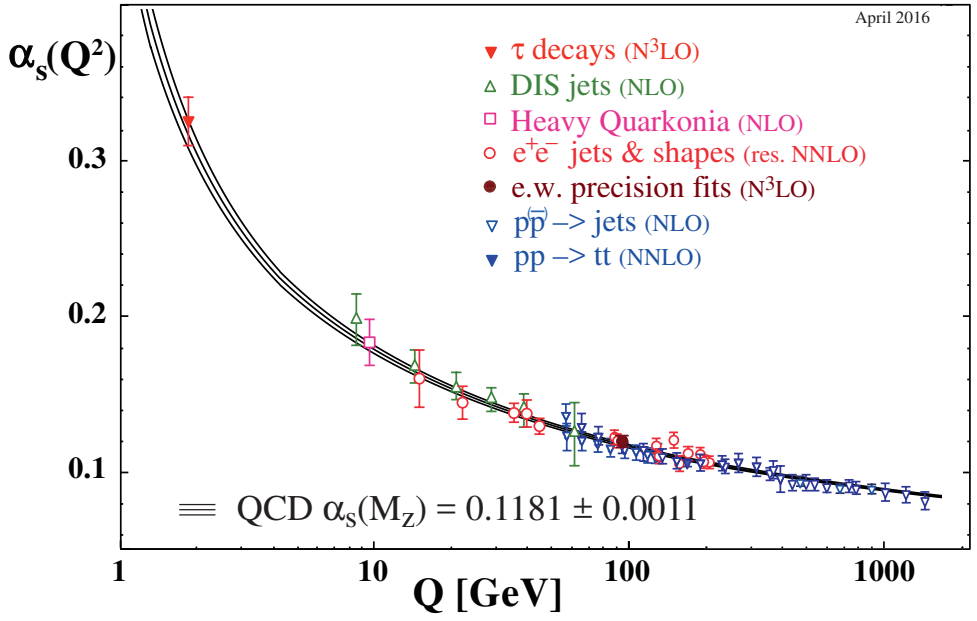

FIGURE 2.2: Strong coupling constants α_s against scale of the interaction Q. Results obtained by various measurements with different methods as well as their uncertainties are shown. [18]

N_f is the number of quark flavors contributing at the scale Q^2 and β_0 refers to the LO coefficient of the β-function expansion, which models the running of α_s. Fig. 2.2 shows α_s depending on Q as well as results obtained by various measurements using different approaches over a large Q^2 range. For large values of Q^2, which corresponds to small distances, α_s is very small allowing quarks to be studied as approximately free particles in this range. This effect is called asymptotic freedom. At low Q^2 the coupling constant increases rapidly and the series shown in Eq. 2.5 does not converge anymore. Perturbation theory breaks down below a specific scale. The scale at which perturbative expansions are not usable anymore is at $\Lambda_{\mathrm{QCD}} \approx 220\,\mathrm{MeV}$ considering all flavors except the top quark. The theory for calculation at higher scales is referred to as perturbative QCD.

Empirically the strong interaction at large distances r can be described by a potential which shows a linear behavior $V \sim r$. For this reason there is a certain distance between two colored

particles where it is energetically favored to produce a quark anti-quark pair. Additionally, quarks and gluons carrying high momentum lose energy by emitting gluons which produce subsequently quark anti-quark pairs. If the energy of these particles is sufficiently low it is energetically favored to form color neutral bound states, so-called hadrons.

2.2 Parton Density Functions

The proton is a baryon and thus a composite object [4]. It consists of three valence quarks - one d and two u - and a dynamically changing ensemble of mostly strongly interacting particles in the so called sea. The characteristics and properties of each fundamental point-like particle type inside the proton is quantified by a set of parton density functions (PDF) [32] $f_{a/A}(x_a, Q^2)$. In this notation $f_{a/A}(x_a, Q^2)$ is the probability that the parton of type a carries the momentum fraction x_a of the proton A at the momentum scale Q^2. The Q^2 dependence can be motivated by its correspondence to a certain resolution. A high Q^2 value allows more and smaller substructures to be resolved.

PDF sets are not theoretically obtainable and have to be determined by global QCD fits using an accumulation of measurements as input. Deep inelastic scattering data (DIS), which is collected in proton-lepton collisions, has the most constraining power at low x. Relevant data of this has been collected by the ZEUS [33] and H1 [34] experiments which were located at the HERA accelerator in Hamburg. Additionally, fixed target DIS experiments [35] are used to probe PDFs at higher x values. Conversely, jet properties studied using data collected in high energy proton-proton collisions by ATLAS and CMS probe a large range of x and Q^2 values.

To obtain PDF sets a generic functional form for each quark and gluon contribution is assumed at a reference scale Q_0^2. This reference scale Q_0^2 is usually at $\mathcal{O}(1\ \text{GeV}^2)$. NNPDF3.0 [36] for example chose $Q_0^2 = 1\ \text{GeV}^2$. Eq. 2.27 shows the functional form of the PDF $f_i(x, Q_0^2)$ which is usually used.

$$f_i(x, Q_0^2) = A_i x^{-\alpha_i} (1-x)^{\beta_i} F_i(x, \vec{\gamma}_i) \tag{2.27}$$

The index i refers to the parton type. In the following, instead of f_i, q_i will be used for the quark PDFs and g for the gluon PDF. α_i and β_i are parameters which are fixed by the global fit. A_i is a normalization constant and $F_i(x, \vec{\gamma}_i)$ is a smooth function depending on x. The introduction of additional fit parameters $\vec{\gamma}_i$ allows more flexibility. These functions $F_i(x, \vec{\gamma}_i)$ differ for each parton type. In practice the fit is conducted using multiple linear combinations of all parton PDFs $f_i(x, Q_0^2)$ as basis. In the procedure used to determine the NNPDF3.0 [36] set the linear combinations are constructed in a way that they diagonalize the DGLAP equations [37][38][39],

which are used to extrapolate to different scales Q^2. In previous iterations these combinations were defined with the object that each of them is sensitive to data measured in a specific set of experiments. The DGLAP equations are shown in Eq. 2.28 and Eq. 2.29.

$$\frac{\partial q_i(x,Q^2)}{\partial \log(Q^2)} = \frac{\alpha_s}{2\pi}\int_x^1 \frac{dz}{z}\left[\sum_j P_{q_iq_j}(z,\alpha_s)q_j\left(\frac{x}{z},Q^2\right) + P_{q_ig}(z,\alpha_s)g\left(\frac{x}{z},Q^2\right)\right] \tag{2.28}$$

$$\frac{\partial g(x,Q^2)}{\partial \log(Q^2)} = \frac{\alpha_s}{2\pi}\int_x^1 \frac{dz}{z}\left[\sum_j P_{gq_j}(z,\alpha_s)q_j\left(\frac{x}{z},Q^2\right) + P_{gg}(z,\alpha_s)g\left(\frac{x}{z},Q^2\right)\right] \tag{2.29}$$

Here, α_s is the strong coupling constant introduced in Sec. 2.1.3 and P_{if} $(i, f \in q_i, g)$ are the Altarelli-Parisi splitting functions [40]. They give the probability for the initial parton i to undergo a process which leads to a parton f. This process is either an emission or some kind of splitting. P_{qq} and P_{gg} represent the cases in which gluons are emitted and the initial parton type stays the same. P_{qg} and P_{gq} on the other hand describe the emissions of quarks, in which the initial parton changes its type - either from quark to gluon or the reverse. These splitting functions are expanded perturbatively. Results for these calculated up to NLO and NNLO are available [41].

Fig. 2.3 shows the NNPDF31 [42] set of NNLO parton distribution functions at two different scales - $Q^2 = 10$ GeV^2 and $Q^2 = 10^4$ GeV^2. All objects which contribute only to the sea of the proton show a steeply falling behavior. This is more pronounced at higher scales since the sea components tend to carry a larger fraction of the proton momentum. The curves describing the u and d momentum fractions have maxima due to their additional permanent existence as valence quarks.

Limitations of different origins lead to various uncertainties assigned to the PDF sets. The measurements used as an input have uncertainties associated to them. Parameters of the PDF parametrization are highly correlated which is the reason why additional steps need to be performed to estimate the impact on the density functions. The Hessian method [43] can be used to resolve this. To obtain a systematic variation the covariance matrix is rotated into an orthogonal eigenvector basis. This allows to propagate uncorrelated sets of fit uncertainties directly to the PDFs. Additionally, the parametrization, choice of α_s and the extrapolation to the desired Q^2-scale introduce uncertainties.

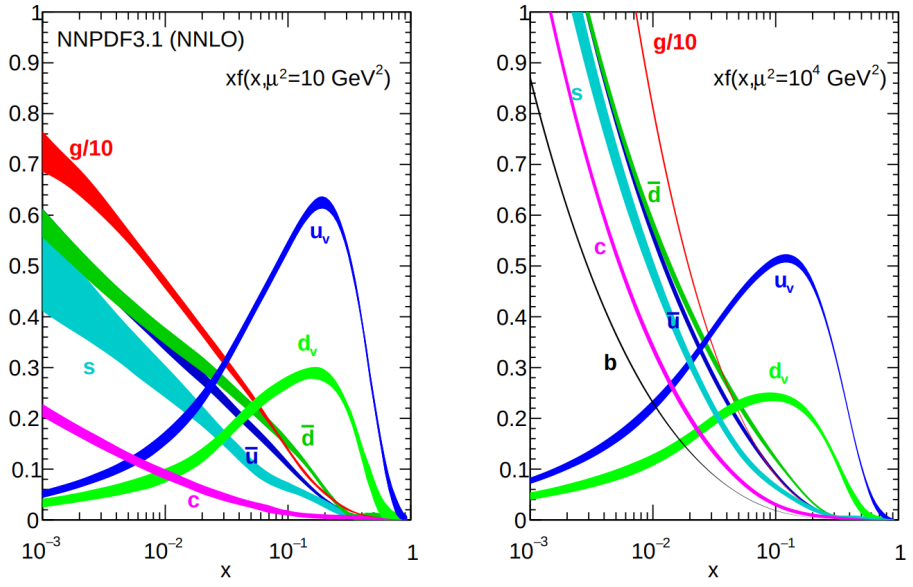

FIGURE 2.3: NNPDF31 parton density distributions at a scale of $Q^2 = 10$ GeV^2 and $Q^2 = 10^4$ GeV^2. Different colors indicate the distributions of different particle types with the width of the line indicating the one σ uncertainties. The gluon contribution is scaled by 1/10 for better visibility. [42]

2.3 Proton-Proton Scattering and Factorization Theorem

Due to the compound nature of the protons [6][7] the distribution of scales at which the parton level interactions are taking place is not discrete. Most of the processes happening in the sea of the proton take place well below the QCD scale Λ_{QCD} which is the reason why perturbative QCD can not be used to obtain model predictions. The interacting partons carry only a fraction of the protons momentum, which is described by PDFs.

However, due to the energies considered the cross-section of the hard-scattering process on parton level $\hat{\sigma}_{ab}$ - between particles a and b - can be calculated using perturbative theories by following the steps discussed in Sec. 2.1. Non-perturbative contributions are described by the phenomenologically determined PDFs. The factorization theorem [44], shown in Eq. 2.30, gives a relation between the cross-section σ_{AB} on proton level - between protons A and B - the parton density functions of each proton - $f_{a/A}(x_a)$ and $f_{b/B}(x_b)$ - and the cross-section calculated perturbatively $\hat{\sigma}_{a,b}$.

$$\sigma_{AB} = \sum_{a,b} \int dx_a dx_b f_{a/A}(x_a, \mu_F^2) f_{b/B}(x_b, \mu_F^2) \hat{\sigma}_{a,b}(x_a, x_b) \tag{2.30}$$

μ_F is the factorization scale, which is chosen with the intent to separate long- and short-distance physics. The cross-section $\hat{\sigma}_{a,b}$ is only calculated at finite order and introduces a dependency on the renormalization scale, as discussed in Sec. 2.1.1. Due to the fact that only finite numbers

of higher order corrections are considered the numerical value of the cross-section σ_{AB} depends on the choice of the parameters μ_r and μ_f. This effect is taken into account by theoretical uncertainties.

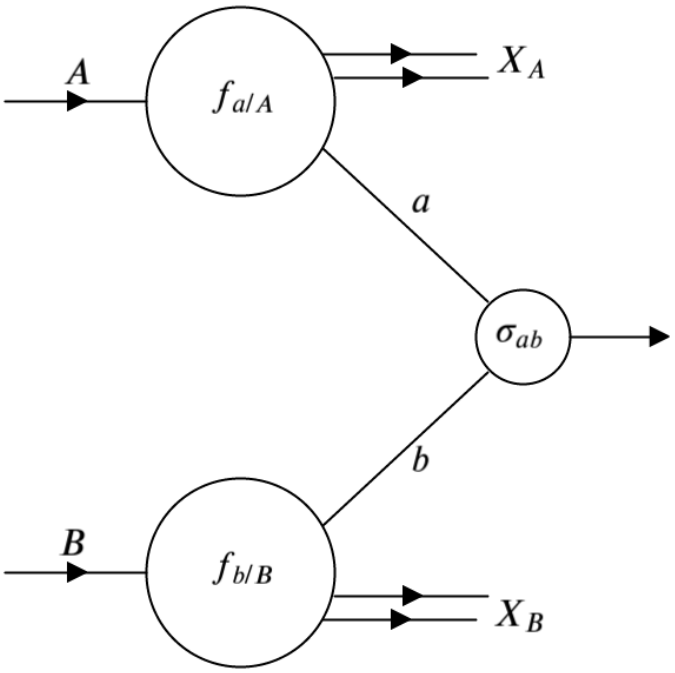

FIGURE 2.4: Schematic illustration of deep inelastic proton-proton scattering of the protons labeled with A and B. The partons a and b interact with the cross-section σ_{ab}. Their probability distribution is described by the corresponding PDFs $f_{a/A}$ and $f_{b/B}$. The remnants of the protons that are not participating in the hard scattering process are represented by X_A and X_B.

Fig. 2.4 illustrates schematically the deep inelastic scattering of two incoming protons A and B, indicated by the large circles with the corresponding PDFs of the interacting partons a and b. The circle with the cross-section σ_{ab} describes the relevant process on parton level. The outgoing lines, labeled X_A and X_B, represent the partons of protons which do not participate in the hard scattering process.

These remnants X_A and X_B are colored objects and cannot exist as free particles. The same holds true for quarks and gluons which are produced by the hard scattering process. Gluons will split into $q\bar{q}$-pairs, while quarks will emit gluons to decrease their energy. The ensemble of partons produced this way is called parton shower. Once the partons energy is sufficiently low the shower stops and hadrons are formed. This step is called hadronization. The proton remnants X_A and X_B, particles created by additional interactions inside the proton and initial- (ISR) and final-state radiation (FSR) are referred to as underlying event. The description of these concepts is detailed in more depth in Ch. 5 where the simulation of proton-proton scattering events will be discussed.

2.4 Extensions of the Standard Model

The SM is very successfully describing observations made in high energy physics. However, some shortcomings, conceptual problems and measurements suggest that the SM is not a complete theory. First some of the most prominent problems as well as in this context observations, which deviate the most from SM predictions will be discussed in Sec. 2.4.1 and Sec. 2.4.2. Afterwards an overview of some extensions which would address and solve some of the problems will be given in Sec. 2.4.3 and Sec. 2.4.4. The emphasis here is on models to which the analyses presented in this thesis are sensitive. The discussion is separated with respect to Part I and Part II.

2.4.1 Conceptual Problems

By construction the amount of particles and anti-particles created during the big bang should be almost the same. Violations under CP transformations can introduce asymmetric behavior in the production of matter and anti-matter. However, considering the imbalance observed in our universe the CP violation present in the SM is not sufficient to explain the level of matter-antimatter asymmetry observed.

Many observations in cosmology hint at the existence of so-called dark matter and dark energy. Observations [45] of rotation velocities of luminous matter in galaxies can not be explained by the known interactions of visible matter only. The existence of non-luminous matter distributed as halo around a galaxy is one viable explanation for this. There are no particle candidates in the SM which could make up the whole amount of dark matter necessary to explain the observations. Furthermore, due to the acceleration of the universe expansion rate an additional energy contribution - referred to as dark energy - needs to be introduced. By probing the cosmic microwave background [46] the energy composition of the universe has been estimated to be 27% dark matter, 68% dark energy and 5% baryonic matter.

Additionally, the necessary precision of the parameter tuning inside the SM is unsatisfying and is called the naturalness or hierarchy problem. Assuming the SM is only an effective theory, it should be only valid at a certain energy scale. The mass of the higgs is influenced by higher order quantum corrections, which are introduced via loops in its propagator. These corrections become very large at high energy scales resulting in the fact that the LO mass term is orders of magnitude smaller than the different corrections applied. To obtain the measured mass of the higgs particle, the SM parameters have to be fine tuned to cancel the majority of these corrections.

The inclusion of the neutrino masses and their size in the SM is by design unsatisfactory as well. The mass terms of neutrinos must have contributions from right-handed spinors which do not take part in any interaction within the SM. Additionally, the fact that the mass values of

neutrinos are orders of magnitude smaller than other fermions is not motivated or explained by any mechanism inside the SM.

Similar to the description of the electromagnetic and weak force in the electroweak theory, the unification of all forces observed based on a symmetry group as source for all interactions is explored. These models are referred to as grand unifying theories (GUTs) [12]. Often they have the problem of allowing the decay of protons which is not observed and thus require a mechanism which suppresses this process.

2.4.2 Flavor Anomalies

The SM predicts lepton universality. This means by construction observations should be approximately invariant under the exchange of the lepton type, considering processes at energy scales E orders of magnitude larger than their masses m_l ($E \gg \mathrm{m}_l$). At the energy ranges probed at the LHC and other accelerators this requirement remains true - especially for the consideration of electrons/positrons and muons/anti-muons.

However, multiple observations made in flavor physics challenge the universality assumption. The recent ones were made by LHCb [47] and observables probed consist of a combination of branching ratios of meson decays.

One of the observation [48], which deviates the most from SM predictions, was made while studying double ratios of branching fractions $\mathcal{B}$ - for example $R_{K^{*0}}$. These double ratios are commonly used to cancel correlated uncertainties between both decay channels and within themselves. Its definition is shown in Eq. 2.31.

$$R_{K^{*0}} = \frac{\mathcal{B}(B^0 \to K^{*0}\mu^+\mu^-)}{\mathcal{B}(B^0 \to K^{*0}J/\psi(\to \mu^+\mu^-))} \Big/ \frac{\mathcal{B}(B^0 \to K^{*0}e^+e^-)}{\mathcal{B}(B^0 \to K^{*0}J/\psi(\to e^+e^-))} \tag{2.31}$$

The B^0 consists of a d and a $\bar{b}$ quark and the K^{*0} of a d and a $\bar{s}$ quark. The decay is included in the SM by two Feynman diagrams on LO: an electroweak penguin diagram and a box diagram involving a neutrino. Both are shown in Fig. 2.5 (a) and (b) and neither of them introduce any violation to the lepton universality, leading to an expected value of $R_{K^{*0}} \approx 1$.

However, the result of the measurement conducted by LHCb [49] is deviating by over two standard deviations in two different q^2 regions probed and is shown in Eq. 2.32.

$$R_{K^{*0}} = \begin{cases} 0.66^{+0.11}_{-0.07}(\mathrm{stat}) \pm 0.03(\mathrm{syst}) & \text{for } 0.045\ \mathrm{GeV}^2 < q^2 < 1.1\ \mathrm{GeV}^2 \\ 0.69^{+0.11}_{-0.07}(\mathrm{stat}) \pm 0.05(\mathrm{syst}) & \text{for } 1.1\ \mathrm{GeV}^2 < q^2 < 6.0\ \mathrm{GeV}^2 \end{cases} \tag{2.32}$$

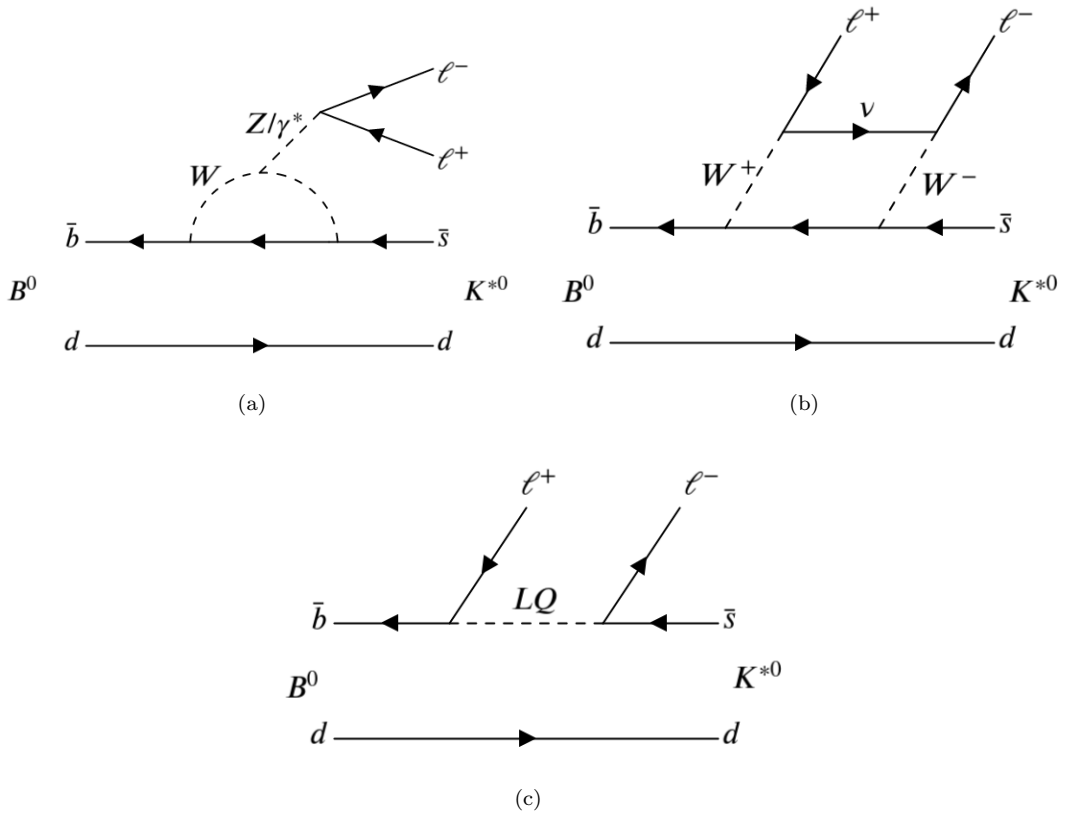

FIGURE 2.5: LO Feynman diagrams of a B^0 decay into a K^{*0} and charged lepton anti-lepton pair. Diagrams shown in (a) and (b) are included in the SM and do not violate lepton universality. (c) shows the decay via a new particle introduced to the SM to address the from the SM deviating observations - the so-called LQ.

Measurements of R_{K^*} conducted by the Belle experiment [50] - a so-called B-factory - have already shown a similar trend toward lower values. But the statistical uncertainty is too large for the observed deviation to be significant on its own. In the definition of the observable R_{K^*} decays of charged B mesons into charged kaons are considered as well, which is the reason why it is not directly comparable to the LHCb measurement. The result is

$$R_{K^*} = 0.83 \pm 0.17(\text{stat}) \pm 0.08(\text{syst}). \tag{2.33}$$

Similarly, deviations from the SM expectation have been observed by LHCb [51] studying the ratio of branching fractions R_K of the decays $B^+ \to K^+ l^+ l^-$ with $l \in \{e, \mu\}$. The analysis has been conducted using data recorded in proton-proton collisions with a center of mass energy of 7, 8, 13 TeV. The result is displayed in Eq. 2.34 and shows a 2.5 standard deviation discrepancy to the SM expectation.

$$R_K = 0.846^{+0.060\,+0.016}_{-0.054\,-0.014} \qquad \text{for } 1.1 \ \text{GeV}^2 < q^2 < 6.0 \ \text{GeV}^2 \tag{2.34}$$

Due to these deviations multiple extensions of the SM introduce additional lepton flavor universality violations. One of the most prominent new particle types considered is the so-called leptoquark (LQ), which couples to leptons and quarks simultaneously. These models will be discussed in more detail in Sec. 2.4.4. The LO Feynman diagram of a B^0 decay involving a LQ is shown in Fig. 2.5 (c).

2.4.3 New Physics with a Charged Lepton and a Neutrino

In this section the most prominent model extensions which are explored in Part I are introduced. This includes the arbitrary benchmark model which is commonly used for comparison to other measurements - the Sequential Standard Model. All extensions which give rise to a signal with a charged lepton and missing transverse energy in the final state are probed in Part I.

Sequential Standard Model In the Sequential Standard Model (SSM) [52] heavy partners of the SM W bosons are introduced. They carry the same quantum numbers and have the the same coupling strength to SM fermions, differing only in invariant mass. The width of the boson is roughly 3% of its mass within this model. This extension does not address any specific conceptual problem of the SM and has no theoretical motivation but serves as a benchmark signal hypothesis for searches conducted in this channel across multiple experiments. Interference between the SSM W' and SM W bosons lead to more distinct signal shapes and thus higher sensitivities. However, these effects are model and coupling dependent themselves and contradict the aim of making the fewest model assumptions possible. This is the reason why no interference effects on the signal shape are considered in the analysis presented in Part I. The use of this model allows comparison to searches conducted previously using it as signal hypothesis. The results obtained in this thesis are assessed in context to other analysis in Sec. 9.

Supersymmetry One of the most popular extensions to the SM is supersymmetry [15] since it tackles many of the conceptual problems discussed in Sec. 2.4.1 simultaneously. The core concept is the introduction of an additional symmetry between bosons and fermions. At least one super-partner is assigned to each particle - integer spin particles to fermions and half-integer spin particles to bosons. Since energies of known particles have been explored by many experiments the symmetry to their super-partners must be broken as they have to differ in mass to be compatible with observations. This is the reason why many new parameters are necessary within this theory.

Supersymmetric models are most commonly characterized as R-parity conserving or violating. SM particles have R-parity of $+1$ while their super-partners have R-parity of -1. In case R-parity is conserved the lightest supersymmetric particle (LSP) is stable as it can not decay into

SM particles. Therefore this LSP serves as a dark-matter candidate. Since supersymmetric particles couple to the higgs as well, they contribute to higher order corrections to its mass. The additional terms cancel other corrections to the higgs mass and thus solve the hierarchy problem to some extent. However, to avoid any parameter fine tuning the masses of most supersymmetric particles have to be at scales which have already been excluded by LHC experiments. Additionally, within supersymmetry the unification of all three forces can be achieved at very high energies.

The linear combination of the wino and the charged higgsinos - the super-partners of the W and higgs bosons - are the so-called charginos $\tilde{\chi}^{\pm}$. These would be produced in combination with neutralinos $\tilde{\chi}^{0}$ which decay into particles that can not be detected. The decay of the chargino, as implemented in some simplified models [53], into a charged lepton and a neutrino leads to the final state of a charged lepton and a large missing transverse momentum.

Left-right-symmetric model Left-right-symmetric model extensions [54][55] postulate that right-handed fields form $SU(2)_R$ doublets similar to the $SU(2)_L$ doublets introduced for the electroweak theory. In the conventional SM right-handed fermion fields are $SU(2)$ singlets. With this extension the resulting symmetry group is given by

$$SU(2)_R \times SU(2)_L \times U(1). \tag{2.35}$$

Due to the observation of parity violation of the weak interaction the symmetry has to be broken at low energy scales. However, as long as the additional bosons introduced by the $SU(2)_R$ group - $W_R'^{\pm}$ and Z' - are heavy enough, suppressions at low energies can restore cohesiveness with observations. Masses of the $W'^{\pm}_R$ and Z' bosons are obtained via spontaneous symmetry breaking similar to the other heavy electroweak bosons. The $W'^{\pm}_R$ bosons can decay similarly to the SM model W bosons. However, the decay into a right-handed heavy neutrino is possible as well. This would then most likely decay into other SM particles leading to a different final state.

This extension motivates the small neutrino masses observed via the introduction of the so-called seesaw-mechanism [56]. When breaking the left-right symmetry large masses are associated to the right-handed neutrino, which leads as a consequence to very low masses for the left-handed ones.

2.4.4 Leptoquarks

One of the most prominent type of extensions to the SM addressing lepton flavor universality violations postulate the existence of additional particles. These couple to a quark and a lepton at tree level - the so-called leptoquarks (LQ). It was first introduced in 1973 by Pati and Salam [16] in a SU(4)-model. This representation of the LQ introduces flavor changing neutral currents and already lepton family number violations.

Generally in Grand Unified Theories (GUTs) - for example SU(5)-models [57] - quarks and leptons share multiplets and thus require the existence of LQ serving as bosons connecting those. To make these models consistent with observations the lepton-quark symmetry must be broken at the GUT scale which leads to the high masses expected for these bosons. In general 14 different types LQ can be defined divided into scalar and vector fields. Each of them comes with the corresponding anti-particle and the absolute value of the electric charge they carry varies in a range of $1/3\,e$ to $5/3\,e$. This property is defined by the particles they interact with. However, besides GUTs based on SU(15) symmetry groups [58] most models postulate only the existence of a subsets of these 14 LQs. The couplings to different generations of quarks and leptons vary in these models, which introduces lepton flavor universality violations. Due to the fact that one of the LQ decay products is a quark, they carry color themselves.

The following discussion is based on the models used in this thesis as signal hypothesis [59][60]. Scalar LQ coupling fermions is described by a Yukawa Lagrangian using a scalar $SU(2)_L$ triplet representation of the LQ. The three constituents have charge $4/3\,e$, $1/3\,e$, $-2/3\,e$ and each of them introduces the associated anti-LQ. The branching fraction of a LQ into a quark and a charged (anti-)lepton is given by β. Due to electric charge conservation the scalar LQ with charge $4/3\,e$ decays exclusively into a charged anti-lepton and a quark ($\beta = 1$). Most models introduce an additional singlet and triplet vector field - V_1 and V_3. By construction these models allow the decay of a proton, which is not observed. Therefore there must be some mechanism in place which forbids this. Since measurements are expected to be more sensitive to the scalar field its characteristics and phenomenology are discussed in the following.

The Yukawa couplings to different particle generations are expressed by the 3×3 flavor space coupling matrix λ shown in Eq. 2.36. Between rows the lepton flavor index is varied and between columns the index describing the quark type.

$$\lambda = \begin{pmatrix} \lambda_{de} & \lambda_{d\mu} & \lambda_{d\tau} \\ \lambda_{se} & \lambda_{s\mu} & \lambda_{s\tau} \\ \lambda_{be} & \lambda_{b\mu} & \lambda_{b\tau} \end{pmatrix} \tag{2.36}$$

In case such a scalar LQ exists and fully explains the deviations observed for R_{K^*} the following requirement has to be fulfilled:

$$\lambda_{b\mu}\lambda^*_{s\mu} - \lambda_{be}\lambda^*_{se} \sim 1.1\frac{\mathrm{m}_S^2}{(35\ \mathrm{TeV})^2}. \tag{2.37}$$

m_S refers to the mass of the scalar LQ.

Under the assumption that the hierarchies of the quark Yukawa-couplings are similar to the LQ ones it follows that the coupling to the third generation of quarks should be dominant.

In case of kinematical accessibility they can be produced at hadron colliders in two different modes: Singly in combination with a charged lepton at LO and in pairs. The former production channel has the advantage of a larger mass reach in certain parts of the LQ-quark-lepton coupling λ_{lq} parameter space. On the other hand the pair production channel is completely independent of λ_{lq} since its production happens purely via the strong interaction. These aspects are discussed in more detail in Part II.

S_1 is given by the representation of a scalar LQ with charge $1/3\,e$ and $\tilde{S}_1$ by the one with charge $4/3\,e$. These two are used as signal hypothesis in this thesis for the decay into up and down type quarks.

LQ in these models are expected to have masses in the TeV range. Multiple searches have been performed, the most sensitive ones by the big multipurpose detectors ATLAS and CMS located at the LHC. The strongest 95% confidence level mass limit on the first and second generation Leptoquarks have been obtained using $139\,\mathrm{fb}^{-1}$ of data recorded at $\sqrt{\mathrm{s}} = 13$ TeV in proton-proton collisions by ATLAS [61]. The coupling to different quark types have been probed separately. Mass exclusion limits between 1.6 TeV and 1.8 TeV have been obtained under the assumption of $\beta = 1$ for the LQ decay into electron or muons in combination with a light-flavor (up, down, strange), charm or bottom quark. The mass limits on third generation LQ obtained by ATLAS using the same data set are on the order of 1 TeV [62][63]. So far searches using ATLAS data have been performed in the pair production channel exclusively. CMS published results probing similar parameter ranges in the LQ pair [64][65] and single [66][67] production channel. No significant deviations have been observed and the exclusion limits obtained are in the same range.

2.5 Search for new Particles

The existence of a new heavy particle X decaying into SM particles is done most commonly by exploiting the shape in the invariant mass distribution of the decay products.

In the determination of the matrix element $\mathcal{M}$, the propagator of a heavy exchange particle introduces a distinct shape due to the LO s-channel diagram. The relation between the matrix element amplitude contribution $\mathcal{M}_\mathrm{s}$ of the this diagram, originating from this process, the particles' mass m_X and the centre of mass energy of the initial state particles $\sqrt{\mathrm{s}}$ is shown in Eq. 2.38.

$$\mathcal{M}_\mathrm{s} \sim \frac{1}{\mathrm{s} - \mathrm{m}_X^2} \tag{2.38}$$

This creates a resonance around the particles' mass with zero width $\Gamma = 0$. The divergence can be resolved by considering higher order corrections and the time evolution of the on-shell produced particle X. This way the mass m_X can be decomposed into a complex number, where the real part gives its mass m_0 and the imaginary part its width Γ. The following discussion only holds true under the assumption of the s-channel diagram being the dominant contribution including no or only very small interference effects with other processes. By insertion Eq. 2.39 follows for $\mathcal{M}_s$ and thus for $\mathcal{M}$. The cross-section σ is proportional to the absolute square of the matrix element amplitude and is shown in Eq. 2.40.

$$\mathcal{M} \sim \frac{1}{\mathrm{s} - (\mathrm{m}_0 - i\Gamma/2)^2} = \frac{1}{(\sqrt{\mathrm{s}} + (\mathrm{m}_0 - i\Gamma/2)) \cdot (\sqrt{\mathrm{s}} - (\mathrm{m}_0 - i\Gamma/2))} \tag{2.39}$$

$$\sigma \sim \frac{1}{(\sqrt{\mathrm{s}} - \mathrm{m}_0)^2 + (\Gamma/2)^2} \tag{2.40}$$

This leads to a Breit-Wigner curve, which would be visible at a mass m_0. When comparing measured data to simulation effects parton distribution functions are taken into account.

Fig. 2.6 illustrates the typical resonant shape of a Breit-Wigner curve. Exemplary, all curves are centered around 0 and curves are shown for width of 1, 2 and 3. The amplitude of each curve is set to 1 for better comparability. The existence of a new heavy particle decaying into the final state particles considered creates such a signal. The convolution of this signal with the background expectation and additional detector effects can then be observed in the data.

Furthermore, for the decay channels considered in this analysis the invariant mass of the decay particles is not unambiguously accessible. The sensitive variables used are defined in a way to be highly correlated to the invariant mass. In Part I the transverse mass m_T is used. This is, visually speaking, a mass projection, assuming the decay took place in the transverse-plane.

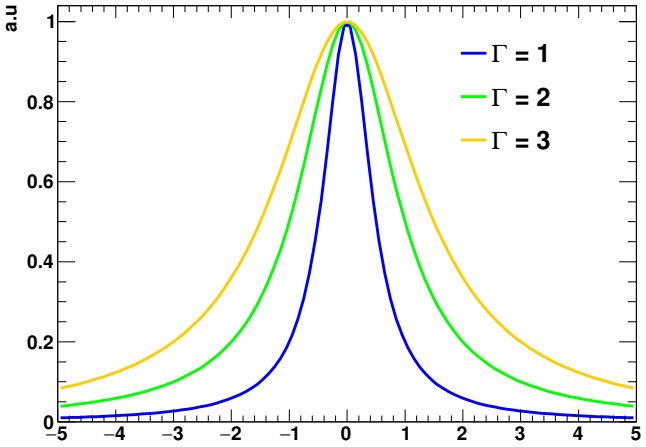

FIGURE 2.6: Breit-wigner curves centered around 0 with varying width. The amplitudes are set to 1 for comparability.

When searching for the decay of singly produced Leptoquarks (in Part II) the problem is of a combinatorial nature. This is addressed by the fact that the pair originating from the decay of a heavy new particle is expected to have a high invariant mass.

Chapter 3

The ATLAS Experiment

This chapter starts in Sec. 3.1 by giving an overview of the accelerator system providing high energy particle collisions to ATLAS. Afterwards various components of the ATLAS detector used to measure and reconstruct event products are discussed. A description of the coordinate system and observables used in analysis is given in Sec. 3.2.1. Then the inner detector, which reconstructs tracks of charged particles, and the calorimeter system are detailed in Sec. 3.2.2 and Sec. 3.2.3. Afterwards in Sec. 3.2.4, the most outer part of the detector - the muon spectrometer - is described. Then an overview of the trigger system is given in Sec. 3.2.5, which is responsible for selecting interesting events to store on disc. The chapter ends with descriptions of methods used to determine the luminosity of data in Sec. 3.3 and a discussion of the data acquisition as well as processing procedures in Sec. 3.4.

3.1 The Accelerator System

Collisions are provided to ATLAS by the Large Hadron Collider (LHC) [13], a 27 km long hadron-hadron collider located underground at the European Center for Nuclear Research (CERN) near Geneva. The accelerator operates either with proton or heavy ion beams. For the searches presented in this thesis proton-proton collisions have been studied at a center of mass energy of $\sqrt{s} = 13$ TeV. The accelerator is designed to operate at $\sqrt{s} = 14$ TeV with an instantaneous luminosity of $L = 10^{34}\,\mathrm{cm}^{-2}\mathrm{s}^{-1}$. This is achieved using 2808 bunches per beam in a time-spacing of 25 ns. Each bunch contains roughly $1.5 \cdot 10^{11}$ protons. Collisions are provided at four interaction points. There are two multipurpose detectors - ATLAS [14] and CMS [68] - as well as LHCb [69] and ALICE [70]. The latter two are designed to target the exploration of flavor physics and to investigate heavy ion collisions. Data used in this thesis was recorded by the ATLAS experiment in the years 2015, 2016, 2017 and 2018. While recording data, a

peak instantaneous luminosity of $2.2 \cdot 10^{34}\,\mathrm{cm}^{-2}\mathrm{s}^{-1}$ has been achieved, by optimizing the filling scheme, the beam focussing and the opening angle of colliding proton bunches.

A pre-accelerator complex - consisting of three additional synchrotrons and one linear accelerator - is used to reach the minimal particle energies required to fill and operate the LHC. Fig. 3.1 shows a schematic view of the accelerator complex at CERN, indicating for each part the year of construction, particle types which can be accelerated and a rough indication of its dimensions. The route of the protons begins at the linear accelerator LINAC2 providing protons with an energy of roughly 50 MeV. Afterwards they pass through a series of three synchrotrons - the BOOSTER, Proton Synchrotron (PS) and Super Proton Synchrotron (SPS). The energy achieved by protons after leaving the BOOSTER is around 1.4 GeV. After cycling in the PS the proton energy is around 26 GeV and in the final acceleration step in the SPS before being fed into the LHC proton energies of 450 GeV are achieved.

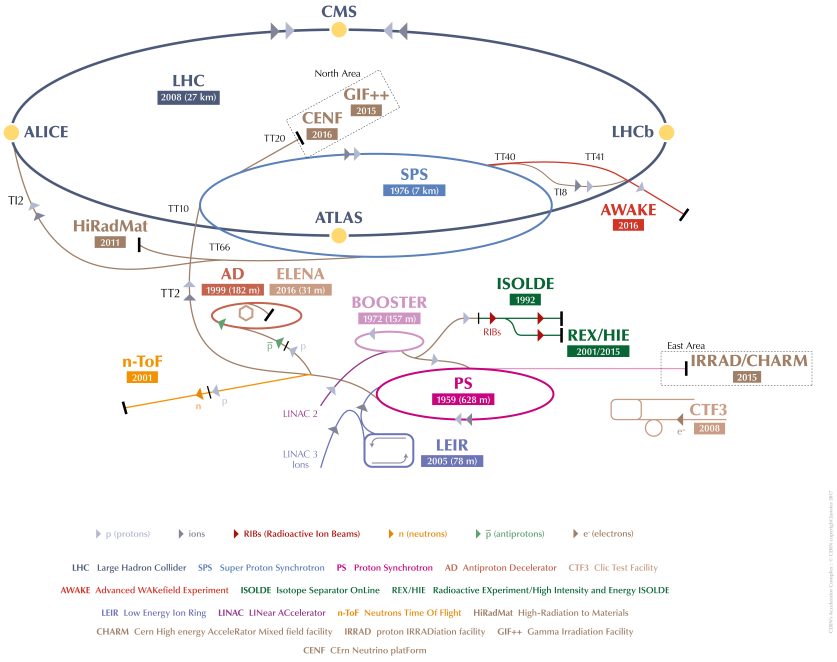

FIGURE 3.1: Schematic view of the accelerator complex at the European Center for Nuclear Research (CERN). [71]

3.2 The ATLAS Experiment

The ATLAS experiment is one of two multipurpose detectors located at a collision point of the LHC. It is constructed with the aim to reconstruct and identify as many different types of particles as possible over a wide phase space range. The cylindrical apparatus is installed around the beam-axis, is symmetric in relation to the interaction point and covers a wide solid angle.

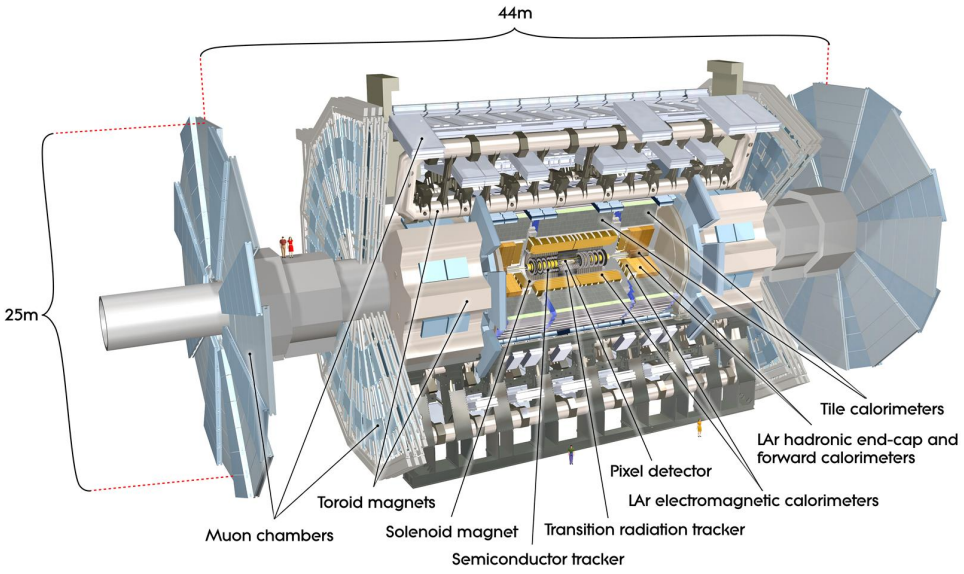

FIGURE 3.2: Schematic view of ATLAS detector. [72]

Fig. 3.2 shows a schematic illustration of the ATLAS detector. The inner most part - the inner detector - reconstructs tracks and vertices of charged particles which are curved by an external magnetic field of 2 T. A solenoid magnet surrounding the inner detector generates this field parallel to the beam-axis. It is followed by the calorimeter system which is used to stop and measure the energy of hadrons, photons, electrons and positrons. The outer most parts of the detector are the muon spectrometers measuring the tracks of (anti-)muons since they traverse the calorimeter system without being stopped. Their tracks are curved toward the beam-axis due to a toroid magnet installed around the muon spectrometers creating a field circular around the beam-axis. The detector systems combined are 44 m long and have a total diameter of 25 m.

3.2.1 The Coordinate System

This thesis uses a coordinate system that has its origin at the interaction point. The y-axis points toward the surface of the earth, the x-axis toward the center of the LHC and the z-axis is parallel to the beam-axis. x, y and z are defining a right-handed coordinate system. The azimuthal angle ϕ lies in the $x-y$-plane and is measured with respect to the x-axis. Its values range from $-\pi$ to π with positive values covering the upper part of the detector and negative values the lower part. The R-axis points toward the direction of the particle's flight path. The polar angle θ is measured with respect to the z-axis and lies in the $R-z$-plane.

Typically, instead of θ the pseudorapidity η and the rapidity Y are studied. Eq. 3.1 shows η and Y of a particle expressed in terms of its absolute momentum $|\vec{p}|$, its momentum component along the beam-axis p_z and its energy E.

$$\eta = \frac{1}{2} \ln \frac{|\vec{p}| + p_z}{|\vec{p}| - p_z} \qquad Y = \frac{1}{2} \ln \frac{E + p_z}{E - p_z} \tag{3.1}$$

For massless particles the pseudorapidity is equal to the rapidity. This can also be assumed in case the particle's energy is significantly higher than its mass. Rapidity differences are invariant under Lorentz boosts along the beam-axis, which is of importance for analyses using data collected in proton-proton collisions. Eq. 3.2 shows the relation between the particles η and θ.

$$\eta = -\ln\left(\tan\left(\frac{\theta}{2}\right)\right) \tag{3.2}$$

In the transverse $x-y$-plane η is 0. It is $+\infty$ along the positive z-axis and $-\infty$ in the opposite direction. Due to the unknown initial momentum of interacting partons, quantities measured in the transverse-plane are studied. Here the initial momentum of interacting partons are assumed to be negligible. A Lorentz boost along the beam-axis can be used to describe the transition from the center of mass frame of the partons to the lab frame. However, quantities in the orthogonal plane are invariant. Therefore in practice the transverse momentum p_T and the transverse energy E_T are studied. Eq. 3.3 shows their definition.

$$p_T = \sqrt{{p_x}^2 + {p_y}^2} \qquad E_T = E \sin\theta \tag{3.3}$$

In the transverse-plane energy and momentum conservation can be used under the assumption that the rest masses of particles leaving signatures in the detector are negligible compared to the initial energy of the parton. This is the reason why the transverse energy imbalance in an event - the so-called missing transverse energy $\vec{E}_T^{miss}$ - is correlated to the vectorial sum of all particle transverse momenta leaving the detector without being reconstructed. Eq. 3.4

shows the the definition of $\vec{E}_T^{miss}$ depending on all particles' transverse energy E_T^i and momenta direction projected on the $x-y$-plane originating from the primary vertex at the interaction point, represented by the unit vector $\vec{e_i}$.

$$\vec{E}_T^{miss} = -\sum_i E_T^i \, \vec{e_i} \tag{3.4}$$

Distances between particle directions ΔR are studied in terms of pseudorapidity and azimuthal angle differences - $\Delta\eta$ and $\Delta\phi$ - as displayed in Eq. 3.5.

$$\Delta R = \sqrt{(\Delta\eta)^2 + (\Delta\phi)^2} \tag{3.5}$$

3.2.2 The Inner Detector

The the detector system [73] closest to the interaction point reconstructs charged particles' tracks and interaction vertices. The so-called inner detector consists of a silicon based pixel and silicon strip (SCT) detector and a transition radiation (TRT) detector. The entire tracker has a diameter of 2.5 m and is 5.4 m long. A surrounding solenoid magnet [74] creates a 2 T magnetic field in line with the beam-axis, which bends charged particles' flight direction passing trough in ϕ direction. This way the transverse momentum can be measured from its tracks curvature with a precision of $\Delta p_T/p_T = 0.05\% \cdot p_T/\text{GeV} + 1\%$.

To avoid a large impact on energy measurements outside the inner detector its material amount between the interaction point and calorimeter system is minimized in its design.

Fig. 3.3 gives a schematic view of the inner detector. The interaction point lies in the center of the picture, followed by multiple layers of pixel and silicon strip detectors as well as transition radiation trackers. The orientation of the detector in the different pseudorapidity regions is visualized as well as the spacial dimensions of the inner detector.

The Pixel-Detector The component closest to the beam-axis is the Pixel-Detector [76][77]. In the central region silicon pixel modules are mounted in four layers cylindrical around the beam-axis covering a pseudorapidity range of $|\eta| < 2.5$. The forward region modules are placed on discs perpendicular to the beam-axis. Ideally, each charged particle traversing all four layers of the pixel detector will allow the measurement of four space points. It provides an average resolution of 115 µm along the z-axis and 10 µm in the $R-\phi$-plane. To achieve this precision approximately 105 million readout channels are utilized. Each silicon pixel module has dimensions of $50 \times 400\,\mu m^2$ in terms of $R-\phi \times z$.

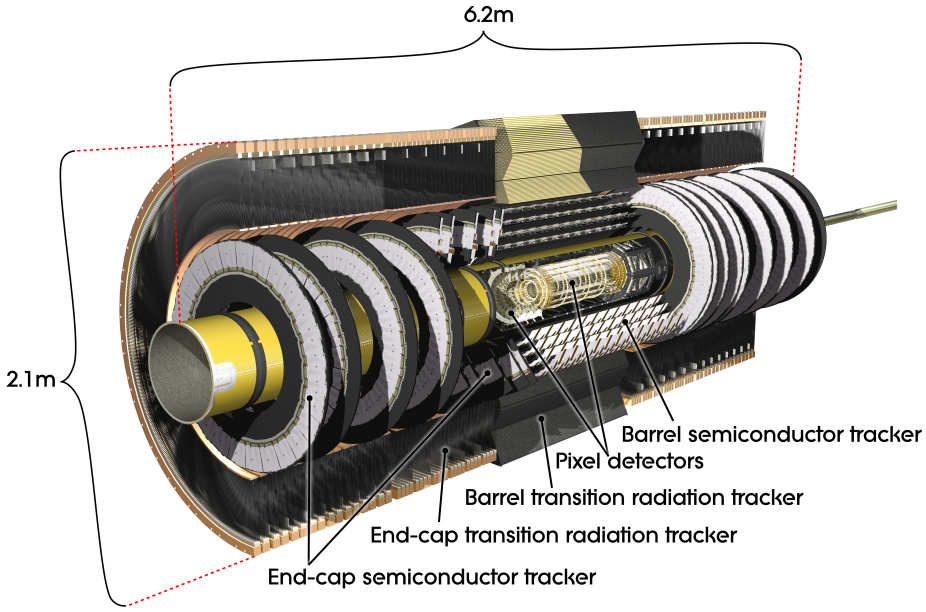

FIGURE 3.3: Schematic view of the tracking system of ATLAS experiment. [75]

The SCT-Detector The next component of the inner detector - the SCT-Detector - aims to provide four additional space points per track for reconstruction. In the central region it consists of eight layers of silicon strip detectors covering a range of $|\eta| < 1.4$. The combined measurements of two layers are used to obtain one space point. In the forward regions ($1.4 < |\eta| < 2.5$) there are nine discs on each side to achieve a resolution of similar magnitude. Each layer is twisted by 40 mrad relative to its neighbor in order to be sensitive to all spacial dimensions of the trajectory. The resolution along the beam-axis is 580 µm and 17 µm in the $x-y$-plane. The total number of the SCT readout channels is around 6.3 million.

The TRT-Detector The final inner detector component consists of an ensemble of tubes filled with Xe gas with a thin wire at the center. Each of these cylindrical chambers has a diameter of 4 cm and is surrounded by a material which emits electromagnetic radiation if a charged particle passes trough. The intensity is proportional to the $\gamma = \mathrm{E/m}$ factor of the particle traversing it. E is the energy of the particle and m its mass. In the central region these chambers are placed parallel to the beam-axis while in the forward regions their orientation is perpendicular. This so-called Transition Radiation Tracker allows to measure two aspects.

On one hand it is used to obtain additional information on the track by operating as drift chambers. Charged particles passing the gas filled volume of a tube create free electrons by ionization. These drift toward the thin wire due to a potential applied. The strong electric field near the wire induces secondary ionization processes creating a sufficient amount of electrons to measure a signal. A spacial resolution of 130 µm is achieved.

On the other hand the intensity of the radiation emitted can be used to classify particle types by their mass. For this an energy measurement conducted in any other component of the detector is required. In practice this information is mainly used to differentiate between electrons respectively positrons and charged pions.

3.2.3 The Calorimeter System

Two processes are responsible for the creation of electromagnetic showers, which are induced by electrons, positrons and photons. The emission of electromagnetic radiation from charged particles when accelerated - the so-called bremsstrahlung - and the creation of an electron-positron pair by the decay of a photon near a nuclei. This process is only possible if the photon carries sufficient energy E_γ larger than twice the electron mass m_e ($E_\gamma > 2 \cdot m_e$). The fact that only two types of processes are involved, which happen in cascades, leads to compact shapes. Since both processes are fully elastic - meaning no energy is invested to dissolve bound states - there is a strict correlation between the number of charged particles and the particles' energy. The energy deposited per cell and by summation per electromagnetic shower is reconstructed by measuring the number of charged particles created. When the energy of the photon is too small to create the mass of an electron-positron pair or at the point where the electron (positron) energy is so low that the energy loss due to other processes than bremsstrahlung - for example ionization - becomes dominant the evolution of an electromagnetic shower stops. This threshold is defined by the critical energy E_C at which the rates of electrons participating in bremsstrahlung and ionization are equal.

In contrast showers induced by hadrons are created by a large ensemble of different process types. Therefore they are less compact and have a larger variation in their spacial shapes. The dominating processes are the inelastic scattering of light hadrons on the protons and neutrons in the nuclei of the absorber material, hadron production and nuclear de-excitation. The energy invested to dissolve bound states is lost and cannot be measured directly. Therefore additional corrections in a more complicated calibration procedure are necessary to reconstruct the energy of strongly interacting particles.

Due to the fact that energy depositions created by electrons, positrons and photons are compact compared to the ones of strongly interacting particles the inner part of the calorimeter system - the electromagnetic calorimeter - is designed to fully stop and precisely reconstruct the energy of electromagnetic energy depositions. The hadronic calorimeter surrounds the electromagnetic calorimeter in order to fully capture energy depositions of hadrons. The material in a calorimeter needs to comply two purposes. On one hand it should initiate and propagate the processes which create the shower, the so-called passive material. On the other hand it needs to measure the number of charged particles created, the so-called active material. Each component of the

ATLAS calorimeter system is constructed with alternating layers of active and passive material. These types of detectors are called sampling calorimeters.

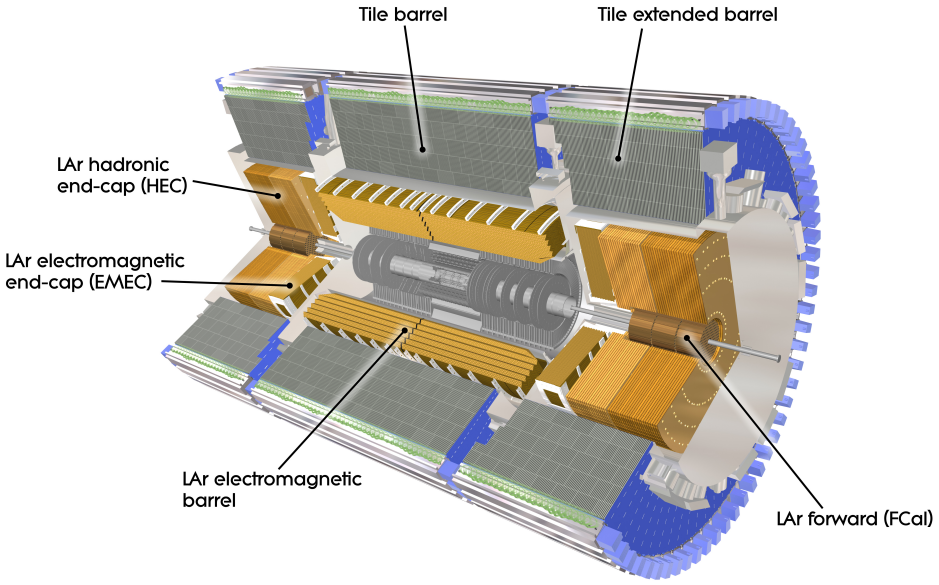

FIGURE 3.4: Schematic view of the calorimeters system of the ATLAS experiment. [78]

Fig. 3.4 shows a schematic view of the calorimeter system of the ATLAS experiment. The cut out shows the interaction point in the middle surrounded by the electromagnetic calorimeter which is displayed in gold, followed by the hadronic calorimeter in gray. The hadronic calorimeter in the end-caps is displayed in a similar color to emphasize the fact that the same active material is used in this region of the detector. Transition regions between different components of the calorimeters are also visible.

The Electromagnetic Calorimeter The system of electromagnetic calorimeters [79] covers a pseudorapidity range of $|\eta| < 4.9$. It consists of the central barrel component ($|\eta| < 1.375$), the end-caps ($1.375 < |\eta| < 3.2$) and the forward calorimeters ($3.1 < |\eta| < 4.9$). The solid angle of $|\eta| < 2.5$ is used for the most precise reconstruction of electrons and positrons due to a higher cell granularity and the accessibility of track information. Only electrons and positrons detected in this region are studied in this thesis which is the reason why the following description focuses on the barrel calorimeter and end-cap components up to $|\eta| < 2.47$. Each of these components is surrounded by a cryostat providing the necessary cooling. The forward system serves simultaneously as electromagnetic and hadronic calorimeter. Objects detected in this region enter the analysis only in the $\vec{E}_T^{miss}$ reconstruction as jets. Therefore relevant components of the forward regions are addressed in the hadronic calorimeter discussion.

The barrel as well as the end-cap components consist of 1.9 mm thick lead layers with a stainless steal coating on the surface. The functionality of these layers is to induce processes involved in

creating an electromagnetic shower. Between those liquid argon is used as a sensitive material. These layers are ordered in a structure similar to an accordion resulting in a ϕ symmetric homogeneous electromagnetic calorimeter. There are three layers in the central region with varying cell size. Each of them is designed with an emphasis on a specific task. The main task of the first layer is to identify $\pi_0 \to \gamma\gamma$ decays, and minimizing mis-identification rates. For this a high resolution in η is desired which is achieved by cells of the size $\Delta\eta \times \Delta\phi = 0.0031 \times 0.982$. For this differentiation the η resolution is most relevant since the electromagnetic showers and their shapes are impacted by the magnetic field. Due to its orientation shapes in ϕ direction are washed out. The main purpose of the second layer is the shower position determination. Additionally, it is designed to absorb most of the particles' energy. The spacial resolution is granted by cells with the size of $\Delta\eta \times \Delta\phi = 0.025 \times 0.0245$. To quantify the stopping power and thickness of an electromagnetic calorimeter the radiation length X_0 is used. It is given by the distance in which a high energetic electron loosing all but $1/e$ of its initial energy by bremsstrahlung. The thickness of the whole electromagnetic calorimeter system is roughly $22 \cdot X_0$ in the central and more than $24 \cdot X_0$ in the end-caps. The second layer alone accounts for 16 radiation lengths. The last layer is used as a transition to the hadronic calorimeter. Its main purpose is to identify depositions which are not fully captured by the electromagnetic calorimeters and correct the energy reconstruction accordingly. For this a larger cell size of $\Delta\eta \times \Delta\phi = 0.05 \times 0.0245$ is sufficient.

The energy resolution of an electromagnetic sampling calorimeter can be expressed in the functional form shown in Eq. 3.6.

$$\frac{\sigma_E}{E} = \frac{c_1}{\sqrt{E}} \oplus \frac{c_2}{E} \oplus c_3 \tag{3.6}$$

The magnitude of the parameters c_i with $i \in \{1, 2, 3\}$ are η dependent. c_1 is called sampling term and is associated to the statistical uncertainty which is connected to the practice of counting charged particles. The contribution of this term is large when measuring low energies. The second term c_2 is the noise term, which is introduced by the electronics used and impacts the total energy resolution independently of the energy value itself. Similar to the sampling term, c_2 becomes less relevant when measuring high energy values. For the measurement of particles with high energy the constant term c_3 becomes dominant which is originating from the calorimeter itself. For the electromagnetic calorimeter system c_3 has a design value of 0.7%. The noise term can be parametrized for a cluster in the barrel region under the assumption of $\langle\mu\rangle = 20$ - the mean number of inelastic proton-proton interactions per bunch crossing - by $c_2 \approx (350 \times \cosh\eta)$ MeV. By design the first term of Eq. 3.6 can be estimated for low pseudorapidities by $10\%/\sqrt{E/\text{GeV}}$. It increases with $|\eta|$ due to the increasing amount of material between the calorimeter system and the interaction point. With all three therms combined,

the electromagnetic calorimeter achieves an energy resolution [80] of approximately 1% for an electron respectively a positron with an energy of 1 TeV.

The Hadronic Calorimeter The hadronic calorimeter system [81] consists of the barrel and the extended barrels in the central region ($|\eta| < 1.7$), the end-caps ($1.7 < |\eta| < 3.2$) and the forward calorimeters ($3.1 < |\eta| < 4.9$). Similar to the electromagnetic calorimeter it is composed of a series of alternating absorber and sensitive layers, characteristic for a sampling calorimeter. The system in the forward region serves simultaneously as electromagnetic and hadronic calorimeter.

In the barrel and the extended barrels iron is used as absorber material and scintillating tiles serve as sensitive layers. These are read out on two sides by photo multipliers which are connected via wavelength shifting fibers. The barrel and extended barrel calorimeters are divided in 64 modules in the azimuthal dimension. To quantify the stopping power of a hadronic calorimeter the interaction length λ is used. The hadronic calorimeter has a thickness of $10 \cdot \lambda$ in the central region, increasing the more particle trajectories are aligned to the beam-axis. In the end-caps copper is used as absorber material and liquid argon as sensitive material. The relative energy resolution achieved in a region of $|\eta| < 3.2$ is given by Eq. 3.7.

$$\frac{\sigma_{\mathrm{E}}}{\mathrm{E}} = \frac{50\%}{\sqrt{\mathrm{E}/\ \mathrm{GeV}}} \oplus 3\% \tag{3.7}$$

The forward calorimeter systems [82] cover the ranges of $3.1 < |\eta| < 4.9$. It consists of three modules on each side. It is designed to reconstruct energy depositions of electromagnetic particles as well as jets. This is the reason why the first layer is made of copper, providing good characteristics to measure the energy of electrons, positrons and photons. The second and third layer consist of tungsten and have the main purpose to measure energies of hadrons. The depth of the forward calorimeters on each side of the detector correspond to approximately 10 interaction lengths. Eq 3.8 displays the energy resolution and is by construction significantly worse than the one achieved in the central region of the detector.

$$\frac{\sigma_{\mathrm{E}}}{\mathrm{E}} = \frac{100\%}{\sqrt{\mathrm{E}/\ \mathrm{GeV}}} \oplus 10\% \tag{3.8}$$

3.2.4 The Muon Spectrometer

In the energy ranges considered muons are minimal ionizing particles and thus pass the calorimeter system without being stopped while loosing only a minor part of their energy. Their typical energy loss in the calorimeter is around 3 GeV. The muon spectrometers [83] are the most outer part of the cylindrical apparatus and serve the function of identifying muons. Furthermore they allow more precise momentum and energy measurements by providing more space points to a track curved by an additional magnetic field. The information collected in the muon system can be used to conduct an independent momentum measurement. Two different types of chambers can be differentiated by their purpose. The trigger chambers are responsible for identifying events with high p_T muons while the target of the precision tracking chambers is to precisely reconstruct the space points and trajectories of muons [84].

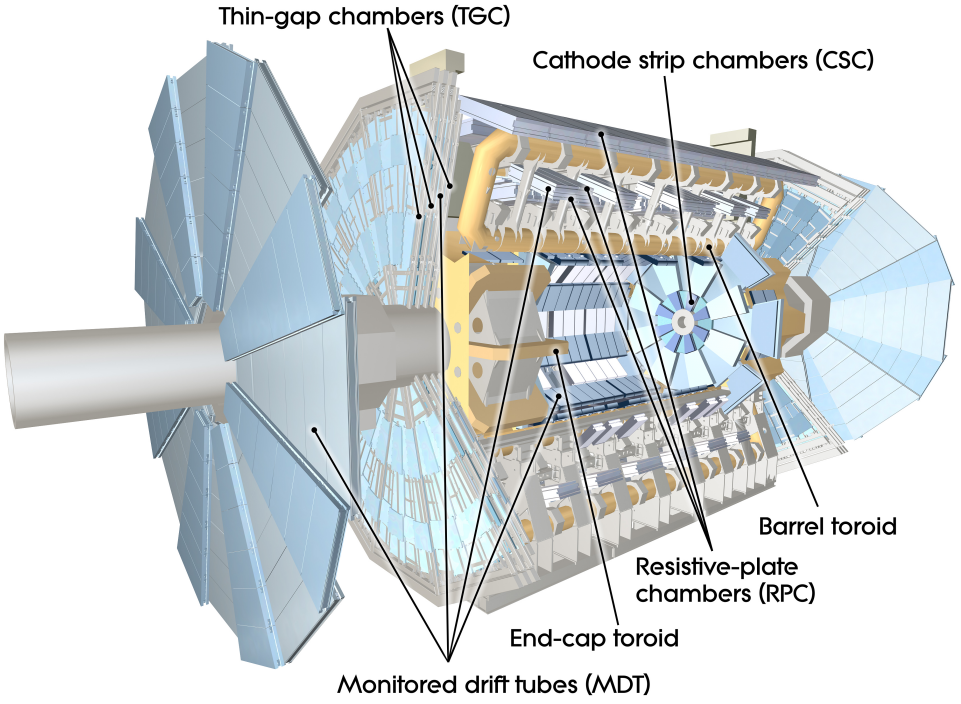

FIGURE 3.5: Schematic view of the Muon Spectrometers of the ATLAS experiment. [85]

The magnetic field present in the muon spectrometer is induced by superconducting air-core toroid magnets [86][87] made out of eight coils each. One large toroid is covering the barrel region of the detector - $|\eta| < 1.4$ - and end-cap toroids cover each side of the detector in pseudorapidity ranges of $1.6 < |\eta| < 2.7$. These toroids create circular magnetic field lines surrounding the beam-axis, which are approximately orthogonal to the trajectory of muons assuming they are created at the interaction point. In the transition regions ($1.4 < |\eta| < 1.6$) between end-cap and barrel toroids a combination of the fields created by neighboring magnets provides bending power with reduced strength. In the central region the bending capacity varies approximately

between 1.5 and 5.5 Tm and between 1.0 to 7.5 Tm in the end-caps. The integral bending power provided is 2.5 Tm and 6 Tm.

Fig 3.5 shows a schematic view of the muon spectrometer in the ATLAS experiment. The cut out illustrates the structure and orientation of the different types of chambers used to identify events containing muons and precisely measuring their trajectory. Additionally, the layout of the toroidal magnets - in the barrel and both end-cap regions - is visualized by the yellow coils.

Trigger Chambers The purpose of the trigger chambers is to identify muons quickly and to give a corresponding signal to the trigger system. This is the reason why they are designed to provide fast signals and use these to identify a corresponding crossing of proton bunches. Since these beam crossings occur at a rate of 25 ns the signals must be read out in a very narrow time window. The space points measured in η and ϕ give additional information to track reconstruction. The trigger chambers in the barrel region ($|\eta| < 1.05$) are so-called Resistive Plate Chambers (RPC) and in the end-cap regions ($1.05 < |\eta| < 2.4$) Thin Gap Chambers (TGC) are used. The RPCs accomplish a resolution of 10 mm in the η- and the ϕ-plane while the TGCs have a precision of 2 to 7 mm in the η- and 3 to 7 mm in the ϕ-plane.

Precision Tracking Chambers The most precise energy and momentum measurement of muons is conducted in the muon spectrometers due to the larger dimensions of the measured trajectory. To obtain a good momentum resolution the precise reconstruction of space points in the plane in which the muons' flight path is bent is required. There are three layers of so-called Monitor Drift Tube (MDT) chambers in the central region of the detector. The innermost layer of MDT chambers covers a pseudorapidity range of $|\eta| < 2.0$ which is extended by Cathode-Strip Chambers (CSC) to cover the regions $2.0 < |\eta| < 2.7$. The second and third layer of MDT chambers cover pseudorapidity ranges of $|\eta| < 2.7$. Each MDT chamber consists of three to eight layers of drift tubes. Per chamber a resolution of approximately 35 µm is achieved. The CSCs are proportional chambers. For ϕ determination the precise time measurement can be used by evaluating the time charges take to drift to the cathodes. This gives a resolution of 5 mm in the plane transverse to the beam-axis and 40 µm in the parallel-plane. A relative momentum resolution of 10% can be achieved for 1 TeV muon with this detector system. There are gaps in the coverage of the muon spectrometers for services and cables of the inner parts - the calorimeters and solenoid magnet - of the detector, most notable at $\eta \approx 0$. This leads to varying reconstruction efficiencies in the transverse-plane.

3.2.5 The Trigger System

While operating the LHC and ATLAS in standard proton-proton collision mode particle bunches collide at a rate of 40 MHz at the interaction point. The necessity of a system preselecting interesting events becomes apparent when considering the amount of information stored per event - $\mathcal{O}$(MB) - and the finite disc space available.

The trigger system of ATLAS consists of two stages. The hardware based level 1 trigger (L1) [88] and a software based high level trigger (HLT) [89]. The L1 trigger is made of the L1Muon system which gets information from the muon spectrometers and the L1Calo system using measurements made by the calorimeters. A topological processor (L1Topo) reconstructs more complex event wide quantities and the central trigger processor (CTP) takes the final decision of the L1 trigger system. The L1 trigger setup in its entirety is a system of high speed electronic boards. Field Programmable Gate Arrays (FPGAs) are extensively used at many steps conducted at a very high speed. During the time the L1 trigger requires to take a decision on each event the signals of the detector are digitized and stored in temporary pipeline memories.

The main tasks of the L1Calo system is to define regions of interest in the detector, reconstruct energy clusters and data formatting. L1Calo modules identify and reconstruct energy clusters induced by different particles. The cluster processors are used in case of electrons, positrons and photons and the jet energy processors (JEP) in case of jets Trigger towers are defined as the sum of calorimeter cells in a window of roughly $\Delta\eta \times \Delta\phi = 0.1 \times 0.1$ in order to save time and computing consumption. Both of these processors use a sliding window algorithm to reconstruct energy clusters. The CP uses smaller window sizes of 2×2 trigger towers compared to the JEP system which searches for jet candidates with varying sizes of $\Delta\eta \times \Delta\phi = 0.4 \times 0.4$, $\Delta\eta \times \Delta\phi = 0.6 \times 0.6$ and $\Delta\eta \times \Delta\phi = 0.8 \times 0.8$.

There are two different types of muon chambers used in the L1Muon system - the RPC and the TGC. As a first step the muon candidate p_T is estimated with a simple tracking algorithm and categorized within six p_T windows ranging from 5 GeV to > 35 GeV. In the second step a coincidence of hits in various specific trigger chambers is required. The ensemble of chambers considered for this is determined using an extrapolated track. A rough estimate of the muon candidates p_T is required for this step. Low p_T muons correspond to a large window, in which the trigger chambers are evaluated for a coincident hit, due to the strong trajectory curvature expected. In the last step the muon to CTP interface (MuCTPI) combines the information of RPC and TGC.

Both sub-systems (L1Muon and L1Calo) pass information of reconstructed objects to the topological processor L1Topo which calculates more complex topological quantities - e.g. angular variables and invariant masses of particle pairs. This information is then fed to the central trigger processor (CTP) whose responsibility is to make the final decision if the event in question is

accepted. The aim of the L1 trigger system is to reduce the approximate event rate of 40 MHz provided by the LHC to roughly $\mathcal{O}(100\,\text{kHz})$.

Events passing the L1 trigger system are forwarded to the high level trigger (HLT) which reduces the event rate from $\mathcal{O}(100\,\text{kHz})$ to $\mathcal{O}(1\,\text{kHz})$ by making decisions on each incoming event within a few milliseconds. For the decisions made by the HLT the full resolution of the calorimeters is available as well as the reconstructed particle track. Additionally, identification and isolation algorithms are applied to objects to evaluate the quality of a signature. During this decision all information connected to the events probed is stored in local buffers.

Triggers which are usually used for searches demand one or multiple particles with high transverse energy or momenta. The energy resp. momentum threshold required gives a handle on limiting the rate at which events are accepted by these triggers. When collecting data to calibrate sub-detectors and monitor operations lower thresholds are used. Trigger rates are limited by the introduction of pre-scales. A trigger with a pre-scale of x accepts $1/x$ of all suitable events. By adjusting these values a constant data recording rate can be assured while the interaction rate and instantaneous luminosity is decreasing over the course of a LHC fill. The typical duration of a fill used for nominal data taking of proton-proton collisions is multiple hours - up to $\mathcal{O}(12\,\text{h})$.

3.3 Luminosity Measurement

In order to specify theoretical model predictions a precise quantification of the data recorded is a necessity. The amount of data is measured using the integrated luminosity L_{int}. To obtain information on this the instantaneous luminosity L while operating the detector is measured and integrated over the run time. The luminosity of the LHC is determined in multiple ways to minimize uncertainties and ensure well known running conditions.

The ATLAS experiment contains multiple detector components which can be used to determine the instantaneous luminosity while running - for example the LUCID [90], the beam condition monitor (BCM) [91] and minimum bias triggers [92]. The principle of each of those is to measure an event rate R and obtain with the knowledge of the inelastic proton-proton scattering cross-section σ information about the instantaneous luminosity L. For this the following correlation is used.

$$R = \sigma \cdot \text{L} \tag{3.9}$$

Considering a storage ring, the event rate R can be decomposed into the product of number of average inelastic interactions per bunch crossing μ, number of bunches b colliding per circulation and the revolution frequency f leading to equation Eq. 3.10.

$$\mathrm{L} = \frac{\mu b f}{\sigma} \tag{3.10}$$

Each sub-detector with the aim to determine the luminosity is measuring μ. In practice this is done by counting inelastic events, tracks or hits in the detector and correcting for acceptance and efficiency effects.

Another relation which describes the instantaneous luminosities in a storage ring is displayed in Eq. 3.11.

$$\mathrm{L} = \frac{b f N_1 N_2}{4\pi\sigma_x\sigma_y} \tag{3.11}$$

Here, N_1 and N_2 are the number of particles per bunch. These quantities as well as the number of bunches b and the revolution frequency f are initial design parameters of the accelerator and are known. The dimensions of the beam overlap in the plane orthogonal to the beam-axis - usually being the beam dimensions - at the interaction point are given by σ_x and σ_y. These are measured by van der Meer (vdM) scans [93]. To conduct these scans only a single bunch of protons is inserted into each beam and the opening angle between both beams is set to zero. With this configuration the beam positions are varied in each dimension separately and the event rate is determined at each step. The profile of the event rate against the beam position follows a Gaussian shape and the width of these distributions can be identified with the beam overlap σ_x and σ_y.

In combination Eq. 3.10 and Eq. 3.11 give a relation between the inelastic cross-section σ, the beam dimensions and μ. Each luminosity detector is calibrated using the inelastic cross-section and vdM scans. The number of particles per bunch and per beam is determined by current measurements conducted by the LHC group. The systematic uncertainty on the luminosity value is originating from varying results obtained from different sub-detectors and specific algorithms as well as from assumptions made to extrapolate the conditions during vdM scans to normal physics run conditions.

3.4 Data Acquisition and Processing

Detector operation and data taking is conducted using the so-called RunControl system [94]. This system initializes, configures and monitors all detector components. A cycle of data taking is called run and is usually connected to one fill of the LHC. Each run is identified by a unique run number. Periods in which the instantaneous luminosity is approximately constant are given by time spans of approximately a minute and are called luminosity blocks. Blocks in which running conditions were good and all sub-detectors crucial for analysis were functional are specified in the so-called Good Runs List (GRL).

In order to record and reconstruct all relevant information of events which are selected by the trigger system, it is crucial to store information of detector components during trigger decisions. Signals are digitized and buffered in pipelines to achieve this. In case an event is accepted in this step the data is transferred to the data acquisition system and stored in local buffers. An event building system is used by the next trigger stage - the HLT - reconstructing the whole event and taking a final trigger decision. In the next steps information of events passing are stored in a RAW data format in the CERN computing center.

The data in the RAW format has to be calibrated and converted into other file formats for efficient usage in analysis. This includes the reconstruction of objects associated to particles created in the beam interaction which is detailed in Ch. 4. The first processing step is performed by the LHC Computing Grid [95][96]. This grid consists of various computer clusters located around the world. These are categorized in different Tiers. There is only one Tier-0 location based at CERN, which is responsible for running reconstruction algorithm and calibrations. The results of those comes in a data format which consists of fully reconstructed physics objects and is called Event Summary Data (ESD). These ESDs are transferred to Tier-1 centers around the world. Here re-calibrations are performed and the data is formatted to Analysis Object Data (xAOD). These files contain objects which are relevant for analysis and can be read by the program ROOT [97] - a statistical analysis framework used in this thesis. Due to limited disc space and the substantial file size of xAODs another pre-selection is performed. On one hand events which are obviously not relevant for the analysis conducted are dismissed. On the other hand information and objects in an accepted event, which are not used later on, are removed as well. The data format obtained is called DAOD. Tier-2 centers provide processing power for simulation and physics analysis, while Tier-3 centers are only used by local users of the corresponding institutes. Data used in this thesis has been stored at the local Tier-3 center *mainzgrid*. Computations conducted for this thesis have been done using the computing cluster *mogon*2 [98].

Chapter 4

Particle Reconstruction and Identification in ATLAS

In this chapter object reconstruction algorithms used for data analysis at the ATLAS experiment are discussed. First in Sec. 4.1 the procedure to reconstruct tracks of charged particles is described, which is followed by an introduction of vertex reconstruction techniques in Sec. 4.2. Sec. 4.3 gives a detailed overview of particle reconstruction and identification algorithms as well as corrections and calibration sequences applied for electrons, muons and jets separately. Finally, in Sec. 4.4 the reconstruction of the missing transverse energy per event is detailed.

4.1 Track Reconstruction

Multiple algorithms [99] are used to reconstruct the path of charged particles inside the ATLAS detector. These reconstructed trajectories are referred to as tracks. In this procedure measurements in the inner detector serve as input. For tracks of muon candidates, signals in the muon spectrometers are considered additionally.

Three dimensional space points and so-called clusters are obtained by running a connected component analysis (CCA) on signals in the silicon tracking detectors. During this procedure pixels and strips within one sensor are combined if the energy deposited passes a certain threshold and share a common edge or corner. Clusters obtained from pixel hits yield one space point each while space points reconstructed from signals in the SCT require two clusters, one on each site of a SCT strip. These are used for the primary track reconstruction.

In a first step loose track candidates are determined by taking all combinatorial allowed ensemble of hits, starting the propagation from a so-called seed. For this perfect helical trajectories and

a uniform magnetic field are assumed. Sets of three space-points serve as a seed to find good-quality tracks. Seed types are classified according to the sub-detector in which the space points have been measured - pixel, SCT and mixed. Additional space points, which are compatible with the seed, are added and a combinatorial Kalman filter [100] is used to create track candidates. In this step material effects are taken into account, by allowing an up to 30% energy loss at each material interaction. One seed can be used to create more than one track candidate in case multiple space-point extensions are compatible.

Afterwards a track score is calculated for each track by comparing candidates to each other in an attempt to solve ambiguity problems. This track score takes the χ^2 of the track fit as well as the presence of a matching localized energy deposition in the calorimeter - so-called clusters - or expected signals, that are missing in sensitive material, into account. The reconstruction of high energy tracks is favored by the inclusion of the logarithm of their momenta in the score. The problem of multiple tracks matching a cluster - indicating in most cases incorrect assignments - is resolved by imposing additional quality criteria on track candidates.

A neural network is used to identify merged clusters. The amount of energy deposited and relative position of pixels in the cluster are used as input parameters. The neural network identifies clusters, that are created by two particles, with an efficiency of 90% and clusters, which are created by at least three particles, with an efficiency of 85%.

In a final step all candidates passing the ambiguity solver are used for a high-resolution fit using with all available information. The positions of the space points and their uncertainty are taken from an additional neural network, which is the reason why the reconstructed cluster positions and space points might slightly differ. The same cluster information which is used in the neural network identifying clusters created by multiple charged particles serves as input. Material effects are incorporated in the fits by the inclusion of an additional noise terms.

4.2 Vertex Reconstruction

Reconstructed tracks serve as an input to vertex finder algorithms [101]. The purpose of those is to assign each track to a vertex. Each reconstructed vertex is required to be connected to at least two tracks. The procedure is using fits to define the ensemble of tracks associated to a vertex and its position. First a seed position for a vertex is selected. Then the best position is obtained by a series of fits taking the seed and all tracks into account. In each iteration, less compatible tracks are considered with a decreasing weight and the vertex position is recomputed. In the last step, tracks, which are incompatible with the final vertex position, are removed and used to reconstruct additional vertices by following the same procedure with the remaining tracks.

The primary vertex in an event is characterized by having the most energetic outgoing particles. For this the vertex with the highest sum over the assigned tracks' transverse momenta squared is identified. The position of this vertex is used to measure the beam position assuming a gaussian distribution. A resolution of about 30 µm along the beam-axis and a resolution better than 20 µm in the transverse direction are achieved. In a second step secondary vertices and photon conversions are investigated using additional algorithms.

The distances of a track to the associated vertex are used to characterize and quantify the compatibility of a track with the respective vertex. The transverse track impact parameter d_0 is given by the shortest transverse distance of the track in question to the beam line and the longitudinal track impact parameter z_0 is the distance along the beam-axis to the associated vertex. Commonly the transverse impact parameter is studied with respect to its uncertainty. $\sigma_{d_0} = d_0/\Delta d_0$ is called the d_0-significance. The longitudinal impact parameters z_0 is addressed in combination to the polar angle θ by usage of the quantity $|z_0 \sin\theta|$. This is motivated by the fact, that the determination of z_0 is more challenging in case the particle is emitted close to the beam-axis.

4.3 Particle Reconstruction and Identification

Since the signature of electrons and positrons in the detector only differs in their curvature direction of their tracks, there will be no explicit differentiation in the following sections. The term electrons includes positrons. They are separated again by addressing the sign of their electric charge. The same holds true for muons and anti-muons. Additionally, the name charged lepton is including all types of charged leptons and anti-leptons considered in the final state of the signal processes, namely: electrons, positrons, muons and anti-muons.

4.3.1 Electrons

In this section the reconstruction of electrons will be detailed. The typical signature is a bent track which is matched to an energy deposition in the electromagnetic calorimeter. Fig. 4.1 shows a schematic view of an electron's flight path drawn in red through the different detector components. In this picture the electron is produced with a transverse distance to the beam line of d_0 and is traversing the different layers of the tracking detectors before reaching the pre-sampler and electromagnetic calorimeter.

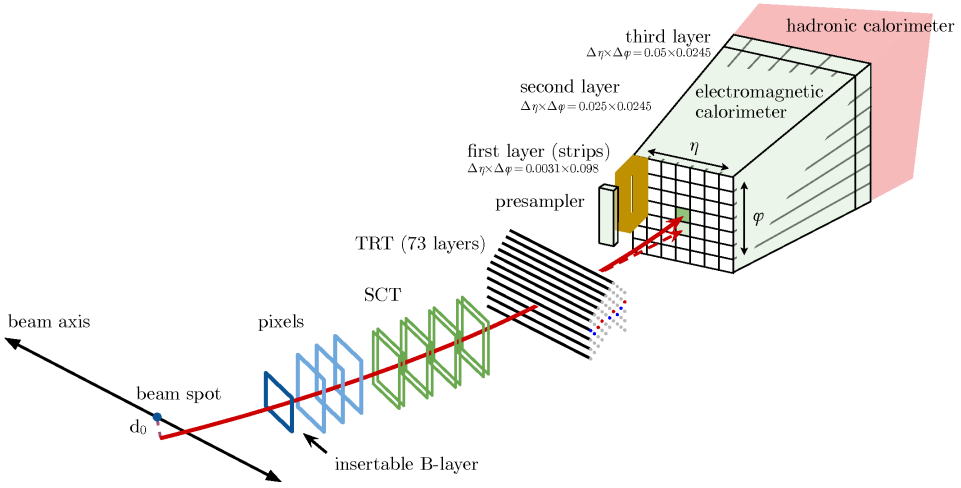

FIGURE 4.1: Schematic view of the path of an electron being produced at the interaction point and its interaction with relevant detector components. [102]

4.3.1.1 Reconstruction

Signals in the calorimeter system serve as a starting point for electron reconstruction [103]. For this so-called topo-clusters are build by combining topological connected calorimeter cells with significant signal to noise ratio. Specifically, cells, that are selected by the '4-2-0' topo-cluster reconstruction algorithm, serve as a starting point for the combination. These must have an energy significance $\sigma_{\text{cell}}^{\text{EM}}$ of more than four. The significance is given by the ratio of the

deposited energy in the cell and the expected noise - which includes electronic sources as well as the typical pile-up noise during normal run conditions. All neighboring cells fulfilling this criterion form a so-called proto-cluster. The pre-sampler and first layer of the electromagnetic calorimeter are not considered in this step to suppress clusters initiated by noise. Then all neighboring cells with $|\sigma_{\text{cell}}^{\text{EM}}| \geq 2$ are assigned as additional seeds and are included together with their neighbors into the proto-cluster. These clusters are merged in case they contain a mutual cell passing the criterion $|\sigma_{\text{cell}}^{\text{EM}}| \geq 2$. In the final step all neighboring cells with $|\sigma_{\text{cell}}^{\text{EM}}| \geq 0$ are added to the cluster. By construction this includes all cells with finite noise. The absolute value of the energy significance is used to avoid introducing a bias toward high energies. Proto-clusters are split in case two or more local maxima are measured. A local maximum is defined as a cell with energy $\text{E}_{\text{cell}}^{\text{EM}} > 500$ MeV and at least four neighbors with a smaller signal. For electron reconstruction only clusters with an energy deposition of more than 400 MeV in the electromagnetic calorimeter are considered. Additionally, clusters must have more than half of their energy deposited in the electromagnetic calorimeter to suppress contributions of pile-up effects.

In the next step tracks, which have already been obtained by the track reconstruction, are re-fitted. For this clusters, which were previously determined, are used to define regions-of-interest and use a Kalman filter formalism based algorithm [100]. This allows to consider bremsstrahlung effects and significant energy losses at each material intersection. These re-fitted, loosely matched tracks are extrapolated to the second layer of the calorimeter. For this either the track momentum or the cluster energy is used as an input parameter. A track is successfully matched to a cluster in case the criteria $|\Delta\eta| < 0.05$ and $-0.10 < \text{q} \cdot (\phi_{\text{track}} - \phi_{\text{cluster}}) < 0.05$ are fulfilled. The requirement of the azimuthal angle is asymmetric, since photons emitted by bremsstrahlung might impact the curvature of the trajectory despite being detected and reconstructed within the cluster.

In the final step so-called super-clusters are formed. For this all topo-clusters are classified as seed or satellite cluster candidates. The latter are required to pass selection criteria, which identifies them to be created by bremsstrahlung or due to topo-cluster splitting. These are added to the seed candidate in question. All topo-clusters are sorted according to their E_{T} starting with the highest one. A seed candidate must have $\text{E}_{\text{T}} > 1$ GeV, which is matched to a track reconstructed using at least four hits in the silicon tracking detectors. If a seed candidate has been identified, neighboring clusters inside a window of $\Delta\eta \times \Delta\phi = 0.075 \times 0.125$ are classified as satellites. In case the best matched track to the satellite candidate is mutual to the one of the seed, the window is widened to $\Delta\eta \times \Delta\phi = 0.125 \times 0.300$. In the end, cells from the pre-sampler and the first three layers of the electromagnetic calorimeter are associated to a given super-cluster. The size of each constituent topo-cluster is limited to a maximal width of $\Delta\eta < 0.075$ in the barrel and $\Delta\eta < 0.125$ in the end-cap region in an attempt to become less sensitive to pile-up effects.

4.3.1.2 Identification

Electron identification algorithms [104] are used to suppress background originating from misidentified objects - which mostly consist of jets. A likelihood based approach is considered for a high signal efficiency and good background rejection. The likelihoods are obtained using a multivariate technique. The full list of independent quantities used, each having sizable discrimination power between background and signal are displayed in Tab. 4.1. They are classified by the detector system used for the specific measurement. The last column specifies rejection power against the potential background sources light-flavor jet (lfj), heavy-flavor jet (hfj) - which are originating from b and c quarks - and photons (γ). Energy ratios and shower width describing the shape of the energy deposits are used to classify the cluster measured in the calorimeter system. Additionally, the transverse impact parameter d_0 as well as the momentum loss of the particle by traversing the inner detector is considered. Finally the spacial match of track and energy deposition in η and ϕ is used.

Using the variables x_i listed in Tab. 4.1 likelihoods for the background L_b and signal L_s hypothesis can be defined as shown in Eq. 4.1.

$$L_b = \prod_i P_{b,i}(x_i) \qquad\qquad L_s = \prod_i P_{s,i}(x_i) \tag{4.1}$$

Here $P_{s,i}(P_{b,i})$ are the probability functions for variable x_i under the signal (background) hypothesis. The optimization of these functions is done using $pp \to Z \to ee$ simulation (See Ch. 5) in the signal case and simulation with two jets in the final state for the background hypothesis.

With these definitions a combined discriminating quantity d is constructed as displayed in Eq. 4.2.

$$d = \frac{L_s}{L_s + L_b} \tag{4.2}$$

The three different identification levels *lhLoose*, *lhMedium* and *lhTight* are defined by varying requirements on the minimal value of d and are optimized to give a signal efficiency of 90%, 80% and 70% over the whole transverse momentum range. Increasing the signal efficiency leads vice versa to a worse background rejection power.

The *lhMedium* and *lhTight* working-point have a rejection factors against multijet background - determined using simulated samples with two jets in final state - which are 2.5 and 5 times higher compared to the *lhLoose* rejection.

detector part	description	rejects
calorimeter systems	R_{had1}: Ratio of E_T measured in the first layer of the hadronic calorimeter and the one in the electromagnetic cluster (for candidates with $\|\eta\| < 0.8$ or $\|\eta\| > 1.37$)	lfj, γ
	R_{had}: E_T ratio measured in the hadronic calorimeter to the one in the electromagnetic cluster (for candidates with $0.8 < \|\eta\| < 1.37$)	lfj, γ
	$f_1(f_3)$: ratio of energy measured in the first(third) layer to the total energy measure in the electromagnetic calorimeter (f_3 only for candidates with $E_T < 80$ GeV and $\|\eta\| < 2.37$)	f_1: γ, hfj f_3: lfj
	$w_{\eta^2} = \sqrt{(\sum E_i \eta_i{}^2) / (\sum E_i) - ((\sum E_i \eta_i) / (\sum E_i))^2}$, with the energy E_i and pseudorapidity value η_i of cell i is correlated to the shower width. The sum is taken in a window of 3×5 cells	lfj,γ
	R_ϕ: energy ratio of 3×3 cell window over 3×7 cell window around the cluster position	lfj,γ
	R_η: energy ratio of 3×7 cell window over 7×7 cell window around the cluster position	lfj,hfj,γ
	E_{ratio}: Ratio of differences between maximum energy deposit and second largest energy deposit to the sum of these energy values	lfj,γ
inner detector	d_0: Transverse track impact parameter	hfj,γ
	$\sigma_{d_0} = d_0/\Delta d_0$: Significance of the transverse track impact parameter	hfj,γ
	$\Delta p/p$: Momentum lost by the track between the perigee and the last measurement point	lfj
combined/match	$\Delta\eta_1$: Pseudorapidity difference between the cluster position and extrapolated track	lfj,γ
	$\Delta\phi_{res}$: ϕ difference between the cluster position in the second layer of the electromagnetic calorimeter and momentum rescaled track times the charge	lfj,γ

TABLE 4.1: Input parameters used in the likelihood based electron identification algorithm. Each of them provide discrimination power between electrons and background. The sub-detector used for measurement and a detailed description is given for each quantity. The last column specifies against which type of background objects each parameter gives the best rejection power - (lfj) light-flavor jets, (hfj) heavy-flavor jets and (γ) photons.

4.3.2 Isolation

Electron candidates are required to be isolated, which ensures a clean signature for efficient object reconstruction as well as reliable energy and momentum measurements [103]. The activity in the immediate environment of the electron is quantified using tracks of nearby charged particles or energy depositions in the calorimeters.

The calorimeter isolation is studied using the variable E_T^{cone20}. Its definition is shown in Eq. 4.3.

$$E_T^{cone20} = E_{T,raw}^{20} - E_{T,core} - E_{T,leakage}(E_T, \eta) - E_{T,pile-up}(\eta) \tag{4.3}$$

It is defined as the total transverse energy detected in a cone with opening angle $\Delta R = 0.2$ around the barycenter of the cluster $E_{T,raw}^{20}$ subtracting the particles energy $E_{T,core}$ and correcting for pile-up and leakage effects. The latter one refers to cases in which the energy deposition is not fully captured in the electromagnetic calorimeters. These corrections are η - and in case of the leakage correction - E_T dependent.

For track based isolation $p_T^{varcone20}$ is considered. All tracks, that are not matched to the cluster, with $p_T > 1$ GeV within a cone centered around the electron track are summed up. Tracks must pass additional quality criteria to be included in the following calculation. Since electrons originating from high momentum heavy particles are expected to be relatively close to others, the cone size is decreasing with p_T. The relation is displayed in Eq. 4.4.

$$\Delta R = \min\left(\frac{10}{p_T/\text{ GeV}}, 0.2\right) \tag{4.4}$$

The isolation criterion [105], that is used in this thesis, is designed to behave uniformly in η providing an isolation efficiency of 90% for electrons with $p_T = 25$ GeV and 99% at $p_T = 60$ GeV. Eq. 4.5 shows the efficiency of this working-point and is achieved simultaneously for the track and calorimeter based isolation. Requirements imposed on $p_T^{varcone20}$ and E_T^{cone20} are derived using $pp \to J/\Psi \to ee$ and $pp \to Z \to ee$ Monte Carlo simulations.

$$\epsilon_{calo/track} = 0.1143 \times p_T/\text{ GeV} + 92.14\% \tag{4.5}$$

4.3.2.1 Corrections and Calibration

The electron energy scale is calibrated using $Z \to ee$ decays [102]. For this the difference in the energy scale between data and simulation is quantified using the relation shown in Eq. 4.6. The energy resolution is parametrized by Eq. 4.7, assuming that the difference in resolution can be addressed by introducing an additional constant term which is added quadratically. Corrections to the energy scale α_i are applied to data, while the energy resolution is weakened by c_i in the simulation.

$$E_i^{data} = E_i^{MC}(1 + \alpha_i) \tag{4.6}$$

$$\left(\frac{\sigma_E}{E}\right)_i^{data} = \left(\frac{\sigma_E}{E}\right)_i^{MC} \oplus c_i \tag{4.7}$$

Here, E_i^{data} and σ_E is the energy measured in data and its uncertainty, E_i^{MC} is the corresponding value in the simulation and α_i is quantifying the scale difference in each pseudorapidity region i considered. c_i gives the difference in energy resolution. The measurement is conducted by studying the invariant mass of the electron pair m_{ij}. Therefore, relations displayed in Eq. 4.6 and Eq. 4.7 are extended using quantities incorporating the two η regions - i and j - in which each electron candidate is detected. The resulting equations are shown in Eq. 4.8 and Eq. 4.9.

$$m_{ij}^{data} = m_{ij}^{MC}(1 + \alpha_{ij}) \qquad \alpha_{ij} = (\alpha_i + \alpha_j)/2 \tag{4.8}$$

$$\left(\frac{\sigma_m}{m}\right)_{ij}^{data} = \left(\frac{\sigma_m}{m}\right)_{ij}^{MC} \oplus c_{ij} \qquad c_{ij} = (c_i \oplus c_j)/2 \tag{4.9}$$

The parameters α_i and c_i are extracted by fitting mass distributions, that are selected in the data and the simulation. The uncertainty on the electron energy scale [103] ranges from 0.2% in the end-caps to 0.04% in the barrel region.

Additional corrections are applied to Monte Carlo simulation to correct for efficiency differences between data and simulation. Efficiencies in data are obtained using a tag-and-probe method in $Z \to ee$ decays and compared to the ones in simulation. The tag-and-probe method allows to collect a relatively pure sample of real electrons in data. This is achieved by selecting one tag electron candidate, which fulfills very strict identification criteria. A second so-called probe candidate builds together with the tag electron a pair with an invariant mass near the Z-peak and is used for efficiency measurements. This method exploits the fact that the Z-peak region is dominated by real electrons. Corrections associated to reconstruction, isolation, identification and trigger efficiencies are considered and assigned on an event-by-event basis, dependent on the electron candidate characteristics. Uncertainties connected to different aspects of reconstruction are estimated by varying parameters and methods when determining these corrections.

4.3.3 Muons

Muons and anti-muons are minimal ionizing particles, in the considered energy ranges. Therefore, they traverse the detector without being stopped. However, they create signals in different components of the detector along their trajectories - namely the inner detector (ID), the calorimeter systems and the muon spectrometers (MS).

4.3.3.1 Reconstruction

The ATLAS muon reconstruction [106] differentiates multiple types of muon objects, which are classified by the detector information accessible.

So-called stand-alone (SA) muons are build by the trajectory, which is reconstructed using only hits in the MS. This is done by building local track segments within each chamber layer and combining them. The track is extrapolated to the beam line while accounting for energy loss effects. These types of muons are mostly used in regions which are not covered by the inner detector $2.5 < |\eta| < 2.7$.

Combined (CB) muons provide the best performance and highest purity, which is the reason why they are used in this thesis. These objects are obtained by conducting track reconstruction separately with the hits in the ID and MS. Afterwards the combination of those two tracks must be successful. Each track, which uses ID measurements as starting point, is required to be associated to a minimum number of hits (> 1 pixel hit, > 5 SCT hits) to be considered.

Two different methods [107] are used to reconstruct the muon in the MS and for the incorporation of the ID and MS information. One of them combines the track parameters of the SA muons and the ID track using the corresponding covariance matrix. The other one uses all space points detected in the ID and MS as input for a global re-fit of the muon track in question. For this the energy loss of a few GeV is taken into account, that occurs when muons traverse the calorimeter system. A combination of both methods is used in an attempt to gather the advantages of each individual one.

4.3.3.2 Identification and Isolation

Muon identification algorithms [84] are applied with the aim to reject fake muons, which originate mostly from pion and kaon decays. The working-point is optimized to minimize systematic uncertainties associated to muon reconstruction and calibration while maximizing the momentum resolutions of tracks with high p_T. Combined muons are required to have at least three hits in at least two layers of the MDT. In the central detector region of $|\eta| < 0.1$ this criteria is relaxed to at least one layer due to worse coverage. Additionally, the compatibility

between the momentum value measured in the ID and MS is tested to suppress contributions of misidentified hadrons.

To improve the performance at high energies muons must have at least three hits in three different precision layers. Regions of the MS in which alignment might be problematic are excluded. These requirements drastically worsen the signal efficiency but guarantee good muon momentum reconstruction.

For reconstructed muons only a track based isolation is required [105]. For this the quantity $p_T^{\text{varcone30}}$ is used. The definition is similar as for the electrons shown in Eq. 4.4 with the only difference being the slightly larger maximal cone opening angle of $\Delta R = 0.3$. The requirement is shown in Eq. 4.10.

$$p_T^{\text{varcone30}} < 0.06 \cdot p_T \tag{4.10}$$

4.3.3.3 Corrections and Calibration

At first order the ATLAS detector simulation [108] - which considers its geometry and material distributions - provides a good modeling of the momentum of reconstructed muons. Additional corrections are applied to the transverse momentum obtained in simulation $\tilde{p}_T$ [84]. Effects influencing the resolution and scale are propagated to the simulated values. This is contrary to the electron corrections, where the energy scale is corrected in data. Consequently, the Z and J/ψ peak position in data do not exactly match the values listed by the Particle Data Group [18]. The calibrations are parametrized using the relation shown in Eq. 4.11.

$$p_T = \frac{\tilde{p}_T + (s_0 + s_1 \cdot \tilde{p}_T)}{1 + \mathcal{N}(\alpha; \mu = 0, \sigma = 1) \cdot \sqrt{(\Delta r_0/\tilde{p}_T)^2 + \Delta r_1^2 + (\Delta r_2 \cdot \tilde{p}_T)^2}} \tag{4.11}$$

s_0 accounts for energy losses in material and s_1 for radial distortions and mis-modeling of the magnetic field integral. Both of them are responsible for correcting the energy scale. $\mathcal{N}(\alpha; \mu = 0, \sigma = 1)$ returns a normal distributed random number for α - statistically varying the weight of the changes applied - to model the impact of resolution effects, which are quantified by the parameters Δr_i. Δr_0 covers energy loss fluctuations and is becoming less influential for high p_T muons. This correction is not considered for ID tracks. Conversely, effects introduced by detector mis-alignment and intrinsic resolution effects, which are addressed by Δr_2, are enhanced for high p_T candidates. The constant term Δr_1 accounts for multiple scattering and local magnetic field distortions.

These corrections are obtained separately for ID and MS momentum measurements using template-based likelihood fits to the p_T spectrum selected in $pp \to Z \to \mu\mu$ and $pp \to J/\Psi \to \mu\mu$

events. The final transverse momentum measurement of a reconstructed combined muon is given by Eq. 4.12.

$$p_T^{CB} = f \cdot p_T^{ID} + (1 - f) \cdot p_T^{MS} \tag{4.12}$$

p_T^{ID} and p_T^{MS} are the already corrected p_T values of the track in the ID and MS while f is a relative weight, that is given to each single measurement in the combination. The resolution for muons originating from $Z \to \mu\mu$ decays is roughly 2.5%, while the momentum scale has been determined with an accuracy of 0.05%.

Similar to the corrections applied to electrons, differences in the efficiencies of algorithms used for reconstruction, isolation and other quality criteria in the data and the simulation are considered. These are determined using tag-and-probe methods of $Z \to \mu\mu$ decays and applied in form of weights to the events in simulation. Differences in isolation, track-to-vertex-association, trigger and muon quality criteria efficiencies are considered. Similar to the electron reconstruction the variation of parameters and methods is exploited to estimate an uncertainty of each correction.

4.3.4 Jets

Jets are the products of high energy partons and consist of collimated ensembles of hadrons and other particles. Most of them are fully stopped in the calorimeter system while depositing their energy.

4.3.4.1 Reconstruction

Reconstruction of jets in physics analyses using Run 1 and early processed Run 2 data relied for the jet finding solely on measurements gathered by the calorimeter system [109]. A more sophisticated jet reconstruction approach is the so-called particle-flow algorithm [110], which combines signals in the tracker system and the calorimeters.

Analogously to the electron reconstruction (Sec. 4.3.1.1), clusters are obtained as the first step [111]. Topo-clusters are created by combining neighboring calorimeter cells fulfilling certain signal over noise ratio requirements. One of the main processes in the shower creation is the inelastic scattering of the parton on a proton or a neutron, which consumes parts of the particles' initial energy to resolve the bound state. Therefore, in the non-compensating sampling calorimeter of ATLAS, the energy directly measured from the cluster does not match the initial energy of the particle and has to be corrected afterwards.

Uncorrected topo-clusters serve as input for the jet finding algorithm in case only calorimeter information is used. Jets reconstructed this way are called topo-jets and used in Part I of this thesis. In combination with a measurement of the primary vertex position, angular measurements of cluster η and ϕ can be recomputed. This improves their accuracy. For topo-jets this is conducted on the output of the jet finder algorithm as first step of the calibration sequence.

Particle Flow Algorithm The particle-flow algorithm on the other hand additionally exploits measurements of charged particles in the tracker to obtain a more precise reconstruction. By the end of LHC Run 2 this approach has become the default in ATLAS physics analysis and is used for jets reconstruction in Part II. The most precise angular and momentum measurements of charged particles in the energy range of $\mathcal{O}(10\ \text{GeV} - 100\ \text{GeV})$ is done by the tracking system. The energy resolution is improved by identifying charged particles and subtracting the corresponding energies from the ensemble of calorimeter clusters. Additionally, the effect of low p_T charged particles within the jet, that are leaving the cone due to the impact of the magnetic field, is weakened. In comparison to the topo-clusters the more precise angular measurement and improved matching efficiency of tracks to vertices allows a stronger mitigation of influence due to in and out of time pile-up. The particle-flow algorithm uses an ensemble of topo-clusters and tracks as input. Each of them has to pass multiple quality criteria. First overlaps between the momentum measurements in the inner-detector and energy measurements in the calorimeter are removed to avoid double counting. For this each track is matched to a single topo-cluster and the expected energy, that uses the cluster position and track momentum, is computed. This value is then used to determine a probability that the charged particles deposited its energy in multiple clusters. This occurs commonly in the evolution of a jet. Afterwards, additional clusters are assigned to each track evaluating the probability at each iteration until its momentum matches the sum of topo-clusters energies. As a last step the energies expected for each particle, which produced a track, are removed cell by cell from the corresponding topo-clusters. In case the remaining energy measurements of a cluster match shower fluctuation expectations of a single particle sufficiently well, all topo-cluster remnants matched are removed. In the end a set of tracks, modified and unchanged clusters are given to the jet finding algorithm. In contrast to topo-jets, the recomputation of the η and ϕ measurements to include information of the primary vertex position are already done for all topo-clusters before the jet finding step. For topo-jets this correction is applied in the sequential calibration.

Jet Finder Algorithm There are two quality criteria which are imposed on jet finding algorithms [112]. They are required to be collinear and infrared safe, meaning that the result does not change under gluon emission with low energy and within a small angle. The algorithm, that is most commonly used in ATLAS, is the anti-k_t4 algorithm. For this two different types

of distances are considered. The one between two input objects (topo-clusters or tracks) - i and j - d_{ij} and the distance of each object to the beam d_{iB}. These distances are defined in Eq. 4.13.

$$d_{ij} = \min(k_{t,i}^{-2}, k_{t,j}^{-2}) \frac{(\Delta Y_{ij})^2 + (\Delta \phi_{ij})^2}{R^2} \qquad d_{iB} = k_{t,i}^{-2} \tag{4.13}$$

Here, ΔY_{ij} and $\Delta \phi_{ij}$ are the differences in rapidity Y and ϕ of the objects - i and j. $k_{t,i}$ and $k_{t,j}$ are their transverse momenta while R is connected to the size of a jet and is set to 0.4.

In case d_{iB} is the smallest distance obtained the object i is identified as jet and removed from the procedure. In case a distance between two clusters d_{ij} is the smallest, they are combined.

Jet Vertex Tagging The rejection of background jets, which originate in most cases from pile-up vertices and detector noise, is achieved using a multivariate technique. The so-called jet-vertex-tagging [113]. In this method a score for each jet is computed, which quantifies the likelihood of its origin in a range of zero to one. A jet with score one is most likely coming from the hard scattering vertex and a score of zero connects the jet's origin to pile-up effects.

Additional quality criteria on the shower development and reconstructed tracks, that match the corresponding jet, are used to further suppress background [114].

4.3.4.2 Corrections and Calibration

Jets found by the anti-k_t4 algorithm are still calibrated according to the EM scale. Multiple corrections are applied in sequence to obtain a good estimate of the initial particles properties [111][110].

The direction of topo-jets is adjusted in order to improve the η resolution as a first step. The four-momentum of each jet is recalculated to point toward the primary vertex and not to the detector center, while the jet energy is kept constant.

A certain amount of energy is subtracted to account for excesses, that are induced by objects originating from pile-up. This is done in two ways. A residual correction is derived from simulation and an area-based p_T density subtraction [115] is applied on an event-by-event basis. The density determination in case of particle-flow jets is more complex to account for differences in the jet constituents between charged and neutral particles.

Then the jet four-momentum is corrected to the particle-level energy scale by adjustments derived from simulation of dijet events and studying jets on generator level. This way the the direction and energy of the jet in consideration is calibrated. Additional corrections are obtained by considering calorimeter MS and ID measurements in the so-called global sequential

calibration. This further improves the energy measurement by reducing the impact of the initial parton's flavor and energy leakage effects. The input variables of this calibration differ for topo- and particle-flow-jets as tracks have already been used for the reconstruction in the latter case.

In a last step a residual in-situ calibration is derived using well measured reference objects and is applied to data only.

The magnitude of the jet energy scale uncertainty is similar for topo- and particle-flow-jets. In the central region ($|\eta| < 1.2$) the scale uncertainty of jets with high transverse momentum ($100\ \text{GeV} < p_T < 500\ \text{GeV}$) is around 1% . The jet energy scale of low p_T particle-flow-jets is more accurate due to the superior momentum measurement in the tracker and is connected to an uncertainty of around 0.5%. For central jets - with p_T larger than $\mathcal{O}(400\ \text{GeV})$ - the performance of topo- and particle-flow-jets is comparable. The minimal relative uncertainty is around 0.5%.

4.3.5 Flavor Tagging

A b quark decays predominantly by the emission of a W boson. This introduces characteristics in the signature of jets originating from b quarks, which allow the classification of jets according to the initial parton's flavor. Similar effects are also observed for other parton types - such as charm and gluons. However, for these objects this so-called tagging is performing worse, due to the less distinct features in their signature.

The signature of a jet, which is initiated by a b quark (a b-jet), consists of a primary and a secondary vertex. The typical spacial distance between those is constrained by the lifetime of a b quark. This can be observed due to the dominance of the decay channel discussed previously. Additionally, in some cases the presence of muons - originating most likely from W decays - inside these jets indicates that the signature in question might be initiated by a b quark. In practice the boosted decision tree (BDT) based MV2 algorithm [116] is used which combines outputs of low level tagging algorithms. These low level algorithms are evaluating track impact parameters as well as conducting a precise secondary and displaced vertex reconstruction. Observables serving as input are among others track multiplicity, the invariant mass of tracks, that are associated with the vertices in question, and their energy fraction. The BDT for the high level tagging algorithm has been trained on a hybrid $t\bar{t} + Z'$ sample. Signal spectra (b-jets) are re-weighted to the one defined as background (c and light-flavor jets) according to their p_T and η. These are considered in the training to avoid biases. Likelihood ratios test the b-jet hypothesis against the background hypothesis. Energy fractions of tracks, that are associated to the secondary vertex, as well as distances between primary and secondary vertex serve among other measurements as input.

The working-point used in the analysis in Part II provides a signal efficiency of 77% and rejections of 4.9 against c-jets, 15 against τ-jets and 110 against light-flavor jets for candidates with a transverse momentum above 28 GeV.

4.4 Missing Transverse Energy

Neutrinos interact only weakly and thus leave the experiment undetected. In order to explore final states with neutrinos, the missing transverse energy $\mathrm{E_T^{miss}}$ is studied [117]. This quantity is correlated to the vectorial sum of all neutrino transverse momenta in the event. Eq. 4.14 shows the definition of the $\mathrm{E_T^{miss}}$, as the missing contribution to energy conservation in the case that all momenta are projected on the plane transverse to the beam-axis.

$$\mathrm{E_i^{miss}} = \mathrm{E_i^{e}} + \mathrm{E_i^{\mu}} + \mathrm{E_i^{jet}} + \mathrm{E_i^{\tau}} + \mathrm{E_i^{\gamma}} + \mathrm{E_i^{softterm}} \tag{4.14}$$

Two components $\mathrm{i} \in \{x, y\}$ are considered in the reconstruction of the total $\mathrm{E_T^{miss}}$, which are summed quadratically as displayed in Eq. 4.15.

$$\mathrm{E_T^{miss}} = \sqrt{\left(\mathrm{E}_x^{\mathrm{miss}}\right)^2 + \left(\mathrm{E}_y^{\mathrm{miss}}\right)^2} \tag{4.15}$$

The azimuthal angle ϕ^{miss} is obtained using simple trigonometric methods and the $\mathrm{E_T^{miss}}$ components which is shown in Eq. 4.16.

$$\phi^{\mathrm{miss}} = \arctan\left(\frac{\mathrm{E}_y^{\mathrm{miss}}}{\mathrm{E}_x^{\mathrm{miss}}}\right) \tag{4.16}$$

Each single terms on the right side of Eq. 4.14 is obtained using reconstructed, calibrated and fully corrected objects. For electrons, muons and jets algorithms are detailed in Sec. 4.3. Methods to obtain reconstructed τ and γ as well as the track soft-term $\mathrm{E_i^{softterm}}$ determination are briefly discussed in the following.

4.4.1 Photon Term

Photons are reconstructed and identified in ATLAS using energy depositions in the electromagnetic calorimeter [118]. Likelihoods are defined, which use variables that are describing the shower shape and evolution as input. Additionally, the case where photons decay into electron-positron pairs inside the inner detector has to be considered. These so-called conversion-photons are reconstructed by evaluating their characteristic signature of two oppositely charged tracks

coming from a secondary vertex, which is consistent with the decay of a massless particle. Furthermore, conversion-vertices are reconstructed from a single track, that has no hits in the innermost sensitive layers. In the end an additional unambiguity resolver is used for classification. One signature can be connected to a conversion-photon - with either a two track or a one track conversion-vertex - as well as an electron.

Photons are required to pass the *tight* identification working-point and to have a transverse momentum of more than 25 GeV to be included in the photon term E_i^{γ} computation. Photons detected in the crack regions $1.37 < |\eta| < 1.52$ and outside of the central region $|\eta| > 2.37$ are discarded. In case a photon is produced in this region of the phase space it may enter into the E_T^{miss} calculation as a jet.

4.4.2 Tau Term

Hadronically decaying taus, which are reconstructed as so-called tau-jets [119][120][121], are entering the tau term E_i^{τ}. Their signatures can be identified by their characteristic low track multiplicity and narrow shower shape compared to jets originating from other particles. The classification is done with the help of a boosted decision tree. Similar to other particle types multiple identification levels are defined for tau candidates. Candidates that pass the *medium* identification, that have a transverse momentum of more than $p_T > 20$ GeV and that are reconstructed within $|\eta| < 1.37$ or $1.52 < |\eta| < 2.47$ are selected for the tau term computation.

4.4.3 Track Softterm

The purpose of the softterm is to cover all not reconstructed - mostly low energetic - objects. Here the softterm is determined using tracking information, precisely tracks which are originating from the primary vertex. All tracks which were already used for the reconstruction of another object are not considered. Tracks are associated to a reconstructed electrons if their angular distance is smaller than $\Delta R < 0.05$ and to a hadronically decaying τ in case $\Delta R < 0.2$ is fulfilled. Tracks are neglected in case they are used in the reconstruction of a combined muon as well. Additionally, they are required to have a transverse momentum of $p_T > 0.4$ GeV and lie within the central region of the detector $|\eta| < 2.5$. Each of them must be reconstructed with at least seven hits in the SCT and pixel detector. They are required to have a small transverse and longitudinal track impact parameters - $d_0 < 1.5\,\text{mm}$ and $|z_0 \sin(\theta)| < 1.5\,\text{mm}$. Due to the mostly low particle energies, which have strongly curved tracks, the vertex association is difficult. This is the reason why the softterm is highly sensitive to pile-up effects.

Chapter 5

Theoretical Predictions and Monte Carlo Simulation

Simulations are used to obtain theoretical predictions and expected detector responses of high energy particle physics processes. This chapter gives an overview of methods and steps used to simulate events in proton-proton collisions. To obtain predictions repeatedly random sampling is conducted to get numerical results. This procedure is commonly called Monte Carlo methods, which is the reason why these samples are also called Monte Carlo (MC) samples in the following. First the steps conducted to simulate a particle physics process in an inelastic high energy proton-proton collision are discussed in Sec. 5.1. This includes the prediction of the hard scattering process, parton shower development, hadronization and the behavior of the proton remnants - the so-called underlying event. Afterwards, the simulation of the detector response will be detailed in Sec. 5.2. Finally, corrections to incorporate effects of variations between the run conditions in data and the assumption made for Monte Carlo simulation are discussed in Sec. 5.3. Programs and tools used in this thesis are introduced in the corresponding analyses (Part I and Part II).

5.1 Physics Event Generation

Generators [122] are used to create physics processes on the basis of their cross-section. The information obtained includes all kinematic characteristics of the final state particles and is called truth information in the following chapters. Fig. 5.1 [123] gives a schematic view of a high energy proton-proton event and visualizes different aspects, which are addressed in the simulation process.

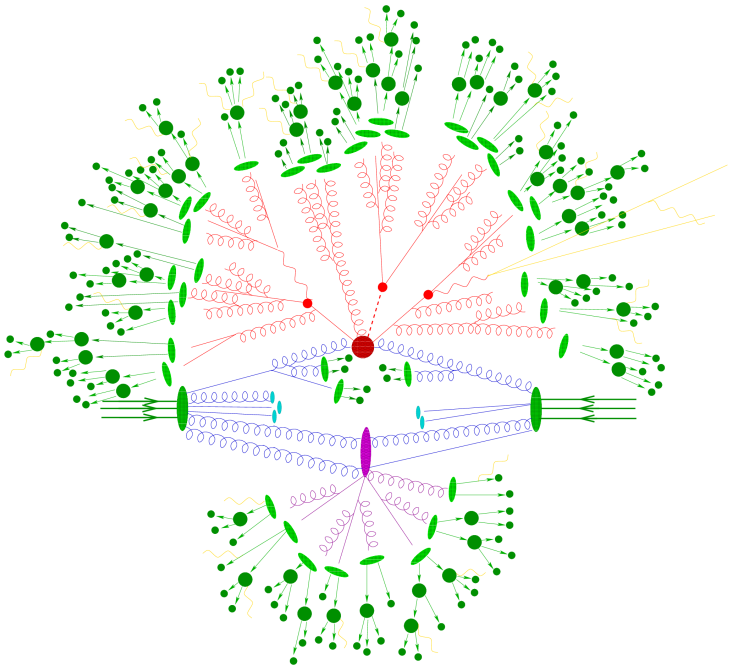

FIGURE 5.1: Schematic view an inelastic proton-proton scattering event. [123]

Events of different processes are simulated according to their cross-section. For this the matrix element of the hard scattering process, which is indicated by the big red circle, is calculated in perturbation theory [22]. Due to the nature of this theory, predictions are only calculated up to a certain precision. Calculations used in this thesis are at leading-order (LO) or next-to-leading-order (NLO). These parton level cross-sections are convoluted with the PDFs, describing the momentum distribution of the incoming partons. Three parallel green lines on each side represent the valence quarks. This convolution gives a probability distribution, which is used to draw randomly generated four-momentum vectors of corresponding product particles. The phase space of outgoing particles is restricted in the generation most of the time. This is done to save computing time, while obtaining sufficient statistics in relevant kinematic regions. All these steps are performed by the so-called event generators [124]. The inclusion of final state radiation (FSR) - in case of real photon - is either performed by the event generator itself or by an additional program.

Particles, that carry color charge initiate extended particle showers. Incoming or outgoing partons emit gluons, that again either into quark anti-quark pairs or more gluons, which might again radiate gluons. This so-called parton shower is simulated with the help of the DGLAP [37][38][39] equations and illustrated by the green ovals, circles and arrows at the margin of Fig. 5.1. These relations describe the momentum transfer as an evolution starting at the momentum scale of the hard scattering process to the scale where perturbation theory breaks down. At this point the remaining partons create color neutral hadrons. In case the matrix element is calculated at NLO the radiation of a parton is included in the generation. This is called initial state radiation (ISR) or final state radiation (FSR) in case its origin is an incoming or

outgoing particle. Parton showers must be valid, in case radiation of low energy partons as well as radiation under small angles is occurring - the soft and collinear limit. Divergences that appear in this calculations are absorbed by the parton shower models [125].

The following creation of hadrons from the partons is done by hadronization models. There are two phenomenological models, which are most commonly used - the so-called string model [126] and cluster model [127]. The parameters that are used in those have been tuned to measured data.

The remnants of the not participating in the hard scattering process partons are left in colored states, which leads to additional parton showers and the creation of low energy hadrons. Similar to the hadronization process, this so-called underlying event is estimated using phenomenological models, that are to data. The proton remnants are indicated by the light blue ovals in Fig. 5.1. Additionally, the possibility of more than one parton scattering in a single proton-proton collision (multi-parton interactions) contributes to the underlying event and is visualized by the purple oval.

Additional corrections are applied to incorporate higher order cross-section calculations and to include in general improved theoretical predictions. They are assigned as weights to each event and are obtained by taking the ratio between the cross-section used in event generation and the available higher order cross-section. These are applied either inclusively - over the whole considered phase space - or dependent on relevant kinematic variables. Negative weights for a small subset of events are possible in the latter case. In combination with limited statistics this may lead to negative total estimates in certain kinematic regions. This non-physical behavior is addressed on a case-by-case basis.

5.2 Detector Simulation

Events are compared to theoretical predictions and their simulated detector responses for analyses. For this a model of the ATLAS detector [108] has been created using GEANT4 [128]. GEANT4 describes the interactions and processes occurring between varying particles and many different materials over a wide energy range. Final state particles are propagated through the different layers and materials of the detector model to simulate signals and the expected responses of different components. These signals are digitized analog to real responses, that are obtained during data taking. At this point the same reconstruction chain is used for simulated events to keep the best compatibility with the collected data.

5.3 Pile-Up Corrections

Assumptions on the running conditions of the LHC are made to simulate processes and the corresponding response of the detector. The average number of inelastic collisions per bunch crossing $\langle\mu\rangle$ - the so-called in time pile-up - has a large impact on the expected activity in the detector. Out of time pile-up is originating from long drift times and signals left by particles inside the calorimeter systems. They can last up to hundreds of nanoseconds, which gives the possibility of overlapping signals, that originate from events initiated by different bunch crossings. Fig. 5.2 [129] shows the integrated luminosity recorded against $\langle\mu\rangle$. $\langle\mu\rangle$ is obtained by averaging over one bunch train - which consists of roughly 70 proton bunches - and a luminosity block - that last a few minutes. Each year of data taking is displayed by a different color.

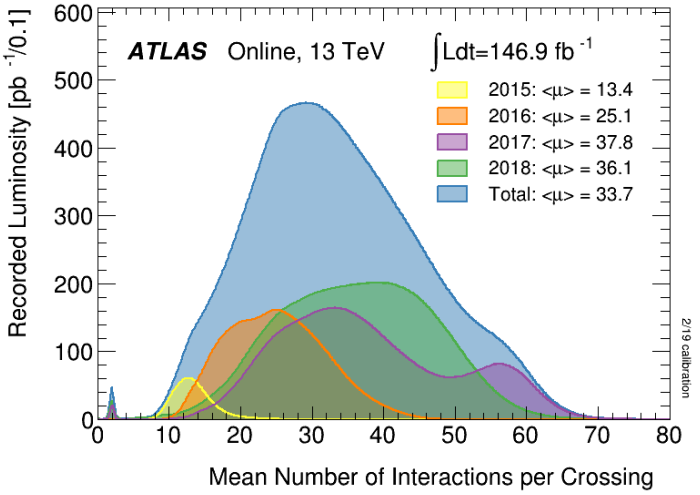

FIGURE 5.2: Recorded luminosity against the average number of inelastic collisions for each year of data taking and in total. [129]

MC samples are corrected on an event-by-event basis [130] since the simulations have been produced before the actual data taking took place and the underlying $\langle\mu\rangle$-profile was known. For this the ratio of the normalized distribution as shown in Fig. 5.2 in the MC and the data is assigned to each event as weight according to its $\langle\mu\rangle$. This procedure increases the statistical uncertainty depending on the agreement of the initial distributions. This re-weighting is only possible if the distributions in data and MC are overlapping in the whole range. Otherwise the ratio to calculate the weight might not be well defined. Since the data-taking conditions differ significantly between years, three sets of simulated samples have been produced in an attempt to make a precise prediction of the distributions separately for different time periods. There are separate sets of MC samples describing run conditions in 2015 and 2016, 2017 as well as 2018.

Part I

Search for New Physics in Final States with One Lepton Plus Missing Transverse Energy

Chapter 6

Motivation

Despite the fact that the Standard Model (SM) has a very successful history describing observation made in high energy particle physics experiments, its conceptual problems have to be addressed. Many theories extend the Standard Model in an attempt to describe the nature of dark matter or to address the hierarchy problem. Often times SM gauge groups are extended. Many of these extensions predict existence of additional heavy particles. For example when introducing additional right-handed fields in $SU(2)$ doublets [54][55], to motivate small neutrino masses, suppressions at low energy scales to restore consistence with observations is required. This is achieved in case the associated new bosons are heavy enough. The data collected in proton-proton collisions at the LHC allows to directly search for new phenomena on the TeV scale.

In this chapter the existence of new heavy charged gauge bosons is investigated. The final state of a charged lepton[1] and the corresponding neutrino is among the cleanest accessible in a hadron collider. This is the reason why the focus of this analysis is on searching for deviations from the SM hypothesis without introducing to many signal model specific assumptions. Multiple well motivated SM extensions which can be probed in events with this final state were discussed in Sec. 2.4.3. As signal to be probed a narrow resonant structure is chosen. For this analysis signals are generated with the Sequential Standard Model (SSM) [52]. It is not well motivated compared to other SM extensions discussed and does not address any shortcoming of the SM but has the advantage of making no strong model assumptions. Additionally, probing this model allows the comparison to other publications since it is widely considered as a benchmark. A heavy partner of the W boson, the W', is postulated, which has the same quantum numbers as its SM partner but a different mass.

[1] The terminology used does not differentiate between particle and anti-particle. This classification is done by referring to its electric charge. The term charged lepton is used for electrons and muons as well as their anti-particle.

The following research is performed on 36.1 fb^{-1} of data collected in 2015 and 2016 by the ATLAS experiment in proton-proton collisions at a center of mass energy of $\sqrt{s} = 13$ TeV. This part is divided into multiple chapters. It starts with a discussion of the analysis strategy and different aspects in Ch. 7. Here, relevant processes and their event topologies are discussed, the analysed data set is detailed and selection criteria are defined. This chapter ends with the description of additional methods used for background estimation, the evaluation of systematic uncertainties and a comparison of the background estimates to spectra observed in data. The second chapter of this part Ch. 8 presents the statistical analysis performed to interpret results. A conclusion and outlook of this search is given in Ch. 9.

Chapter 7

Analysis

The following chapter discusses the analysis strategy as well as general aspects of this search. For this the choice of the sensitive variable is motivated in Sec. 7.1. This includes a detailed discussion of the signal shape and a description of the signal sample generation. Afterwards dominant background processes are examined in Sec. 7.2. This includes programs and tools used to obtain simulated background samples. Then the data set analysed is described in Sec. 7.3. In Sec. 7.4, criteria to select as much signal events as possible while achieving a high background rejection are given, followed by the description of additional methods to obtain background expectations in Sec. 7.5. A data driven method is introduced to cover background contributions from misidentified signatures. Additionally, a procedure to extrapolate background estimates to the high mass region is described. Afterwards in Sec. 7.6 the effects of systematic uncertainties are studied. In Sec. 7.7 measured data is compared to the estimated background. Distributions of quantities which are not sensitive to the signals are considered first to ensure a good background modeling.

7.1 Strategy and Signal Model

The invariant mass ($m_{l\nu}$) spectrum of decay objects originating from a new particle is a good handle to discriminate between the background-only and the signal-plus-background hypothesis. In case the mass of the new particle is in the same energy range as the center of mass energy of the colliding partons, it manifests itself as a resonance in the invariant mass distribution of the decay products (see Sec 2.5). Here, one of the decay particles considered is a neutrino ν. Only its momentum projection on the plane transverse to the beam-axis can be indirectly measured by exploiting its relation to the missing transverse energy $\vec{E}_T^{miss}$. For a precise reconstruction the detection of all particles produced at the primary vertex within the acceptance of the detector is required (see Sec 4.4). Since kinematic properties of the neutrino in beam direction are not

accessible, the transverse mass m_T is used as a sensitive variable in this search. The transverse mass - defined in Eq. 7.1 - uses the three momenta projection to the plane transverse to the beam-axis as input and is strongly correlated to the invariant mass $m_{l\nu}$.

$$m_T = \sqrt{2p_{T,l}p_{T,\nu}\,(1-\cos\Delta\phi)} = \sqrt{2p_{T,l}E_T^{miss}\,(1-\cos\Delta\phi)} \tag{7.1}$$

Here, $p_{T,l}$ is the transverse momentum of the charged lepton and $p_{T,\nu}$ of the neutrino, which can be approximated by the missing transverse energy E_T^{miss}.

7.1.1 Signal Process and Shape

The expected signal shape $\frac{dN}{dm_T}$ can be described by the functional form of a Jacobian peak at the W'-mass $m_{W'}$ given by Eq. 7.2. Similar to the resonant shape expected in the invariant mass distribution of the lepton neutrino pair, a sharp edge at the W' mass is visible. The low mass tail on the other hand is very pronounced. The transverse mass of the neutrino-lepton pair is only close to $m_{W'}$ in case two requirements are fulfilled. On one hand for high mass hypotheses, the W' boson is produced with a small momentum compared to its mass, in which case the decay products are decaying approximately back to back, leading to an opening angle of $\Delta\phi = \pi$. On the other hand the decay must take place in the plane transverse to the beam-axis. The finite width of the decay leads to a few signal events with transverse masses above this edge. However, both of these effects increase the contribution to the low transverse mass tail leading to an asymmetrical signal shape.

$$\frac{dN}{dm_T} \approx \frac{m_T}{m_{W'}^2} \frac{2-\left(\frac{m_T}{m_{W'}}\right)^2}{\sqrt{1-\left(\frac{m_T}{m_{W'}}\right)^2}} \tag{7.2}$$

Additionally, the distribution of the parton-parton luminosity leads to an amplification of the low mass tail. This effect impacts the invariant mass of the decay products and therefore translates to the transverse mass distribution. It becomes more dominant for signal hypotheses with high W' masses, due to the falling Bjorken x-distributions described by the PDF sets and the fact that the probability to find partons with sufficient energy is more unlikely in this region. Fig. 7.1 shows the invariant (a) and transverse (b) mass distributions for several signal mass hypotheses. For shape comparisons the area of each distribution is normalized to one. In the invariant mass distribution $m_{l\nu}$ the characteristic Breit-Wigner peak is visible as well as the low mass tail originating from the parton-parton luminosity distribution. This tail is more pronounced for high mass hypotheses. The transverse mass distribution m_T shows the structure of an Jacobian peak. This includes a sharp edge at the mass of the W' boson and large tails toward low masses.

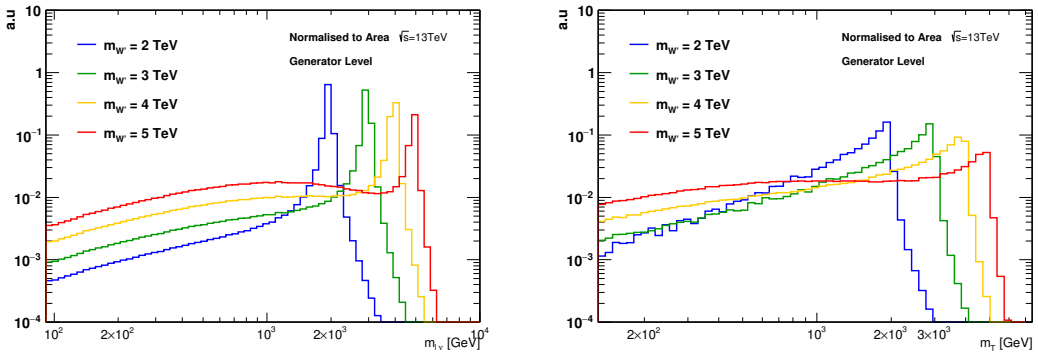

(a) (b)

FIGURE 7.1: Invariant (a) and transverse (b) mass distributions on generator level for several mass hypotheses. Each histogram is normalized to its area for shape comparisons.

7.1.2 Signal Simulation

The aim of the analysis is to cover a wide range of hypothetical pole masses. The necessary signal samples are created by re-weighting a sample which is generated with a flat transverse mass distribution. This approach assures good statistics over the transverse mass range probed by this search. The sample is produced at leading-order (LO) using PYTHIA8.183 [131] and the NNPDF2.3 [132] PDF set. PYTHIA takes care of the parton showering and hadronization, while the final state radiation is modeled by PHOTOS [133]. Couplings of the W' boson are assumed to be identical to the ones of the SM W. Despite this interference effects to the SM W have been neglected to stay more model independent. The mass distribution is at first order flat and obtained by removing the Breit-Wigner term from the event generation of the W' signal samples, which leads to a continuously falling spectrum. To counteract the decreasing behavior, the square of the matrix-element is divided by an $m_{l\nu}$ dependent function.

Such a sample is generated for both search channels - $W' \to e\nu$ and $W' \to \mu\nu$ - while allowing the decay $W' \to tb$, given a boson mass that does not suppress this. Due to the presence of the top quark it is also selected by the signal selection. Additionally, the mode $W' \to \tau\nu_\tau \to e\nu_e\nu_\tau\nu_\tau$ contributes dominantly at low transverse masses. In case neutrinos are emitted in opposite directions, the event has low E_T^{miss} and therefore low transverse mass. This decay is neglected in the analysis since the focus is to have a narrow resonance as signal. The weight applied to an event is given by the cross-section ratio of the desired signal with fixed pole mass $\sigma_{W'}$ and of the flat samples σ_{flat} at the charged lepton-neutrino invariant mass $m_{l\nu}$ in each event.

Additionally, two benchmark signal samples, using the same setup for generation, with fixed pole masses of 4 and 5 TeV have been generated in each channel to validate the re-weighting procedure. Tab. 7.1 gives the signal cross-sections of the considered model in both channels for three pole masses - 3 TeV, 4 TeV and 5 TeV. The mass difference between the electron and muon

process	pole mass	$\sigma \times$ B [fb]
$W' \to e\nu$	3 TeV	11.4
	4 TeV	1.8
	5 TeV	0.4
$W' \to \mu\nu$	3 TeV	11.4
	4 TeV	1.8
	5 TeV	0.4

TABLE 7.1: Signal cross-sections of the W' boson decay for each channel considered at pole masses of 3, 4 and 5 TeV using PYTHIA8.183 as generator and the NNPDF2.3 PDF set.

is negligible compared to the pole mass of the W' bosons probed by this search. Therefore the signal cross-section depends almost exclusively on the pole mass and not on the decay channel.

Fig. 7.2 shows the m_T distribution of the flat sample and the signal templates obtained using the re-weighting procedure for pole masses of 4 and 5 TeV in the muon channel. The analog distributions in the electron channel are identical since the mass difference between the electron and the muon is negligible compared to the W' masses considered. Additionally, the distribution of the validation samples are shown. The distributions obtained by re-weighting agree with the explicitly generated samples within statistical uncertainties, validating the procedures functionality.

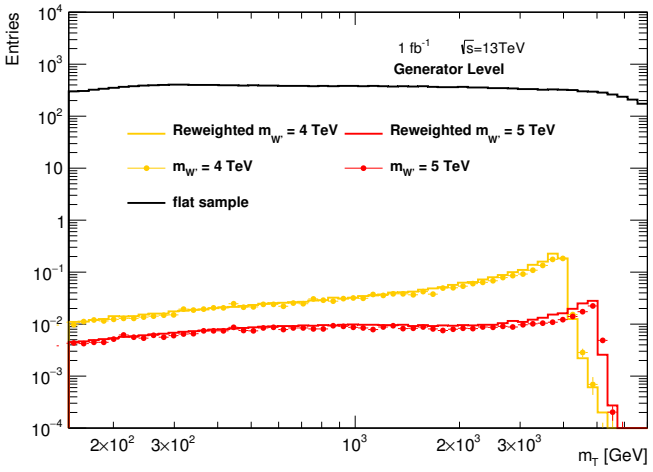

FIGURE 7.2: Transverse mass distribution of the flat signal sample (black line), the validation signal samples with mass hypotheses of 4 and 5 TeV and the signal templates obtained by re-weighting for comparison. The muon channel distributions are shown. All spectra are scaled to 1 fb^{-1}.

7.2 Background Processes

In this section relevant background processes with correctly identified leptons in the final state are discussed. Contributions of misidentified signatures will be discussed in Sec. 7.5.1.

7.2.1 Charged Current Drell-Yan

The dominant irreducible background contributions is the high mass charged current Drell-Yan process. Its tree level Feynman diagram is displayed in Fig. 7.3. A quark anti-quark $q\bar{q}$ pair annihilates to a W boson, with mass $m_W = 80.379$ GeV [18], decaying into a charged lepton and a neutrino. Therefore the contribution of this process in the transverse mass distribution peaks around this value. Only events with high transverse mass contribute to the background since the search region starts well above 100 GeV ($m_T \gtrsim 150$ GeV).

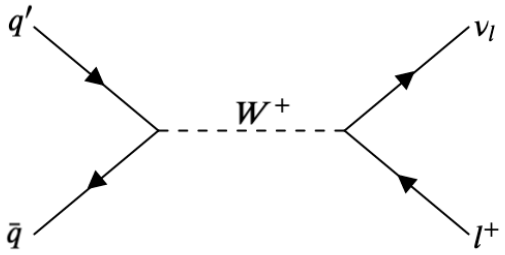

FIGURE 7.3: Leading order (LO) Feynman diagram of the charged current Drell-Yan process decaying leptonically. The charged conjugated process contributes to the total background as well.

The cross-section times branching ratio of these processes is in the order of $\mathcal{O}(10\,\text{nb})$ for a positively charged W boson as well as the negatively charged one. Here, the decay into the selected charged lepton $W \to e/\mu\,\nu$ as well as the subsequent decay via a τ ($W \to \tau\nu \to e/\mu\,\nu\nu\nu$) is included.

Specific new physics models introduce a left-handed W' boson resulting into interference effects between the signal and charged current Drell-Yan process. These effects are not considered in this search to be more model independent. Studies show that when including these into the shape of the signal the sensitivity for this specific model increases. A negative interference slightly below the W' mass leads to sharper shapes which give more discrimination power to the background-only hypothesis [134][135].

7.2.2 Neutral Current Drell-Yan

The leading-order (LO) Feynman diagram of the neutral current Drell-Yan process is shown in Fig. 7.4. A Z/γ^* is produced by $q\bar{q}$ annihilation and decays into a pair of oppositely-charged same flavor leptons l^+l^-. The fact that there are two charged leptons and no neutrino in the final state gives a good handle to reduce the background contribution in the selected region. Considering the decay into electrons or muons, a lepton leaving the experiment undetected results in missing transverse energy strongly correlated to the p_T of the lepton. The E_T^{miss} created this way has a non-vanishing opening angle to its reconstructed lepton partner, due to the mass of the Z. This results in a high transverse mass and the same signatures in the detector as the signal process. Similar to the charged current Drell-Yan the contribution of this background is expected to peak below the search region at the mass of the Z boson around $m_Z = 91.1876$ GeV [18].

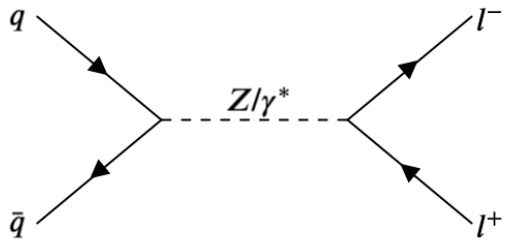

FIGURE 7.4: Tree level Feynman diagram of the neutral current Drell-Yan process decaying leptonically.

Additionally, the process with a $\tau^+\tau^-$ pair in the final state contributes to the total background via W boson decays. τ leptons that decay leptonically lead to a final state of a muon or electron and two neutrinos, while the hadronic decay results in pions. The LO Feynman diagrams of these decays are shown in Fig. 7.5. Due to this, the combination of one hadronically and one leptonically decaying τ lead to exactly one charged lepton and E_T^{miss}. Since the charged lepton is originating from a secondary vertex, criteria on the distance of the extrapolated track to the beam line - the track impact parameters - give suppression power. However, on average, the produced charged lepton has low energy compared to the ones of other processes. In addition the missing transverse energy is composed of the vectorial sum of transverse momenta of multiple neutrinos - which introduces cancellation effects. Thus, the background is expected to peak at even lower masses, leading only to a small contribution to the total background. The total cross-section of the neutral current Drell-Yan process, including the decay into the selected lepton type (electrons or muons) - $Z \to l^+l^-$ - and the subsequent decay via τ leptons, is in the order of a few femtobarn [18].

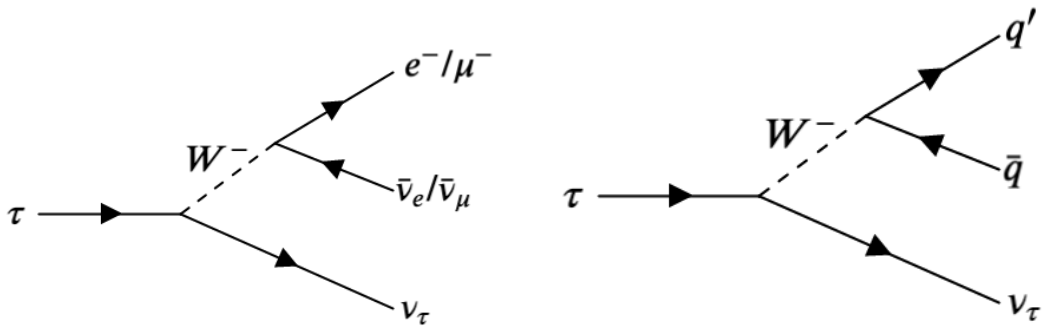

(a) (b)

FIGURE 7.5: LO Feynman diagrams of τ decays. τ leptons decay via a W boson which then decays leptonically or hadronically displayed in (a) and (b).

7.2.3 Top Quark Production

Top quarks decay almost exclusively into a W boson and a bottom quark. These W bosons can then decay either leptonically or hadronically. The tree level Feynman diagrams of the top quark decay are shown in Fig. 7.6. Due to the leptonic decay channel all processes in which at least one top quark is produced contribute to the background.

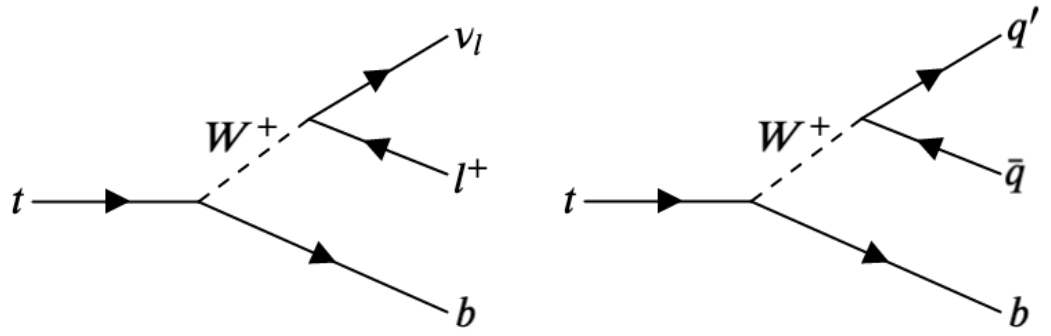

(a) (b)

FIGURE 7.6: LO Feynman diagrams of top quark decays. Top quarks decay into a b quark and a W boson, which then decays into leptons or quarks as displayed in (a) and (b).

The top anti-top production via the strong interaction has the highest cross-section and thus largest contribution. Its Feynman diagrams are shown in Fig. 7.7. One top decaying leptonically gives the selected signature of one lepton and missing transverse energy. In case both top quarks decay leptonically, one lepton might not pass all quality criteria or leave the detector undetected.

Top quarks can also be produced alongside a W boson or other quarks. The cross-sections of these processes are low and give therefore only small contributions to the total background. LO Feynman diagrams of the production of a top quark in association with a W boson are shown

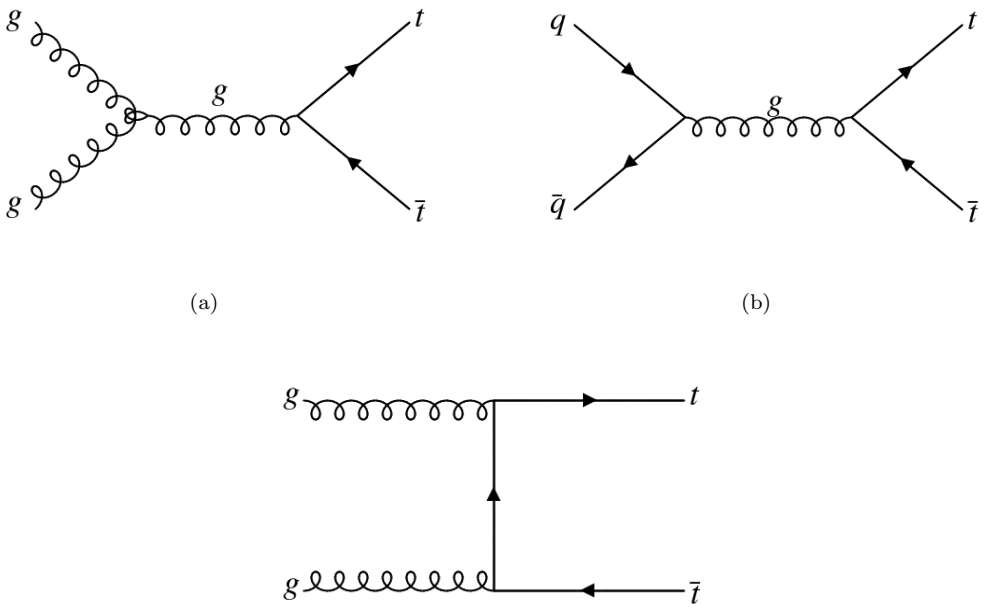

FIGURE 7.7: LO Feynman diagrams of the strong production process of a top anti-top quark pair.

in Fig. 7.8. The mechanism how each final state enters the signal selection follows the one given previously for $t\bar{t}$ processes.

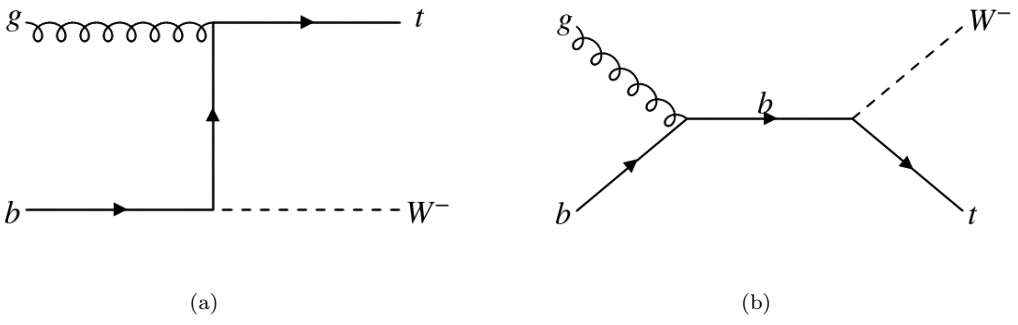

FIGURE 7.8: LO Feynman diagrams of top quark production in association with a W boson.

The top production processes in association with lighter quarks are displayed in Fig. 7.9. These processes enter directly the signal selection.

Considering the sum of all cross-section times branching ratios of the processes including top quarks the total cross-section of these background contributions is in the order of $\mathcal{O}(1\,\text{nb})$ [18].

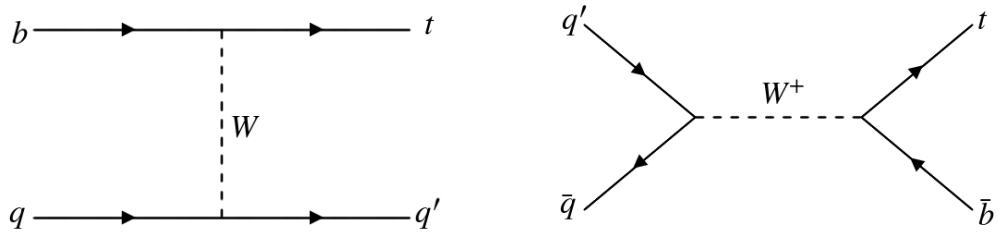

(a) (b)

FIGURE 7.9: LO Feynman diagrams of top quark production in association with lighter quarks.

7.2.4 Diboson Production

Two electroweak bosons can be produced simultaneously. These processes might enter the signal selection since each of their final states can include muons or electrons. The production processes via quark exchange have the highest cross-section and are shown in Fig. 7.10. In addition two electroweak bosons can be produced by a charged triple gauge coupling displayed in Fig. 7.11.

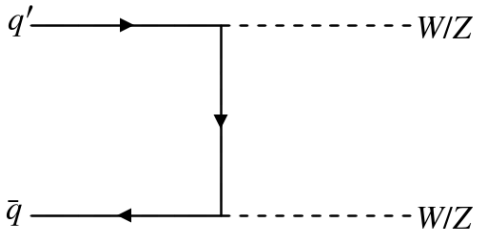

FIGURE 7.10: LO Feynman diagram of the production of two electroweak bosons by quark exchange.

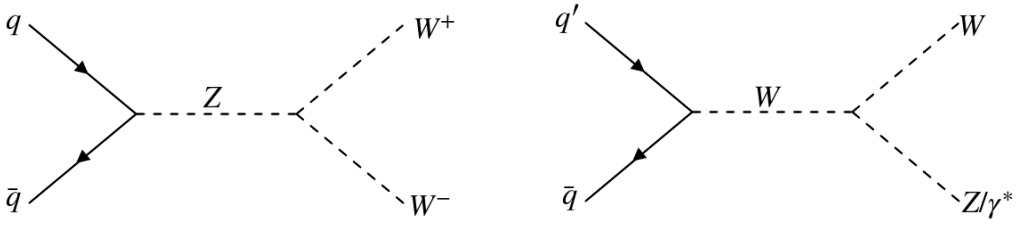

(a) (b)

FIGURE 7.11: LO Feynman diagrams of the production of two electroweak bosons via a charged triple gauge coupling vertex.

The combined cross-section of these processes is low compared to the one of previous discussed background processes and in the order of $\mathcal{O}(10^{-1}\,\text{nb})$ [18], which is the reason why diboson production gives the smallest contribution to the background considered.

7.2.5 Background Simulation

In the following details about the setup, which was used to produce MC samples for the background estimation, are given, starting with the most relevant processes. In App. A.1 there is an overview over all MC samples used, including their generator cross-section, number of events and the corresponding generated integrated luminosity.

Charged Current Drell-Yan The simulation of the dominant charged current Drell-Yan (CCDY) background process uses for the hard scattering matrix element POWHEG-BOX v2 [136] in combination with the CT10 PDF set [137], while PYTHIA 8.186 [131] is used for the modeling of the parton shower and hadronization. QED final state radiation effects are incorporated using PHOTOS [133]. The total background estimate is obtained by combining 18 samples which are generated in different mass windows of $m_{l\nu}$ between 120 GeV $< m_{l\nu} <$ 5000 GeV as well as an inclusive sample describing the on-shell production. This procedure ensures low statistical uncertainties in the whole search region. There are in total six sets of samples - one for W^+ as well as W^- and each lepton generation.

The matrix element used within POWHEG-BOX v2 for the initial simulation is calculated at NLO. On top of that, corrections in the form of event weights are applied to correct the underlying cross-section to incorporate NNLO QCD effects. These are derived using VRAP [138]. Additional corrections [139] to account for electroweak effects beyond QED final state radiation - for example ISR and ISR/FSR interference effects - are obtained using MCSANC [140][141].

Neutral Current Drell-Yan The simulation of neutral current Drell-Yan processes with charged leptons in the final state are produced using the same configurations and programs as the dominant charged current Drell-Yan process. All corrections discussed in the previous subsection in case of the CCDY background are obtained analogously and applied in the same way. To obtain sufficient statistics in the tail of the mass distribution with reasonable computing consumption the samples are again generated in multiple dilepton mass (m_{ll}) intervals. Three sets of samples are considered, one for each lepton generation. The same window sizes have been chosen in the MC sample production.

Top Quark Processes As discussed in Sec. 7.2.3, top quarks decay dominantly into a bottom quark and a W boson. Each production process detailed previously is simulated separately - top anti-top pair production, single top quark production as well as top quark production in association with a W. In the generation of each of these samples POWHEG-BOX v2 [136] in combination with the CT10 PDF set [137] is utilized for the hard scattering process. The matrix elements consider QCD effects up to NLO. Particle decays, hadron shower and parton shower are simulated with PYTHIA 6.428 [142], while PHOTOS [133] is used for the influences of QED FSR.

To save computing consumption events with no lepton in the final state are filtered out directly after event generation.

Diboson Production The simultaneous production of two electroweak bosons (ZZ, WZ, WW, $W\gamma$) constitute the smallest background fraction. These processes are simulated with SHERPA 2.1.1 [143] on NLO in QCD. For this the CT10 PDF set [137] is used. SHERPA is also simulating effects of parton shower, hadronization, particle decays and QED FSR. A unique feature of these samples is that in contrast to previously discussed processes, the final state is defined and not the specific intermediate process. For this search samples with the following final states have been used: $llll$, $lll\nu$, $ll\nu\nu$, $l\nu\nu\nu$, $l\nu qq$ and $llqq$.

7.3 Data Sample

The data set analysed was recorded by the ATLAS experiment in 2015 and 2016. During recording the LHC was delivering proton-proton collisions at a center of mass energy of $\sqrt{s} = 13$ TeV. An integrated luminosity of 36.1 fb^{-1} of data was recorded.

Events for this search were recorded in case a single high energy electron or muon has been identified.

For the electron channel a set of triggers is used for data collection. Their configuration changed in the 2016 data taking period with respect to runs in 2015, which is the reason why a different combination of triggers is required each year. The set used in 2015[1] contains three setups with lower p_T thresholds of 24 GeV, 60 GeV and 120 GeV. In 2016 only two triggers[2] were used with p_T requirements of > 60 GeV and > 140 GeV. No isolation and two efficient identification working-points are used on the trigger level (see Sec. 4.3.1.2).

[1] e24_lhmedium_L1EM20VH, e60_lhmedium, e120_lhloose
[2] e60_lhmedium, e140_lhloose

Events recorded for the muon channel were selected by a single trigger requiring a muon candidate with $p_T > 50$ GeV. This trigger was active in both years of data taking and is therefore used for the whole data set studied in this channel.

Good data quality is ensured by vetoing events in which problems in any relevant detector components have been reported. This includes events with noise bursts in one of the calorimeters since those might give an energy deposition which can be mistaken as a particle in the detector. The traversing of high energy charged particles through electronic modules can cause malfunctioning of the SCT detector. Additionally, while running, parts of the trigger system need to be restarted. Data taking periods in which one of these problems occur are not considered in this analysis.

Fig. 7.12 shows the cumulated integrated luminosity which was delivered by the LHC as well as the fraction which has been recorded by the ATLAS experiment against time. (a) corresponds to the year 2015 and (b) to 2016.

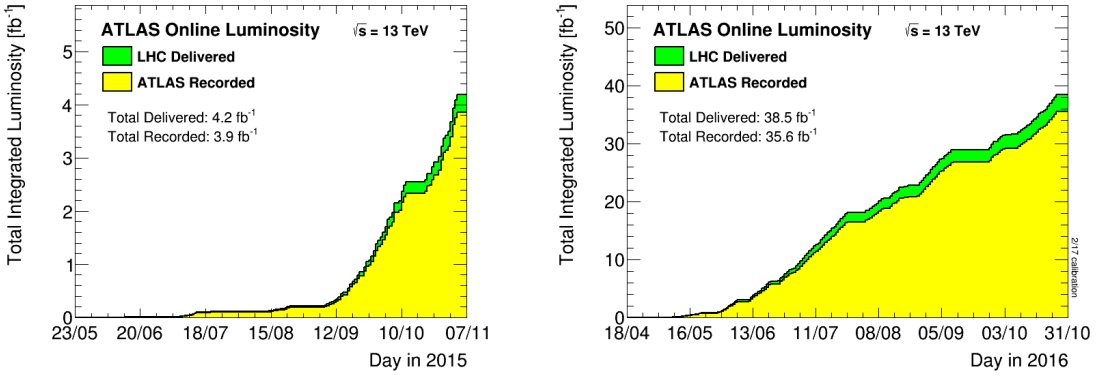

(a) (b)

FIGURE 7.12: Cumulated integrated luminosity against time in 2015 (a) and 2016 (b). The green histogram shows the luminosity delivered by LHC and the yellow one the fraction recorded by ATLAS. [129]

7.4 Signal Selection

This discussion of the signal selection is divided into two parts. First requirements on the objects considered per event are detailed for each channel. Afterwards criteria on event level quantities are described.

7.4.1 Electron Channel Object Selection

Electron candidates need to be reconstructed in the central region of the detector. The inner detector coverage extends up to $|\eta| = 2.5$. Selected candidates are required to have $|\eta| < 2.47$ to ensure that both the track in the inner detector and the energy deposition in the calorimeters are recorded in their entirety. Electrons detected in transition regions $1.37 < |\eta| < 1.52$ between calorimeter end-caps and barrel are rejected due to poor energy resolution. There are multiple measurements of the pseudorapidity of each particle by different detector components. Since the aforementioned cut is made on the calorimeter η, this value is used subsequently.

Electron candidates must have a transverse momentum of more than 65 GeV. This value is chosen to be 5 GeV higher than the lowest trigger threshold used in 2016 to ensure a good trigger efficiency. Trigger perform worse close to the threshold due to a less precise energy reconstruction on trigger level.

Additionally, tracks of electron candidates have to pass a requirement on the significance of their transverse track impact parameter d_0. The d_0-significance σ_{d_0} is given by the distance of the track to the beam line in the $R - \phi$-plane divided by its uncertainty combined with the beam spot uncertainty. It is required to be lower than five. This cut verifies that the electron candidates originates from the primary vertex and rejects most of the electrons coming from secondary decays. The impact of a cut on the longitudinal track impact parameter z_0 has been studied. The efficiency was low in comparison to the gain in background rejection which is the reason why this requirement is neglected in the electron channel.

Furthermore, the identification criteria of the *lhTight* working-point and *Gradient* isolation is required to be fulfilled by electron candidates. More details on identification and isolation algorithms are given in Sec. 4.3.1.2 and Sec. 4.3.2.

7.4.2 Muon Channel Object Selection

Combined (CB) muons are used as muon candidates. Algorithms used for their reconstruction were discussed in Sec. 4.3.3. The detector acceptance in which muon candidates are reconstructed is limited by an explicit requirement of $|\eta| < 2.5$. However, effectively only events with

a muon candidate up to absolute pseudorapidities of 2.4 are selected due to the limited muon trigger chamber coverage.

The transverse momentum of selected muon candidates is larger than 55 GeV. This is again motivated by the fact that triggers perform worse near their momentum threshold.

The requirements on the track impact parameters of muon candidates are stronger compared to the ones for electron candidates. This helps to reject candidates from secondary vertices and additionally suppresses the muon background originating from cosmic rays. The criteria of reconstructed track impact parameter quantities are $|\sin\theta \cdot z_0| < 0.5\,\mathrm{cm}$ and $\sigma_{d_0} < 3$.

Muon candidate reconstruction with good energy resolution is challenging at high transverse momenta. The *highPt* muon identification algorithm was optimized for high energy muon candidates in the detector and is used in this analysis. An isolation requirement is imposed as well using the working-point *LooseTrackOnly*.

7.4.3 Event Level Selection

Events passing either the muon channel or electron channel object selection have to pass additional requirements to reduce the background contamination. Since there is exactly one charged lepton selected in the final state of the LO signal process, events containing more than one are vetoed. This cut significantly suppresses contributions from the neutral current Drell-Yan process and $t\bar{t}$ production. To count additional leptons a second object selection for muon and electron candidates with higher selection efficiency is used. The minimal p_T required is lowered to 20 GeV for these leptons due to the fact that the selected high energy signal lepton is supposed to activate the trigger. Identification working-points with lower background rejections are used. For electron candidates *lhMedium* identification and for muon candidates the *medium* selector working-point are used.

Criteria on E_T^{miss} are applied symmetrically to the transverse momentum requirement in each channel. This results in the selection of events with $E_T^{miss} > 65$ GeV in the electron and $E_T^{miss} > 55$ GeV in the muon channel. In theory most of the W' bosons are produced with low transverse momenta resulting in an event topology leaning toward a symmetric p_T distribution of the decay products. This criterion removes large parts of the charged current DY background. Its contribution is peaking around $E_T^{miss} = 40$ GeV. However, the final state of this background is identical to the one of the signal process, resulting in the fact that the high mass tail of the peak is an irreducible background in the signal region. Combined with the additional lepton veto discussed previously, this cut greatly suppresses $t\bar{t}$ events. The case of both W bosons decaying leptonically is covered by the additional lepton veto, while the majority of semi-leptonically decaying $t\bar{t}$ pairs will fail the E_T^{miss} requirement.

Finally, the selected signal lepton and E_T^{miss} must have a combined transverse mass larger than twice the p_T thresholds. This gives the requirements $m_T > 130$ GeV and $m_T > 110$ GeV in the electron and muon channel, respectively. The additional suppression of background processes with W bosons given by this cut is comparably low after having already applied a cut on E_T^{miss}. However, missing transverse energy can be created by particles leaving the experiment undetected. This leads to an imbalance in the event resulting in additional missing transverse energy. The transverse mass requirement favors a large opening angle $\Delta\phi_{l,E_T^{miss}}$ between the lepton and the direction of the $\vec{E}_T^{miss}$ in the transverse-plane. This ensures a signal-like event topology.

7.4.4 Selection Acceptance and Efficiency

The signal selection has been defined to select the largest fraction of signal events while simultaneously suppressing reducible background as much as possible. Tab. 7.2 and Tab. 7.3 show the selection acceptance and efficiency for each cut applied for a signal with 4 and 5 TeV pole mass for the electron and muon channel separately. Each value listed is calculated with respect to the amount of events passing the previous cut. The requirements limiting the acceptance of the selection are the implicit and explicit η requirements on the leptons as well as to some extent the criteria imposed on the candidates p_T and the events E_T^{miss} and m_T.

electron channel	criteria	$W' \to e\nu$ (4 TeV)	$W' \to e\nu$ (5 TeV)
detector level	event cleaning	100.0%	100.0%
	primary vertex	100.0%	100.0%
	trigger	88.4%	82.8%
lepton level	pseudorapidity	99.2%	99.1%
	$p_T > 65$ GeV	96.3%	95.9%
	d_0-significance	99.8%	99.8%
	identification	92.6%	92.7%
	isolation	98.9%	99.3%
event level	additional electron veto	99.9%	99.9%
	additional muon veto	100.0%	100.0%
	$E_T^{miss} > 65$ GeV	99.3%	98.8%
	$m_T > 130$ GeV	99.8%	99.8%
	total selection efficiency	76.6%	71.2%

TABLE 7.2: Selection efficiency of the electron channel signal selection given for each cut separately with respect to the ensemble of events passing the previous requirement. Values are listed for mass hypotheses of 4 and 5 GeV.

Both tables show that every requirement requested lets most of events with signal-like topology pass given a high pole mass. Most signal events are rejected by the inefficiency of the trigger used with 88.4%(82.8%) - for a 4(5) TeV pole mass - in the electron and 70.1%(67.4%) in the muon channel. The lower efficiency of the trigger and p_T requirements for higher pole masses

muon channel	criteria	$W' \to \mu\nu$ (4 TeV)	$W' \to \mu\nu$ (5 TeV)
detector level	event cleaning	100.0%	100.0%
	primary vertex	100.0%	100.0%
	trigger	70.1%	67.4%
lepton level	combined muon	100.0%	99.9%
	$p_T > 55$ GeV	99.0%	98.5%
	selector cut	80.6%	80.5%
	d_0-significance	99.6%	99.7%
	z_0	98.7%	98.5%
	isolation	99.4%	99.5%
event level	additional muon veto	99.9%	99.9%
	additional electron veto	98.3%	98.6%
	$E_T^{miss} > 55$ GeV	99.5%	98.9%
	$m_T > 110$ GeV	99.8%	99.7%
	total selection efficiency	53.3%	50.6%

TABLE 7.3: Selection efficiency of the muon channel signal selection given for each cut separately with respect to the ensemble of events passing the previous requirement. Values are listed for a mass hypotheses of 4 and 5 GeV.

can be explained by the larger fraction of off-shell W' bosons being produced which populate the low m_T tail. Other notable rejections are introduced by the identification algorithm and p_T cut of the electron channel. Similar to the electron channel, the identification criterion of muons imposed by the selector tool give the largest inefficiencies besides the trigger. All remaining cuts have an efficiency around or above 99% leading to a total selection efficiency of 76.6%(71.2%) in the electron and 53.3%(50.6%) in the muon channel.

Fig. 7.13 displays the product of acceptance and efficiency of the electron and muon channel signal selection against $m_{W'}$. For low mass hypotheses cuts on p_T, E_T^{miss} and m_T limit the acceptance of both channels' selection, leading to values below 0.2 for a pole mass of 150 GeV. Afterwards, the curves are increasing steeply, reaching their maxima for pole masses between 1 and 3 TeV. The highest value in the electron channel is 0.8 and in the muon channel 0.5. The explanation for the difference in signal efficiency is the identification requirement. Criteria imposed on the muon candidates are very strict and candidates which are detected in not perfectly aligned parts of the detector are vetoed due to potential momenta mis-measurements. The energy measurements for electron candidates is done using the calorimeter system which performs better at high energies. Additionally, a worse trigger efficiency of muons due to an incomplete detector coverage is leading to this observation. Toward high pole masses a small decline can be observed. This can be explained by the fact that a larger fraction of the W' bosons are produced off-shell populating the low mass tail (see Sec. 7.1.1). Thus, the p_T, E_T^{miss} and m_T cuts become gain relevance again.

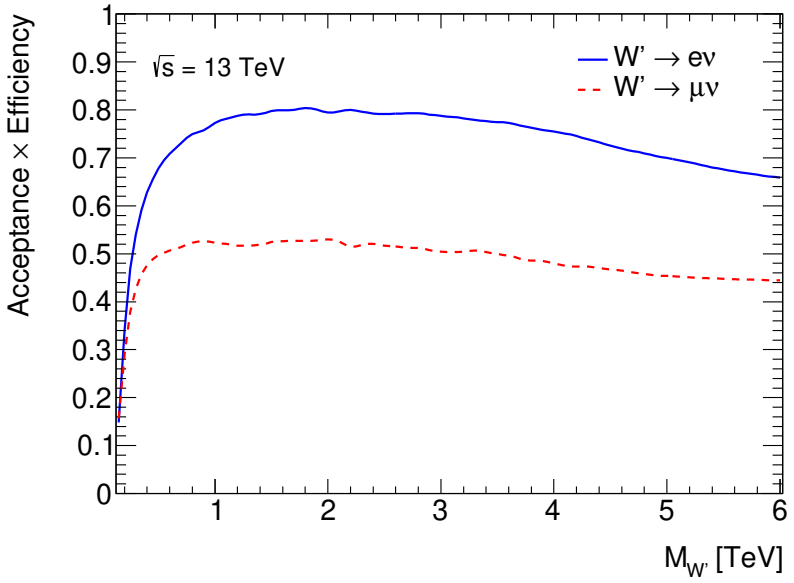

FIGURE 7.13: Product of detector acceptance and selection efficiency for the electron (blue solid line) and muon channel (red dashed line) against W' mass. Each product value is obtained by the ratio of integrals over the transverse mass distribution on generator and reconstruction level.

7.4.5 Cut Flow

Tab. 7.4 and Tab. 7.5 list the number of events measured in data passing each selection criteria in the electron and muon channel. Additionally, the corresponding number of events expected as background (see Sec. 7.2.5) is listed. Background contributions of mis-identified signatures, the so-called fake or QCD background, are not included. The number of background events are scaled to the integrated luminosity measured in data $L_{int} = 36.1\,fb^{-1}$ and corrections are applied on an event-by-event basis. However, corrections accounting for deviations in experimental efficiencies between data and simulation are not included. For each selection step previous to the additional lepton vetoes, it is not unambiguous which corrections should be applied, since most of them are calculated with respect to each lepton candidate's properties.

The final numbers of events selected in each channel, shown in the last row of the corresponding table, have similar orders of magnitude. One has to consider the fact that the fake background is not included for the background numbers and that an excess observed in data here does not necessarily need to be signal-like. The starting numbers - at the GRL requirement - are lower for the background contributions compared to the data. This is expected due to the fact that background numbers are determined only considering contributions from processes with real leptons in the final state. The numbers listed for data on the other hand are obtained from a sample containing entries from misidentified events. Here, the background rejection of the selection is more clearly visible due to the less clean initial sample of events considered. The large difference between the initial electron channel and muon channel is introduced by

the different requirements applied when creating the input files[3] (see Sec. 3.4). When creating the input files for the electron channel all events which do not contain at least one electron candidate with $p_T > 60\,\text{GeV}$ are rejected while for the muon channel this requirement on the muon candidate is loosened to $p_T > 50\,\text{GeV}$. This explains why there are roughly twice the number of events in the muon channel compared to the electron channel, considering the falling spectrum of the lepton candidates p_T.

electron channel	cut	data	background
detector level	GRL	52597554	27491683
	event cleaning	52597554	27491683
	primary vertex	52597554	27491683
	trigger	34366643	21487580
lepton level	pseudorapidity	34171449	20011530
	$p_T > 65$ GeV	25114055	15617102
	d_0-significance	24638919	15560798
	identification	18671614	14929642
	isolation	17420091	14720064
event level	additional electron veto	15809803	13112746
	additional muon veto	15686829	12979591
	$E_T^{miss} > 65$ GeV	2071452	1886193
	$m_T > 130$ GeV	806849	756618

TABLE 7.4: Number of events passing each criteria in the electron channel signal selection. The number in the background column only include contributions from processes estimated with a Monte Carlo simulation. An event is fulfilling each object level criteria if it contains at least one lepton candidate passing the requirement in question.

muon channel	cut	data	background
detector level	GRL	114198117	53594214
	event cleaning	114198117	53594214
	primary vertex	114198117	53594214
	trigger	79371952	40124865
lepton level	combined muon	79197071	40110512
	$p_T > 55$ GeV	53030256	27345611
	selector cut	42569787	23032718
	d_0-significance	32443894	22801032
	z_0	32302122	22705804
	isolation	23875064	22575672
event level	additional muon veto	20423114	19148852
	additional electron veto	20305526	19019055
	$E_T^{miss} > 55$ GeV	4260111	3775157
	$m_T > 110$ GeV	2149932	1996647

TABLE 7.5: Number of events passing each criteria in the muon channel signal selection. The number in the background column only include contributions from processes estimated with a Monte Carlo simulation. An event is fulfilling each object level criteria if it contains at least one lepton candidate passing the requirement in question.

[3] electron channel DAOD_EXOT9, muon channel DAOD_EXO17

7.5 Background Estimation

In this section methods used to estimate background expectations - other than MC simulation - are discussed. Details on MC simulations, tools and generators used are given in Sec. 7.2.5. The data driven method used to derive a background estimate of events with misidentified lepton candidates is detailed in the following. Furthermore, the high mass extrapolation procedure conducted on background estimates which suffer from low statistics in the high mass tail is introduced.

7.5.1 Fake Background Estimation

For the determination of the background, which consists of events with as leptons misidentified objects, the data driven Matrix Method is used. In contrast to other background contributions the direct use of a Monte Carlo simulation is not practical. On one hand the modeling of properties and distinctive variables to identify leptons are not well modeled in Monte Carlo. On the other hand large amounts of events must be simulated to get sufficient statistics in the signal region. This is explained by the fact that the rejection of the signal selection on this background is strong by construction. The use of a data driven method saves computing time and gives a more reliable result.

7.5.1.1 The Matrix Method

The underlying idea of the Matrix Method is to lower the rejection of lepton identification and isolation criteria and measure efficiencies for objects reconstructed in this larger sample to also pass the signal selection. The amount of events selected in both identification categories, combined with the efficiencies for real and fake reconstructed leptons, give a handle on the number of background events in the signal region originating from misidentified signatures. In the following discussion lepton candidates passing the object selection with loosened identification criteria are named *loose*-leptons and the ones passing the signal object selection are denoted as *tight*-leptons. The sample of events passing the additional event level criteria are given by N_L in case *loose*-leptons, and by N_T in case *tight*-leptons are used in the object selection. The real and fake efficiency - r and f - are given by the transition probabilities of real and so-called fake leptons which pass the *loose* object criteria to also fulfill the *tight* requirements. Eq. 7.3 gives a relation between the 'true' amount of events which include a real lepton that is selected N_R, the amount of events including misidentified lepton signatures N_F, and the quantities N_L and N_T. Due to the fact that the ensembles N_R and N_F are defined in an exclusive way, N_T must not be a subset of N_L. This leads to the additional requirement that events in N_L must fail the

tight object selection.

$$\begin{pmatrix} N_T \\ N_L \end{pmatrix} = \begin{pmatrix} r & f \\ 1-r & 1-f \end{pmatrix} \begin{pmatrix} N_R \\ N_F \end{pmatrix} \tag{7.3}$$

The total background in the signal region is represented by N_T and (using Eq. 7.3) given by

$$N_T = rN_R + fN_F. \tag{7.4}$$

While the contribution of processes with real leptons in the final state rN_R is estimated using a Monte Carlo simulation described in Sec. 7.2.5 the fake background contribution fN_F depends on the not directly measurable quantity N_F. To get an expression of N_F in terms of measurable quantities N_T and N_L, the matrix shown in Eq. 7.3 is inverted. This leads to the following relation

$$\begin{pmatrix} N_R \\ N_F \end{pmatrix} = \frac{1}{r(1-f) - f(1-r)} \begin{pmatrix} 1-f & -f \\ r-1 & f \end{pmatrix} \begin{pmatrix} N_T \\ N_L \end{pmatrix}. \tag{7.5}$$

Using Eq. 7.5 the background including misidentified objects N_T^{fake} in the signal selection can be written as

$$N_T^{fake} = fN_F = \frac{fr}{r-f} N_L + \frac{f(r-1)}{r-f} N_T. \tag{7.6}$$

The negative term is proportional to N_T and considers the case of real leptons not being identified properly. These cancellations are embedded in the method itself and result in the fact that a considerable difference between the values of f and r is necessary to derive stable estimates with low statistical uncertainties. In practice it is studied for each event if it passes the specific requirements to enter N_L or N_T and the weight corresponding to the coefficients in Eq. 7.6 is filled into histograms. Low weights and a large number of selected events are needed to obtain a stable estimate. The number of events selected in N_L increases with larger background rejection differences between *loose* and *tight*. Additionally, similar values of f and r lead to high weights since their difference is in the denominator of both coefficients.

The real and fake efficiency - r and f - can be estimated using data and a Monte Carlo simulation. They are given by the ratio of the number of real respectively fake *tight* leptons (N_{tight}^{real}, N_{tight}^{fake}) over the the total number of real or fake *loose* leptons ($N_{loose}^{real}, N_{loose}^{fake}$) as shown in Eq. 7.7. In contrast to the definitions of N_L and N_T, the samples described by quantities with index *loose* are a subset of the corresponding ones with index *tight*.

$$r = \frac{N_{tight}^{real}}{N_{loose}^{real}} \qquad\qquad f = \frac{N_{tight}^{fake}}{N_{loose}^{fake}} \tag{7.7}$$

7.5.1.2 Electron Channel

The *tight* lepton selection is using the same object criteria used in signal selection. In the electron channel for the sample of *loose* leptons no isolation requirement is imposed in contrast to the signal selection. Furthermore, electrons candidates with $p_T < 145$ GeV the *lhMedium* identification working-point and for candidates with $p_T > 145$ GeV the *lhLoose* working-point is used. The usage of the *lhLoose* identification leads to lower fake efficiencies f compared to the *lhMedium* identification while the impact on the real efficiency r is orders of magnitude smaller and thus leads to a more stable estimate in the high mass tail. In the low p_T region the *lhMedium* working-point is used to avoid biases introduced by the identification requirement imposed by the trigger in this kinematic region.

Real Efficiency The real efficiency r is given by the fraction of electron candidates which are associated with a real electron in the *loose* selection passing the *tight* selection criteria as shown in Eq. 7.7. It is determined using the charged current Drell-Yan simulation. Candidates are matched with real electrons at generator level by requiring the angular distance ΔR to be smaller than 0.1. The real efficiency is shown in Fig. 7.14 against the lepton candidates' p_T in different pseudorapidity intervals. It is higher than 90% over the range with a slightly decreasing behavior when going from the central to the end-cap region of the detector. Overall an expected symmetry between positive and negative pseudorapidities is observed.

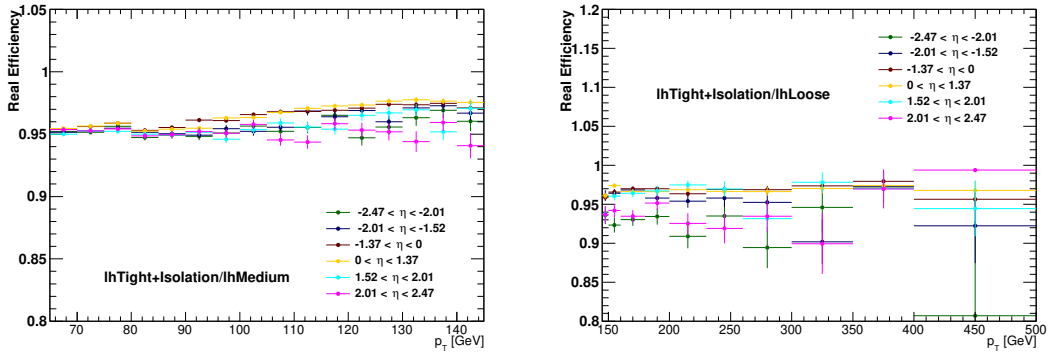

(a) (b)

FIGURE 7.14: Electron candidate real efficiencies against p_T in different η intervals. (a) displays the efficiency for candidates with $p_T < 145$ GeV using *lhMedium* identification in the *loose* selection, while (b) shows the efficiency for candidates with $p_T > 145$ GeV using *lhLoose* identification.

Fake Efficiency The fake efficiency is the probability for candidates reconstructed from signatures, which are not created from an initial electron, passing the *loose* selection to also pass the *tight* selection. This efficiency can not be reliably determined in simulation since the composition of the object ensemble which fake electron candidates is hard to estimate and mostly unknown. This is the reason why the object samples used in the determination are selected in data by imposing requirements to suppress the contribution of real electrons. In most cases these are produced in electroweak boson decays.

To suppress electrons produced by W boson decays, the missing transverse energy is required to be lower than 55 GeV. This cut is also chosen to avoid overlap between the selected sample and the signal region. Additionally, events with two electron candidates passing the *lhLoose* identification requirements and $p_T > 20$ GeV, whose combined invariant mass is in a 20 GeV window around the Z peak are rejected. This suppresses electrons coming from on-shell Z decays. Off-shell decays are taken care of by vetoing events containing more than one electron candidate passing the $lhMedium$ identification.

Even after applying these cuts the contribution of candidates created by real electrons is not negligible in the selected samples. Therefore, the contribution is estimated by applying the same criteria to simulated samples of all processes with real electrons in the final state. The real electron contribution determined this way is subtracted before taking the ratio.

$$f = \frac{N^{fake}_{tight,Data} - \sum N^{fake}_{tight,MC}}{N^{fake}_{loose,Data} - \sum N^{fake}_{loose,MC}} \tag{7.8}$$

Here, the sum over the samples describing different processes leading to electrons is taken and the $fake$ symbol implies that the criteria to suppress real electron contributions are applied.

Fig. 7.15 displays data as well as contributions of real electrons estimated with MC for each process stacked against the candidates' p_T. In (a) and (b) candidates with $p_T < 145$ GeV are shown for the *loose* and the *tight* selection. In (c) and (d) the analog distributions are depicted for objects with high transverse momenta. Shapes present in data and real electron contributions is very similar in each region. When considering equidistant p_T intervals, falling spectra are observed. The rise in the distributions in (c) and (d) are only due to binning effects. For candidates with highp_T the real electron contribution is around 25% in the *loose* selection and 60% in the *tight* selection. The identification working-point with higher background rejection which is used in the *loose* selection for candidates with $p_T < 145$ GeV leads to a high electron contribution of approximately 65%. In the *tight* selection this value increases to 80%.

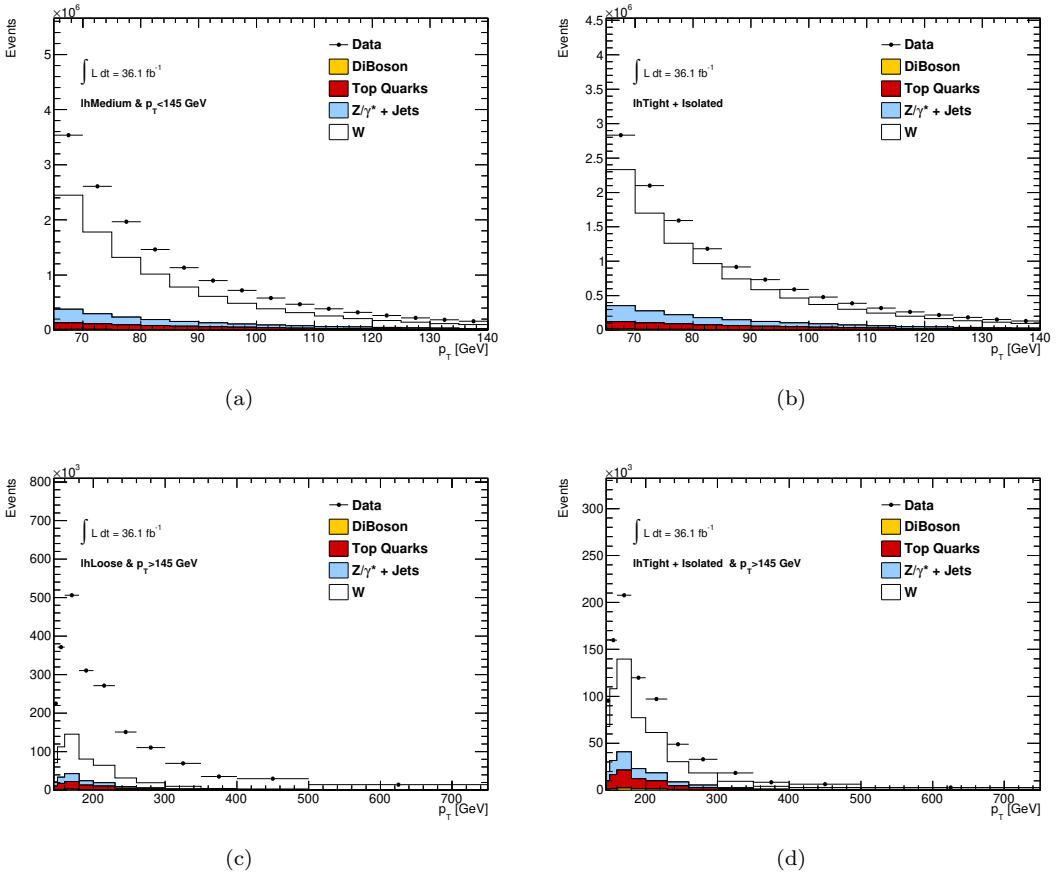

FIGURE 7.15: Samples selected to determine fake efficiencies. Data and estimated real electron contribution is shown for the *loose* and *tight* selection separately for low ($p_T < 145$ GeV) and high p_T candidates ($p_T > 145$ GeV) against their transverse momentum.

In Fig. 7.16 the fake efficiency is shown against the candidates η, the E_T^{miss} in the event and the angular distance $\Delta\Phi_{l,E_T^{miss}}$ of the candidate to the $\vec{E}_T^{miss}$. The efficiency for candidates with $p_T > 145$ GeV is drawn in blue while the red points depict the efficiencies for candidates with $p_T \in [65\ \text{GeV}, 145\ \text{GeV}]$. Structures in η are introduced by the variation in material in the detector. In $\Delta\Phi_{l,E_T^{miss}}$ and E_T^{miss} only low p_T candidates show significant dependencies. These quantities are closely correlated to the event topology. Efficiency variations with E_T^{miss} are problematic as this correlation can not be resolved, since the phase space, in which the fake efficiency is determined, as well as the signal region are defined exclusively. However, the use of $\Delta\Phi_{l,E_T^{miss}}$ dependent fake efficiencies have been found to resolve this problem by providing the desired event topology to a sufficient extent. Eq. 7.1 illustrates that small opening angles between the lepton and the $\vec{E}_T^{miss}$ result in small transverse masses in most cases and vice versa. Therefore, the fake efficiencies applied are candidates' p_T and $\Delta\Phi_{l,E_T^{miss}}$ dependent.

Fig. 7.17 illustrates the fake efficiencies against candidates' p_T in different $\Delta\Phi_{lE_T^{miss}}$ intervals. The opening angle steps shown are used in the determination of the fake background estimate.

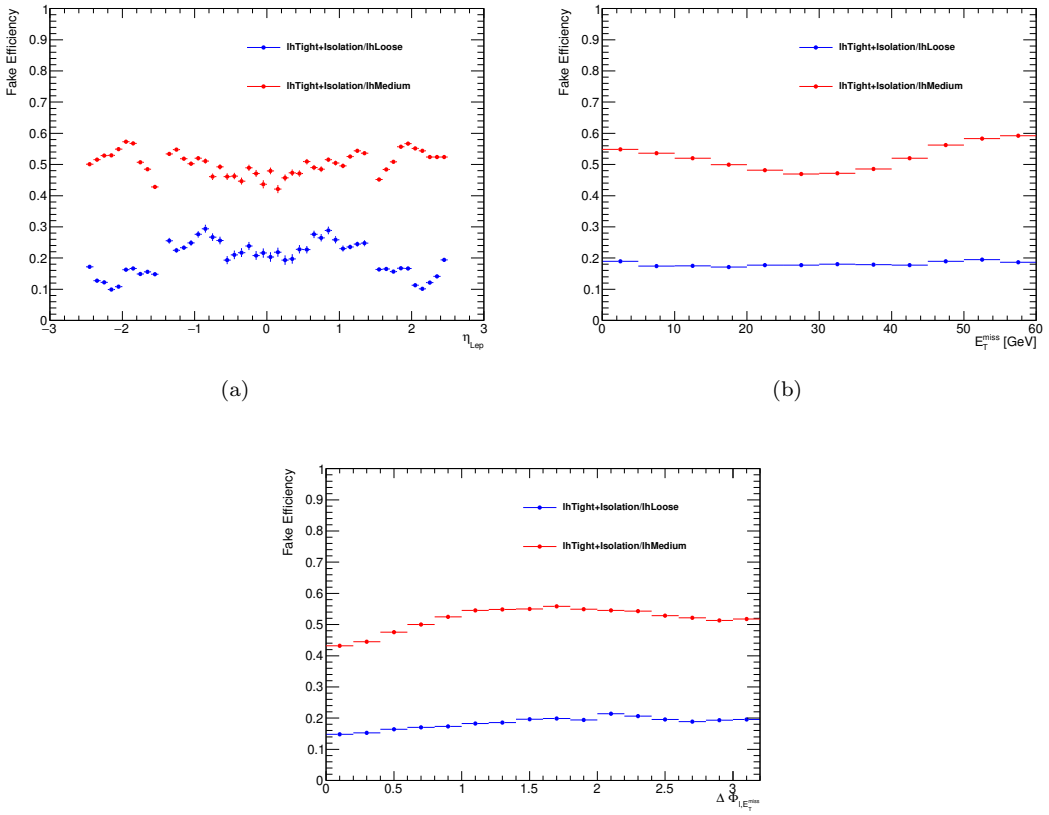

(a) (b)

(c)

FIGURE 7.16: Electron fake efficiency against (a) η, (b) E_T^{miss} and (c) $\Delta\Phi_{lE_T^{miss}}$. To determine the fake efficiency drawn as red points candidates with $p_T \in [65\ \text{GeV}, 145\ \text{GeV}]$ are considered. The blue points correspond to efficiencies of objects with $p_T > 145\ \text{GeV}$.

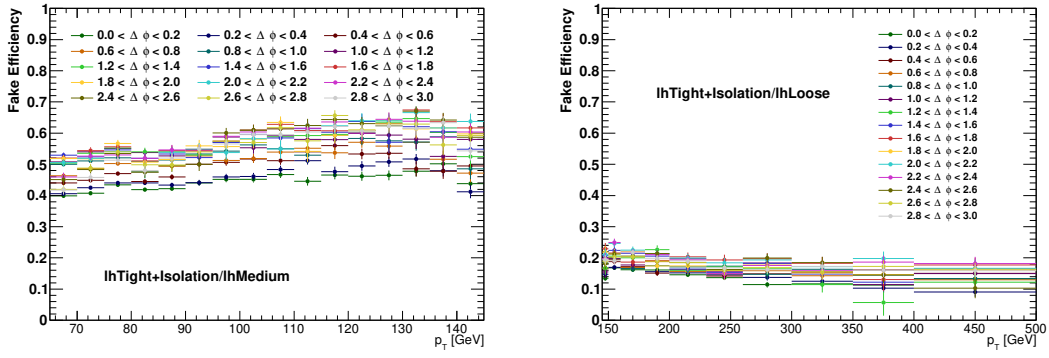

(a) (b)

FIGURE 7.17: Electron candidate fake efficiencies against p_T in different $\Delta\Phi_{l,E_T^{miss}}$ intervals. (a) displays the efficiency for candidates with $p_T \in [65\ \text{GeV}, 145\ \text{GeV}]$ while (b) shows the efficiency for candidates with $p_T > 145\ \text{GeV}$.

Uncertainty Estimation To get an uncertainty associated to the background estimate obtained by this data driven method, several variations of the fake efficiency are determined. For each of them a fake background estimate is determined and the envelope of these serve as an systematic uncertainty. The luminosity value which is entering the fake efficiency through the subtraction of real contributions is varied by 2.2% up and down, which is the uncertainty value provided by ATLAS. Furthermore, cleaning cuts to suppress the real electron contribution are varied - namely cuts to suppress events from $Z \to ee$ decays and a different set of $\mathrm{E_T^{miss}}$ cuts.

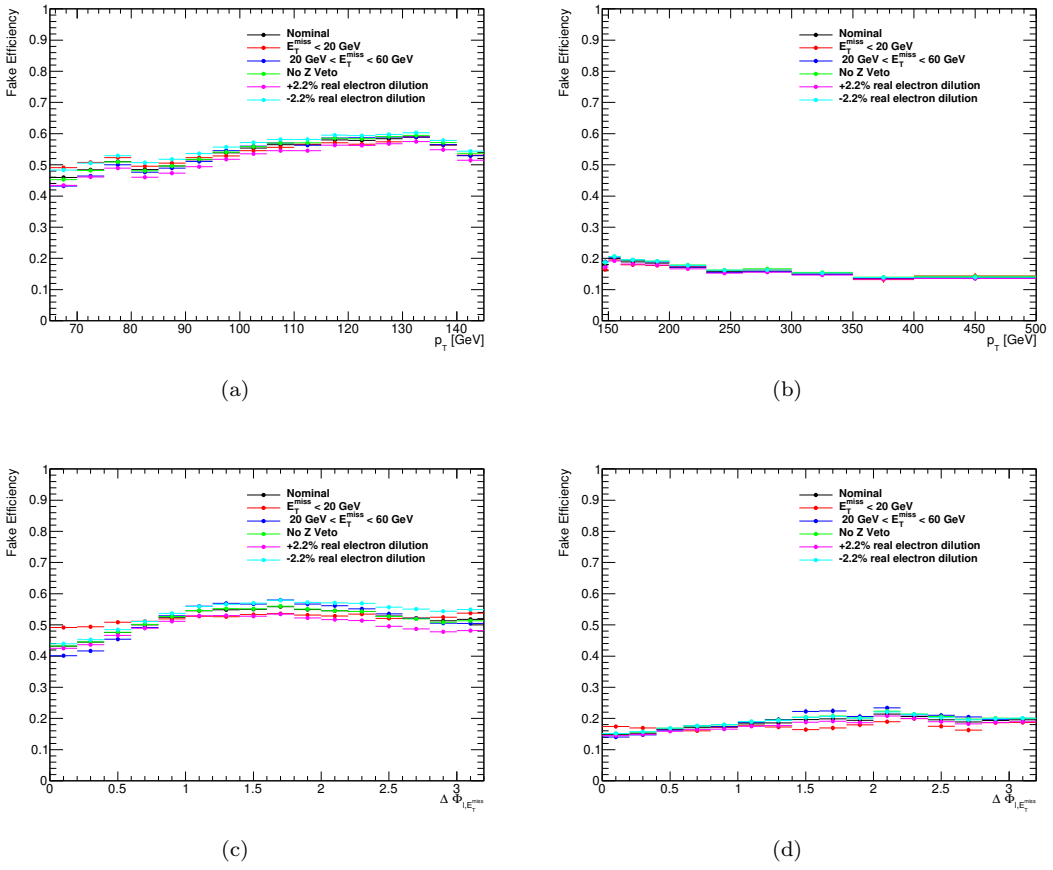

FIGURE 7.18: Fake efficiencies determined with variations in the procedure to estimate an uncertainty on the fake background estimate. (a) and (b) show the fake efficiency depending on the electron candidates' $\mathrm{p_T}$, while (c) and (d) illustrate the $\Delta\Phi_{l,\mathrm{E_T^{miss}}}$ dependency. In the left column candidates with $\mathrm{p_T} \in [65\ \mathrm{GeV}, 145\ \mathrm{GeV}]$ and in the right column candidates with $\mathrm{p_T} > 145\ \mathrm{GeV}$ are considered.

Fig. 7.18 displays these systematic variations of the fake efficiency against $\mathrm{p_T}$ and $\Delta\Phi_{l,\mathrm{E_T^{miss}}}$ separately for candidates with $\mathrm{p_T} > 145$ GeV and $\mathrm{p_T} \in [65\ \mathrm{GeV}, 145\ \mathrm{GeV}]$. Varying the determination procedure of the fake efficiencies leads to efficiency variations of up to 10% in some phase space regions. The efficiency behavior against $\mathrm{p_T}$ and $\Delta\Phi_{l,\mathrm{E_T^{miss}}}$ is at first order unchanged for each variation. Not applying the requirement suppressing Z decays has the least significant effect, while the variation of the $\mathrm{E_T^{miss}}$ interval and the uncertainty induced by the normalization of the real electron are most relevant.

In Fig. 7.19 the ratio between each variation and the nominal estimate is shown as a function of m_T. The largest deviation observed at low m_T is at 15%. At high masses the variations rise up to 40%. In this region an additional uncertainty is introduced by the extrapolation procedure described in Sec. 7.5.2. The largest of deviations is induced by the variation of the real electron contribution scaling as well as narrowing the E_T^{miss} interval to $0 < E_T^{miss} < 20$ GeV. At low E_T^{miss} the fake background is expected to have the largest contributions due to the composition of events capable of faking electrons. Here events with low E_T^{miss} with only jets in the final state dominate. However, this effect will be counteracted in the signal region by requiring a minimal E_T^{miss} of 65 GeV per event. These observations motivate a 15% relative uncertainty on the fake background in the electron channel.

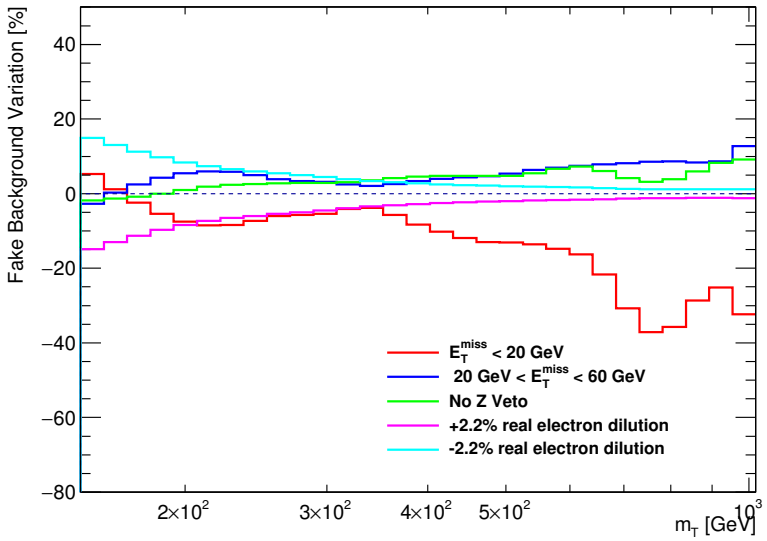

FIGURE 7.19: Fake background variations in % compared to the nominal estimate in the electron channel. Each variation is determined using fake efficiency obtained with a different set of cleaning cuts applied.

7.5.1.3 Muon Channel

The dominant contribution to the muon channel fake background comes from jets which were created by heavy-flavor quarks. It is very unlikely for a light-flavor jet to fake the signature of a combined muon. Overall the fraction of the events containing fakes to the total background estimate is expected to be smaller in case of the muon channel due to its more distinctive signature. The *tight* lepton selection is given again by the signal selection, while for the *loose* selection requirements the isolation criteria is removed since this gives the most discrimination power to jets.

Real Efficiency The real efficiency is again determined using charged current Drell-Yan Monte Carlo and identifying real muons using generator level information. Similar to the electron channel the requirement of an angular distance of $\Delta R < 0.1$ between the reconstructed muon candidate and a muon on generator level is applied for a candidate to be classified as *real*.

Fig. 7.20 shows the real efficiency in the muon channel against the candidates' p_T in (a) and η in (b). The real efficiency is above 99% in the entire spectrum rising very close to 100% for high transverse momentum. This is expected due to the high efficiency of the applied isolation cut, which is the only cut distinguishing between the *loose* and *tight* object selection. The real efficiency shows approximately flat behavior in η only indicating a slight decrease toward higher absolute pseudorapidity values. The real efficiency used in the background determination is obtained while only considering the candidates' p_T dependency. This is motivated by the high uncertainties due to low statistics.

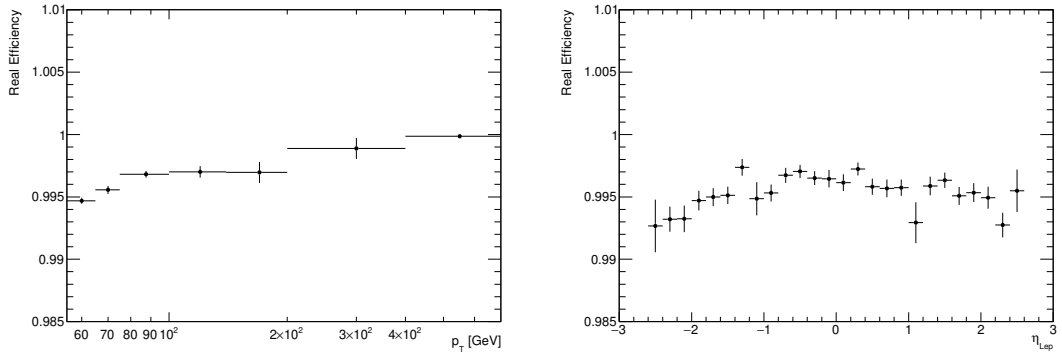

(a) (b)

FIGURE 7.20: Muon real efficiency against the candidates p_T and η.

Fake Efficiency The fake efficiency is determined in data by selecting a sample of objects which fake the signature of muons. It is important to obtain a similar composition to that which passes the signal selection.

The largest fake background contributions are expected at low $\mathrm{E_T^{miss}}$. A criteria on the $\mathrm{E_T^{miss}}$ per event is motivated similar to the electron channel. It is required to be smaller than 55 GeV to stay exclusive to the signal region as well as to introduce some suppression of charged current Drell-Yan events. Another dominant source of real muons in the data sample is the neutral current Drell-Yan process. To suppress muons originating from on-shell Z decays, events with two muons each passing the *loose* object selection and a relaxed $\mathrm{p_T}$ cut (no isolation, $\mathrm{p_T} > 20$ GeV) which have a combined invariant mass $\mathrm{m_{\mu\mu}}$ within 25 GeV of the Z mass are vetoed.

The remaining cuts of the fake enriched sample selection aim to increase the contribution from heavy-flavor jets. Signatures of b-jets, the most relevant objects contributing to the fake background in the muon channel, are characterized by a displaced secondary decay vertex. This leads to increased track impact parameters. Additionally, muons in a b-jet are produced in combination with neutrinos leading to $\vec{\mathrm{E}}_\mathrm{T}^\mathrm{miss}$ parallel to the muons flight direction projected on the transverse-plane. To account for this, candidates are required to have a non-vanishing $\mathrm{d_0}$ significance $1.5 < \sigma_{\mathrm{d_0}} < 3$. Furthermore, each candidate must be aligned to the $\vec{\mathrm{E}}_\mathrm{T}^\mathrm{miss}$ in the event by demanding a maximum angular difference of $\Delta\Phi_{\mu,\mathrm{E_T^{miss}}} < 0.4$. To increase the contribution of heavy-flavor dijet production each event is required to have at least one additional jet with $\mathrm{p_T} > 40$ GeV that is detected outside a cone around the muon candidate ($\Delta R_{\mu,j} > 0.2$).

The contributions of real muons which are not created within a jet are estimated similar to the electron channel using MC simulation. Eq. 7.8 is used for the determination of the fake efficiency.

Contributions of real muons are approximately 53% in the *tight* selection and 17% in the *loose* selection. The statistics of the ensembles used to determine the fake efficiency is weaker compared to the electron channel, which is the reason why the efficiencies correlations are only studied in one dimension. The quality of the fake estimate is limited by this. However, this is not problematic due to the low fraction this background contributes to the total background.

Similar to the procedure in the electron channel, cuts applied in the fake efficiency determination are varied to estimate an uncertainty. Again, one way to vary the selection is to narrow the $\mathrm{E_T^{miss}}$ interval considered ($0 < \mathrm{E_T^{miss}} < 20$ GeV and 20 GeV $< \mathrm{E_T^{miss}} < 55$ GeV) and to neglect the Z veto. Additionally, the impact of not applying the high $\mathrm{p_T}$ jet veto and the $\Delta\Phi_{\mu,\mathrm{E_T^{miss}}}$ requirement, as well as the usage of a smaller $\mathrm{d_0}$ interval of $2 < \sigma_{\mathrm{d_0}} < 3$ is studied.

Fig. 7.21 shows the fake efficiency dependency on the candidates' $\mathrm{p_T}$ (a) and η (b). The result of the nominal selection procedure is displayed together with the previously discussed variations. Fake efficiencies show a strong dependence on the candidates' $\mathrm{p_T}$. At 60 GeV it is found to be

0.15 rising to roughly 0.55 at 200 GeV. This can be explained by the fact, that jets containing non-isolated muons or other objects which can fake muons have a more narrow signature. This increases the probability of them passing the isolation requirement which is the only difference between the *loose* and *tight* selection. A significant η dependence is also observed in (b). The value of the fake efficiencies doubles toward high absolute η values compared to the central region. This can be explained by the fact that muons in the central region of the detector need to traverse less material before leaving their signature in the muon spectrometers. As stated previously, limited statistics only allow a one dimensional binning. The p_T dependence was found to be most relevant considering the region of interest in this search, which is the reason why it is considered in the fake background estimation.

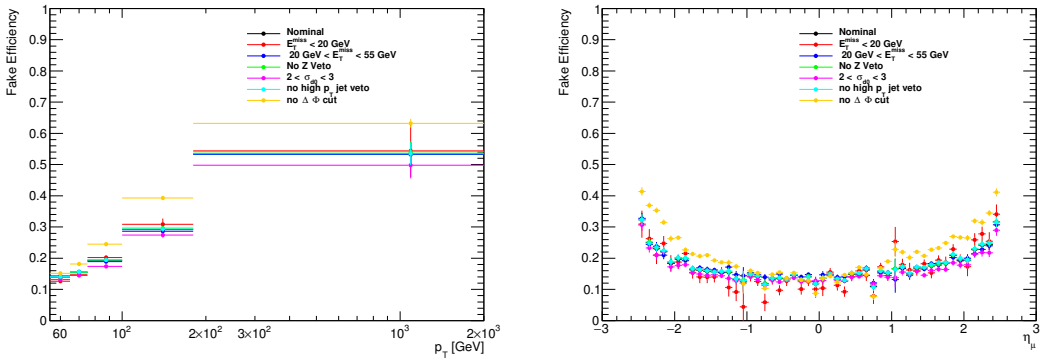

(a) (b)

FIGURE 7.21: Multiple fake efficiencies determined in order to estimate an uncertainty on the fake background estimate in the muon channel. For this selection criteria imposed are varied. (a) shows the fake efficiency against the muon candidates' p_T and (b) against the muon candidates' η.

Fig. 7.22 illustrates the impact of each fake efficiency variation on the QCD background estimate by displaying its ratio to the nominal one. The largest deviation observed is 50%. This motivates the choice of a constant 50% relative uncertainty on this background contribution itself. Since the contribution to the total background is small the uncertainty relative to the total background is below 3% in the entire mass range.

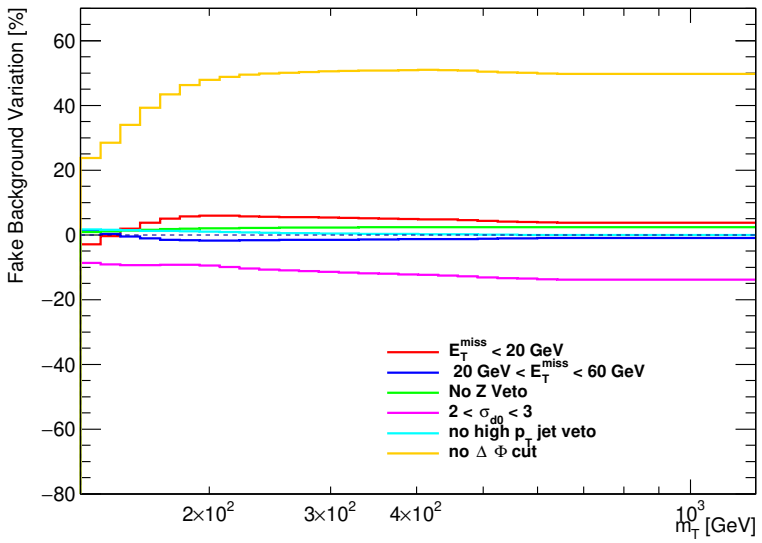

FIGURE 7.22: QCD background variation in % compared to the nominal estimate in the muon channel. Each variation is determined using fake efficiencies obtained while varying the selection.

7.5.1.4 QCD Background Validation

The highest contribution of fake background events is expected at low m_T and low E_T^{miss}. This is explained by the fact that high E_T^{miss} in an event is usually created by a single high p_T particle leaving the detector undetected. In most cases, this is either a neutrino or a lepton leaving the detector acceptance. Most events containing a misidentified lepton entering the signal selection have high jet activity and low E_T^{miss} by pure chance considering the composition of all events produced in collisions at a hadron collider. To identify hypothetical problems in the description of the fake background, data to background comparisons are studied in the region defined by the signal selection, but neglecting the E_T^{miss} and m_T cut. In the following, mainly contributions of the QCD background and general agreement of data to background estimate is discussed. A more in depth shape discussion of each variable is given in Sec. 7.7 when evaluating the background modeling in the signal region.

Fig. 7.23 shows distributions of kinematic variables using the electron channel signal selection without the requirement on m_T and E_T^{miss}. Angular distributions of the electron candidates are shown in (a) and (b). The ϕ distribution is flat due to the homogeneous detector coverage while the η distribution is almost flat in the barrel region of the calorimeter. Transition regions between calorimeter barrel and end-cap ($1.37 < |\eta| < 1.52$) are excluded which is consistent with the empty intervals. In the end-caps a falling behavior can be seen. The QCD background contributes slightly more than 10% to the total background. A flat data to background ratio is shown in the lower panels in the intervals corresponding to the barrel region indicating good modeling there. Structures observed in the ratio at high absolute η values can be explained by a

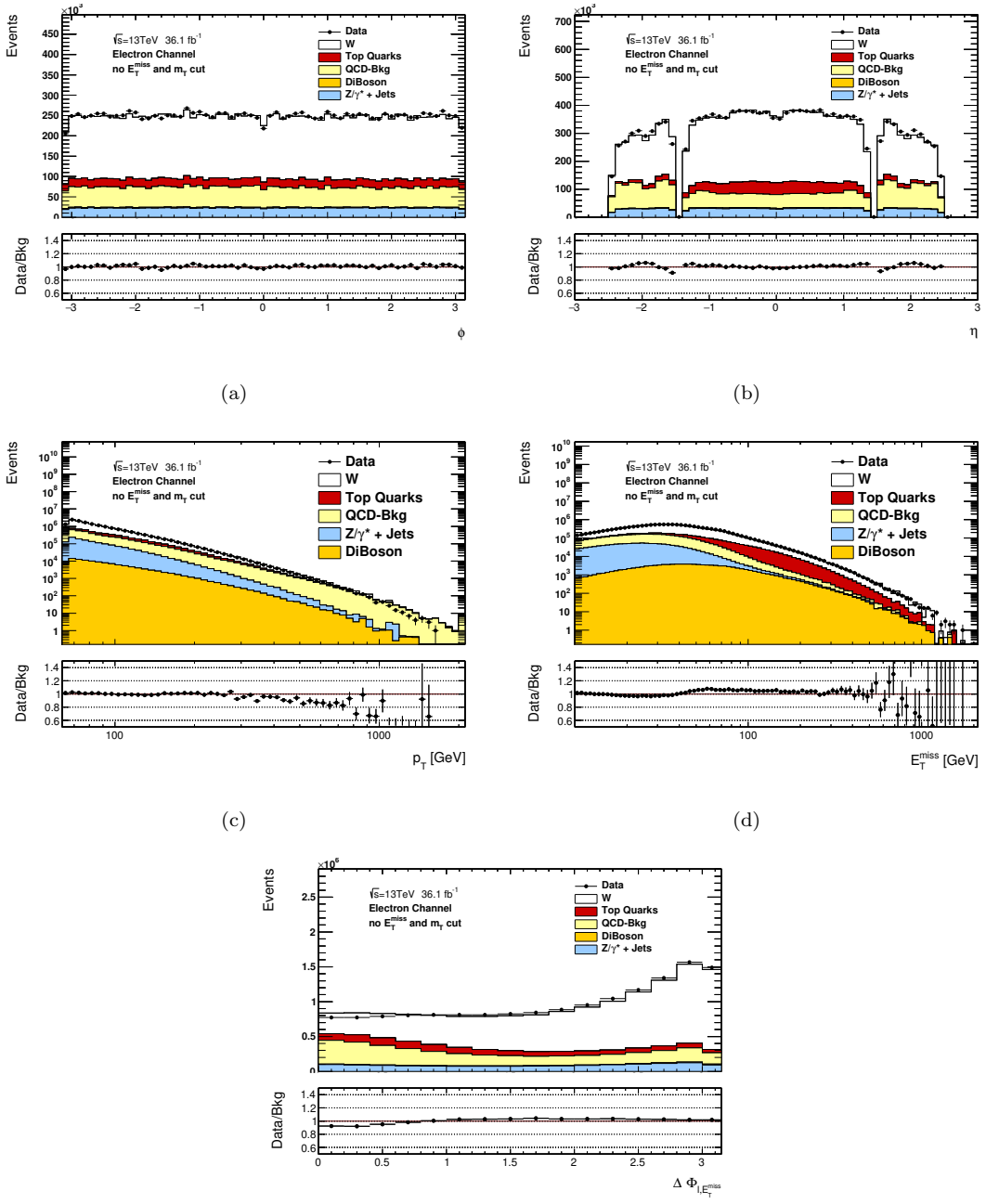

(a) (b) (c) (d) (e)

FIGURE 7.23: Lepton candidates' ϕ, η, p_T and E_T^{miss} as well as the $\Delta\Phi_{l,E_T^{miss}}$ - between the lepton and E_T^{miss} - distributions obtained in the electron channel are shown, while not applying the E_T^{miss} and m_T cut defined in the signal selection. In each upper panel the measured data as well as the background estimation are shown. Each background contribution is drawn separately but stacked. The lower panel illustrates the agreement by showing the ratio between data and background estimate.

different binning used in the scale factor determination which was introduced in Sec. 4.3.2.1. The electron p_T distribution which is displayed in (c) has a steeply falling curvature. This is expected considering that all leptons with $p_T > 65$ GeV originate from the high tail of resonances. At

high transverse momentum, the fake background becomes the dominant contribution to the background. The ratio is flat and close to one over almost the whole range studied. At high p_T a slight overestimation of the fake background is visible. This effect originates from events with low $\Delta\Phi_{e,E_T^{miss}}$ and therefore low m_T - which are not entering the signal region. When mis-identifying a jet as an electron the energy reconstruction leads to too low values in most cases due to its energy calibration. This creates $\vec{E}_T^{miss}$ in the direction of the candidates' trajectory projected on the transverse-plane. Data to background comparisons conducted in Sec. 7.7.1 support this explanation. The E_T^{miss} distribution displayed in (d) shows a rising behavior to its maximum at approximately 40 GeV and falling afterwards. This maximum is expected since the dominant CCDY background has its maximum in m_T at roughly 80 GeV due to the W bosons mass. In contrast to the transverse momentum distribution, the fake background is more relevant at the low end of the E_T^{miss} spectrum. A structure is visible in the ratio, indicating a slight mis-modeling of this variable. However, the largest deviation from unity observed is on the percent level. This mis-modelling has only a minor impact on the analysis due to the distinct signal shape probed. The $\Delta\Phi_{l,E_T^{miss}}$ distribution shown in (e) has its maximum at π. This is mainly due to the dominant background contribution of the charged current Drell-Yan process. For the decay of a heavy particle into two objects a large opening angle is expected. When applying the m_T and E_T^{miss} cut, this observation should be even more enhanced since here only off-shell events are considered in which the intermediate state of the W has an even higher mass. On-shell events which are selected must have an initial boost so that the lepton p_T requirement can be met. Other background processes give a constant contribution over the whole $\Delta\Phi_{l,E_T^{miss}}$ range since no such statement can be made here. The QCD background has its maximum at low opening angles for reasons already introduced in the discussion of the E_T^{miss} spectrum. A similar effect is observed to a lesser extent in the opposite region of the detector if the reconstructed energy is too high. The flat ratio shown indicates good modeling of the fake background in this variable as well.

In Fig. 7.24 analogous kinematic distributions are shown for the muon channel signal selection, while neglecting the m_T and E_T^{miss} cut. The ϕ distribution is, in contrast to the electron channel, not flat due to varying detector coverage of muon spectrometers in the plane transverse to the beam-axis. The data to background agreement observed shows that this aspect of the detector is well modeled. A general offset between data and background expectation is observed in all distributions, which is introduced by a mis-modeling observed in the E_T^{miss} spectrum. Again, varying detector coverage impacts the η spectrum, introducing inefficiencies most visible in the barrel regions. The fake background is overestimated in the central region and underestimated in the end-caps resulting in the curvature observed in the ratio. This can be explained by the fact that the fake efficiency shows a strong dependence on the candidates' η and is rising toward high pseudorapidity values (see Fig. 7.21). However, the η correlation is not considered due to limited statistics available in the fake efficiency determination. This is the reason why the

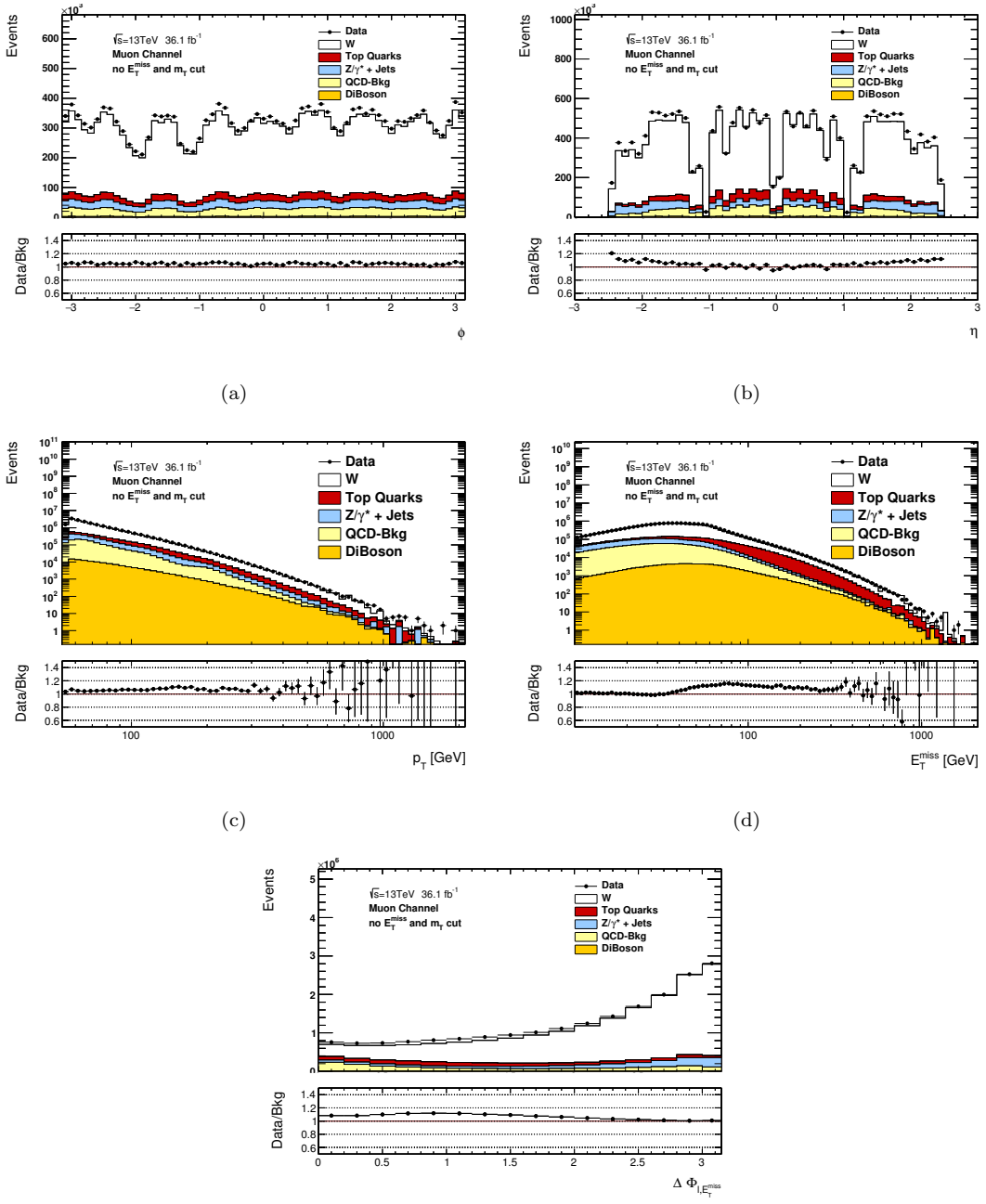

FIGURE 7.24: Lepton candidates' ϕ, η, p_T and E_T^{miss} as well as the $\Delta\Phi_{l,E_T^{miss}}$ - between the lepton and E_T^{miss} - distributions obtained in the muon channel are shown, while not applying the E_T^{miss} and m_T cut defined in the signal selection. In each upper panel the measured data as well as the background estimation is shown. Each background contribution is drawn separately but stacked. The lower panel illustrates the agreement by showing the ratio between data and background estimate.

efficiencies are considered as an average over the whole η range, leading to an overestimation of the fake efficiency and thus fake background in the barrel region. Shapes of the spectra observed for the candidates' p_T, E_T^{miss} and $\Delta\Phi_{l,E_T^{miss}}$ are similar to the ones discussed in the

electron channel. Differing effects in the ratio and QCD background shapes can be explained by the fake efficiency correlations considered. In the falling p_T distribution the fake background contribution shows clear steps which appear at the interval edges of the fake efficiencies. This effect is pronounced due to the steep increase of the fake efficiency with the candidates' p_T. The E_T^{miss} distribution shows good data to background agreement only in the region in which the fake efficiency is determined. Afterwards the fake background seems to be underestimated. This behavior is less pronounced in the electron channel due to the usage of $\Delta\Phi_{l,E_T^{miss}}$ dependent efficiencies which is correlated to the events topology and thus E_T^{miss}. The $\Delta\Phi_{l,E_T^{miss}}$ distribution shows reasonable data to background agreement. The shapes in the ratio can be explained by the fact that the fake efficiency of muons is determined in a narrow $\Delta\Phi_{l,E_T^{miss}}$ window. This is the reason why it is not incorporating any $\Delta\Phi_{l,E_T^{miss}}$ dependence for high values. The fake background contribution is in the order of 10% in this region and is expected to be significantly lower in the signal region. Its modeling is found to be sufficient considering its small contribution to the total background.

7.5.2 Background Extrapolation to High Masses

Some spectra used for background estimation suffer from low statistics in the high transverse mass tail. This problem is circumvented for the Drell-Yan processes by generating multiple samples in varying invariant mass intervals of the lepton pair produced. Background contributions from top quark decays, double electroweak boson production as well as the fake background estimates are extrapolated.

Two functional forms are considered and the fit range is varied to obtain an ensemble of fits, which was then used to estimate an uncertainty of the procedure. Eq. 7.9 displays the fit functions, which are used to extrapolate the background in searches for dijet resonances performed by ATLAS [144].

$$f(m) = e^{-a} m^{b} m^{c \log(m)} \qquad f(m) = \frac{a}{(m+b)^{c}} \tag{7.9}$$

A selection procedure is in place which selects all fits which describe the tail of the distribution reasonably well. Above the stitching bin b_s the result of this extrapolation is taken as the background estimate replacing the MC prediction. The envelope of all fits passing the requirement discussed in the following are taken as an uncertainty.

The quantity Q shown in Eq. 7.10 is evaluated for each fit. Q quantifies the agreement between each function obtained and the MC prediction in the tail.

$$Q = \frac{1}{N.o.B.} \sum_{b>b_s}^{N_b^{est}>0} \frac{\left(N_b^{est} - N_b^{fit}\right)^2}{\sigma_b^2} \tag{7.10}$$

channel	background	lower range [GeV]	upper range [GeV]	$\chi^2/n_{d.o.f}$
$W' \to e\nu$	top	[220,360]	[700,1100]	1.16
	diboson	[140,220]	[850,1400]	1.11
	QCD	[300,400]	[800,1300]	0.92
$W' \to \mu\nu$	top	[220,360]	[700,1100]	0.99
	diboson	[140,220]	[850,1400]	0.74
	QCD	[200,320]	[800,1300]	0.95

TABLE 7.6: Fit ranges used in the extrapolation procedure for each background separately for the electron and muon channel as well as the χ^2/n_{dof} of the fit which gives the nominal value of the extrapolation.

N.o.B. is the number of bins, b_s the stitching bin, N_b^{est} and N_b^{fit} the entry numbers in the MC prediction and the fit. The uncertainty in the bin b is given by σ_b. This quantity has a similar functional form to a reduced χ^2 definition. Fits which describe the MC distribution reasonably well should correspond to Q-values close to one. However, this is only valid at first order since the minimization is not done in the same bins used for the Q calculation and uncertainties are not strictly Gaussian distributed. The fit with the Q-value closest to one is taken as a central value of the estimate and all fits with $Q < 2$ are taken as the ensemble to estimate the uncertainty.

In Tab. 7.6 fit setups are listed for each channel and background. The ratio of χ^2 and number of degrees of freedom $n_{d.o.f}$ of the fit which gives the nominal value of the extrapolation is shown as well.

Fig 7.25 (a) depicts the m_T distribution of the electron channel top quark background in the signal region as well as the ensemble of fits conducted for this procedure. The one taken as a central value is drawn as a red dashed line. All fit results considered in the uncertainty determination describe the falling spectrum reasonably well. In (b) the nominal estimate obtained and its uncertainty is displayed. (c) and (d) serve as diagnostic plots and ensure that the nominal value obtained with its uncertainty covers the simulated input sufficiently. For this purpose the integral of the mass tail to the high end of the spectrum is shown with its uncertainty in (c). (d) illustrates the ratio of the extrapolated background and the input data. The ratio is reasonably close to unity for all starting points and deviations observed are covered by estimated uncertainties.

Fig. 7.26 shows similar diagrams to the one depicted in Fig. 7.25 (a) for each channel and background considered.

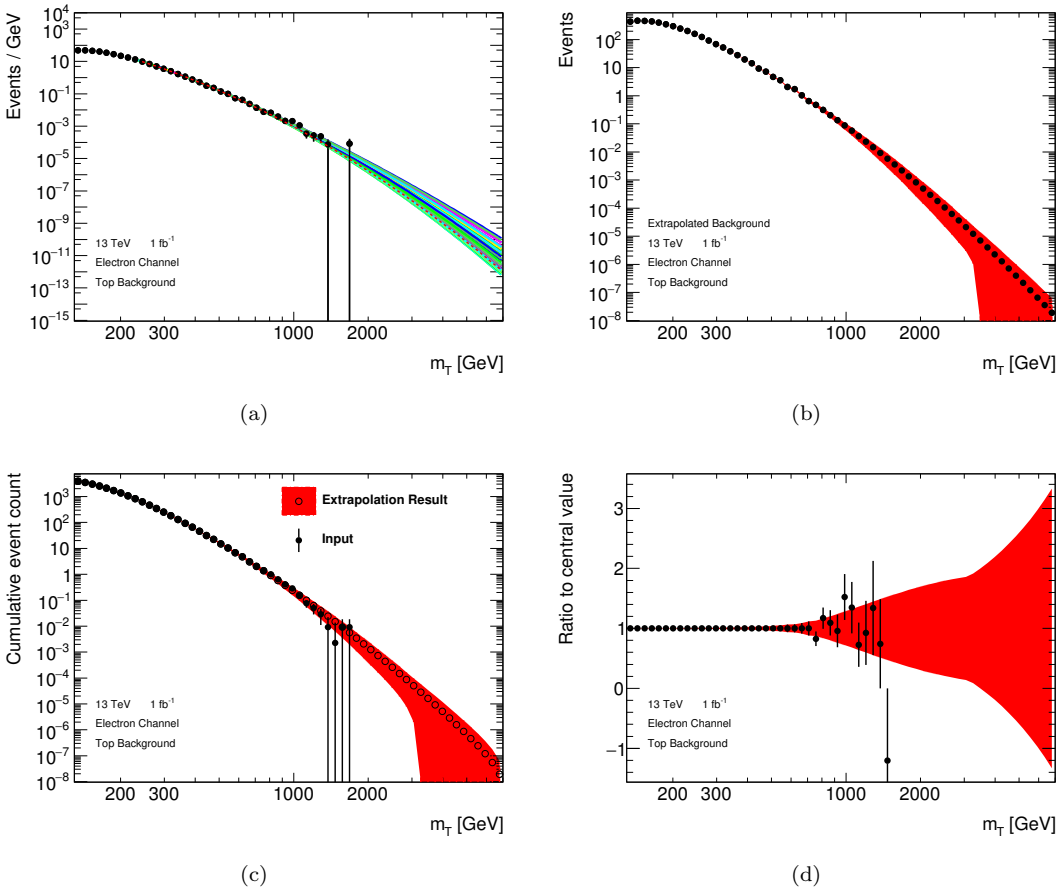

FIGURE 7.25: Diagrams illustrating the result of the extrapolation method. m_T spectra of the top quark background are shown. (a) depicts the ensemble of all fits. The one used as nominal value is drawn as a red dashed line. (b) shows the final estimate for this background with its uncertainty indicated as a red area. (c) illustrates in each mass bin the integral over the tail starting from the respective bin with its uncertainty in comparison to the input data and (d) the ratio of this distribution.

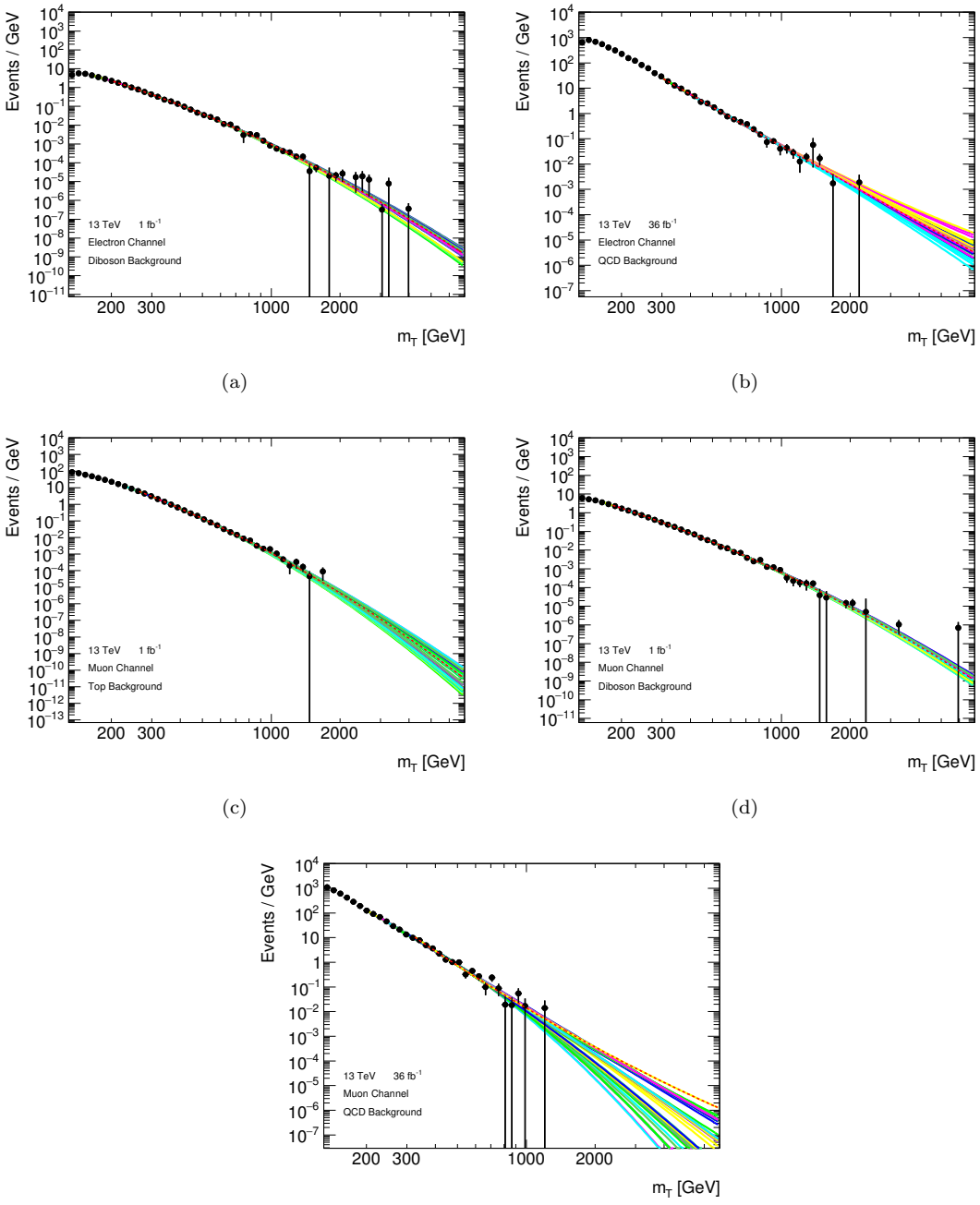

FIGURE 7.26: Fit based extrapolation procedure conducted on different background contributions in the electron and muon channel. The black data points show the distribution to be extrapolated to high masses and the red dashed line the nominal extrapolation result. Additionally, the ensemble of fits used for uncertainty estimation is displayed.

7.6 Systematic Uncertainties

In this section experimental and theoretical uncertainties are evaluated in the phase space defined by the signal selection and their influence on different distributions is studied. The origin of uncertainties related to particle reconstruction and calibration are discussed in Sec. 4 for each particle type separately. The uncertainty determination of the luminosity is detailed in Sec. 3.3.

7.6.1 Experimental Uncertainties

7.6.1.1 Electrons

Fig. 7.27 shows the impact of uncertainties on the transverse mass distribution of the background expected in the electron channel signal region. These variations were provided centrally by an ATLAS performance group. To determine these, relevant parameters in the electron reconstruction [103] and calibration [102] are varied up and down by one σ. The up variations are displayed in (a) and the down variations in (b). The impact of uncertainties originating from misjudgments of experimental isolation, reconstruction and trigger efficiencies in the simulation is on a sub-percent level over the whole considered mass range. The same is observed when varying the energy resolution. Therefore these sources are neglected in the statistical analysis to save computing time.

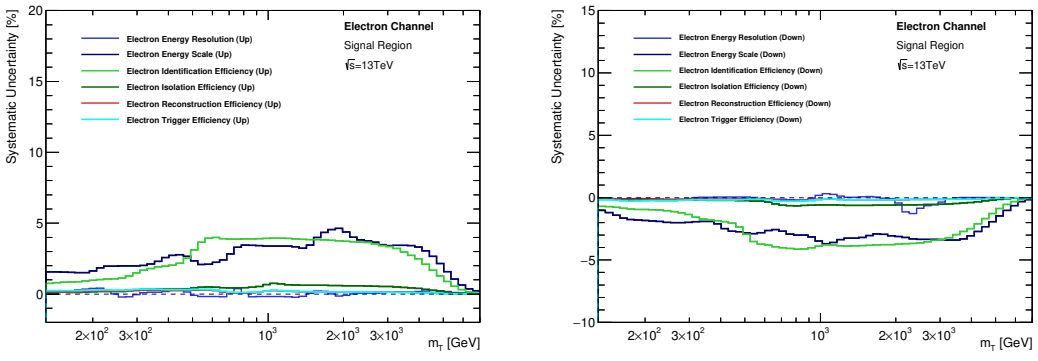

(a) Up Variations

(b) Down Variations

FIGURE 7.27: Uncertainties associated to the reconstruction and calibration of electron in ATLAS. The impact is studied on the m_T distribution of the total background estimate in the electron channel signal region. (a) shows the effect of the up variations and (b) of the down variations.

Furthermore, the at first order symmetric behavior of the up and down variations shown motivates the symmetrization of uncertainties. This is done by only considering the up variation and allowing negative pulls in the statistical analysis.

The maximum of the energy scale uncertainty at low masses can be explained with an effect introduced by the cut applied at the lower edge of the first considered bin. Energy scale variations shift slightly energy measurements of electrons after calibration. Migration effects can only be observed in only one direction at the lowest bin considered. Uncertainties increase with m_T due to the fact, that the calibration is determined using the precisely measured J/ψ, Υ and Z peak. The typical energy of electrons considered is higher than the references used in the calibration, which is the reason why the uncertainty increases with electron p_T and therefore with m_T. The impact of this uncertainty is below 3% over the whole mass range.

The identification efficiency uncertainty is rising to high masses due to the high p_T extrapolation performed in the determination and reaches its maximum at around 500 GeV at a value of 4%.

At very high m_T all uncertainties are decreasing due to a change of background composition. The extrapolated fake background becomes more relevant here, which is not impacted by the shown uncertainties.

7.6.1.2 Muons

As for the electrons, variations of the calibration and efficiencies assumed in the reconstruction as well as selection of muons are provided by ATLAS performance groups to quantify uncertainties [84]. Fig. 7.28 (a) shows the impact of the up variations and (b) of the down variations on the m_T background distribution in the muon channel.

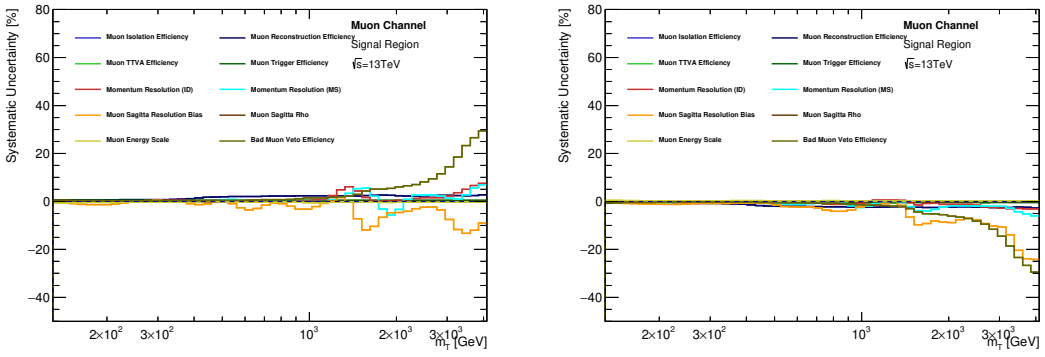

(a) Up Variations

(b) Down Variations

FIGURE 7.28: Uncertainties associated to the reconstruction and calibration of muons in ATLAS. The impact is studied on the m_T distribution of the total background estimate in the muon channel. (a) shows the effect of the up variations and (b) of the down variations.

Corrections accounting for efficiency differences between data and simulation are obtained using tag-and-probe methods at the $Z \to \mu\mu$ and $J/\Psi \to \mu\mu$ peak. Variations in this procedure, for example in the tag-and-probe method or background subtraction, are applied to estimate

uncertainties on the trigger efficiency, reconstruction efficiency, isolation efficiency and track-to-vertex-association (TTVA) efficiency. Large deviations between data and MC are observed when applying the bad muon veto. An additional uncertainty is included to cover this. Fig. 7.28 illustrates that the impact of the TTVA and isolation efficiency uncertainties are negligible. The trigger efficiency uncertainty is at first order flat and around 2%. Reconstruction efficiency uncertainty as well as bad muon veto uncertainty are the most significant ones and each increases toward high masses.

Muon calibration is performed by a parametrization of the energy scale and fitting correction constants so that the invariant mass spectrum of $Z \to \mu\mu$ processes observed in data matches the one in simulation (see Sec. 4.3.3.3). Each potential source of data MC disagreement is associated with a model parameter. Variations in this procedure, such as parametrization and alignment assumptions, are made to estimate uncertainties on the energy calibration. This is done separately for the scale applied to the energy measurement in the inner detector (ID) and the muon spectrometers (MS) [84].

A charge dependent bias has been observed in the sagitta calculation. Corrections to address this are not applied in data due to potentially large impacts and overcorrection in the high mass tail, which could have a great impact on the result of the search. To account for this effect additional uncertainties are included.

All experimental uncertainties increase toward high transverse masses. For the efficiency uncertainties this can be motivated by the fact that an extrapolation is performed since efficiencies are obtained with tag-and-probe methods in a lower energy regime. Uncertainties due to the energy scale, resolution and bias effects are expected to rise at high masses and high muon energies due to the small curvature of trajectories. This makes the momentum measurement less precise and more challenging.

Due to the symmetric behavior of most sources and in order to save computing time only up variations with significant impact are used in the statistical analysis. The trigger, reconstruction and bad muon veto efficiency uncertainties as well as the uncertainty introduced by the sagitta bias are included.

7.6.1.3 Missing Transverse Energy and Jets

Besides the impact of uncertainties connected to objects used to calculate the E_T^{miss} in each event, the procedure to include not fully reconstructed objects in the calculation introduces additional uncertainties. A handle to estimate the uncertainty on the E_T^{miss} scale and resolution is provided centrally by an ATLAS group and is propagated to the calculation via the soft-term [117]. These variations were obtained by studying $Z \to \mu\mu$ events and comparing the muon p_T

with the track soft-term obtained when excluding one of the muons from the E_T^{miss} calculation. The resolution uncertainty is split up into a component longitudinal and transverse to the muon p_T.

Jets are only indirectly considered in this analysis by their contribution to the E_T^{miss} reconstruction. Their energy scale and jet energy resolution effects are studied in simplified models which disregard some correlations between different uncertainty sources [111]. These are designed for analysis which are not very sensitive to jet activity. The models come with three and seven independent nuisance parameters. Additionally, the impact of different aspects of mis-modelings such as of flavor composition or disagreements observed between the reconstruction in the positive and negative pseudorapidity regions of the detector have been studied and found to be not relevant for this analysis.

Fig. 7.29 quantifies the E_T^{miss} and jet related uncertainties and their impact on the m_T distribution. Electron channel diagrams are shown as an example, due to the similarity between both channels. (a) shows the complete set of variations included in the simplified uncertainty model of the jet energy scale and resolution and (b) the ones introduced directly by the reconstruction of the E_T^{miss}.

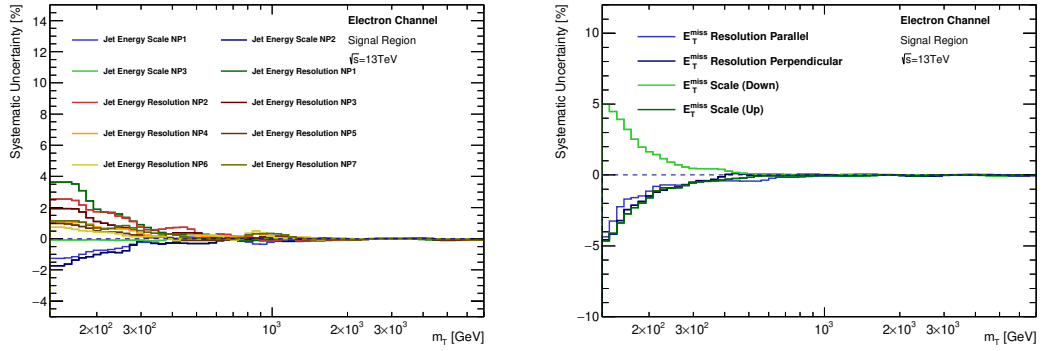

(a) Jet Related Uncertainties

(b) E_T^{miss} Related Uncertainties

FIGURE 7.29: Uncertainties evaluated on the transverse mass distribution of the background expected in the electron channel connected to the jet (a) and E_T^{miss} (b) reconstruction and calibration.

The jet related uncertainties displayed in Fig. 7.29 (a) are on the percent level over the whole mass range and dominant at low transverse mass. This is expected, since at high transverse masses and thus high E_T^{miss} the relative contribution of jets becomes less relevant. Here, high p_T neutrinos or other particles missing the detector acceptance are dominant. The similar trend of the uncertainties induced by the E_T^{miss} reconstruction shown in Fig. 7.29 (b) can be motivated by the same argument. Similar to the experimental muon and electron reconstruction uncertainties only the up variations are considered, which is justified by the symmetric behavior observed.

All E_T^{miss} and jet related uncertainties are treated fully correlated between electron and muon channels.

7.6.1.4 Luminosity Uncertainties

The luminosity uncertainty is determined to be 2.2% for the data obtained in 2015 and 2016 [145]. This uncertainty is directly propagated to the normalization of all MC used in this analysis. A detailed description on methods and procedure used to determine the integrated luminosity of data can be found in Sec. 3.3.

7.6.2 Background Extrapolation Uncertainties

The estimate of some background contributions suffers from low statistics in the high mass tail. Therefore extrapolations are performed which introduce additional uncertainties. The procedure describing how the nominal value of each extrapolation and its uncertainty are determined is detailed in Sec. 7.5.2. Fig. 7.30 shows the size of extrapolation uncertainty with respect to the total background against m_T (a) for the electron channel and (b) for the muon channel.

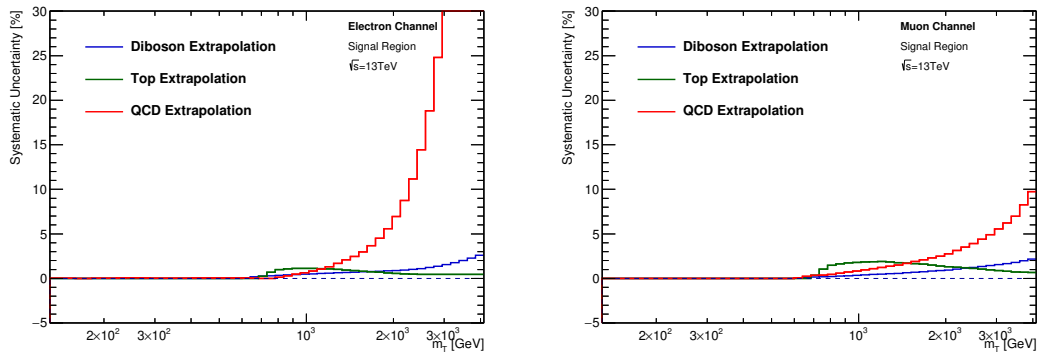

(a) Electron Channel

(b) Muon Channel

FIGURE 7.30: Uncertainties induced by the extrapolation procedure conducted for each contribution separately in the (a) electron and (b) muon channel.

By construction it is expected that extrapolation uncertainties rise in the high m_T tail. In case of the top background this is counteracted by the fact that the fraction of the processes considered become less relevant in the high mass tail due to the more steeply falling transverse mass spectrum of the dominant top anti-top contribution. Since all uncertainties are studied with respect to the total background the top extrapolation uncertainty has its maximum around 900 GeV. The higher relative contribution of the QCD background in the electron channel explains the larger uncertainty observed compared to the muon channel.

7.6.3 Theoretical Uncertainties

The theoretical uncertainties are dominated by the ones which are connected to the PDF. Every experiment using hadrons as initial scattering particles requires a PDF set to make theoretical predictions. The uncertainty on the PDF sets originate from the uncertainties of the initial measurements used to determine the PDF set as well as approximations done in the procedure. Details about PDF determination can be found in Sec. 2.2. Fig. 7.31 shows the impact of the theoretical uncertainties considered on the m_T distribution of the signal selection in the electron channel in (a) and the muon channel in (b). All theoretical uncertainties affect the spectrum in the electron and muon channel very similarly, since their difference in mass - the only distinguishing aspect in the theoretical predictions - is negligible in the considered energy scales. The similarity between the channels is obvious by comparing the shape of each uncertainty in Fig. 7.31 (a) and (b). However, due to the less precise energy measurements of high p_T muons the distributions smear out leading to smaller theory uncertainties in the muon channel.

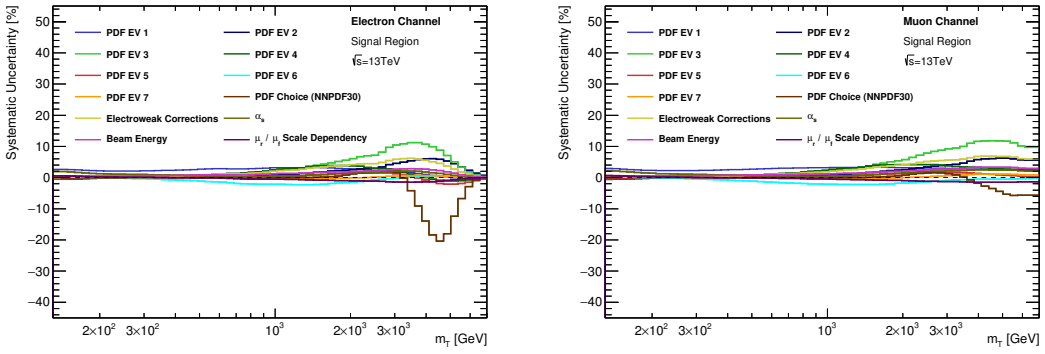

(a) Electron Channel

(b) Muon Channel

FIGURE 7.31: Dominant theoretical uncertainties against the transverse mass in the (a) electron channel and (b) muon channel. All uncertainties shown here are obtained by varying the dominant charged and neutral current Drell-Yan processes.

The CT14NNLO PDF set [146] is used for the dominant charged current Drell-Yan background. 25 error sets are provided which estimate its uncertainty. They have been grouped and simplified to seven sets of eigenvector variations [139]. All evaluated eigenvector variations (PDF EV X) have only small impact at low transverse masses and become more dominant at high m_T. This is due to the fact that the measurements used to determine the set of PDFs were conducted at lower energies. In the high energy tails only very limited data statistics is available to constrain fits. This is the reason why uncertainties connected to evolving procedures become more relevant.

An additional uncertainty is used to consider the strong dependence of the charged current Drell-Yan cross-section to the nominal PDF used in the calculation. This is estimated by comparing

the background obtained by the CT14NNLO PDF set to the one estimated using NNPDF3.0 [36]. Similar to the eigenvector variations the impact of this uncertainty at low masses is minor. The deviation between both nominal values becomes large at high m_T, where differences in the procedure conducted by both groups to extrapolate these PDF sets are more visible.

When estimating electroweak corrections two different approaches - an additive and a multiplicative one - were studied. To respect differences between those the additive approach is used in the nominal background estimate correction and the difference to the multiplicative approach is used to estimate a corresponding uncertainty.

Additionally, a variation of the strong coupling constant is studied by varying α_s by 0.0003. This represents the uncertainty determined for α_s at the scale of the Z mass ($Q^2 = m_Z^2$) and is recommended by PDF4LHC [147]. The impact of this uncertainty is on the sub-percent level and therefore neglected in the statistical analysis. This statement holds true for the uncertainty which estimates the impact of renormalization and factorization scale choice variations.

The cross-section of top anti-top quark production is associated with a 6% uncertainty. Considering the background composition in the signal region this accumulates to less than 2% on the total background. Even when introducing a conservative uncertainty of 10% on the cross-section of all considered diboson processes the uncertainty on the total background is less than 1%. This is the reason why these sources of uncertainties are neglected in the statistical analysis.

7.6.4 Summary

This section summarizes the selection of relevant uncertainties to be included in the statistical analysis. Tab. 7.7 shows the dominant uncertainties for the background estimation and gives values of the one σ variation of the total background evaluated at transverse masses of 3 TeV and 5 TeV in a 200 GeV window around these values. In Tab. 7.8 the corresponding uncertainties on the signals with 3 TeV and 5 TeV pole mass are displayed.

The numbers displayed in Tab. 7.7 are evaluated on the steeply falling transverse mass distribution of the background. Uncertainties associated with jet and E_T^{miss} reconstruction have the largest impact at low masses which is the reason why all numbers listed here are very low. The decreasing behavior of the PDF eigenvector variation uncertainties in the electron channel - comparing 3 and 5 TeV columns - can be explained by the composition of the total background. At high masses the fake background contribution, which is not impacted by PDF variations, becomes more dominant. This is not the case in the muon channel which is the reason why this is not observed here. A similar argument holds true for the uncertainty associated to the luminosity value. This uncertainty impacts all background contributions except the fake background. The lepton energy scale and reconstruction efficiency become better at high electron

background uncertainties				
source	electron channel		muon channel	
	3 TeV	5 TeV	3 TeV	5 TeV
lepton energy scale	3.4%	2.2%	7.6%	41.6%
lepton identification/reconstruction	3.3%	1.3%	14.7%	39.0%
E_T^{miss} scale	<0.1%	<0.1%	<0.1%	<0.1%
perpendicular E_T^{miss} resolution	<0.1%	<0.1%	<0.1%	<0.1%
longitudinal E_T^{miss} resolution	<0.1%	<0.1%	<0.1%	<0.1%
jet energy scale (NPX)	<0.1%	<0.1%	<0.1%	<0.1%
jet energy resolution (NPX)	<0.1%	<0.1%	<0.1%	<0.1%
PDF eigenvector var 1	2.1%	0.2%	2.9%	2.6%
PDF eigenvector var 2	4.5%	5.4%	4.0%	6.2%
PDF eigenvector var 3	10.5%	7.1%	9.1%	11.9%
PDF eigenvector var 4	2.4%	1.1%	3.7%	2.7%
PDF choice	1.6%	18.0%	1.2%	4.2%
PDF electroweak corrections	5.9%	3.7%	5.5%	6.9%
Top cross-section	<0.1%	<0.1%	<0.1%	<0.1%
QCD background	2.6%	9.9%	<0.1%	<0.1%
luminosity	1.8%	0.8%	2.2%	2.2%

TABLE 7.7: Dominant background uncertainties evaluated at transverse masses of 3 TeV and 5 TeV.

signal uncertainties				
source	electron channel		muon channel	
	3 TeV	5 TeV	3 TeV	5 TeV
lepton energy scale	15.3%	27.8%	5.6%	9.1%
lepton identification/reconstruction	4.0%	3.3%	11.9%	34.6%
E_T^{miss} scale	<0.1%	0.1%	0.1%	0.4%
perpendicular E_T^{miss} resolution	0.4%	<0.1%	0.3%	0.4%
longitudinal E_T^{miss} resolution	0.5%	<0.1%	0.3%	1.6%
jet energy scale (NPX)	0.5%	0.5%	0.3%	0.9%
jet energy resolution (NPX)	0.9%	0.5%	0.7%	1.7%

TABLE 7.8: Dominant signal uncertainties for pole mass hypothesis of 3 TeV and 5 TeV.

energies due to the characteristics of energy measurements in a sampling calorimeter. An opposite behavior can be observed in the muon channel. This is expected due to the fact that the curvature of the muon candidates' trajectory becomes less pronounced.

Uncertainties listed in Tab. 7.8 are determined in the peak region of the corresponding signal hypothesis considering a 50 GeV mass window around the maximum. Since each signal sample has lower statistics compared to the total background estimate, the values listed have a larger uncertainty themselves. This is the main explanation why the uncertainties connected to jet and E_T^{miss} reconstruction obtained for the signal are slightly higher than for the background. The great increase of the lepton energy scale uncertainties can be explained by the shape of the distribution which is used to calculate these numbers. To obtain the lepton energy scale

uncertainty, energy values and thus the peak position itself are slightly shifted. This leads to greater deviations when evaluating its impact on a peak like structure, which is present in the signal and not in the background. The effect is stronger in the electron channel due to the better energy resolution and therefore more sharp shape of the resonance.

7.7 Background to Data Comparison

To ensure good background modeling in the signal region, distributions of variables which are not as sensitive to new physics effects as the m_T distribution are studied first. In Sec. 7.7.1 the data to background estimation agreement is evaluated for the electron and in Sec. 7.7.2 for the muon channel. First the least sensitive angular distributions - lepton candidates' η, ϕ and $\Delta\Phi_{l,E_T^{miss}}$ - are studied. Followed by the slightly more sensitive lepton candidates' p_T and E_T^{miss} distributions. In all diagrams the data collected in 2015 and 2016 is shown as black points in the upper panel and the total background estimate is illustrated by drawing each contribution separately, but stacked. The lower panels display the ratio of data to background estimate and the grey bands illustrate the systematic uncertainty. For this the square root of the quadratic sum of all uncertainties considered in the statistical analysis - listed in Tab. 7.7 - is taken.

7.7.1 Electron Channel

Fig. 7.32 shows the electron candidates' ϕ (a), η (b) and $\Delta\Phi_{l,E_T^{miss}}$ (c) distribution. The ϕ distribution in the electron channel is flat due to the detector layout. All sub-detectors used to reconstruct electron candidates have homogeneous coverage in the plane transverse to the beam-axis. This flat distribution is present in the data and the background which agree reasonably well within the uncertainties considered. The electron candidates' η distribution has its maximum at $\eta = 0$ and is falling continuously toward high absolute pseudorapidity values. This decreasing behavior can be explained with two arguments. The main one being that to get a hard scattering vertex providing sufficient center of mass energy the Bjorken x_i of the interacting partons can not be very imbalanced, thus the majority of final states is not highly boosted. On the other hand, by construction, equidistant bins in the polar angle θ correspond to η intervals with decreasing width closer to the beam-axis. The almost empty intervals at $1.37 < |\eta| < 1.52$ correspond to the transition regions between barrel and end-cap of the electromagnetic calorimeter. These regions of the solid angle are excluded due to worse energy resolution and reconstruction efficiencies - see Sec. 7.4.1. These intervals are not completely empty in the diagram, since the cut is performed on η_{cut}, which is measured in the second layer of the electron magnetic calorimeter while the η filled into the histogram is taken either using the reconstructed track in the inner detector or the calorimeter measurement, depending on the number of hits in the pixel and SCT detector. In the barrel region ($-1.37 < \eta < 1.37$) the ratio of data and background expectation is flat

showing good agreement. Structures observed in the ratio at higher absolute pseudorapidity values can be explained by the binning used to apply scale factors correcting for deviating efficiencies differing from the one used for illustration here. The $\Delta\Phi_{l,\mathrm{E_T^{miss}}}$ distribution has its maximum at π. To get sufficiently high $\mathrm{m_T}$ in an event, a non-vanishing opening angle between the lepton candidate and $\mathrm{E_T^{miss}}$ is mandatory, which is the reason why there are almost no events expected and measured at low $\Delta\Phi_{l,\mathrm{E_T^{miss}}}$. In the dominating background contribution - off-shell charged current Drell-Yan production - the electron candidate and $\mathrm{E_T^{miss}}$, which is correlated to the neutrino's $\mathrm{p_T}$, are produced in a decay of the same heavy particle. Therefore, this background contribution and thus the total background expectation peaks at an opening angle of π. Other background contributions are more flat. The data and the background expectation show a good agreement, resulting in a flat ratio displayed in the lower panel.

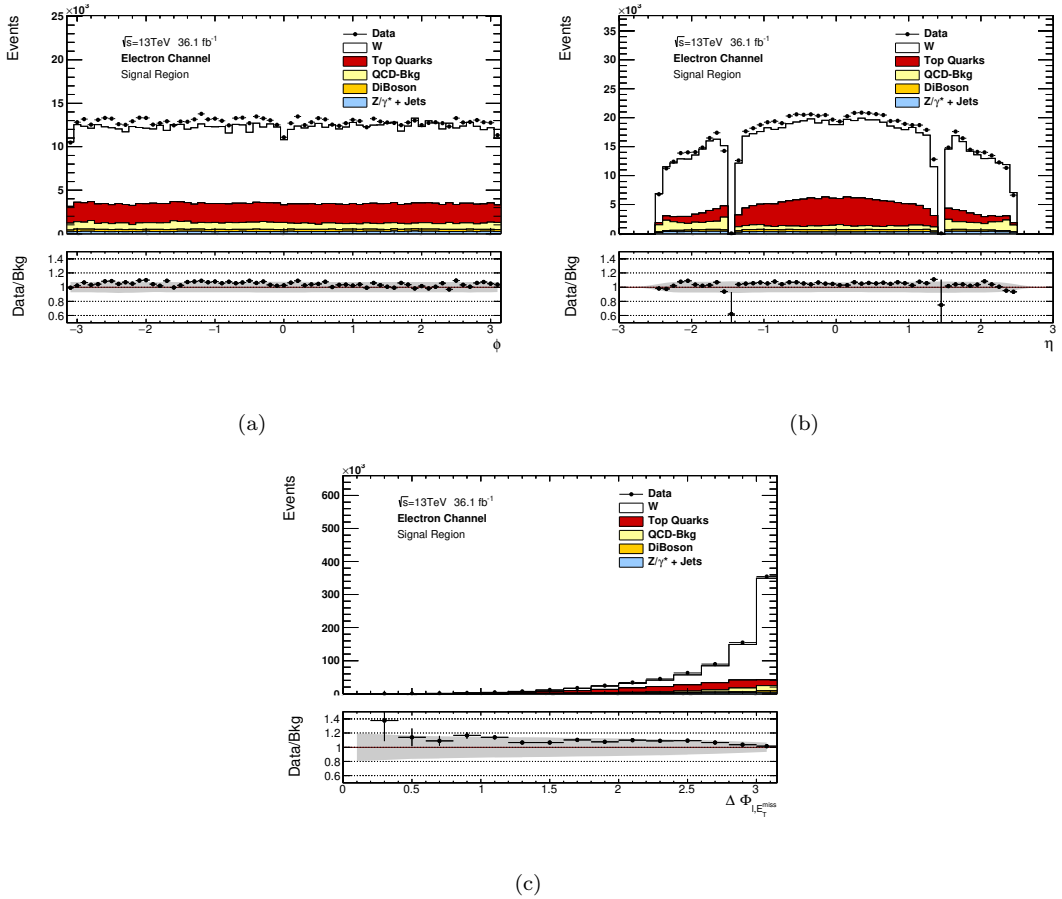

FIGURE 7.32: Electron candidates' ϕ, η and $\Delta\Phi_{l,\mathrm{E_T^{miss}}}$ - between the lepton and $\mathrm{E_T^{miss}}$ - distributions. In each upper panel the measured data as well as the background estimation is shown. Each background contribution is drawn separately but stacked. The lower panel illustrates the agreement by showing the ratio between data and background estimate. The gray band indicates the magnitude of relevant uncertainties.

In Fig. 7.33 the $\mathrm{E_T^{miss}}$ and electron candidates' $\mathrm{p_T}$ distribution is displayed. Both spectra are steeply falling - corresponding to the falling $\mathrm{m_T}$ tail - which is predicted and described by the cross-section of all relevant background processes. On one hand, the diagram shown in (a)

illustrates that the fake background contributes the largest fraction to the total background at low E_T^{miss}. The ratio between data and background shows a falling behavior at low E_T^{miss} indicating modeling problems. However, this does not have an impact on the most sensitive phase space region of this search in the high transverse mass tail. Furthermore, the signal shape tested against can be well differentiated from the slope observed. This mis-modeling in the region giving the highest statistics to the signal selection is the reason for the constant offset observed in other distributions shown. On the other hand, the p_T distribution displayed in (b) shows a flat ratio, indicating good modeling in this variable. This holds true even at high transverse momenta where the QCD background contribution becomes more relevant.

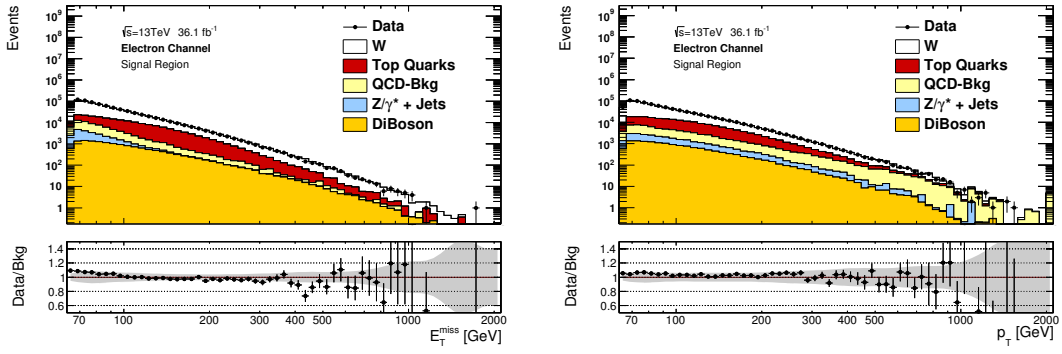

(a) (b)

FIGURE 7.33: E_T^{miss} per selected event and electron candidates' p_T distributions. In each upper panel the measured data as well as the background estimation is shown. Each background contribution is drawn separately but stacked. The lower panel illustrates the agreement by showing the ratio between the data and the background estimate. The gray band indicates the magnitude of relevant uncertainties.

In summary the data to background comparison shows that the background modeling is sufficiently good and disagreements observed in the ratio are understood and covered by the estimated systematic uncertainties.

7.7.2 Muon Channel

In Fig. 7.34 the distributions of the muon candidate ϕ (a), η (b) and ϕ difference between muon candidate and E_T^{miss} (c) - $\Delta\Phi_{l,E_T^{miss}}$ - is shown. In contrast to the spectra measured in the electron channel the ϕ distribution is not expected to be flat due to variations in the detector coverage of the muon spectrometers. The structures observed in the data are well described by the background estimate, suggesting a good modeling of this aspect in the detector simulation. A flat ratio of data and the background estimate is depicted. The same effects can be observed in the η distribution shown in Fig. 7.34 (b). The curvature of the spectrum observed in the electron channel - not considering the transition regions - is convoluted with shapes induced

by the incomplete coverage. This leads to a strong pseudorapidity dependence of the muon reconstruction efficiency. Similar to the ϕ distribution, the flat ratio and thus good agreement observed to the background expectation allows the conclusion that these effects are well modeled. The shape of the $\Delta\Phi$ distribution shown in (c) is similar to the one observed in the electron channel. The large transverse mass required in the selection leads again to the fact that the selected lepton candidate and E_T^{miss} have a back to back topology in most cases. This manifests itself with the maximum of the distribution being at π. The data to background ratio shown in the lower panel is relatively flat at a value of 1.2 but decreasing in the intervals with most statistics. A similar trend is observed in the electron channel.

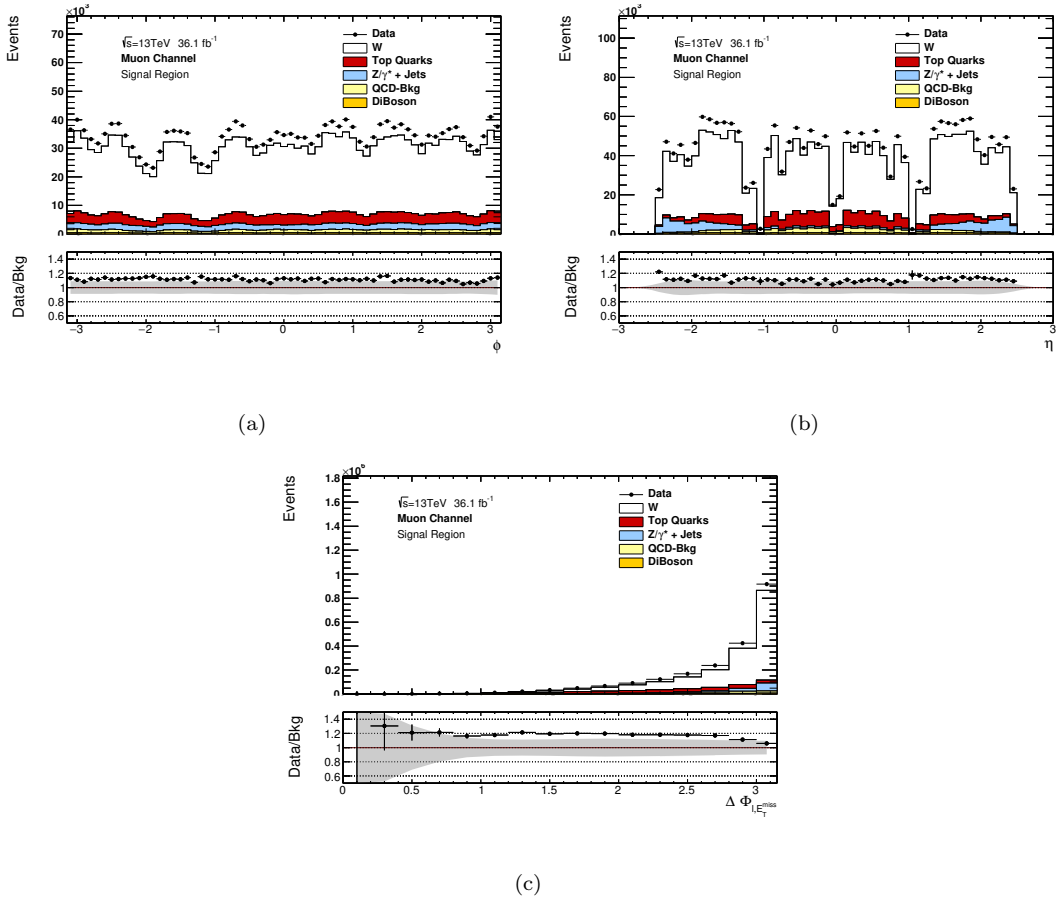

(a) (b)

(c)

FIGURE 7.34: Muon candidates' ϕ, η and $\Delta\Phi_{l,E_T^{miss}}$ - between the lepton and E_T^{miss} - distributions. In each upper panel the measured data as well as the background estimation is shown. Each background contribution is drawn separately but stacked. The lower panel illustrates the agreement by showing the ratio between data and background estimate. The gray band indicates the magnitude of relevant uncertainties.

Fig. 7.35 displays the E_T^{miss} and muon candidates' p_T distribution. Each distribution shows an expected falling behavior similar to the one observed in the electron channel distributions discussed in Fig. 7.33. The ratio of data to background is observed to be flat against p_T, which is shown in Fig. 7.35 (b). As in the electron channel, a constant offset when comparing data to background is observed which is introduced by a mis-modeling of the E_T^{miss} per event. At

low $E_T^{miss} < 100$ GeV data overshoots the expected background significantly. However, the conclusion that this kind of mis-modeling can not be mistaken for a signal due to the shape difference and not being present in the most relevant phase space region holds also for the muon channel.

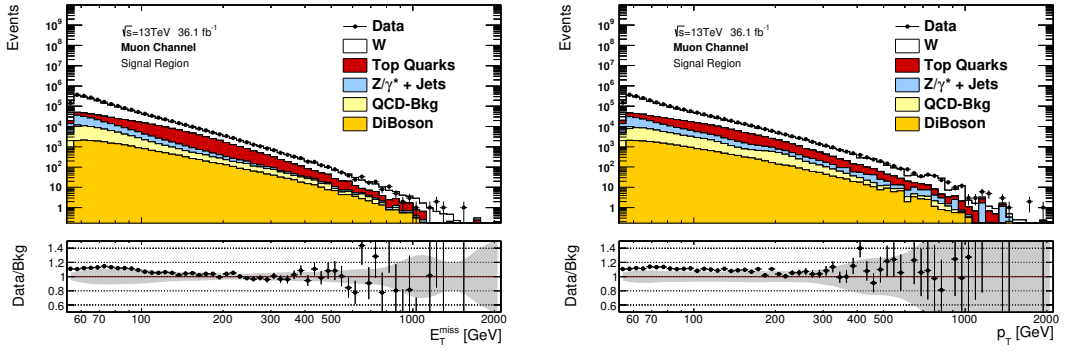

(a) (b)

FIGURE 7.35: E_T^{miss} per selected event and muon candidates' p_T distributions. In each upper panel the measured data as well as the background estimate is shown. Each background contribution is drawn separately but stacked. The lower panel illustrates the agreement by showing the ratio between data and background estimate. The gray band indicates the magnitude of relevant uncertainties.

It is concluded that the background is describing the data reasonably well and mis-modelings observed in E_T^{miss} are found not to be a concern due to the difference in shape compared to the signal hypothesis. Deviations are covered or on the edge of the estimated uncertainties.

7.8 Transverse Mass Distribution

Fig. 7.36 shows the result of the search in form of a data to background comparison of the transverse mass distributions in (a) the electron channel and (b) the muon channel. The top panel shows the data distribution, the background estimate as well as hypothetical signals exemplary for a boson mass of 3 and 4 TeV. In both channels a falling behavior has been measured, which appear to be very similar in shape. No significant deviation of data from the background expectation is observed, giving no signs of new physics. The falling spectrum is described by the tail of the off-shell charged current Drell-Yan production, which is the dominant background contribution in both channels. The decreasing behavior is also present in the other background processes. In the lower panel the ratio of data to the nominal background estimate is displayed. At high transverse masses $m_T > 250$ GeV the ratio is flat and agrees with unity within the systematical and statistical uncertainties. At low m_T, a falling slope of the ratio against m_T is observed in both channels, starting from a 10% overshoot in the data. This indicates a mis-modeling of the background observed in both channels, which is covered

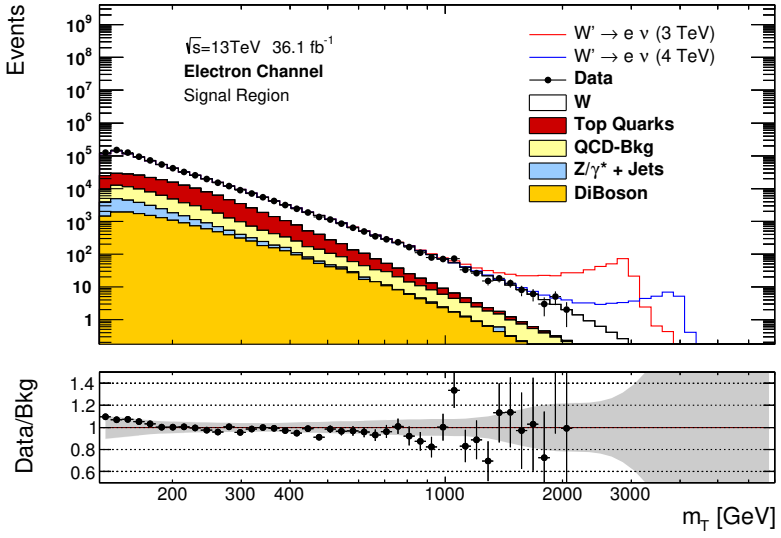

(a) Electron Channel

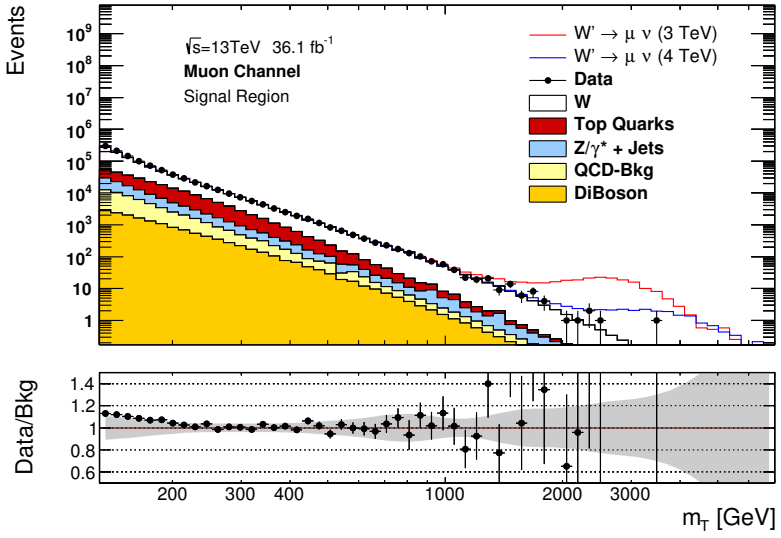

(b) Muon Channel

FIGURE 7.36: Transverse mass distributions of the electron (a) and muon channel (b). The upper panel shows the measured data as well as the background estimate subdivided to each of its contribution. Additionally, signal hypotheses of W' bosons at pole masses of 4 TeV and 5 TeV are displayed. The lower panel illustrates the agreement between the data and the background estimate by taking their ratio.

by relevant systematic uncertainties. This is related to the mis-modeling of the E_T^{miss} already observed in Fig. 7.35 (a) and Fig. 7.33 (b) and is most likely introduced by the problematic calibration used for the lepton candidates in the fake background determination. This deviation does not have a signal-like shape and the phase space in the low m_T range has already been probed by analyses conducted in the past [148][149]. In conclusion no significant signal-like

deviation can be observed by eye.

Chapter 8

Statistical Interpretation

In this chapter the observations shown in Sec. 7.8 - namely the absence of a resonant signal - are quantified. First the likelihood functions and probability distributions considered are introduced in Sec. 8.1. This is followed by a specific description of the likelihood ratio test conducted to quantify deviations observed in Sec. 8.2. This chapter ends with the computation of the 95% exclusion limits on $\sigma \cdot \mathrm{B}$ and the W' pole mass. Sec. 8.3 introduces the method itself, including Bayesian statistics, first.

8.1 Methodology

The likelihood function L used in the statistical analysis is given by the product of the Poisson probabilities in each mass interval considered in each channel c. Eq. 8.1 displays this relation.

$$L_c = \sum_{m=1}^{N_{Bins}} \frac{{\lambda_{cm}}^{n_{cm}} \cdot e^{-\lambda_{cm}}}{n_{cm}!} \tag{8.1}$$

The index c stands either for the electron e or muon channel μ, m identifies each bin in the $\mathrm{m_T}$ distribution, λ_{cm} is the expectation and n_{cm} the number of events selected in an interval m and the channel c. Combined results of the muon and electron channel are determined by using the likelihood product of both channels.

$$L = L_e \cdot L_\mu \tag{8.2}$$

The expectation value λ is given by the sum of background expectation $b(\vec{\theta})$ and signal events $s(\sigma \cdot \mathrm{B}, \vec{\theta})$.

$$\lambda = s(\sigma \cdot \mathrm{B},\vec{\theta}) + b(\vec{\theta}) \tag{8.3}$$

Uncertainties are considered using a set of log-normal distributed nuisance parameters. They are treated in a correlated way across channels for the combination. Uncertainties on signal expectations are constructed in a way that these parameters only vary the shape in $\mathrm{m_T}$ and do not change the total number of signal events. Eq. 8.4 and Eq. 8.5 illustrates how the uncertainties are propagated to the number of signal and background events in the channel c and in the $\mathrm{m_T}$ interval m, via the set of nuisance parameters θ_i.

$$s_{cm}(\sigma \cdot \mathrm{B}, \vec{\theta}) = \overline{s_{cm}}(\sigma \cdot \mathrm{B}) \left(1 + \sum_{i=1}^{N_{sys}} \theta_i \frac{(\delta_{s_{cm}})_i}{\overline{s_{cm}}} \right) \tag{8.4}$$

$$b_{cm}(\vec{\theta}) = \overline{b_{cm}} \left(1 + \sum_{i=1}^{N_{sys}} \theta_i \frac{(\delta_{b_{cm}})_i}{\overline{b_{cm}}} \right) \tag{8.5}$$

Here, $(\delta_{s_{cm}})_i$ and $(\delta_{b_{cm}})_i$ are the one σ variations of the uncertainty i on the number of events in bin m and channel c on the signal hypothesis and background expectation. $\overline{s_{cm}}(\sigma \cdot B)$ and $\overline{b_{cm}}$ are the nominal values for the signal hypothesis probed and the background estimation in the bin and channel considered.

8.2 Likelihood Ratio Test

To quantify the significance of deviations observed between the data and the background expectation, a likelihood ratio test [150] is performed using RooStats [151]. For this the test-statistic shown in Eq. 8.6 is defined by:

$$t = \begin{cases} 0 & \hat{\mu} < 0 \\ -2 \ln \frac{L(0,\hat{\hat{\theta}}(0))}{L(\hat{\mu},\hat{\theta})} & 0 \leq \hat{\mu} \end{cases} \tag{8.6}$$

L is the likelihood function. The dependency on the signal cross-section has been parametrized by the signal strength parameter $\mu = \sigma\mathrm{B}/(\sigma\mathrm{B})_{\mathrm{SSM}}$. $\hat{\mu}$ is the value of μ which maximizes the likelihood L for the measured data $\vec{\mathrm{n}}$ in combination with the set of NPs $\hat{\theta}$ in an unconditional fit. $\hat{\hat{\theta}}(0)$ is the set of NPs which maximizes the likelihood under the $\mu = 0$ (background-only) assumption. The first line of Eq. 8.6 ensures that only positive signals are considered and no negative interference effects. This truncates half of the test statistics distribution at 0, representing downward fluctuations.

The observed p-value - also called p_0 - for the given data is obtained by integrating the test-statistics probability distribution under the background-only hypothesis in the tail, starting from the observed t_{obs}.

$$p_0 = \int_{t_{obs}}^{\infty} f(t|\hat{\mu} = 0, \hat{\theta})\, dt \tag{8.7}$$

The probability distribution $f(t|\hat{\mu}, \hat{\theta})$ is obtained by varying the background-only hypothesis. For each of these pseudo-experiments the observed values of nuisance parameters $\hat{\theta}$ are used.

p-values are quantified by Gaussian standard deviations using Eq. 8.8 with the inverse cumulative Gaussian probability density function Φ^{-1} for better comparison.

$$z = \Phi^{-1}(p_0) \tag{8.8}$$

To reduce computing time an asymptotic approximation [152] using Wilks' theorem [153] is used in practice. It says that the test-statistic distribution $f(t)$ for the background-only hypothesis follows in a χ^2 distribution with one degree of freedom. Eq. 8.9 illustrates the simple relations between the significance z, p_0 and t_{obs} following this approximation.

$$p_0 = 1 - \Phi(\sqrt{t_{obs}}) \qquad z = \sqrt{t_{obs}} \tag{8.9}$$

Conventionally, a discovery of a new particle is announced in case a signal with a $5\,\sigma$ significance is observed.

8.2.1 Global Significances

In the previous discussion, the deviation between data and background estimate has been quantified under the assumption of one new heavy gauge boson with a fixed pole mass $m_{W'}$. In case multiple mass hypotheses are tested with the mass tail observed the so-called 'look elsewhere effect' needs to be taken into account. This effect considers the fact that its more likely to observe a significant deviation at any point the more hypotheses are tested, which is the reason why there is a discrimination between local and global significance values. Local significances per hypothesis p_0 are obtained using the method described in Sec. 8.2 and are mapped to global significances p_{gl} by considering the amount of masses probed.

To obtain the distribution of significances f(z), pseudo-experiments are performed by varying the background-only hypothesis and calculating the significance z for each variation. The global significance is given by integrating the tail of this distribution, starting from the observed local

significance z_{obs} as displayed in Eq. 8.10. This quantifies the likelihood that a deviation like the one observed comes from statistical fluctuations.

Fig. 8.1 illustrates the relation between local and global significance for the electron channel in blue and the muon channel in red. To obtain the diagram shown in (a), a large number of pseudo-experiments is performed, statistically varying the background-only hypothesis and calculating the maximum local significance. For the electron channel this distribution peaks around $2\,\sigma$ and in the muon case around $1.5\,\sigma$. This means that even if the background-only hypothesis is true in most cases a local significance larger than $2\,\sigma$ or $1.5\,\sigma$ respectively is observed. The diagram in (b) shows the mapping of local and global significance values for each channel. Only local significances larger than $2\,\sigma$ will lead to a significant deviation on the global scale when considering the 'look elsewhere effect'.

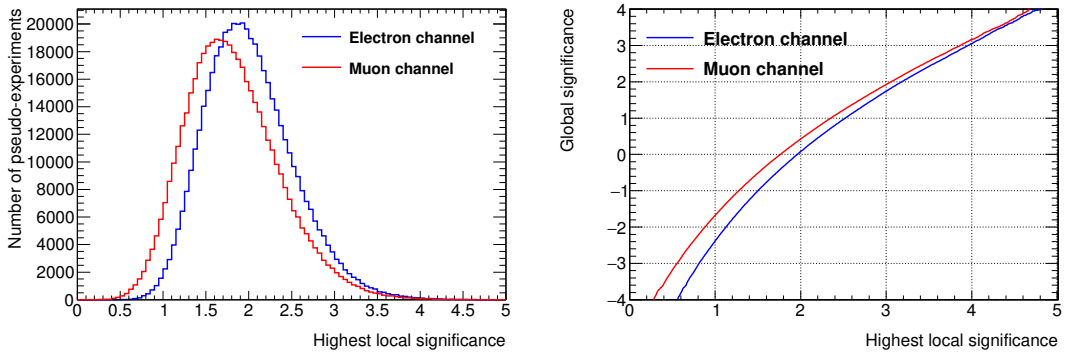

(a) (b)

FIGURE 8.1: Diagrams quantifying the impact of the 'look elsewhere effect' and the correlation between global and local significance with respect to each considered channel. In (a) the highest local significance obtained, when running the likelihood ratio test procedure on a statistical variation of the background-only hypothesis, is displayed for the electron and the muon channel. In (b) the corresponding correlation between the global significance on the y-axis against the largest observed local significance on the x-axis is displayed.

$$p_{gl} = \int_{z_{obs}}^{\infty} f(z)\,dz \tag{8.10}$$

8.2.2 Results

Fig. 8.2 shows the observed local significance p_0 for each mass hypotheses between 150 GeV and 6 TeV. In (a) the result of the electron channel is shown. The most significance excess observed in the electron channel is for low mass hypotheses of around 150 GeV and corresponds to a $3.04\,\sigma$ local significance. This is induced by the E_T^{miss} mis-modeling and therefore not considered in the following discussion. The wider signal shape in the muon channel is the reason why this mis-modeling is only classified as a signal-like deviation in the electron channel. The second highest local significance is observed to be at a pole mass of 400 GeV with $1.60\,\sigma$.

When including the 'look elsewhere effect' this deviation is not significant on a global scale. The largest deviation observed in the muon channel - shown in (b) - is for a mass hypothesis of 700 GeV with a local significance of $1.31\,\sigma$. In the combination of both channels there are multiple excesses in the range of 1 to $1.4\,\sigma$ local significance observed. When considering the number of parameters included in this analysis all deviations observed are not significant on a global scale.

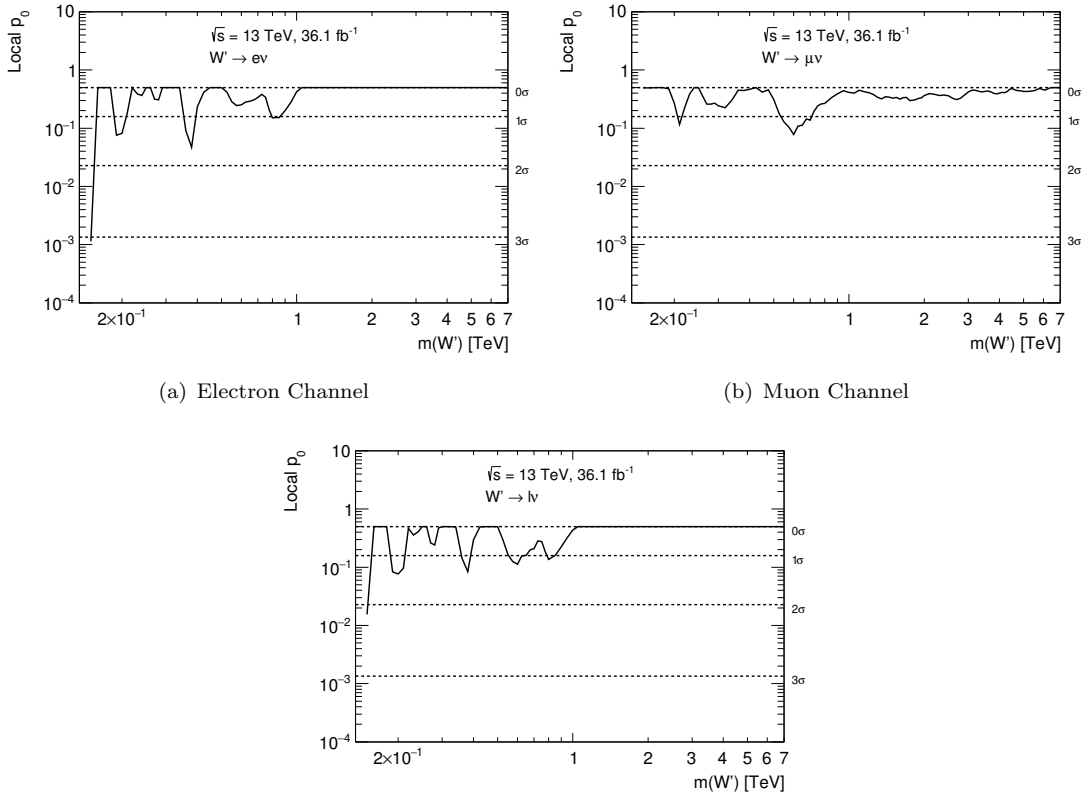

(a) Electron Channel

(b) Muon Channel

(c) Combination

FIGURE 8.2: Likelihood ratio test results quantifying the signal-like deviations observed in data in comparison to the background-only scenario for each mass hypotheses. On the y-axis the p_0 value is shown and the dashed lines indicate the corresponding local significances. The results are shown separately for the electron channel (a), muon channel (b) and the combination (c).

This quantification confirms the previous conclusion that no significance excess has been observed and thus exclusion limits are calculated in the following section.

8.3 Exclusion Limits

Due to the fact that no significant deviations from the background-only hypothesis are observed, exclusion limits on the parameter of interest $\sigma \cdot \mathrm{B}$ are determined. With the use of additional signal model information these cross-section confidence limits can be converted into limits on hypothetical W' masses. In the following calculation Bayes' probability interpretation [150] - identifying probability as a measure of certainty - is assumed.

$$P(A|B) = \frac{P(B|A)P(A)}{P(B)} \tag{8.11}$$

This allows the use of Bayes' theorem shown in Eq. 8.11. It gives a relation between the probability for A given B ($P(A|B)$) and the probability for B given A ($P(B|A)$). $P(A)$ and $P(B)$ are the total probabilities for A and B. For this analysis Eq. 8.11 can be written as

$$P(\sigma\mathrm{B}, \vec{\theta}|\vec{\mathrm{n}}) = \frac{P(\vec{\mathrm{n}}|\sigma\mathrm{B}, \vec{\theta})P(\sigma\mathrm{B}, \vec{\theta})}{P(\vec{\mathrm{n}})} = \frac{L(\vec{\mathrm{n}}|\sigma\mathrm{B}, \vec{\theta})P(\sigma\mathrm{B}, \vec{\theta})}{P(\vec{\mathrm{n}})}. \tag{8.12}$$

$P(\sigma\mathrm{B}, \vec{\theta}|\vec{\mathrm{n}})$ is the probability for the parameter of interest $\sigma\mathrm{B}$ with $\vec{\theta}$ given the measured data $\vec{\mathrm{n}}$ and thus is normalized to 1.

$$\int_0^\infty P(\sigma\mathrm{B}, \vec{\theta}|\vec{\mathrm{n}}) d\sigma\mathrm{B} = 1 \tag{8.13}$$

The upper X% Bayesian confidence limit on the parameter of interest is defined by the parameter value $(\sigma\mathrm{B})_{\mathrm{CL}}$ at which Eq. 8.14 is fulfilled.

$$\frac{\mathrm{X}}{100} = \int_0^{(\sigma\mathrm{B})_{\mathrm{CL}}} P(\sigma\mathrm{B}, \vec{\theta}|\vec{\mathrm{n}}) d\sigma\mathrm{B} \tag{8.14}$$

$P(\sigma\mathrm{B},\vec{\theta}|\vec{\mathrm{n}})$ is accessible using Bayes' theorem and the right side of Eq. 8.12. The probability $P(\vec{\mathrm{n}}|\sigma\mathrm{B}, \vec{\theta})$ can be identified by the likelihood function introduced in Sec. 8.1. $P(\vec{\mathrm{n}})$ gives a normalization constant for the probability distribution $P(\sigma\mathrm{B},\vec{\theta})$ of the parameter of interest, also called prior. The nuisance parameters are assumed to be following a Gaussian shape. This leads to the fact, that the prior can be decomposed to

$$P(\sigma\mathrm{B},\vec{\theta}) = P(\sigma\mathrm{B}) \prod_{j=1}^{N_{sys}} G(\theta_j). \tag{8.15}$$

$G(x)$ is a probability density function following the Gaussian normal distribution. The choice of prior $P(\sigma B)$ impacts the result and needs to be well motivated. A conservative approach is the use of a flat prior shown in Eq. 8.16. It is constantly flat for positive σB values, assuming there is no knowledge of the parameter of interest space and neglecting negative interferences - as implemented in some signal models (see Sec. 2.4.3).

$$P(\sigma B) = \begin{cases} k > 0 & \sigma B \geq 0 \\ 0 & \sigma B < 0 \end{cases} \tag{8.16}$$

One could also use the results of searches performed in the past to adjust the prior, limiting the parameter space beforehand and obtain stronger limits as a result. However, the choice of a flat prior allows comparisons to previously conducted analysis.

By inserting the likelihood function, Eq. 8.15 and the integration over the nuisance parameters it follows

$$P(\sigma B|\vec{n}) = \int P(\sigma B,\vec{\theta}|\vec{n})d\vec{\theta} = \frac{1}{P(\vec{n})} \int \prod^{e,\mu} \prod_{b=1}^{N_{bins}} \frac{\lambda_b^{n_b} \cdot e^{-\lambda_b}}{n_b!} \prod_{j=1}^{N_{sys}} G(\theta_j)d\vec{\theta}. \tag{8.17}$$

Results are obtained for each channel separately. This is done by considering each final states exclusively and not taking the product over both channels. The integration over the nuisance parameters is called marginalization and is done using a stochastic process called Marcov Chain MC. For the determination of exclusion limits including this marginalization the Bayesian Analysis Toolkit (BAT) [154] has been used.

Observed limits are determined by following this procedure using the measured and selected data set as input $\vec{n}$. To get expected limits and to estimate their uncertainty, the background expectation is varied following a Poisson distribution in each bin separately multiple times. The median of limits determined this way is taken as the nominal expected limit. The distribution of the obtained variations gives the opportunity to estimate $1\,\sigma$ and $2\,\sigma$ uncertainty bands.

8.3.1 Results

Fig. 8.3 shows the Bayesian 95% confidence level exclusion limits on the product of signal cross-section and branching ratio σB obtained using the electron channel (a), the muon channel (b) and the combination of both (c). In each diagram σB is displayed on the y-axis against W' pole mass. The black solid line gives the observed limit, the dashed line the expected limit and the green and yellow band indicates its 1 and 2 σ uncertainty bands. For each of these diagrams limits have been obtained for 118 different signal hypotheses with pole masses in 50 GeV steps

between 150 GeV and 6000 GeV. The overlaid red line is the theoretical prediction of the signal model. The intersection of this line with the expected and observed limit can be interpreted as a lower limit on the W' pole mass.

The curvature of each expected and observed limit shown in Fig. 8.3 is very similar. For low pole masses the exclusion limit becomes stronger, the main reason being the low signal acceptance for lower pole masses due to the transverse mass requirement - 0.15 for signals with $m_{W'} = 150$ GeV. The limit curves flatten at higher pole masses obtaining their strongest limits at around 2 TeV. For high masses the limit becomes weaker again. This is due to the fact that the acceptance is becoming worse again in both channels due to the larger contribution of the parton parton luminosity tail. Additionally, the low amount of signal events expected in this region can be more easily covered by statistical fluctuations.

In both separate channels and the combination structures in the observed limit deviating about $1\,\sigma$ from the expected curves are present at low masses below 1 TeV. In the electron channel the observed limit lies consistently $1\,\sigma$ below the expected limit. Considering the m_T distributions shown in Fig. 7.36 (a) a minor undershoot of data compared to the background expectation and a slight slope in the ratio can be identified. This is the reason why the observed limit obtained is stronger than the expected.

In the muon channel, the observed limit lies consistently slightly above the expected. The slope and undershoot of data in the high mass tail observed in the electron channel is not present here. Thus the observed limit is very close to the expectation. Since the electron and muon channel show opposite deviations from the expectations the observed limit of the combination is very close to the expected one in the high mass range. In conclusion the observed limits obtained agree within $1\,\sigma$ over almost the whole mass range with the expectation.

	mass limits [TeV]	
channel	expected	observed
electron	5.19	5.31
muon	4.69	4.61
combined	5.42	5.43

TABLE 8.1: Observed and expected 95% C.L. lower exclusion limits on the hypothetical mass of a W' boson within the SSM model.

In Tab. 8.1 the 95% confidence level expected and observed lower mass limits on hypothetical bosons are displayed. The values are obtained by determining the intersection of the theory curve with the expected and observed limits. The limits obtained in the electron channel are stronger compared to the muon channel due to the better lepton reconstruction and energy measurement in the relevant range. The observed limit in the electron channel is better at 5.31 TeV than the expected one - 5.19 TeV. In the muon channel the opposite is the case with the observed limit being 4.61 TeV and the expected 4.61 TeV. This is expected since there is a

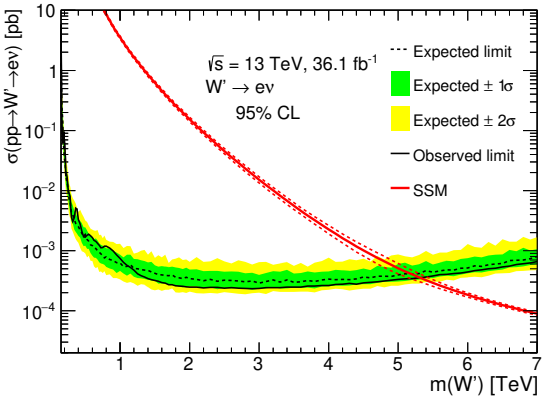

(a) Electron Channel

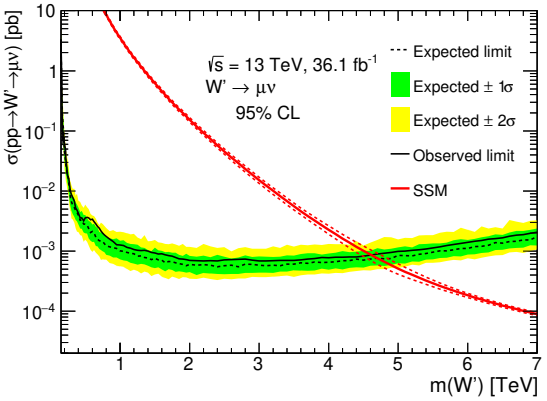

(b) Muon Channel

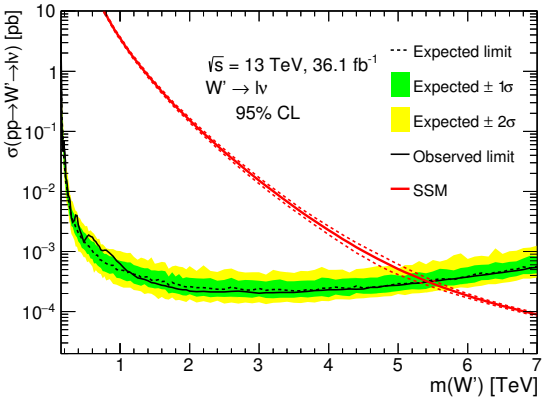

(c) Combination

FIGURE 8.3: 95% C.L. upper limit on the product of cross-section and branching ratio of a W'_{SSM} separately for the electron channel (a), muon channel (b) and the combination of both (c). The black dashed line represents the expected limit with the $1\,\sigma$ and $2\,\sigma$ uncertainty bands, drawn in yellow and green. The solid black line is the observed limit determined. The red line illustrates the signal cross-section expected within the nominal model. The intersection between this prediction and the cross-section limits determined can be interpreted as a lower limit on the probed boson mass.

direct and clear correlation of these values to the discussion of the limit curves in the previous paragraph. In the combination the expected and observed mass limits are almost identical - with 5.42 TeV and 5.43 TeV - which matches the observation of the exclusion limits determined on the product of cross-section and branching ratio.

Chapter 9

Conclusion

A search for new heavy charged gauge bosons has been presented using data collected by the ATLAS experiment in proton-proton collisions during 2015 and 2016. The total amount of data analysed corresponds to $36.1\,\text{fb}^{-1}$. To use a minimal amount of model assumptions the Sequential Standard Model [52] serves as a signal model. A selection has been defined with the aim to select events with an intermediate particle decaying into a charged lepton - electrons and muons - and a neutrino. The transverse mass of the charged lepton and the missing transverse energy per event has been examined, hence a resonant structure in the spectrum of this variable would indicate the existence of a new particle.

The modeling of the background expectation - consisting of contributions estimated with Monte Carlo simulations and data driven methods - has been studied using kinematic variables, which are not sensitive to the signal process, as well as a relaxed signal selection. Relevant systematic uncertainties have been studied and included in the statistical analysis. Two statistical methods were performed to interpret the results for each channel separately and combined. First a likelihood ratio test has been conducted to quantify signal-like deviations observed in the transverse mass spectrum. No globally significant deviation has been observed. In the last step 95% confidence level exclusion limits have been determined on the signal cross-section times branching ratio. Using the theory prediction of the signal model, the intersections of these limits with the prediction can be interpreted as lower limits on the hypothetical W'_{SSM} boson mass. The observed mass limits are 5.31 TeV in the electron channel, 4.61 TeV in the muon channel and 5.43 TeV when considering both channels simultaneously.

The most sensitive searches probing the existence of such a new particle conducted previous to Run 2 of the LHC have been performed with approximately $20\,\text{fb}^{-1}$ of data collected in proton-proton collisions at $\sqrt{s} = 8$ TeV by each the ATLAS [148] and CMS [149] experiment. 95% confidence level exclusion lower mass limits of 3.21 TeV and 3.28 TeV have been obtained. The large increase in sensitivity shows the significant impact of a high center of mass energy.

In 2019 the ATLAS collaboration published an analysis setting stronger limits on this model using the full 139 fb^{-1} Run 2 proton-proton data set [155]. Even with in this larger data set the observation is coherent with the result of this thesis as no significant deviation could be observed. The strongest limits to date are 6.0 TeV obtained in the electron channel and 5.1 TeV in the muon channel. A search in this final state will not gain significantly more sensitivity when increasing the data statistics available while staying at the same center of mass energy. Studies into pole mass ranges which can be probed by exploiting the full Run 3 and Run 4 data set of ATLAS have been published [156]. For Run 3 the assumption is made that 300 fb^{-1} will be collected and in Run 4 3000 fb^{-1} at a center of mass energy of 14 TeV. The lower expected SSM mass limits are obtained with a similar search strategy and found to be 6.7 TeV using Run 3 data only and 7.9 TeV when including the whole data set of 3 ab^{-1}.

Part II

Search for the Singly Produced Leptoquarks

Chapter 10

Motivation

Lepton flavor universality is one of the fundamental predictions of the Standard Model (SM). Experiments at LEP [157] concluded that the coupling strength of photons and Z bosons to leptons of all three generations is the same. Consequently, any observation which deviates from this hypothesis implies the existence of physics beyond the SM. Multiple observations, which are inconsistent with SM predictions, have been made by experiments that probe the flavor sector in various rare B decays [49][51][50]. A representative ensemble of those have been discussed in Sec. 2.4.2.

A wide range of new physics models are capable of explaining these observations. Some of the most prominent ones introduce particles, which carry baryon and lepton quantum numbers - so-called Leptoquarks (LQ). These are introduced in a variety of SM extensions, for example Grand Unified Theories (GUTS) [12]. They carry color charge and can exist either as scalar- (spin-0) or vector-like (spin-1) particle. The mechanism which allows LQs to introduce violation of lepton flavor universality is detailed in Sec. 2.4.4 within a specific model [60][59]. LQ production channels can be classified into two categories at hadron colliders. The pair wise production takes place via the strong interaction, which allows to make only a few model dependent assumptions. In the following a search for singly produced LQ is presented. Especially for first generation quarks the LQ mass parameter space, which can be explored, reaches higher LQ mass hypothesis compared to the pair production under certain assumptions of the LQ-lepton-gluon coupling λ_{lq}.

The following search is separated into multiple chapters. Ch. 11 covers the analysis strategy. This includes a detailed discussion of the signal and the background processes, of methods for background estimation as well as a description of the defined selections. Additionally, systematic uncertainties are evaluated and the background modelling is investigated. In Ch. 12 the result of the search is presented and interpreted. For this general methodologies as well as two different statistical methods are discussed. A likelihood ratio test assesses deviations observed from the

background-only hypothesis and a frequentist approach is used to set upper exclusion limits on the signal cross-section times branching ratio. This part of the thesis ends with a dedicated conclusion in Ch. 13.

Chapter 11

Analysis

First the signal process and search strategy are discussed in Sec. 11.1. This includes specifics on the signal simulation. Afterwards characteristics of background processes as well as tools to estimate their expected contributions to each kinematic region are detailed in Sec. 11.2. Sec. 11.3 discusses the data set examined, which is followed by an in depth description of the event selection procedure and definitions of kinematic regions in Sec. 11.4. Data driven methods to estimate so-called fake backgrounds as well as a background extrapolation technique are described in Sec. 11.5. Afterwards sources of systematic uncertainties as well as their magnitude are explored in Sec. 11.6. This chapter concludes with a data to background comparison in control and validation regions to investigate the quality of the background modeling Sec. 11.7. These selections are designed to have negligible signal contribution.

11.1 Strategy and Signal Model

11.1.1 Production Channel

Leptoquarks (LQ) [16][158], which were introduced in Sec. 2.4.4, decay into a lepton and a quark. They carry baryon and lepton quantum numbers as a consequence. Their production occurs in pairs or singly. The single production channel allows to probe higher mass hypothesis in a specific parameter range of the LQ-quark-lepton coupling λ_{lq}. On the other hand the production of a LQ pair takes place via the strong interaction and is independent of λ_{lq}. Hence the pair production channel has been exploited in previous ATLAS searches [159]. In this case, the production cross-section depends on the strong coupling parameter only.

In Fig. 11.1 [59] (a) the cross-section of the single LQ production - under the assumption of $\lambda_{lq} = 1$ - and pair production is displayed against the mass of the LQ (m_{LQ}). Both show decreasing behavior. The less steep slope of the single production yields greater sensitivity

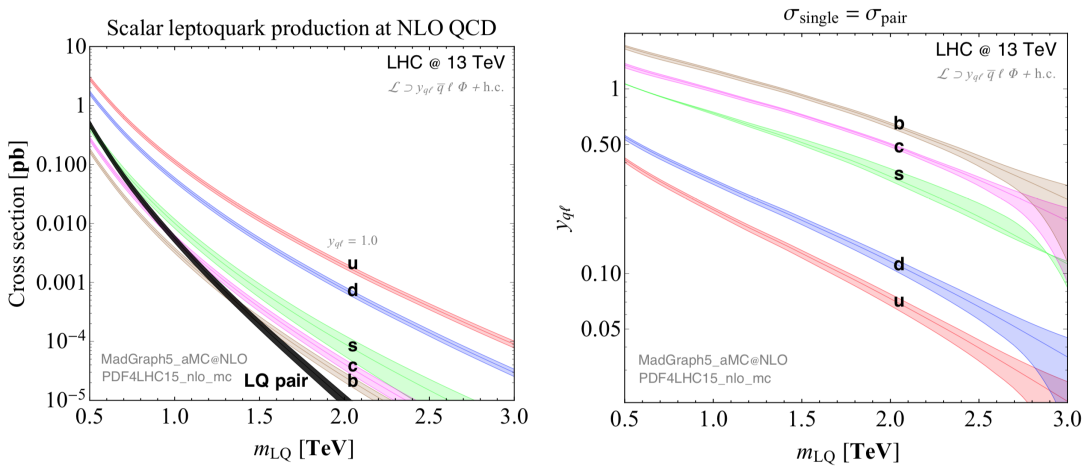

(a) (b)

FIGURE 11.1: (a) shows the cross-section against the LQ mass m_{LQ} for the LQ pair production and single production separately for different quark flavors. The single production curve is shown for $\lambda_{lq} = y_{ql} = 1$. (b) displays the coupling value $\lambda_{lq} = y_{ql}$ at which the pair production channel cross-section has the same size as the single production channel separated in quark flavors against m_{LQ}. [59]

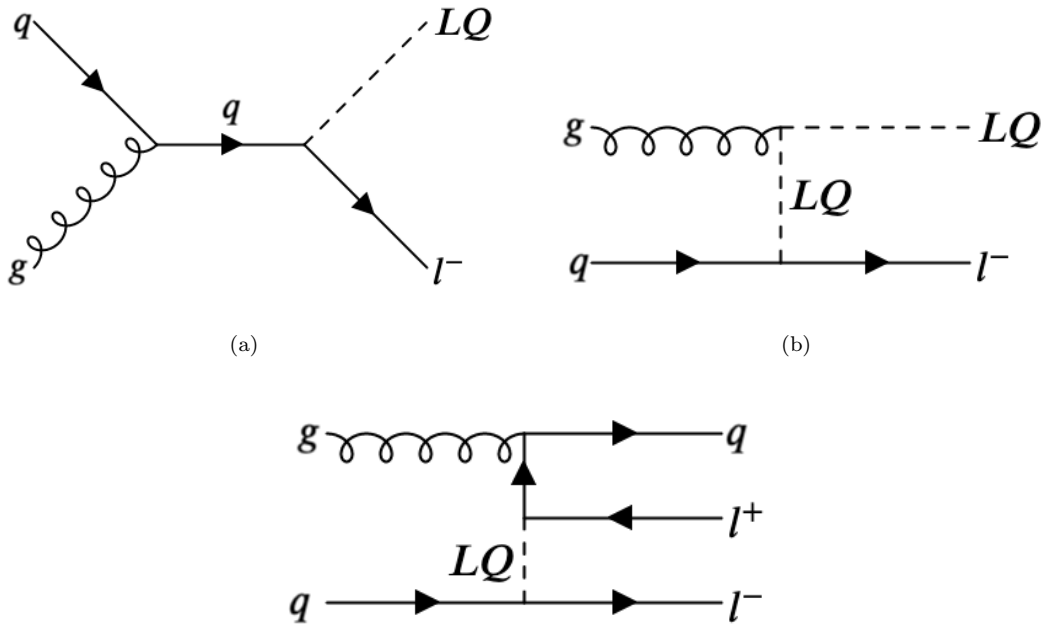

(a) (b)

(c)

FIGURE 11.2: LO Feynman diagrams of the single LQ production in combination with a charged lepton in the s-, t- and u-channel - (a), (b) and (c) - in proton-proton collisions. The charge-conjugated diagrams are investigated as well in the search.

compared to the other channels at high m_{LQ}. At which point the single production becomes dominant is connected to the λ_{lq} parameter. Fig. 11.1 (b) illustrates the coupling strength λ_{lq} at which the single production channel cross-section is equal to that of the pair production at

a given m_{LQ} for each quark flavor separately. The publication these plots are taken from uses different symbols, denoting λ_{lq} as y_{ql}.

Fig. 11.3 shows the leading-order (LO) Feynman diagrams of LQ pair production, while in Fig. 11.2 all tree level diagrams of single leptoquark production are shown.

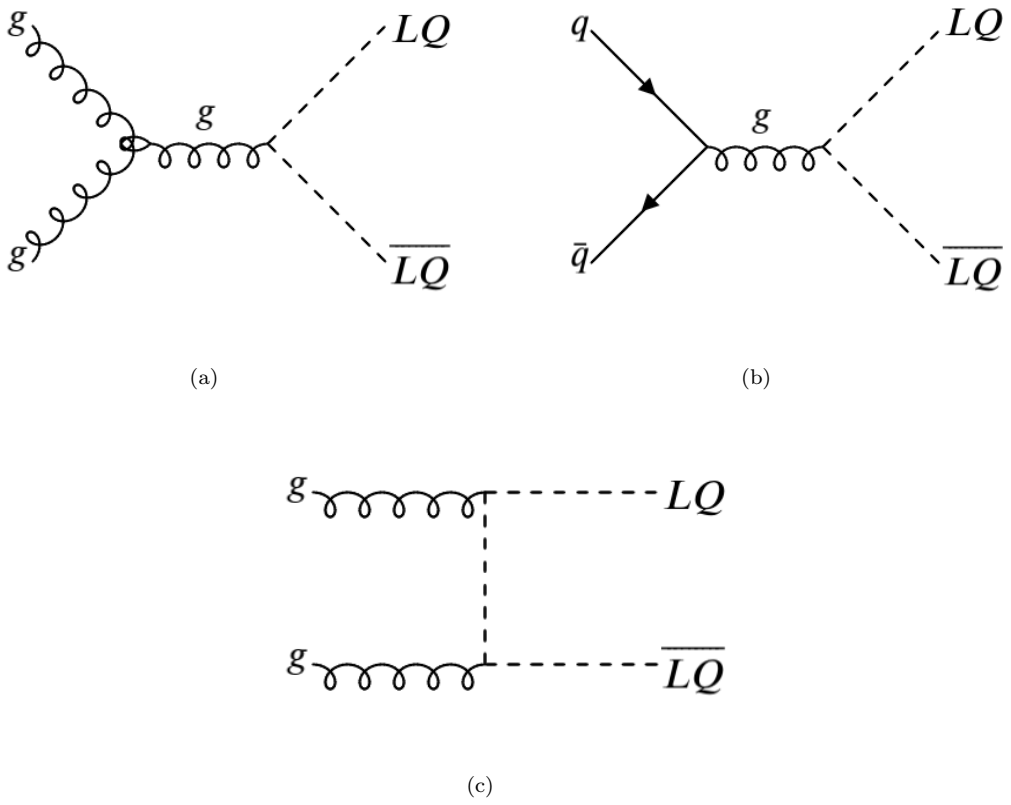

FIGURE 11.3: LO Feynman diagrams of hypothetical LQ pair production in proton-proton collisions.

11.1.2 Sensitive Variable

The main contribution of the expected single LQ signal for $\lambda_{lq} \approx 1$ is created via the s-channel diagram shown in Fig. 11.2 (a). The LQ production in this diagram is entirely resonant, which is the reason why a distinctive structure in the total differential signal cross-section $d\sigma_s/dm_{lj}^{LQ}$ is predicted. m_{lj}^{LQ} is the invariant mass of the LQ decay products. The t-channel diagram illustrated in Fig. 11.2 (b) leads to partially resonant and non-resonant effects, while the u-channel diagram in Fig. 11.2 (c) only gives non-resonant contributions. Given the light masses of electrons and muons[1] as well as quarks - with exception of the top quark - the kinematic

[1]The terminology does not differentiate between particle and anti-particle. This classification is done by referring to its electric charge. The term charged lepton is used for electrons and muons as well as their anti-particle.

distributions of this process does not depend significantly on the lepton and quark type in the final state.

The impact of the quark flavor to the kinematic properties of singly produced LQ and its decay products is investigated in App. B.4.

Fig. 11.4 illustrates the signal shape in the m_{lj}^{LQ} spectrum with varying mass hypotheses in (b) assuming $\lambda_{lq} = 1$ and the LQ decay into a muon and a bottom-quark. The signals shown are scaled to an integrated luminosity of 1 fb^{-1}. (a) depicts the decomposition of a signal with $m_{LQ} = 1500$ GeV in resonant and non-resonant contributions.

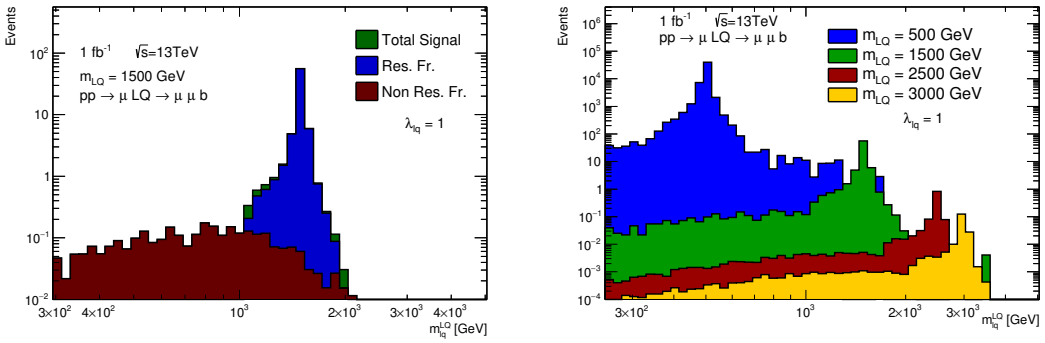

(a) (b)

FIGURE 11.4: Predicted LQ signal shape of the process $pp \to \mu LQ \to \mu\mu b$ against the invariant mass of the LQ decay products m_{lj}^{LQ}. (a) shows a signal distribution with $m_{LQ} = 1500$ GeV decomposed into resonant and non-resonant fractions and (b) multiple distributions for varying LQ masses m_{LQ} in the range of 500 GeV and 3 TeV under the assumption of $\lambda_{lq} = 1$.

The selected signal events contain two oppositely charged same-flavor leptons and a quark in the final state. The latter one is reconstructed as jet. There is no way to directly identify the lepton-jet pair which originates from the LQ decay, since the charged conjugated diagrams of the ones shown in Fig. 11.2 are considered as signal as well. Additionally, due to the nature of hadron collisions most events contain more than one jet. However, the majority of them are expected to be soft, which is the reason why the jet with the highest transverse momentum is selected for the following discussion. Taking both leptons in the signal event into account, the invariant masses of both lepton-jet pairs are defined as m_{LQmax} and m_{LQmin}, which are classified by the condition

$$m_{LQmax} > m_{LQmin}. \tag{11.1}$$

This analysis focuses on probing signal hypotheses with high LQ masses. In this case the m_{LQmax} observable is closely correlated to m_{lj}^{LQ}. For signal processes shown in Fig. 11.2 (a) and (b), the decay of the heavy LQ gives its products a high invariant mass. Thus the identification of the

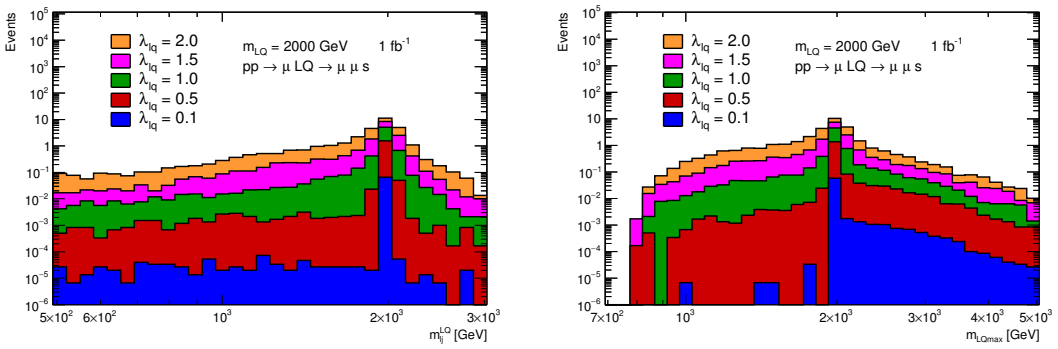

(a) (b)

FIGURE 11.5: Predicted 2 TeV LQ signal shape of the process $pp \to \mu\mathrm{LQ} \to \mu\mu s$ against $\mathrm{m}_{\mathrm{lj}}^{\mathrm{LQ}}$ (a) and the quantity $\mathrm{m}_{\mathrm{LQmax}}$ (b) on a logarithmic scale for varying λ_{lq} coupling values. Signal hypotheses are scaled to an integrated luminosity of 1 fb^{-1}.

lepton-jet pair originating from the LQ decay is very efficient in the resonant case. Fig. 11.5 illustrates this statement by depicting signals of a LQ with a mass of 2 TeV by displaying $\mathrm{m}_{\mathrm{lj}}^{\mathrm{LQ}}$ and $\mathrm{m}_{\mathrm{LQmax}}$ spectra side by side for various λ_{lq} coupling hypotheses on a logarithmic scale. This motivates the use of $\mathrm{m}_{\mathrm{LQmax}}$ as sensitive variable.

11.1.3 Signal Simulation and Input Parameters

A scalar representation of the Leptoquark (LQ) is studied. The Lagrangians of the LQ fields implemented in the signal model [59] are described in [158]. The decay of a LQ into a down type quark (down, strange, bottom) is modeled with the $\tilde{S}_1$ representation, while the decay into the up quark uses the S_1 representation.

Two model parameters impact the differential cross-section $d\sigma_s/d\mathrm{m}_{\mathrm{lj}}^{\mathrm{LQ}}$. The LQ mass m_{LQ} and the LQ-quark-lepton coupling λ_{lq} need to be fixed to get a prediction. A variation of the leptoquark mass changes the position of the resonant structure as well as the total cross-section. This is illustrated in Fig. 11.4.

The number of LQ-lepton-quark vertices per signal diagram shown in Fig. 11.2 indicates the fraction each diagrams contributes to the total cross-section at a given λ_{lq} value. In (a) and (b) there is one of these vertices and in (c) there are two. Thus the contribution of the first two diagrams scale with $|\lambda_{\mathrm{lq}}|^2$ and in case of (c) with $|\lambda_{\mathrm{lq}}|^4$. The parameter space this analysis aims to probe is at m_{LQ} in the TeV range and λ_{lq} couplings of order $\mathcal{O}(1)$. First order correlations between the coupling $|\lambda_{\mathrm{lq}}|^2$ and the signal cross-section are illustrated in Fig. 11.5. Signal hypotheses for a fixed mass of 2 TeV and varying coupling parameters λ_{lq} are shown.

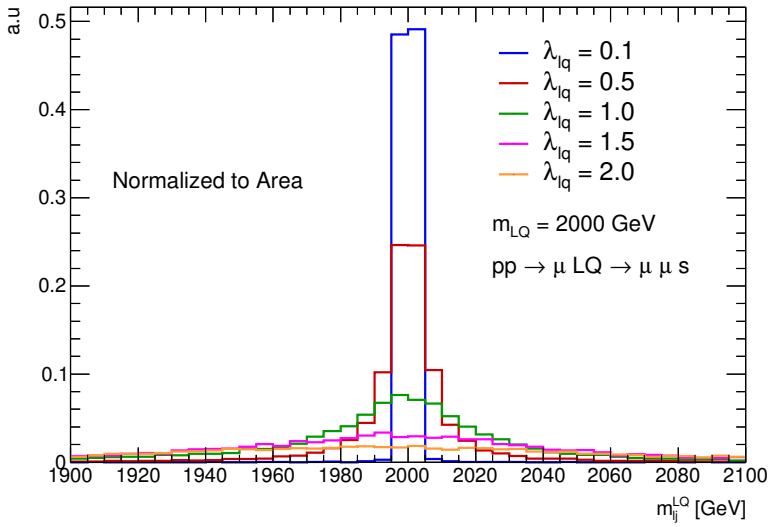

(a)

FIGURE 11.6: Signal shapes in m_{lj}^{LQ} of a 2 TeV LQ signal with varying coupling parameters λ_{lq}. Each spectrum is normalized to its area for shape and width comparison.

Since the coupling parameter impacts the fraction of non-resonant contributions, it influences the width of the signal as well. A larger LQ-lepton-quark coupling leads to an increased signal width. Fig. 11.6 depicts the magnitude of this effect by displaying signal shapes normalized to their area for different λ_{lq} values against m_{lj}^{LQ} for a mass hypothesis of 2 TeV.

In the generation of signal samples the coupling parameter of one lepton flavor (electron, muon) and one quark flavor (down, strange, bottom, up) has been set to $\lambda_{lq} = 1$. This leads to a resonant signal structure, whose widths is narrower than the detector resolution.

LQ models generally allow the decay into a neutrino-quark pair as well. This is quantified by the parameter β, which is at first order the branching ratio for the LQ decay into charged leptons. The $\tilde{S}_1$ representation [158] does not allow the decay into a neutrino due to its hypercharge of 4/3. For the statistical interpretation the decay channel into an up-quark and a lepton is studied with the S_1 LQ representation, which carries a hypercharge of 1/3. For this signal the assumption of $\beta = 1$ is made.

Signal samples were simulated with MADGRAPH5 [160], the "ToolBox" UFO model [59] and the NNPDF3.0NLO[36] PDF set on leading-order. MADGRAPH5 is interfaced to PYTHIA8 [131] using the A14 set of tuned parameters. Four set of different signal samples and the interaction of their final state particles with the detector have been simulated. Electron and muons are chosen as lepton types, while for quarks strange and bottom are considered. The samples with strange quarks in the final state are used to probe signal processes with up and down quarks as well. This is possible since the signal shape does not depend on the quark type at first order and the

b-tagging algorithms [116] performance is the same for up, down and strange quarks. The decay into charm quarks is not investigated due to the varying performance of b-tagging algorithm on jets induced by charm quarks. Samples in a LQ mass range of 500 GeV to 3500 GeV were generated.

11.2 Background Processes

In this section relevant processes which give contributions to the background in the signal regions are discussed. The two most dominant background processes are discussed first. Z/γ^*+ jets events are expected to constitute the largest background contribution when events containing b-tagged jets are neglected. Otherwise $t\bar{t}$ events constitute the largest background fraction. Control regions are defined for the Z/γ^*+ jets process and $t\bar{t}$ production (see Sec. 11.4.4). These are used to investigate background modeling and obtain corrections which are applied in the signal regions. Events of the charge-conjugated diagrams to the ones shown in the following contribute to the background as well.

11.2.1 Z/γ^*+ Jets Process

Fig. 11.7 shows the LO tree level Feynman diagram of the Z/γ^*+ jets process. The two selected opposite-charge, same-flavor leptons are produced by the decay of a Z/γ^* boson. In most cases the highly energetic jet originates from initial state radiation. The transverse momentum distributions of the Z/γ^* decay products peak around $\mathrm{p_T} = 45\,\mathrm{GeV}$, due to the Z mass of $\mathrm{m}_Z \approx 91\,\mathrm{GeV}$ [18]. High-energy leptons created in this process originate from Z/γ^* bosons, which have a high transverse momentum or which were produced off-shell.

Criteria imposed on the invariant mass of the lepton pair m_{ll} give a good handle to define a control region and to suppress background contributions in the signal region. Additionally the imbalance of lepton momenta $\Delta\mathrm{p}_\mathrm{T}^{ll} = |\mathrm{p}_\mathrm{T}^{l1} - \mathrm{p}_\mathrm{T}^{l2}|$ and its discrimination power has been studied. In signal events this value is expected to be large, while the transverse momenta of leptons from a Z/γ^* decay are more likely to be symmetrical. The additional discrimination power has been found to be less valuable compared to the loss in signal efficiency. Therefore, this quantity is not used later on in the event selection.

For each charged opposite-sign lepton pair type, the inclusive cross-section is large compared to other background processes with real electrons. This is the reason why it yields the dominant background contribution in the signal regions in which no b-tagged jets are selected.

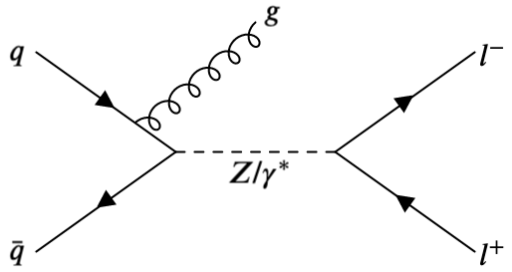

(a)

FIGURE 11.7: Tree level (LO) Feynman diagram of the Z/γ^*+ jets process. The jet is produced by initial state radiation.

11.2.2 Top Anti-Top Production

The other dominant contribution of background events in the signal region originate from $t\bar{t}$ quark production. Most top and anti-top quarks are produced in pairs at the LHC via the tree level diagrams depicted in Fig. 11.8.

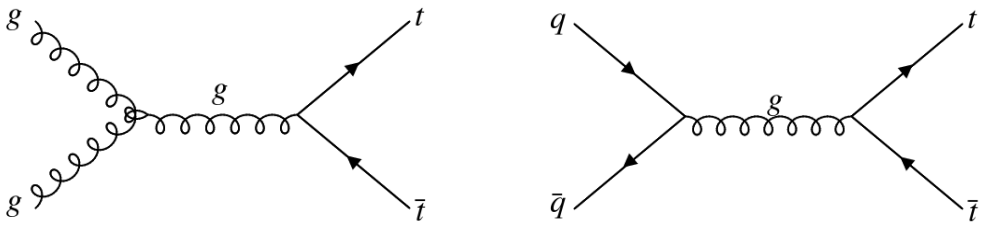

(a) (b)

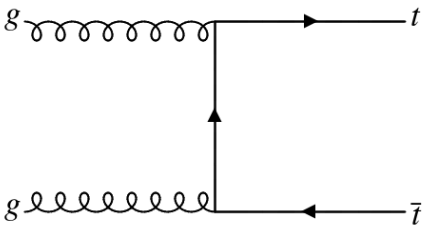

(c)

FIGURE 11.8: Tree level Feynman diagrams of $t\bar{t}$ production at the LHC.

Each (anti-)top quark decays almost exclusively into a (anti-)bottom quark and W boson as displayed in Fig. 11.9. Events in which both W bosons decay into leptons of the same generation constitute a background in this analysis. The selected high energy jet can be either one of the b-jets produced in the top decay or originate from initial or final state radiation. Classifying

events by the number of b-tagged jets allows to suppress $t\bar{t}$ contributions in the signal region and to define a $t\bar{t}$ enriched control region.

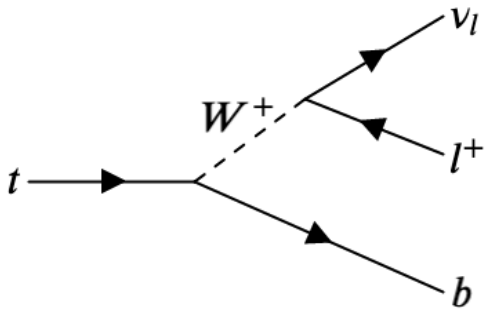

(a)

FIGURE 11.9: LO Feynman diagram of the top quark decay with a charged anti-lepton in the final state.

$t\bar{t}$ production with a subsequent decay into a same-flavor lepton pair in the final state constitutes the largest background fraction in regions where b-tagged jets are selected.

11.2.3 Other Processes with Top Quarks

Other processes with a same-flavor, opposite-sign lepton pair in the final state, which have a top quark as an intermediate state, are discussed here. The largest contribution in this category comes from single top quark production in association with a W boson. The LO s-channel and t-channel diagrams of this process are shown in Fig. 11.10.

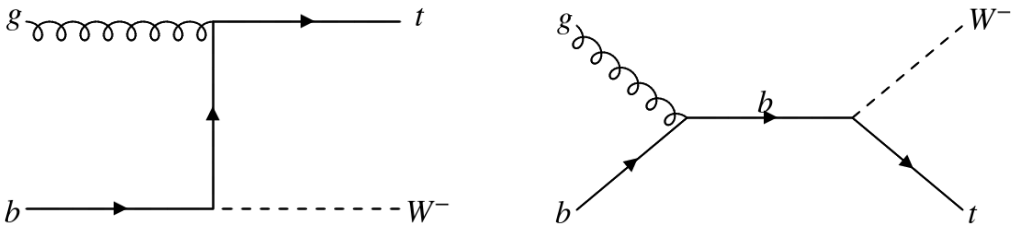

(a) (b)

FIGURE 11.10: LO Feynman diagrams of single top quark production in combination with a W boson. In (a) the s-channel diagram and in (b) the t-channel diagram is depicted.

Top quarks decay as discussed in Sec. 11.2.2 and illustrated in Fig. 11.9. The two decays of oppositely charged W bosons give the opportunity to create an opposite-sign same-flavor lepton pair.

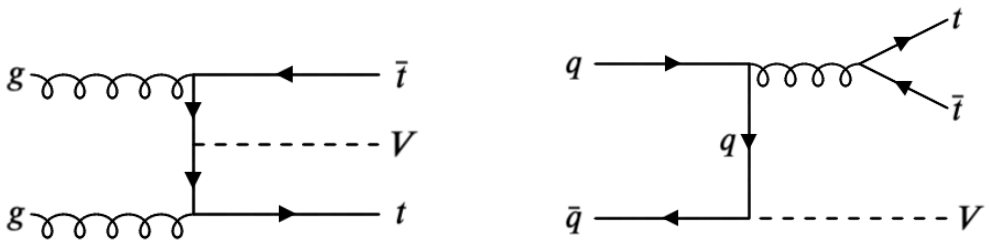

(a) (b)

FIGURE 11.11: LO Feynman diagrams of $t\bar{t}$ production in combination with an additional electroweak boson. In diagram (b) the V can represent either a W or a Z/γ^* boson. The initial state quark flavors are chosen accordingly.

Furthermore, processes, in which an additional electroweak boson is produced alongside the $t\bar{t}$ pair, are contributing to the background. LO diagrams of these processes are shown in Fig. 11.11. Different combinations of electroweak boson decays lead to a lepton pair and high jet activity in an event. Contributions from $t\bar{t}$ plus Higgs boson production are even smaller and therefore neglected.

11.2.4 Diboson Processes

At hadron colliders isolated leptons in the final state originate dominantly from electroweak boson decays. Therefore, processes in which two of these are produced simultaneously contribute to the background. Fig. 11.12 shows the corresponding LO Feynman diagrams. In this category the production diagram depicted in Fig. 11.12(a) without a triple gauge coupling vertex contributes the most background events.

11.2.5 Background Simulation

This section gives an overview of the simulated background samples and their generator setups. More details about event generation methods and about the detector simulation can be found in Sec. 5.1.

$Z/\gamma^*(W)$+Jets Process The Z/γ^*+jets samples are generated by SHERPA 2.2.1 [143] and the NNPDF3.0 [36] next-to-next-to-leading-order (NNLO) set of parton distribution functions. Additionally, this sample is normalized to the NNLO cross-section in QCD obtained by FEWZ [161][162][163] and the MSTW2008 NNLO PDF set [164]. The generation is done in separate phase space intervals of $\max(H_T, p_{T,V})$ to obtain sufficient statistics in the entire fiducial volume. This quantity is given by the maximum of H_T - the scalar sum of the final state particles p_T

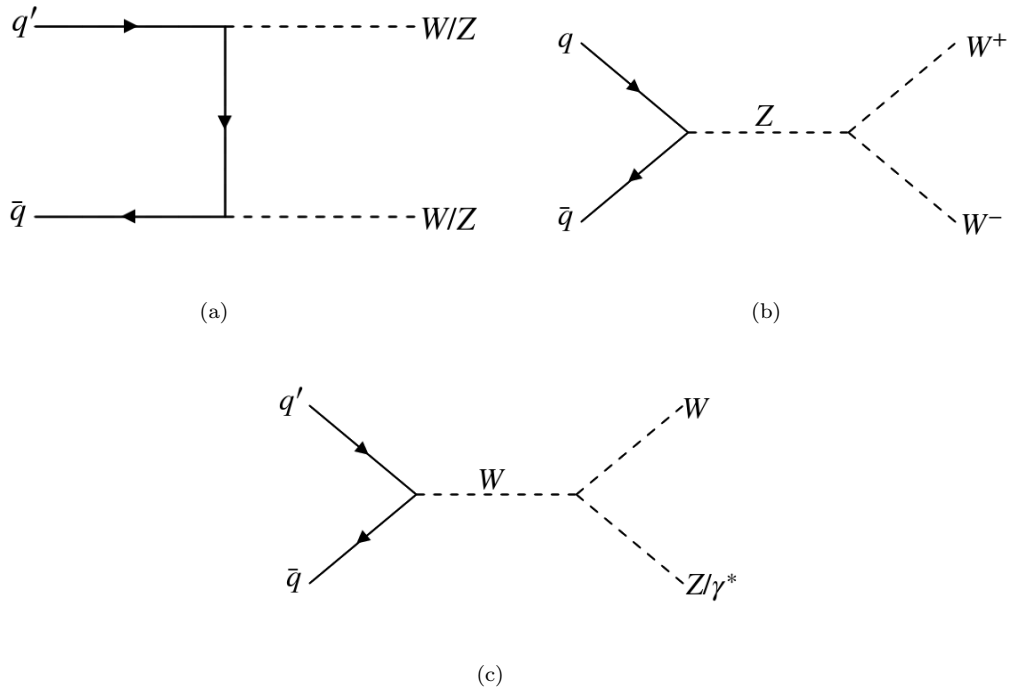

FIGURE 11.12: LO Feynman diagrams of processes in which two electroweak bosons are produced in proton-proton collision.

- or the p_T of the electroweak boson. Both variables are closely correlated to the invariant masses of the lepton-jet pairs. An additional separation is done to gain good statistics for each quark flavor. The following categories are used: c-quark veto + b-quark filter, c-quark filter + b-quark veto and b-quark filter. This classification is done using generator level information of the particles.

For the determination of the fake background a sample of W+jets events is necessary. The generation configuration and tools are the same as for the Z/γ^*+jets sample. Since this process only leads to a single lepton in the final state, events in these samples do not enter the background. Contributions of events with mis-identified objects are very small in the muon channels. In the electron channels these events are estimated with a data driven method, which is introduced Sec. 11.5.1.

Processes with Top Quarks The generation of a top anti-top quark pair and s-channel W+top quark production is done using the POWHEG BOX v2 [136] generator. The CT10 PDF set [137] is considered for the Wt processes, while $t\bar{t}$ events are generated using the NNPDF3.0 [36] set. Electroweak single top quark events in the t-channel are simulated using the POWHEG BOX v1 [136] generator. This generator uses the fixed four flavor PDF set CT10F4 [137] in combination with a four flavor scheme to obtain the NLO matrix elements necessary for the simulation.

In samples with single top quarks the parton shower, fragmentation and underlying event is simulated using PYTHIA8 [131], the CT10 PDF set and the PERUGIA 2012 tune [165]. For the $t\bar{t}$ sample the NNPDF3.0 set and A14 tune is used instead of PERUGIA 2012. The mass of the top quark is set to 172.5 GeV. The so-called *hdamp* parameter, which handles the p_T of the first emission after the born configuration, is set to the top quark mass in single top quark processes. For the generation of the $t\bar{t}$ sample this parameter was set to $1.5 \cdot m_t$. The main purpose of this is to control the recoil of the $t\bar{t}$ pair.

Diboson Processes Processes with two electroweak bosons in the final state are generated by SHERPA 2.2.2 [143]. Decays with at least two charged leptons are included only by considering matrix elements containing all diagrams with four electroweak vertices. Processes with $4l$, $3l$ and $2l$ in the final state are generated at NLO with COMIX [166] and OPENLOOPS [167]. This calculation is combined with the parton shower generation implemented in SHERPA. The CT10 PDF set with a process specific parton shower tune, which has been developed by the SHERPA authors was used. In the simulation the strong coupling parameter has been set to $\alpha_{QED} = 1/129$ instead of the value given by the Particle Data Group [18] of $\alpha_{QED} = 1/132$ as input. This is the reason why the cross-section of the sample is scaled down.

Rare Top Quark Processes Rare top quark processes are synonymous with $t\bar{t} + V$ production, with V being an electroweak boson. The simulation of these processes was performed by MADGRAPH5_AMC@NLO [160] with the NNPDF3.0 [36] PDF set. For parton shower as well as hadronization PYTHIA8 [131] and the NNPDF2.3 [132] with the A14 tune is used.

11.3 Data Sample

The data analyzed in this search was recorded by the ATLAS experiment in the years 2015, 2016, 2017 and 2018 in proton-proton collisions at a center of mass energy of $\sqrt{s} = 13$ TeV. The total amount of data corresponds to an integrated luminosity of $L_{int} \approx 139\,fb^{-1}$.

All events recorded need to pass criteria, which ensure full functionality of relevant detector parts while recording. Events in which noise bursts in one of the calorimeters have been identified are vetoed. These could fake energy depositions of particle signatures. Additionally, the well functioning of the SCT detector is guaranteed. Malfunction is possible when a high energy, ionizing particle crosses through electronic modules. Parts of the trigger system need to be restarted from time to time while taking data. Events which have been recorded during these intervals are rejected as well.

Fig. 11.13 shows the accumulated delivered and recorded integrated luminosity against time for the LHC Run 2. Additionally, the integrated luminosity after filtering events by previously described criteria is shown in blue. Time spans, which were dedicated to accelerator and detector maintenance, are visible as flat periods in the diagram. In total the LHC delivered 156 fb^{-1} of proton-proton collisions at the interaction point of ATLAS. ATLAS recorded 147 fb^{-1} of this, which represents a data taking efficiency of 94.2%. This efficiency drops to 89.1% with respect to the delivered integrated luminosity when the additional quality requirements are imposed.

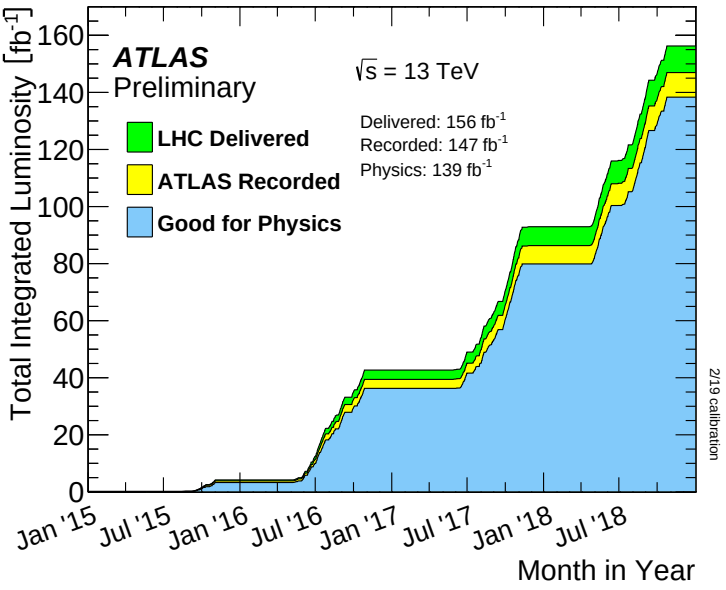

FIGURE 11.13: Accumulated integrated luminosity against time during the LHC Run 2. The delivered integrated luminosity as well as the amount which got recorded by ATLAS, before and after additional data taking quality criteria have been imposed, are shown. [129]

11.4 Selection

The data events are recorded by a single lepton trigger. To record the data sample studied in the electron channel a combination of two trigger setups sensitive to a single electron[2] with varying p_T thresholds and identification criteria are used. By requiring a high candidate p_T a more efficient identification algorithm can be used, while not blocking to much bandwidth of the data acquisition system. To cover lower p_T ranges and thus lower signal mass hypothesis the second trigger setup, which uses an identification working-point with higher background rejection, is included. In case of the muon channel, one trigger sensitive to a single muon with p_T larger than 50 GeV is collecting the data samples.

[2] e60_lhmedium_nod0, e140_lhloose_nod0

11.4.1 Object Selection

In this section requirements on the reconstructed objects and their signatures are defined. Lepton candidates are classified by two different sets of selection criteria - *signal* and *baselevel*. The *signal* object requirements are more stringent than the *baselevel* criteria and give stronger rejection against mis-identification. The sample of objects selected as *signal* is a subset of the *baselevel* ensemble. *Signal* level objects are considered for the final statistical analysis, while the *baselevel* objects are used for event specific cleaning cuts. As long as it is not specified, object level requirements listed are used for both selections.

Electrons Electron candidates are obtained using the standard electron reconstruction algorithm [103] described in Sec. 4.3.1.1. First it is ensured that all electron candidates have been recorded by fully functional detector components.

The best energy resolution and cleanest signatures of electron candidates are obatined in the central regions of the detector. The inner detector covers the pseudorapidity range of $|\eta| < 2.5$. Candidates must be measured within $|\eta| < 2.47$ to avoid border effects and ensure that the track as well as the energy deposition is captured in its entirety. Additionally, electron candidates which enter in the transition region of the calorimeters $1.37 < |\eta| < 1.52$ are not selected, due to less efficient reconstruction and worse energy resolution.

The selected electron candidates are classified into leading and sub-leading according to their transverse momentum. Leading candidates, which are identified as the one with higher p_T, are required to have $p_T > 65$ GeV to avoid inefficiencies near the trigger thresholds. The criteria on the sub-leading candidate is relaxed to $p_T > 30$ GeV, since the lepton originating from the LQ production vertex oftentimes has low energy.

Requirements applied to the track impact parameters d_0 and z_0 are imposed in an attempt to select only candidates originating from the primary vertices. The d_0-significance of selected candidates is smaller than $\sigma_{d_0} < 5$ and the value of $|z_0 \cdot \sin\theta|$ is smaller than 0.5 mm. More details about the track impact parameters and vertex reconstruction are given in Sec. 4.2.

Each electron candidate must pass an identification algorithm. *Signal* candidates are required to fulfill isolation criteria as well. Details on these identification and isolation methods are given in Sec. 4.3. *Signal* level electron candidates must pass the *lhTight* identification, while for *baselevel* electron candidates the *lhLoose* identification is applied. In the *signal* object selection the working-point *Gradient* is used for the isolation criteria.

Muons Muon candidates are reconstructed by the algorithms [84] introduced in Sec. 4.3.3. They must pass additional quality criteria to guarantee good resolution and properly measured

momenta as well. Only combined muons are considered, meaning that the signature is composed of a track measured in the inner detector and muon spectrometers.

The phase space of selected candidates is restricted in two ways in terms of pseudorapidity. On the one hand there is an explicit requirement on the pseudorapidity of muon candidates of $|\eta| < 2.5$. On the other hand the muon trigger chambers only extend up to $|\eta| = 2.4$. The use of the single muon trigger in this channel introduces an additional restriction on the candidate, which issued the trigger, of $|\eta| < 2.4$.

For symmetry reasons the criteria on the muon candidates' transverse momentum are chosen analogously to the electron channel. Consequently the requirement imposed are $p_T > 65$ GeV on the leading candidate and $p_T > 30$ GeV for others. Inefficiencies at the threshold are negated with these cuts as well, since the muon trigger in use has a lower p_T threshold compared to the electron triggers.

Criteria imposed on the track impact parameters - d_0 and z_0 - are more relevant for muon candidates compared to electron candidates, as the suppression of cosmic rays muons is necessary. For $|z_0 \cdot \sin\theta| < 0.5$ the same cut value is used, while the criteria on σ_{d_0} is more stringent by imposing a maximum value of three ($\sigma_{d_0} < 3$).

Similar to electron candidates algorithms to classify the quality of the signature are used. *Baselevel* candidates have to only pass identification criteria, while the *signal* object selection imposes isolation requirements introduced in Sec. 4.3.3.2 additionally. For the identification the *highPt* working-point is used. It is optimized to provide the best energy resolution at high transverse momenta and avoid mis-measurements due to misalignment of the muon chambers. The isolation algorithm with the *FCTightTrackOnly* working-point is applied.

Jets Jets are reconstructed by the anti-k_t algorithm [168] with a size parameter of 0.4. Details about jet reconstruction and calibration in ATLAS are given in Sec. 4.3.4.

Jets must have a p_T larger than 30 GeV and have to be reconstructed in the central region of the detector ($|\eta| < 2.5$) to be selected. Using jet vertex tagging techniques described in Sec. 4.3.4.1 pile-up contributions are suppressed for jets with p_T smaller than 60 GeV and $|\eta| < 2.4$. The *b*-tagging algorithm MV2c10 only considers jets with $|\eta| < 2.5$, which is the reason why forward jets are vetoed. MV2c10 is a combination of multiple *b*-tagging algorithms inside a boosted decision tree and is tuned in such a way that it provides a 77% *b*-tagging signal efficiency. In simulated $t\bar{t}$ events the rejection factor of *c*-jets is found to be approximately at 4 and of light jets to be approximately at 110. More details about *b*-tagging algorithms can be found in Sec. 4.3.5.

11.4.2 Event Selection

The following criteria are designed to ensure that only well measured signatures are considered. Additionally requirements to control the expected fractions of different processes according to the purpose of each kinematic region are discussed.

First a procedure is done, which removes objects with overlapping signatures. This way double-counting of tracks as well as clusters is avoided. In this method all objects tagged as *baselevel* are considered and a fixed prescription is followed. First all electron candidates sharing a track with a muon candidate are removed. In the second step all jets with an angular distance $\Delta R = \sqrt{(\Delta\eta)^2 + (\Delta\phi)^2}$ smaller than 0.2 to any electron candidate remaining are rejected. Afterwards electron candidates with $\Delta R < 0.4$ to the closest jet are neglected. This is motivated by the larger width of jet energy depositions. In the last step jet muon candidate pairs fulfilling $\Delta R < 0.04 + 10\ \text{GeV}/\mathrm{p}_\mathrm{T}^{\mu}$ are investigated, where $\mathrm{p}_\mathrm{T}^{\mu}$ is given by the p_T of the muon candidate. If the tested jet has at most two associated tracks with $\mathrm{p}_\mathrm{T} > 0.5$ GeV the jet is removed from the event. Otherwise the muon candidate is rejected, under the assumption that it was produced inside the jet.

Due to the characteristics of the signal process, events with exactly one pair of oppositely-charged, same-flavor leptons, which are tagged as *signal*, are selected. Events with more than two *baselevel* leptons are neglected, since they most likely contain a mis-identified object or originate from a diboson process. Furthermore, it is ensured that at least one of the selected leptons caused the trigger to be activated.

The invariant mass of the lepton pair m_{ll} and the number of b-tagged jets in an event N_b are used to define various signal and control regions.

11.4.3 Signal Region

Event level criteria to define kinematic regions, which yield the best discrimination between signal and background events, have been investigated. This is done by estimating expected significances of a signal, while varying the cut value of the studied quantity simultaneously.

This way the optimized requirement on the invariant mass of the lepton pair was found to be $\mathrm{m}_{ll} > 400$ GeV. This is explained by the more steeply falling m_{ll} distribution of Z/γ^*+jets events compared to signal events. Additionally, the scalar sum of all *signal* jets in an event H_T is required to be larger than 350 GeV. This criteria suppresses background contributions of $t\bar{t}$ production. Other quantities which have been studied are the imbalance of the lepton candidates' transverse momenta $\Delta\mathrm{p}_\mathrm{T}^{ll} = |\mathrm{p}_\mathrm{T}^{l1} - \mathrm{p}_\mathrm{T}^{l2}|$ and the scalar p_T sum of all selected objects in the final state. The gain in significance, that is obtained by imposing requirements on the

latter two quantities has been found to be not large enough to counteract the loss in signal selection efficiency as well as MC and data statistics.

In each channel two signal regions are investigated. These are characterized by the number of b-tagged jets in events N_b. The ensembles of events with $N_b = 0$ (b-veto regions) and $N_b = 1$ (b-tag regions) are analyzed separately. For discussion of systematic uncertainties the term combined region is used, which refers to the sum of the b-tag and b-veto regions.

In Fig. 11.14 the product of detector acceptance and selection efficiency against the LQ mass of a given signal hypothesis is displayed. This is shown separately for the electron channel and muon channel in the b-veto and b-tag categories. The statistical analysis uses a single-bin approach. The lower threshold on m_{LQmax} imposed in the signal regions is varied for each mass hypothesis to optimize the sensitivity. This is the reason why the product of acceptance and efficiency is calculated in the following by taking the integral of the m_{LQmax} tail starting from $0.6 \cdot m_{LQ}$ of the signal hypothesis in question. The graphs referring to the b-veto categories are shown in red for the electron and orange for the muon channel. Both increase steeply at low masses. The starting values are very low with roughly 0.12 in the muon channel and 0.22 in the electron channel due to the m_{ll} cuts imposed. At low LQ masses the fraction of signal events neglected by this requirement is large. However, the corresponding signal parameter space of these has been probed already by past analyses [159]. Both of them reach a plateau at $m_{LQ} \approx 1.2$ TeV - at values around 0.5 in the electron and 0.3 in the muon channel. The main reason for the large difference here is the use of the *highPt* identification in the muon object selection. Large parts of the detector are vetoed, in which poor muon chamber alignment may lead to problems in the reconstruction of high p_T muon candidates (see Sec. 4.3.3.2).

The graphs describing the product of acceptance and efficiency of the b-tagged signal regions are drawn in green and blue. The increase at low values as well as the over all offset between both can be explained analogously to the b-veto regions. The displayed values are slightly below half of the acceptance times efficiency expected in the b-veto regions and show a slight decrease at high LQ mass signals. The former observation can be explained by a combination of the b-tagging efficiency - being at 77% - and the fact that exactly one b-tagged jet is required. Due to this signal events are vetoed in which additional b-jets have been reconstructed. The decrease for signals with high LQ masses is caused by fact that the b-tagged jet has high p_T most of the time. However, the b-tagging algorithms are optimized with low p_T jets, which gives extrapolation effects relevance at high m_{LQ}.

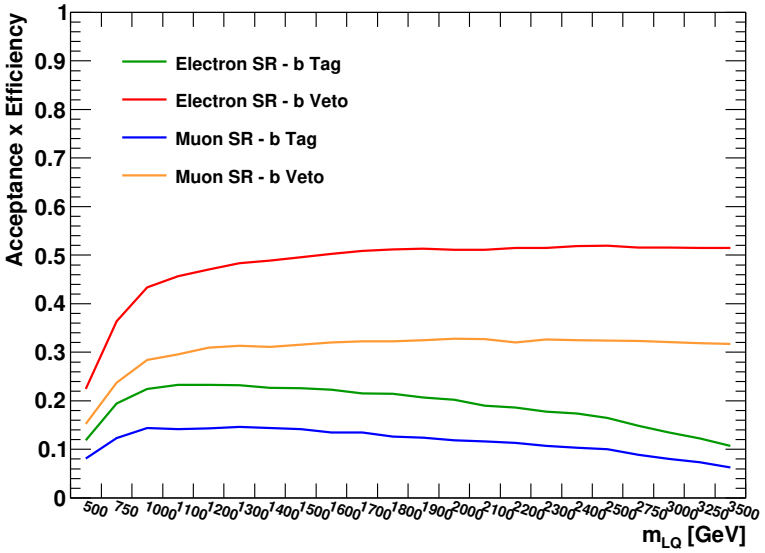

FIGURE 11.14: Acceptance times efficiency of the electron and muon channel signal selection against the LQ mass hypothesis shown separately for the b-tag and b-veto categories. To take the single-bin approach of the statistical analysis into account the numerator and denominator is obtained using events in the high m_{LQmax} range starting from $0.6 \cdot m_{LQ}$.

11.4.4 Control and Validation Regions

In this section the kinematic regions are defined, which are utilized to correct and validate the modeling of dominant background processes. To ensure a signal like event topology only the high m_{LQmax} range is considered. This is established by requiring $m_{LQmax} > 300$ GeV in all selected events.

Fig. 11.15 shows a schematic overview of all kinematic regions. On the x-axis the restrictions on m_{ll} in each region are illustrated, while on the y-axis the criteria on the number of b-tagged jets are depicted.

Z/γ^* Control Region The purest sample of Z/γ^*+ jets events can be selected by requiring the invariant mass of the lepton candidate pair to be within an interval around $m_Z \approx 91$ GeV. Z/γ^*+jets background events, that enter the signal region, contain in most cases the decay of an high mass off-shell Z/γ^*. To define the control region with sufficient statistics, while simultaneously maintaining similarity to the signal region an invariant mass window $130 \text{ GeV} < m_{ll} < 250$ GeV is chosen to define the Z/γ^* control region selections.

To suppress $t\bar{t}$ contributions only events with less than two b-tagged jets are considered. Analogously to the signal regions, b-veto ($N_b = 0$) and b-tag ($N_b = 1$) control regions are defined. However, by requiring a b-tag the fraction of Z/γ^*+jets events in the total background is greatly reduced. This will be further investigated in Sec. 11.7.

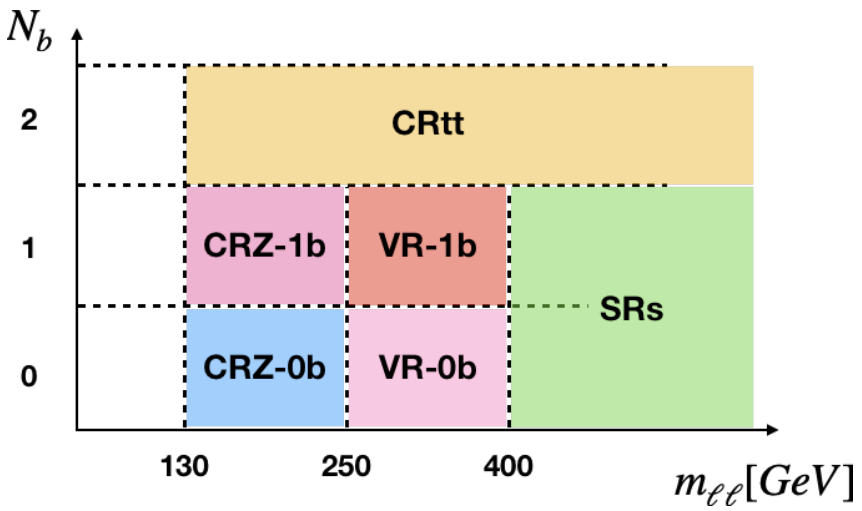

FIGURE 11.15: Schematic view of all kinematic regions. The x-axis illustrates the requirement on $m_{ll}(m_{\ell\ell})$ and the y-axis on the number of b-tagged jets selected in each region. [169]

Top Control Region The $t\bar{t}$ process can be studied by selecting events with two b-tagged jets ($N_b = 2$). Each top quark decays almost exclusively into a W boson and a bottom quark, which leads to two b-tagged jets in the final state.

Commonly events with opposite-flavor leptons are selected to investigate the $t\bar{t}$ process. Usually this is a good handle since mostly events from processes with two W bosons in the final state enter this selection - assuming correct particle reconstruction and identification. Compared to the $t\bar{t}$ production, other processes with two W bosons in the final state have a very low cross-section. However, to avoid overlaps with possible signal regions in searches for lepton flavor violating LQ decays this criteria is not used [59]. These kind of decays are possible in the signal model probed (See Sec. 11.1.3).

Validation Region Additional validation regions are defined. In contrast to the control regions, these are not used in the statistical analysis to constrain nuisance parameters and obtain normalization factors. They are designed to be kinematically closer to the signal region by requiring the lepton candidate pair invariant mass to be within 250 GeV $< m_{ll} <$ 400 GeV. Again a classification in b-veto ($N_b = 0$) and b-tagged ($N_b = 1$) samples is done. The data to background comparisons in these regions are used to validate background modeling and correction factors, that are obtained by the statistical analysis.

11.4.5 Selection Efficiency

In this section the efficiency of the previously defined selection is studied. Tab. 11.1 shows the number of events in data remaining after each object level selection step. In the rows referring to electrons (muons) an event is considered when at least two *signal* level electron (muon) candidates pass the requirement in question. For the jet selection section only the remaining events with at least two *signal* lepton candidates are counted, while at least one *signal* jet has to fulfill the corresponding criteria. For the event level counter all events selected in previous steps are considered.

The number of events listed in the first column are selected using the combination of single electron and muon triggers. For lepton candidates the identification requirement rejects the largest fraction of events within each category. This is expected due to the stringent working-points utilized to achieve strong background rejection. The total numbers of events in the muon object selection is higher than in the electron channel. This is due to the lower p_T threshold on the single muon trigger compared to the ones in the electron channel in combination with the falling lepton candidate p_T spectrum. However, in the last selection step the leading lepton p_T is required to be larger than 65 GeV in both channels. The contribution of events with an electron pair passing this criterion is higher compared to the muon events. This is illustrated by the numbers of events selected in each region which are shown in Tab. 11.2. The large amount of events rejected by the same-flavor requirement can be explained with large contributions from $t\bar{t}$ events.

Tab. 11.2 lists the selected number of data events as well as the expectation of the dominant backgrounds in each control and validation region separately for each channel. The large decrease of the numbers in comparison to the last row of Tab. 11.1 is introduced by the $m_{LQmax} > 300$ GeV and the m_{ll} criteria. In the kinematic regions of the electron channel more events are selected than in the muon channel due to the higher selection efficiency. This has already been indicated by the acceptance times efficiency graphs discussed in Sec. 11.4.3. The purity of the b-veto Z/γ^* and $t\bar{t}$ control region is very high. In the b-veto Z/γ^* around 75% of the selected background events is expected to created by the Z/γ^*+jets process, while 85% of the background in the $t\bar{t}$ control region is created by $t\bar{t}$ events. Rare top quark processes and Wt production are considered as well for this estimation. In the b-tagged Z/γ^* control regions a large contribution from top quark processes is observed. For the statistical analysis simultaneous fits of these regions are utilized to determine normalization coefficients for each contribution. The low purity in the b-tagged Z/γ^*+jets leads to a large uncertainty on the normalization. However, the fraction of Z/γ^*+jets events to the total background is low in the b-tag signal region. The composition of the validation regions are very similar to the Z/γ^* control regions in each channel.

selection step		data
event cleaning and trigger		79215804
electron	η cut	57499192
	track impact parameter	36556699
	identification	8503127
	$p_T > 30$ GeV	5384972
	isolation	4925189
muon	combined muon	63381801
	identification	37001692
	$p_T > 30$ GeV	27810058
	track impact parameter	26050767
	isolation	24277967
jet	η cut	8790849
	$p_T > 30$ GeV	8194045
event	overlap removal	8346933
	same-flavor	4818203
	opposite-charge	4783476
	signal lepton candidates = 2	4783476
	leading lepton $p_T > 65$ GeV	4783237

TABLE 11.1: Number of selected data events after each object level selection step. In the rows referring to electrons (muons) an event is counted when at least two *signal* level electron (muon) candidates pass the corresponding requirement. For the jet selection section, only the remaining events with at least two *signal* lepton candidates are considered while at least one *signal* jet has to pass the criteria in question. The event level counter considers all events which were selected in previous steps.

channel	region	data	Z/γ^*+jets	top processes
electron	Z CR — b-veto	27634	19996	4091
	Z CR — b-tag	6043	840	5018
	VR — b-veto	9917	6065	2111
	VR — b-tag	3803	258	3597
	Top CR	19988	3498	16148
muon	Z CR — b-veto	21675	16728	2921
	Z CR — b-tag	4313	852	3645
	VR — b-veto	7199	4982	1470
	VR — b-tag	2653	217	2591
	CRtt	14104	2760	11714

TABLE 11.2: Selected number of events in each kinematic region - except the signal regions. The expected numbers of background events are shown for the two dominant background contributions - Z/γ^*+jets and processes including top quarks. These numbers are obtained using MC simulation and scaled to the integrated luminosity of data. All corrections considered are applied.

11.5 Background Estimation

11.5.1 Fake Background Estimation

For the estimation of the number of background events, which contain mis-identified leptons the data driven Matrix Method is utilized. Contributions of this type will be referred to as QCD or fake background in the following. In contrast to other background contributions the use of MC simulation is not practical for the determination. On one hand the modeling of properties and distinctive variables to identify leptons such as the isolation variables E_T^{cone20}(see Sec. 4.3.2) are not well modeled in MC. On the other hand large amounts of events must be simulated to get sufficient statistics in each kinematic region, since the background rejection of the *signal* object selection is high. This would make this approach very expensive in terms of computing time.

The background contribution is expected to be negligible in the muon channel, which is the reason why this estimation is performed in the electron channel only. To validate this assumption, the number of events of W+jets and dijet MC samples passing each selection is studied. The event counts when considering muon candidates induced only by real muons are compared to the counts, that are obtained without the so-called 'truth-matching' procedure. No dijet event passed any of the selections probed. The variation in the total number of events between both cases of all other backgrounds plus the W+jets process passing is very small. In most regions a decrease of event yields is observed when disabling the 'truth-matching'. The selection of additional lepton candidates which are used for event vetoes is loosened this way as well and therefore the veto is issued more frequently. The combination of these observations motivate the disregard of the fake background in the muon channel.

11.5.1.1 The Matrix Method in two Dimensions

The general idea of the Matrix Method is to first lower the background rejection of lepton identification and isolation criteria. Afterwards, efficiencies for objects, that are reconstructed in this larger sample, to fulfill the signal selection as well are measured. These probabilities are determined separately for candidates, which are originating from real electrons and other particles (so-called fake electrons). The amount of events passing both identification categories together with these efficiencies give the opportunity to estimate the number of so-called fake background events in each kinematic region.

In the following electron candidates passing the object selection with loosened identification criteria are labeled as *loose* and the ones passing the *signal* object selection are referred to as *tight*. The sample of events passing the additional event level criteria are given by N_{LL}, N_{TL}, N_{LT} and N_{TT} where the capital letters T and L define the object selections - *tight* and *loose*.

The first index of the variables represents the leading and the second one the sub-leading electron candidate. The real and fake efficiency - r and f - are given by the transition probabilities of real and so-called fake electrons, which pass the *loose* object criteria to also fulfill the *tight* requirements.

Eq. 11.2 gives a relation between the 'true' amount of events classified as real (R) and fake (F) electrons and the *loose* (L) and *tight* (T) selected electron candidates. The number of pairs N_{RR}, N_{FR}, N_{RF}, N_{FF} in each category are considered similar to electron candidate pairs N_{LL}, N_{TL}, N_{LT} and N_{TT}. Due to the fact that the property of being a real or a fake electron is exclusive, the same must hold true for the selection of electron candidates. This leads to the additional requirement that each candidate entering for example N_{LL} must not fulfill *tight* object identification requirements.

$$\begin{pmatrix} N_{TT} \\ N_{TL} \\ N_{LT} \\ N_{LL} \end{pmatrix} = M \cdot \begin{pmatrix} N_{RR} \\ N_{RF} \\ N_{FR} \\ N_{FF} \end{pmatrix} \tag{11.2}$$

with

$$M = \begin{pmatrix} r_1 r_2 & r_1 f_2 & f_1 r_2 & f_1 f_2 \\ r_1(1-r_2) & r_1(1-f_2) & f_1(1-r_2) & f_1(1-f_2) \\ (1-r_1)r_2 & (1-f_1)r_2 & (1-r_1)f_2 & (1-f_1)f_2 \\ (1-r_1)(1-r_2) & (1-r_1)(1-f_2) & (1-f_1)(1-r_2) & (1-f_1)(1-f_2) \end{pmatrix}. \tag{11.3}$$

Real r_i and fake f_i efficiencies are determined as a function of object related properties, for example the candidates' $\mathrm{p_T}$. This is the reason why they are listed separately for the leading electron r_1, f_1 and sub-leading electron candidate r_2, f_2. The dependencies are discussed in the following paragraphs.

Using previous equations the fake background is identified as the contribution of electrons containing at least one fake N_{RF}, N_{FR} and N_{FF} to the two *tight* electron candidate sample N_{TT} as shown in Eq. 11.4.

$$N_{TT}^{\mathrm{QCD}} = r_1 f_2 N_{RF} + f_1 r_2 N_{FR} + f_1 f_2 N_{FF} \tag{11.4}$$

To determine the samples of real and fake electrons - N_{RF},N_{FR} and N_{FF} - the matrix M shown in Eq. 11.4 is inverted. This way samples, that are not directly measurable, are expressed in terms of samples of lepton candidates and efficiencies, both of which can be determined in the data. In the following these relations are displayed.

$$\begin{pmatrix} N_{RR} \\ N_{RF} \\ N_{FR} \\ N_{FF} \end{pmatrix} = \frac{1}{(r_1 - f_1)(r_2 - f_2)} \begin{pmatrix} (f_1-1)(f_2-1) & (f_1-1)f_2 & f_1(f_2-1) & f_1 f_2 \\ (f_1-1)(1-r_2) & r_2(1-f_1) & f_1(1-r_2) & -f_1 r_2 \\ (r_1-1)(1-f_2) & (1-r_1)f_2 & (1-f_2)r_1 & -f_2 r_1 \\ (1-r_1)(1-r_2) & (r_1-1)r_2 & r_1(r_2-1) & r_1 r_2 \end{pmatrix} \begin{pmatrix} N_{TT} \\ N_{TL} \\ N_{LT} \\ N_{LL} \end{pmatrix}$$

By inserting this expressions into Eq. 11.4 an estimation for the fake background can be written as the sum of selected candidate pairs in different categories. These ensembles of events are weighted by coefficients, which are calculated with the real and fake efficiencies. The relation can be displayed as

$$N_{TT}^{QCD} = \alpha[r_1 f_2 (f_1 - 1)(1 - r_2) + f_1 r_2 (r_1 - 1)(1 - f_2) + f_1 f_2 (1 - r_1)(1 - r_2)] N_{TT} \quad (11.5)$$

$$+\alpha f_2 r_2 [r_1(1 - f_1) + f_1(1 - r_1) + f_1(r_1 - 1)] N_{TL} \quad (11.6)$$

$$+\alpha f_1 r_1 [r_2(1 - f_2) + f_2(1 - r_2) + f_2(r_2 - 1)] N_{LT} \quad (11.7)$$

$$-\alpha f_1 r_1 f_2 r_2 N_{LL} \quad (11.8)$$

where

$$\alpha = \frac{1}{(r_1 - f_1)(r_2 - f_2)} \,. \quad (11.9)$$

The coefficient of N_{TT} is small and negative and corrects for real electrons that do not pass the *tight* candidate selection. The majority of events selected in this procedure will enter through the N_{TT} ensemble. The coefficients of N_{TL} and N_{LT} are large and positive. This leads in total to a positive number of fake background events being estimated.

11.5.1.2 Real and Fake Efficiencies

Real and fake efficiency are measured using the data and MC simulations. They are given by the ratio of the number of real or fake electrons creating a *tight* electron candidate (N_{tight}^{real}, N_{tight}^{fake}) over the the total number of real or fake electrons, which left a signature of a *loose* lepton candidate ($N_{loose}^{real}, N_{loose}^{fake}$). These ratios are shown in Eq. 11.10. Since these quantities are defined as efficiencies the samples of *tight* lepton candidates are subsets of the *loose* samples.

$$r = \frac{N_{tight}^{real}}{N_{loose}^{real}} \qquad f = \frac{N_{tight}^{fake}}{N_{loose}^{fake}} \quad (11.10)$$

The *tight* electron candidate selection is equivalent to the *signal* object selection discussed in Sec. 11.4.1, which is requiring *lhTight* identification and isolation. Due to the identification algorithm imposed at trigger level, the *loose* candidate selection differs from the *baselevel* selection defined beforehand. A identification working-point with stronger background rejection is used for electrons with $p_T < 145$ GeV to avoid biases introduced by one of the single electron triggers. Therefore, candidates in the *loose* selection must pass *lhMedium* identification in case their p_T is smaller than 145 GeV and *lhLoose* identification for higher transverse momenta. No isolation is required.

To obtain stable estimates small coefficients in Eq. 11.8 are desired. This is achieved by having a large difference between fake and real efficiencies, which is the reason why *lhLoose* identification is used where it is possible without introducing a bias in the *loose* selection. The usage gives lower fake efficiencies f compared to the *lhMedium* identification. In contrast the impact of this choice on the real efficiency r is orders of magnitude smaller.

Real Efficiency The real efficiency r is determined by taking the ratio of electron candidates, whose signatures are created by real electrons, which pass the *tight* and the *loose* selection - as shown in Eq. 11.10. These candidate ensembles are selected using the Z/γ^*+jets MC simulation (see Sec. 11.2.5). Generator level information is utilized to identify electron candidates that originate from real electrons. The matching is implemented by the requirement on the angular distance ΔR between the electron candidate in question and one of the generated electrons to be smaller than 0.2.

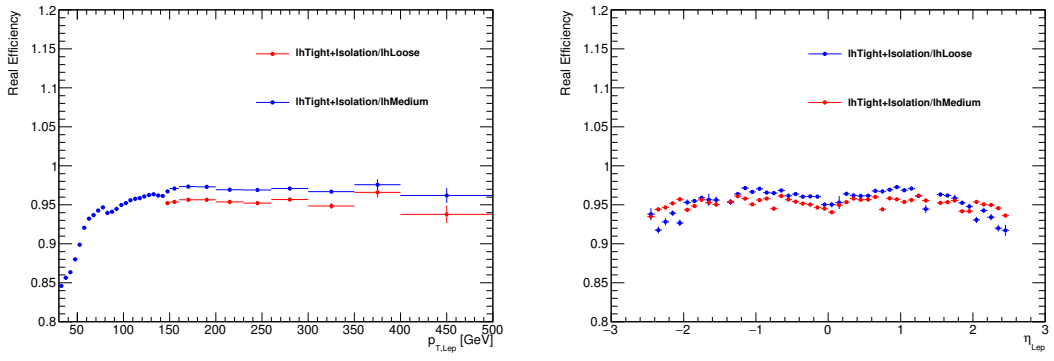

(a) (b)

FIGURE 11.16: Real efficiency depending on the electron candidates' p_T (a) and η (b). Red points are determined using the *lhMedium* identification requirement in the *loose* candidate selection, while for the blue points the *lhLoose* identification is utilized.

The real efficiency against candidates' p_T and $|\eta|$ is shown in Fig. 11.16. These one-dimensional projections offer a simple way to study dependencies. The number of events in the simulation is large enough that, two correlations are resolved simultaneously. The candidates' p_T and η

have been found to be the most relevant ones. Varying detector coverage causes a η dependence of the real efficiency. The p_T dependency is introduced by the identification and isolation requirements. Fig. 11.16 illustrate the efficiencies separated in the p_T and η intervals that are used.

In general the real efficiencies, that use the more stringent identification requirements in the *loose* selection, are higher compared to the other. This is expected since this way candidates, which are more likely to be connected to an electron, are considered in the first place. The real efficiency is around 85% at low p_T and rises steeply to around 95%. This is illustrating the good reconstruction and signal efficiency achieved for real electrons in the high p_T regime. At high absolute pseudorapidity values the real efficiency decreases. Here the distance to the calorimeter and the material budget in front of it is larger. Therefore interactions inside the inner detector are more likely. The symmetric behavior toward $\eta = 0$ is caused by the detector design. Spikes in the p_T distribution - for example around 85 GeV - are introduced by additional requirements imposed in the *lhMedium* identification to electron candidates with an p_T larger than this value.

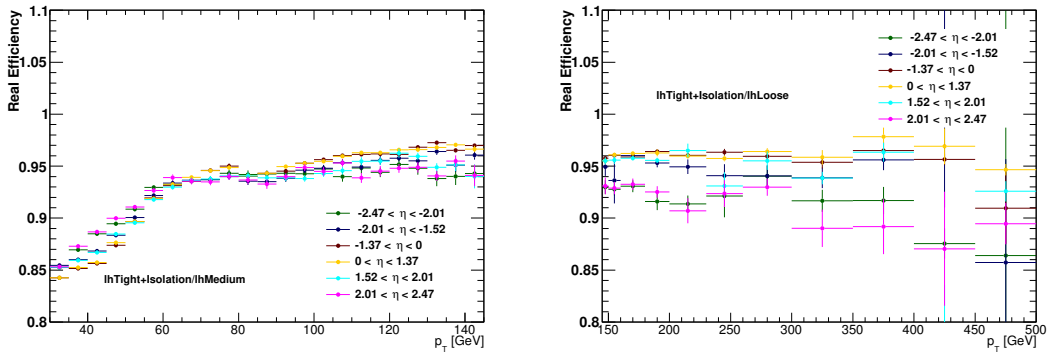

(a) (b)

FIGURE 11.17: Real efficiency depending on the electron candidates' p_T obtained in different η intervals. On the left side the real efficiencies in the low p_T regime are shown and on the right side the ones of high p_T candidates. The *loose* object selection is varied between both diagrams.

Fig. 11.17 depicts the real efficiency of electron candidates depending on their p_T in different η regions. Correlations that are observed in the one dimensional distributions are seen here as well. The p_T dependency illustrated follows the one displayed in Fig. 11.16 (a). The fact that the real efficiency decreases with the absolute η value is also visible comparing various η intervals.

Fake Efficiency The fake efficiency is the probability for candidates, that are reconstructed from signatures left behind by objects other than electrons and pass the *loose* selection to also pass the *tight* selection. This efficiency can not be determined with MC alone since the object composition is difficult to estimate and mostly unknown. This is the reason why the object samples required are selected in data by applying additional criteria to suppress the contribution of real electrons. Simultaneously the composition and properties of objects other than electrons should remain similar to the one in the signal and control regions of this analysis. Event topologies of electron candidates reconstructed close ($\Delta R < 0.4$) and not close to any b-tagged jet are studied separately. In general electrons are predominantly produced by the decay of the electroweak W and Z/γ^* bosons.

To suppress electrons originating from W decays, the missing transverse energy is required to be lower than 40 GeV. Additionally, events with two electron candidates passing the *lhLoose* identification requirements and $p_T > 20$ GeV, whose combined invariant mass is in a 20 GeV window around the Z peak are neglected. This suppresses electrons coming from on-shell Z decays. Off-shell Z decays are removed by vetoing events, that contain more than one electron candidate passing the *lhMedium* identification. To keep similarities between events entering these samples and events selected in the signal and control regions a high energy jet - with $\mathrm{p_T} > 30$ GeV - is required.

Despite these cleaning cuts the contribution of candidates originating from real electrons is not negligible. Therefore, this fraction has to be estimated and subtracted before building the ratio. The fraction itself is determined by applying these criteria to MC samples of all processes with real electrons in the final state. Eq. 11.10 is modified to Eq. 11.11.

$$f = \frac{N^{fake}_{tight,data} - \sum N^{fake}_{tight,MC}}{N^{fake}_{loose,data} - \sum N^{fake}_{loose,MC}} \tag{11.11}$$

Here, the sum is taken over all MC samples of different processes containing real electrons in the final state and the $fake$ symbol implies that cleaning cuts to suppress real electron contributions are applied.

The relative size of this dilution of real electrons is significantly smaller for candidates close to b-jets. Dominant processes with real electrons in the final state - LO electroweak boson production - do not have a b-quark in the final state. In the low $\mathrm{p_T}$ range the contribution of real electrons to the *tight* candidates selection is about 70% and 50% in the object sample that passes the *loose* selection. For candidates with $\mathrm{p_T} > 145$ GeV this fraction decreases to 68% and 30%. In case the candidates are close to a b-jet the dilution is approximately constant at 5%. The only exception is the *loose* sample in the high $\mathrm{p_T}$ regime. Here contributions from top

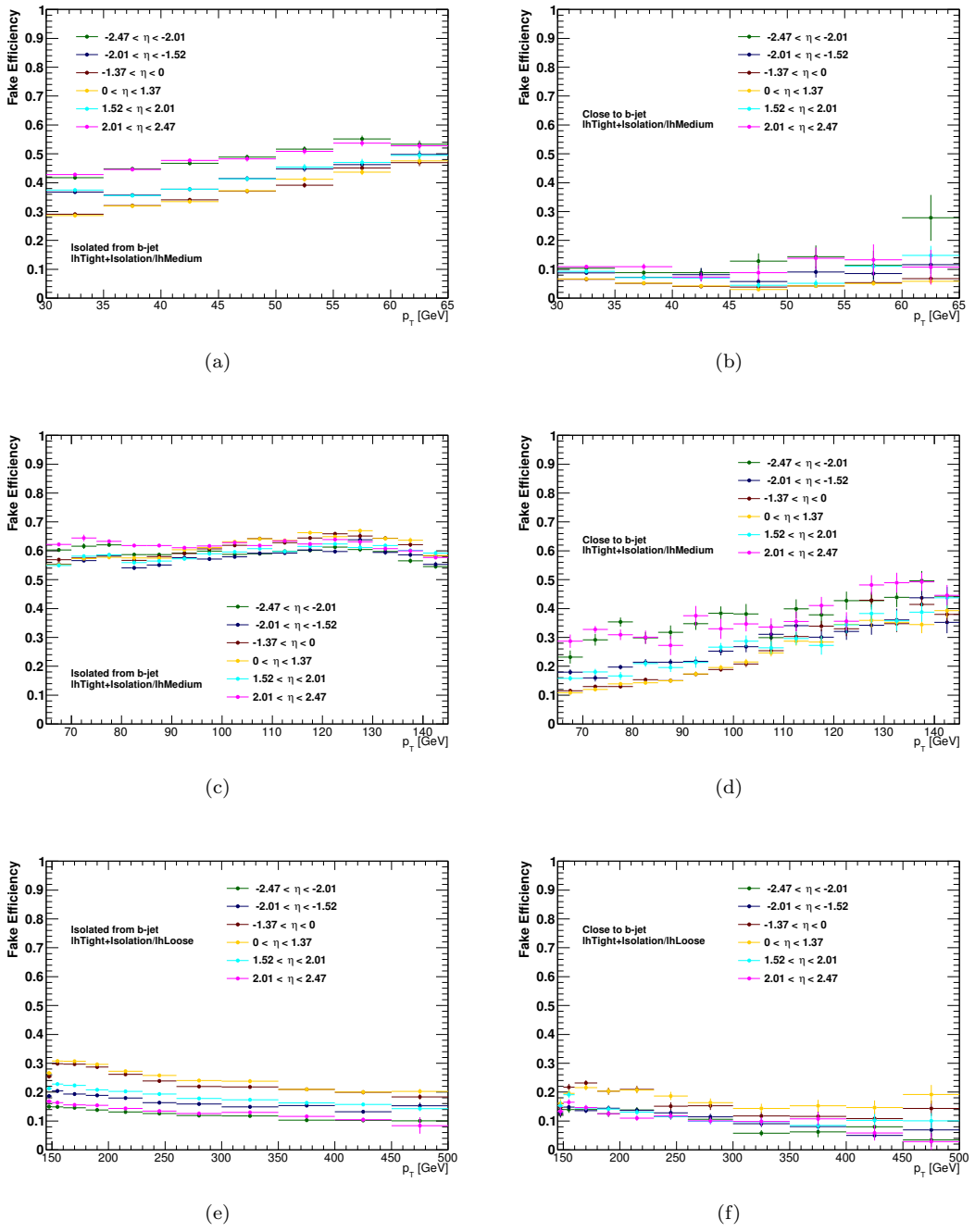

FIGURE 11.18: Fake efficiencies as a function of electron candidates' p_T in different η intervals. Efficiencies shown in the first column are determined for candidates, that are not close to b-tagged jets. For the determination of diagrams in the second column only candidates which are close to a b-tagged jet are included.

quark decays become more relevant leading to a fraction of 25% of events that still contain real electrons.

The fake efficiency is determined in three different p_T regions separately, to avoid biases introduced by the trigger identification requirements and p_T thresholds. This separation is done at

the thresholds $p_T = 30, 65, 145$ GeV. At the highest threshold the *loose* selection identification requirement can be relaxed. Additionally, to obtain fake efficiencies for the least energetic candidates at 30 GeV $< p_T <$ 65 GeV, a pre-scaled trigger[3] with a p_T threshold of 26 GeV has been used. This trigger was active during data taking in 2016 and 2017 and recorded a total amount of $392\,\mathrm{pb}^{-1}$ of data.

Fake efficiencies depicted in Fig. 11.18 are shown as a function of p_T in different η intervals. η and p_T dependencies of the fake efficiencies are resolved. In the first column, fake efficiencies for candidates, that are not close to a *b*-tagged jet, and in the second column the ones for candidates, which are close to a *b*-tagged jet are shown.

Fake background contributions are considered in the statistical analysis using the extrapolation procedure discussed in Sec. 11.5.2. In each kinematic region the procedure is performed on the output of the Matrix Method to obtain functions describing the background shape and normalization of the m_{LQmax} distribution. These are then used to obtain background estimations by integrating over the relevant mass interval. The fake background constitutes approximately a fraction of 3% of the total background expectation in each kinematic region of the electron channels.

11.5.2 Background Extrapolation to High Masses

The estimates of some background processes suffer from low statistics in the high m_{LQmax} range. A fit based extrapolation procedure is utilized in these cases to obtain a prediction. This is done on one hand for background contributions, that originate from top quarks, since all relevant processes are generated inclusively. The second use case is the fake background estimate in the electron channel. The extrapolation is done assuming two different functional forms and varying the start and end point of the fit range. The procedure is described in detail in Sec. 7.5.2.

Fig 11.19 (a) shows the m_{LQmax} distribution of the electron channel top background in the *b*-tag Z/γ^* control region. The utilized ensemble of fits is overlaid. The red dashed line is taken as the central value. All in the uncertainty determination considered fit results describe the falling spectrum reasonably well. In (b) the nominal estimate and its uncertainty is displayed. (c) and (d) serve as diagnostic plots ensuring that the nominal value obtained and its estimated uncertainty cover the simulated input sufficiently. For this purpose the integral of the mass tail starting from different mass bins is shown together with its uncertainty in (c). (d) shows the ratio of the extrapolated spectrum to the input distribution.

[3] e26_lhvloose_nod0_L1EM20VH

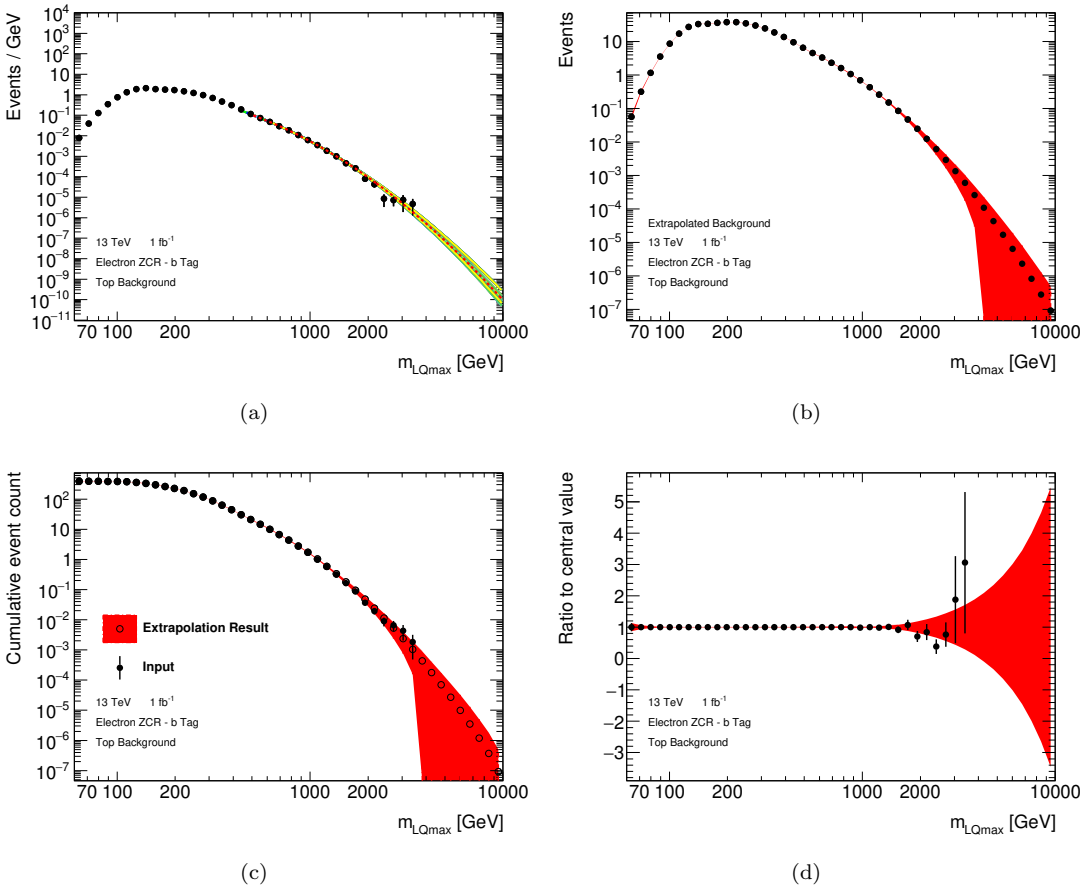

FIGURE 11.19: Diagrams illustrating the fit based procedure to extrapolate the electron channel m_{LQmax} spectrum in the b-tag Z/γ^* control region. (a) shows the ensemble of all fits used to estimate the extrapolation uncertainty and nominal value, which is drawn as a red dashed line. (b) displays the final estimate of this background with its uncertainty indicated as red area. (c) shows the integral over the tail in each mass bin starting from the respective bin with its uncertainty in comparison to the simulated input MC. (d) depicts the ratio of the extrapolation result to the input distribution.

Structures are observed in the highest bins, that have entries in the high m_{LQmax} range of the top background. An example of this is shown in the highest four filled bins in Fig. 11.19(a). By using the extrapolation procedure these structures are smoothed. Dedicated studies on these can be found in App. B.2. Structures are created by the b-tag requirements and migration effects between different b-tag categories. The m_{LQmax} distributions with different number of b-jets in the fiducial volume run out of statistics at varying points.

11.6 Systematic Uncertainties

In this section all major uncertainty sources and their relevance are discussed. They are classified into two large groups according to their origin. The first set of uncertainties is induced by the particle reconstruction, detector specifics and other algorithms used in the experiment and are called experimental uncertainties as a consequence. The other set of uncertainties enters through theoretical predictions.

11.6.1 Experimental Uncertainties

Algorithms to reconstruct lepton candidates [103][84] and jets [111] are using signals in the detector (see. Ch. 4). These procedures have associated uncertainties. Uncertainties connected to the reconstruction, isolation, identification and other experimental efficiency estimations are introduced by models utilized for the determination of those. Additionally, assumptions made and procedures used for the energy (momentum) scale as well as resolution effects - for all considered object types - are studied.

Furthermore, the luminosity value has an uncertainty connected to it [145]. The determination of the luminosity is detailed in Sec. 3.3. This measured value is used to scale the background estimation and signal hypothesis to the corresponding amount of data. The integrated luminosity value for the data taken in 2018 is 2.0%, in 2017 2.4% and for 2015 and 2016 combined 2.2%.

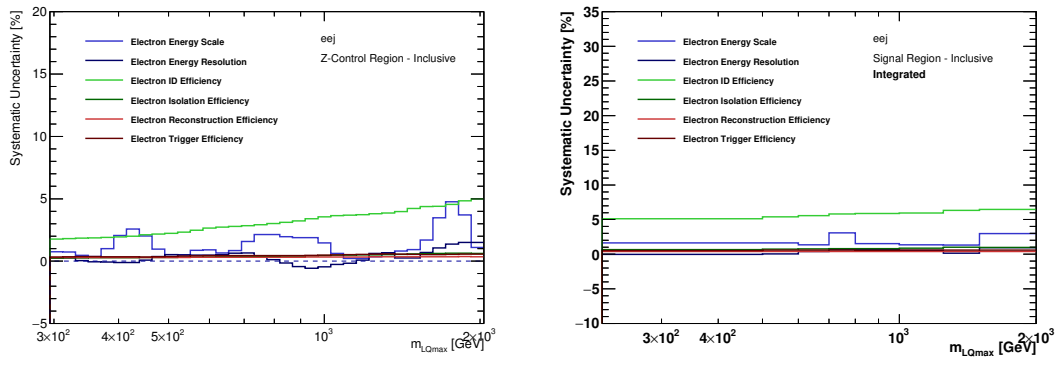

(a) (b)

FIGURE 11.20: Uncertainties related to electron reconstruction. Variations in (a) are determined on the m_{LQmax} spectrum in the electron channel combined $Z/\gamma*$ control region. In (b) the variation in the tail integral of the combined electron channel signal region is probed. The value in each bin is calculated by considering the tail integrals starting from the lower interval margin.

Fig. 11.20 illustrates the impact of the uncertainties related to the electron reconstruction procedures. In (a) the impact of systematic variations on the m_{LQmax} spectrum is shown on the

sum of the b-tagged and b-veto $Z/\gamma*$ control region ensemble as an example. Variations in spectra of other regions are similar in size but differ slightly due to different shapes of underlying distributions. (b) quantifies the uncertainties in the combined signal region (sum of $N_b = 0$ and $N_b = 1$). To estimate the impact to the single-bin statistical analysis, the value shown in each bin is the variation of the tail integral starting from the lower bin margin. The largest uncertainties related to electron reconstruction are approximately 5%. The uncertainty connected to electron identification efficiency differences in the data and the simulation is dominant and is increasing toward high masses. Efficiencies in the data are determined using a tag-and-probe method of $Z \to ee$ events. For electrons with high momentum an extrapolation is utilized, which increases its uncertainty. The second largest uncertainty is introduced by the electron energy scale calibration. Here, the measured energies of electron candidates are slightly varied. Structures observed in the diagrams are related to the spectrum, that is used to determine the variation and the usage of binned samples. An event from phase space interval, which is associated to a high cross-section, is filled with a large weight. In case events like these are reconstructed in the high mass tail and are migrating, large variations are observed. The general increase in this uncertainty toward high mass values can be motivated again by the use of extrapolations. Other studied variations are at approximately 1% and below.

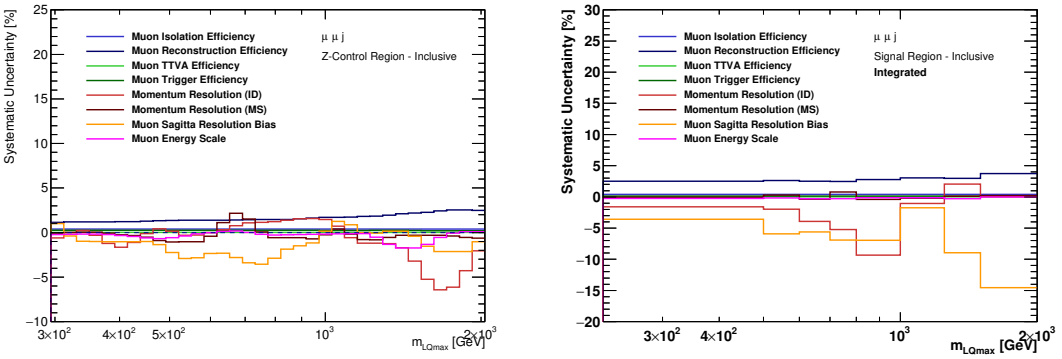

(a) (b)

FIGURE 11.21: Uncertainties related to muon reconstruction. Variations in (a) are determined on the m_{LQmax} spectrum in the muon channel combined $Z/\gamma*$ control region. (b) shows the variation in the tail integral of the combined signal region. The value in each bin is calculated by considering the tail integrals starting from the lower interval margin.

Fig. 11.21 shows the analog plots in the muon channel quantifying the uncertainties related to muon candidate reconstruction in ATLAS. In (a) variations of the m_{LQmax} spectrum of the combined $Z/\gamma*$ control region are shown. In (b) the impact on a single bin in the combined signal region - varying the bin size - is illustrated. The variations displayed are on the percent level. All uncertainties related to efficiency differences between the data and the MC are below 1%, except for the one related to muon reconstruction efficiency. This is observed to be between 3-4% in the signal region. Uncertainties related to the energy measurement are larger as the

trajectories of high p_T muons are only slightly bent by the magnetic field, which makes the measurement of their curvature more challenging. This effect becomes more dominant at high momenta and high m_{LQmax}. Structures observed in (a) can be explained again by the usage of the phase space binned $Z/\gamma*$+jets samples in combination with migration effects.

All variations of nuisance parameters estimating uncertainties related to jet energy scale and jet energy resolution are below 5% in the entire mass range. Experimental uncertainty variations investigated in other kinematic regions are very similar to the ones shown here.

11.6.2 Theoretical Uncertainties

Theoretical predictions in high energy particle physics come with various uncertainties associated to them. In the following paragraphs different sources of uncertainties are discussed.

Each set of parton distribution functions comes with an ensemble of uncertainties. On one hand they originate from the limited amount of data - that only cover certain phase space regions - which is used in the determination. Additionally, there are uncertainties induced by different methods chosen to extract each PDF set. A more detailed description of PDF sets and on how they are obtained can be found in Sec. 2.2. Some generators provide eigenvector variations of the underlying PDF set to quantify these uncertainties. Furthermore, the information on how the simulated distributions would be modified by the choice of a different PDF set is given in form of corrections.

For the dominantly contributing $t\bar{t}$ and Z/γ^*+jets samples PDF replicas are provided as well as weights to study variations using the nominal value of different PDF sets. For the Z/γ^*+jets sample the generation result with central values of the MMHT2014NNLO68CL [170] and the CT14NNLO [146] PDF set and for processes including top quarks the PDF4LHC [147] and CT14NNLO [146] PDF sets are considered.

Since theoretical calculations, that are performed to predict background and signal processes, are only of finite order, the choice of factorization and renormalization scale - μ_f and μ_r - impact the prediction as well. These scales have been introduced Sec. 2.1.1 and Sec. 2.3. To estimate these effects on the Z/γ^*+jets contribution each scale parameter is varied independently by a factor of two up and down. The envelope of these variations is taken as an uncertainty.

Fig. 11.22 shows the relative uncertainties on the Z/γ^*+jets background in the b-veto signal and Z/γ^* control region for the muon channel exemplarily. The variations displayed are determined on the m_{LQmax} distributions. Displayed is the scale variation uncertainty, the impact of strong coupling constant α_s variations as well as deviations, that are observed when using other PDF sets in the cross-section calculations. Uncertainty variations in other regions defined in this search have been found to be almost identical.

By far the largest uncertainty is assigned to the choice of renormalization μ_r and factorization μ_f scale - between 20% and 40%. There are problems observed in the modeling of the jet p_T in these SHERPA Z/γ^*+jets samples, which is assumed to be introduced by the choice of μ_r and μ_f. The mis-modeling is completely covered by these large uncertainties. All other theoretical uncertainties probed are on a percent level. Variations are shown with respect to the Z/γ^*+jets background.

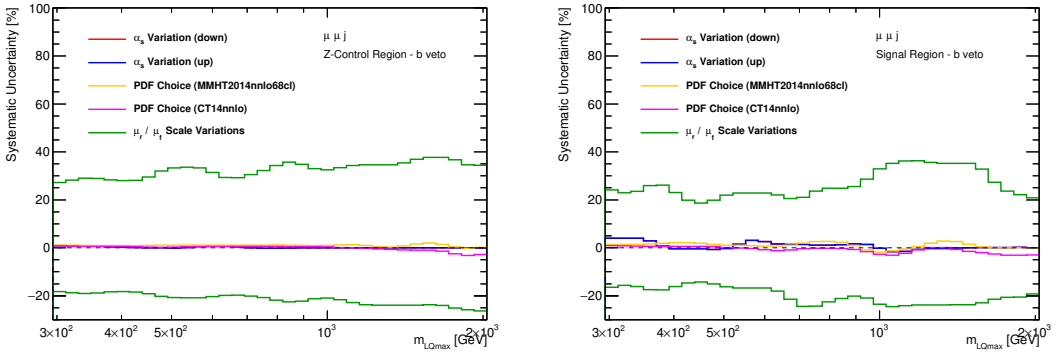

(a) (b)

FIGURE 11.22: Theoretical uncertainties on the Z/γ^*+jets background with respect to the contribution itself. Variations are determined on the m_{LQmax} spectrum in the muon channel b-veto $Z/\gamma*$ control region (a) and b-veto signal region (b).

Fig. 11.23 illustrates the relative theoretical uncertainties on the top background. Additional uncertainty sources in the generation of samples including top quarks are studied. This includes variations of the hadronization model, varying assumptions for initial and final state radiations as well as differences in the hard scattering generation and matching procedures. These uncertainties are estimated by comparing the results, that are obtained by different generators and tools, as well as the samples generated with scale and model parameter modifications. The variations have been obtained by comparing varied m_{LQmax} spectra of $t\bar{t}$ events in the electron channel (a) and muon channel (b) top control regions. The magnitude and shape of these uncertainties does not change significantly in any other kinematic selection defined in this analysis.

Diagrams shown for the electron and muon channel are very similar. The largest uncertainty is connected to the variation of initial state radiation assumptions, which is connected to the choice of μ_r and μ_f. It is around 17% at $m_{LQmax} = 300$ GeV and increases toward high masses. The other dominant theoretical uncertainty is connected to the hadronization and modeling. At high masses the up variation of the final state radiation is observed to be large. The remaining uncertainties probed are on a percent level in the entire mass range.

Furthermore, the total background cross-sections have an uncertainty associated to it. The

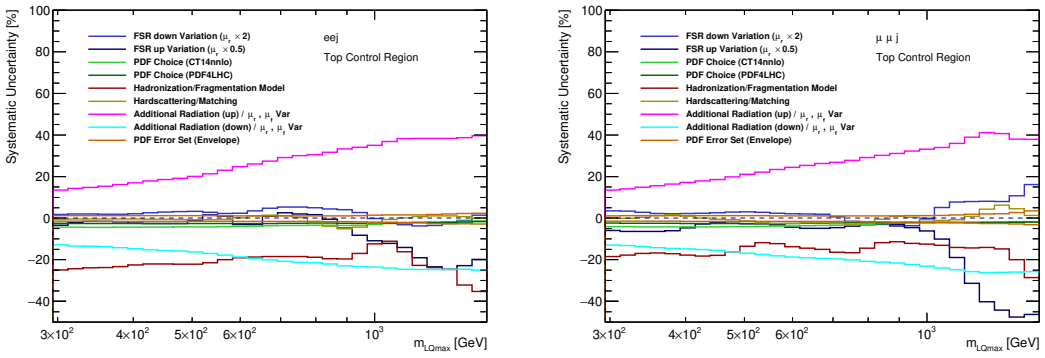

(a) (b)

FIGURE 11.23: Theoretical Uncertainties on the Top background. Variations are determined on the m_{LQmax} spectrum in the $t\bar{t}$ control region. In (a) the electron channel and in (b) the muon channel is shown.

Z/γ^*+jets cross-section has a relative uncertainty of 5% [171]. The uncertainty on the $t\bar{t}$ cross-section is +5.6%/-6.1% and in the case of processes with two electroweak bosons in the final state the uncertainty is 6.1% [172].

11.6.3 Summary

Relevant uncertainties are selected with the statistical analysis setup described in Sec. 12.2. Uncertainties below 0.5% with respect to the total background are neglected in each kinematic region. This analysis step is called pruning. Tab. 11.3 gives an overview of the uncertainty sources and their magnitude on the background expectation in each signal region. Values are determined by integrating over m_{LQmax} starting from 800 GeV(1500 GeV). The combination of each category is obtained by adding its constituents quadratically and taking the square root of the sum. This approach leads in most cases to overestimation.

The signal regions suffer from low statistics, which is the reason why the integrals are taken into account to estimate each systematic variation. Nonetheless, the values, that are obtained, have large statistical uncertainties themselves. Most experimental uncertainties are on the percent level. This includes the ones associated to lepton reconstruction as well as the ones referring to the jet energy measurement. Uncertainties, which are related to the momentum measurement of muons, are large at high masses due to the challenges in the reconstruction of high p_T muons. Theoretical uncertainties are dominant in the high mass range. In the *b*-veto region the ones connected to the prediction of the Z/γ^*+jets background are most relevant since the corresponding process constitutes the largest background fraction. The same argument holds true for the discussion of the uncertainties related to the theoretical prediction of processes with top quarks and the *b*-tag signal regions.

source	electron channel		muon channel	
	b-veto	*b*-tag	*b*-veto	*b*-tag
lepton energy/momentum	4.1%(1.6%)	1.4%(0.8%)	11.2%(11.3%)	5.6%(15.4%)
lepton algorithm efficiencies	6.5%(6.7%)	4.7%(5.7%)	2.7%(3.1%)	2.2%(3.2%)
jet energy scale	3.2%(2.4%)	0.9%(1.1%)	0.5%(0.6%)	1.0%(0.8%)
jet energy resolution	1.2%(3.4%)	1.3%(5.7%)	2.8%(7.3%)	4.9%(0.8%)
Z/γ^* theory unc.	18.7%(25.1%)	3.8%(13.1%)	8.3%(23.9%)	2.6%(2.4%)
top process theory unc.	4.7%	53.1%	4.2%	46.4%

TABLE 11.3: Summary of uncertainties and their impact in the signal regions in each channel. The values are obtained by considering the variation of the m_{LQmax} integral of the background starting from 800 GeV(1500 GeV) with respect to the total background estimate. The single sources discussed in previous sections are combined by adding them quadratically and taking the square root. For the theory uncertainties of processes with top quarks just the value starting from 800 GeV is shown, since above the extrapolation uncertainty replaces all others.

In the statistical analysis the statistical uncertainty of the MC samples is included as well. For the extrapolated top background the uncertainty, that is connected to the extrapolation procedure introduced in Sec. 11.5.2 is used above the stitching bin instead. The extrapolation uncertainty is large enough to cover all other variations investigated and is consequently the dominant background uncertainty in the signal regions in which one *b*-tagged jet is selected.

11.7 Background to Data Comparison

In this section the background modeling in the control and the validation regions is studied. These regions are defined in a way that only very low contributions from the LQ signal process are predicted. Diagrams in the following subsections show in the upper panel the number of selected events in the data and the SM theory prediction. Background events are drawn stacked giving on one hand the opportunity to compare the total number of expected events to the data and on the other hand insight on how the total background is composed. In the lower panel the ratio between the data and the background estimation is shown. The gray band indicates the impact of experimental uncertainties and the one introduced by limited MC statistics. The single sources are combined by adding them quadratically and taking the square root of the sum. A smoothing procedure is used on the uncertainty bands to reduce the effect of statistical fluctuations on the uncertainty values themselves. In regions of the phase space, which do not have a background estimate due to low statistics, uncertainties can not be calculated and are set to zero in the ratio panel. This causes the band to approach zero width in the high p_T and high mass intervals, which is only a matter of this visualization. Considering the mass of the electron and muon in contrast to the center of mass energy the distributions are expected to be very similar in the electron and muon channel.

For the sake of clarity only a selection of distributions are shown as example and discussed in this section.

11.7.1 Z/γ^* Control Region

11.7.1.1 b-Veto Region

The dominant background contribution consists of Z/γ^*+jets events. This is expected since on tree level the jet originates from initial state radiation. As consequence it is induced by a gluon. By design the Z/γ^*+jets process yields the highest background contribution in this region drawn in light blue. Top quark processes (red) and processes with two electroweak bosons (orange) contribute on a percent and sub-percent level. In the electron channel the fake background (yellow) is displayed as well.

In Fig. 11.24 the ϕ and η distributions of the selected muon candidates, electron candidates and jets are displayed. Only the leading objects per event are shown in these plots. The jets depicted are taken from the electron channel. Angular distributions of the sub-leading lepton candidates look very similar and can be found in App. B.3. The ϕ distributions only depend on detector specifics due to the symmetric event topology in the plane transverse to the beam-axis. For electron candidates and jets detector coverage is isotropic in ϕ, which leads to the flat distributions that are shown in (a) and (e). Spikes in the estimation are introduced by limited MC statistics. In (c) effects of the varying detector coverage for muon candidate reconstruction is visible. The ratio panel shown in the bottom illustrates that this aspect is well modeled. The data and the background estimates follow the same structures.

The electron candidates' η distribution, which is shown in (b), has its maximum around $\eta = 0$ and is falling to high $|\eta|$ values. The intervals of $1.37 < |\eta| < 1.52$ correspond to the transition regions between calorimeter barrel and end-caps, which are excluded in the selection due to bad energy resolution. This is the reason why there are no candidates selected. The main cause for the decreasing behavior is that by requiring minimal invariant masses in an event (m_{ll} and m_{LQmax}) the Bjorken x_i of the interacting partons has to be balanced to some extend. Otherwise the center of mass energy of the partons is not sufficient to create heavy intermediate particles present in most background processes. This explains why the majority of final states particles are not highly boosted along the beam-axis. An event is rejected in case one candidate exceeds $|\eta| > 2.47$. One additional aspect is that by definition equidistant pseudorapidity differences correspond to smaller fiducial volumes closer to the beam-axis. This leads to an even steeper slope to high absolute pseudorapidity values. The muon candidate η distribution (d) displays multiple structures. Most of them are introduced by badly aligned muon chambers, which are vetoed in the *highPt* muon identification working-point. Inefficiencies around $\eta = 0$ appear

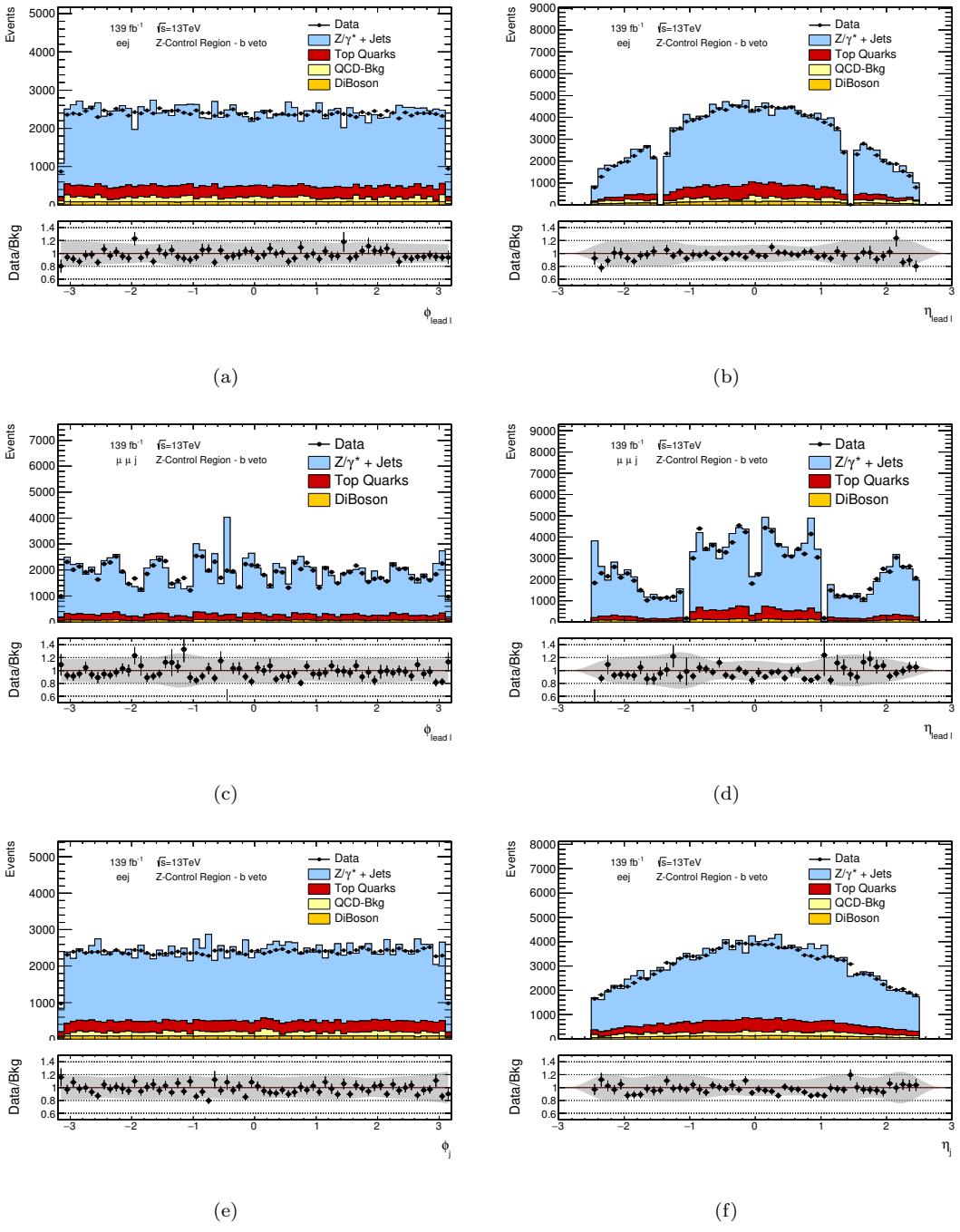

FIGURE 11.24: Angular distributions ϕ and η of the leading electron candidates (a)(b), muon candidates (c)(d) and jets (e)(f). The jet ensemble is selected in the electron channel. The upper panel shows the data points as well as the background prediction, with its contributing fractions drawn stacked. In the lower panel the ratio of the data and the total background estimate is displayed. The gray band indicates the impact of experimental uncertainties and limited MC statistics.

due to gaps for cables supplying the calorimeters. For jet reconstruction the detector coverage does not introduce remarkable shapes to the pseudorapidity distribution, which is visible in (f). As for the electron candidates, the spectrum peaks around $\eta = 0$ and falls toward high absolute values. The calorimeter transition region is not excluded, which explains the smooth

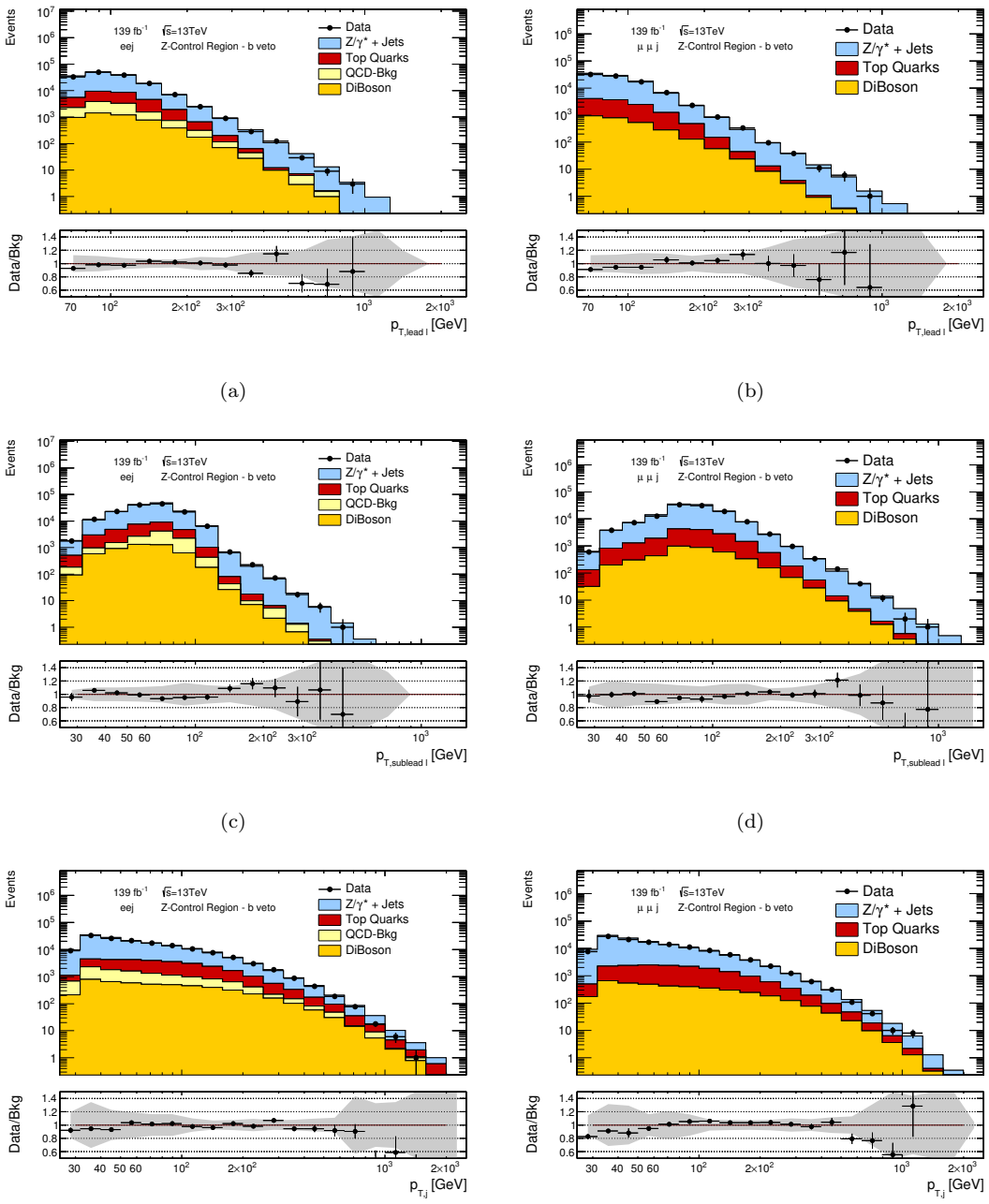

FIGURE 11.25: Transverse momentum p_T distributions of electron candidates (a)(c), of muon candidates (b)(d) and of jets (e)(f). The lepton candidates are shown separated in leading and sub-leading. The upper panel shows the data points as well as the background prediction, with its contributing fractions drawn stacked. In the lower panel the ratio of the data and the total background estimate is displayed. The gray band indicates the impact of experimental uncertainties and limited MC statistics.

decrease before being cut off by the explicit selection criteria of $|\eta| < 2.5$. The slope is less steep compared to (b), since jets are not originating primarily from the decay of a heavy object in this region. The pseudorapidity distributions indicate good background modeling. Fluctuations are covered by the statistical and experimental uncertainties.

These angular distributions look very similar in other control regions due to their strong dependencies on detector design. This is the reason why these are the only ones discussed here as an example.

Fig. 11.25 depicts the transverse momenta distributions of the particle candidates. In the left column diagrams of the electron channel and in the right column diagrams of the muon channel are displayed. The shape of the lepton candidates' p_T spectra in the electron and muon channel differs only due to different energy and momentum resolutions. The lepton candidate pair mass window ($130\ \text{GeV} < m_{ll} < 250\ \text{GeV}$) is in the falling tail above the Z peak. This is the reason why the majority of events contains a lepton candidate pair with m_{ll} that is close to 130 GeV. Therefore, the leading and sub-leading lepton candidate p_T peaks below 100 GeV. Above this all reconstructed objects show a decreasing p_T distribution. The fact that only the projections on the transverse-plane are considered causes the migration of many events from the peak to lower values, making the peak less sharp. The sub-leading lepton candidate spectrum peaks between 60 GeV and 70 GeV and the one of the leading lepton candidates around 80 GeV. These positions are shifted to higher energies due to the recoiling jet. The jet p_T distribution follows a smoothly falling curve in both channels. The measured data agrees with the MC prediction within the uncertainties in the lepton candidates' p_T distributions. For high energy jets a slight mis-modeling is observed, as the data tends to undershoot the prediction in the high p_T tail. The reason for this has been identified to be the choice of μ_r and μ_f in the generation of the Z/γ^*+jets SHERPA MC and is even more pronounced when selecting on-shell Z events. However, this is covered by theoretical scale uncertainties, which were discussed in Sec. 11.6.2.

Fig. 11.26 illustrates the background modeling of angular differences and invariant masses of object pairs in the events. These spectra look very similar in the electron and muon channel, which is the reason why only the electron channel diagrams are shown as example. (a) displays the invariant mass distribution of the LQmax pair - lepton jet pair with higher invariant mass - and (b) of the LQmin pair - lepton jet pair with lower invariant mass. The falling p_T spectra previously discussed are connected to the decreasing behavior. In (c) the difference in ϕ of the electron candidates is shown. The data distribution and the dominant background contribution have their maxima around $\Delta\phi_{ll} = \pi$. This is expected since the majority of events come include the decay of a heavy Z. Its high mass in comparison to its recoil in the transverse-plane causes the decay products to be back-to-back in most cases. This effect becomes more pronounced in events with a small recoil. The pseudorapidity difference of the selected electron candidate pair ($\Delta\eta_{ll}$) shows a falling curvature visible in (d). On one hand the falling $|\eta|$ spectra of the single lepton candidates displayed in Fig. 11.24 causes this. On the other hand, the high center of mass energy of partons required to produce an off-shell Z leans toward symmetric Bjorken x_i values in each event. Therefore most Z bosons are produced centrally, only with a small boost along the beam-axis. Diagrams shown in (c) and (d) display good data to background agreement and good modeling of these aspects. In the m_{LQmax} and m_{LQmin} distribution the

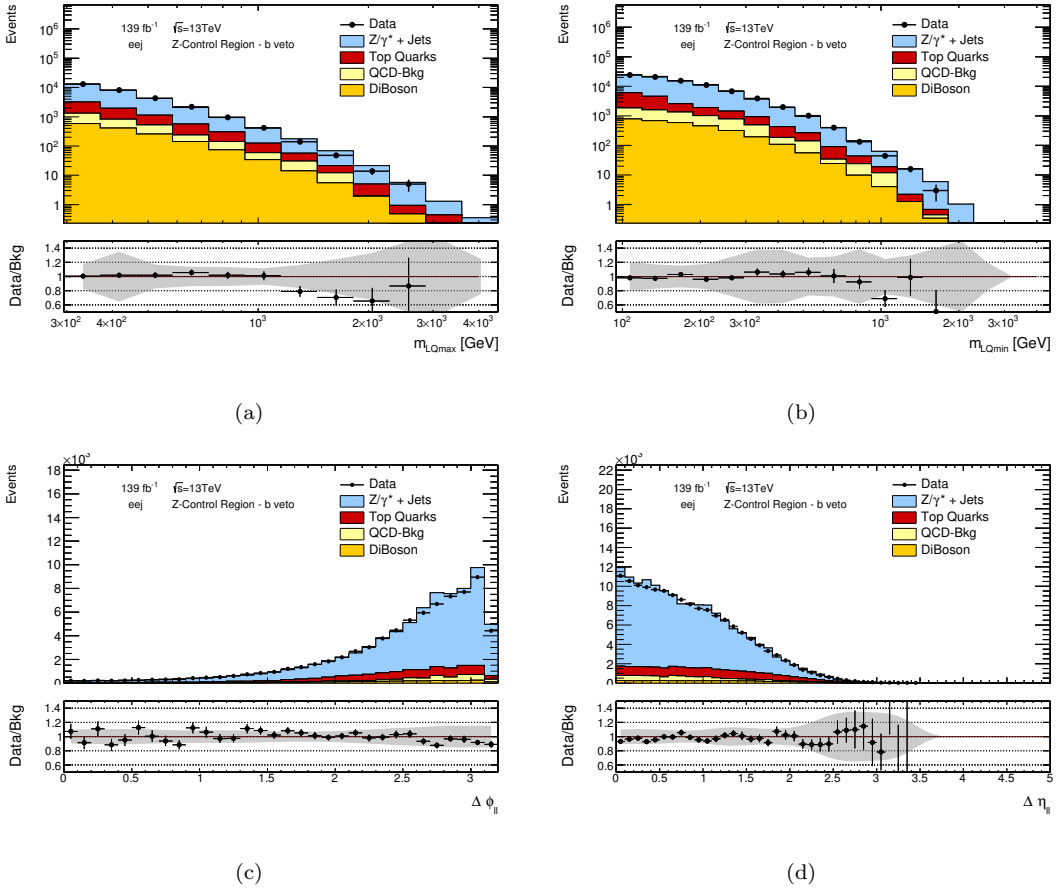

FIGURE 11.26: Distributions of composite quantities reconstructed using object pairs in the electron channel. (a) and (b) show the invariant mass distributions m_{LQmax} and m_{LQmin}. (c) and (d) the angular differences in ϕ and η of lepton candidate pairs. The upper panel shows the data points as well as the background prediction, with its contributing fractions drawn stacked. In the lower panel the ratio of the data and the total background estimate is displayed. The gray band indicates the impact of experimental uncertainties and limited MC statistics.

data undershoots the background prediction in the high mass range. This can be connected to the jet p_T mis-modeling observed in the Z/γ^*+jets SHERPA MC.

11.7.1.2 *b*-Tag Region

In this region the fraction of top quark decay events is enhanced by selecting one *b*-tagged jet. This causes the background fraction from top quarks to be around $\sim 90\%$, while Z+jets events only contribute $\sim 10\%$.

Fig. 11.27 shows a selection of kinematic plots in this region - in the electron channel as example. In all distributions the top background contribution is dominant, while the general shapes are similar to the ones observed in the *b*-veto control region. The mass distributions displayed in (a) and (b) have large statistical uncertainties and show more fluctuations in the ratio. Some deviations, that are observed, are not covered by the gray bands displayed. However, theoretical

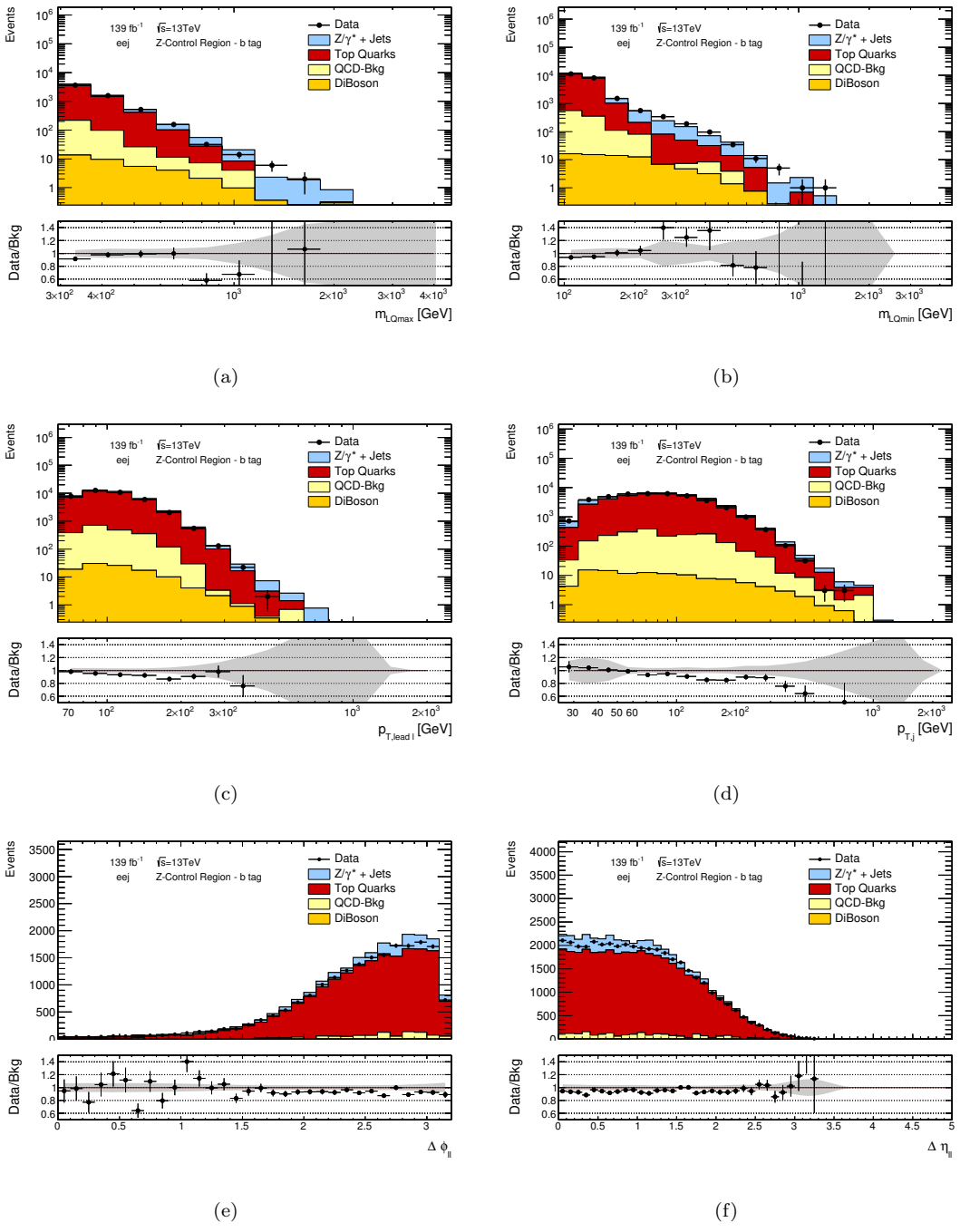

FIGURE 11.27: Kinematic distributions in the b-tag Z/γ^* control region obtained in the electron channel. In (a) and (b) the m_{LQmax} and m_{LQmin} distributions are displayed, (c) and (d) show the p_T spectra of the leading electrons and jets, while (e) and (f) illustrate angular differences between the electron candidates - in (e) $\Delta\phi$ and (f) $\Delta\eta$. The upper panel shows the data points as well as the background prediction, with its contributing fractions drawn stacked. In the lower panel the ratio of the data and the total background estimate is displayed. The gray band indicates the impact of experimental uncertainties and limited MC statistics.

uncertainties on the top background are not included in this illustration. Their estimated impact is large, which was discussed in Sec. 11.6.2. The leading lepton p_T distribution - displayed in (c) - shows the exact same shape as discussed in the previous section. The transverse momentum

of the jet illustrated in (d) has its maximum in a region between 70 and 110 GeV. The jet is required to be b-tagged and is most likely produced by the decay of a top quark. The maximum corresponds to roughly half of the top quarks mass of $m_t \approx 170$ GeV. Differences observed between data and background are smaller than the variations describing theoretical top process uncertainties discussed previously. The $\Delta\phi_{ll}$ and $\Delta\eta_{ll}$ distributions shown in (e) and (f) are wider compared to the ones in the b-veto region. In events of the dominant background fraction - top quark processes - both leptons are not produced by the decay of the same mother particle and consequently have no immediate connection. The angular distributions illustrate good data and background agreement.

11.7.2 Top Control Region

This control region is designed to study the $t\bar{t}$ MC modeling. The contribution from processes including top quarks to the background is enhanced to about 90% by requiring 2 b-tagged jets in each event. Diagrams of the electron channel are shown exemplarily, since there is no qualitative difference in shape to the muon channel distributions.

Fig. 11.28 displays the lepton candidates' and jets' p_T (a)-(c) as well as invariant masses for lepton candidate pairs (d) and the LQmax pairs (e). The lepton candidates' and jet's transverse momenta show decreasing behavior at the high end of the spectrum. In the leading lepton p_T spectrum (a) only a smoothly falling behavior, that starts at the p_T requirement of 65 GeV, is visible. For the sub-leading lepton candidate a rise at low momenta is observed. These originate from decays of heavy W bosons. The leading jet, which is selected and entering the p_T distribution in (c), originates most of the time from the decay of a (anti-)top quark with mass $m_t \approx 170$ GeV and is created by the (anti-)bottom quark produced. Therefore the distribution, that is shown, peaks around $90 - 100$ GeV. This maximum is again shifted by the fact that only the jet with the highest p_T is selected, enhancing the contribution from high energy jets. The data and the background estimates agree reasonably well.

The invariant mass distribution of the lepton candidate pairs - in (d) - reveals that background contributions of Z/γ^*+jets events are expected almost exclusively near the Z peak. Jets produced in Drell-Yan processes predominantly come from initial state radiation and are induced by gluons. The majority of Z/γ^*+jets events entering here come from two jets being mistakenly tagged as b-jets and from processes, in which the emitted gluon decays into a $b\bar{b}$ pair. The underlying $t\bar{t}$ background contribution is flat in the Z peak region, rises smoothly to about $m_{ll} \sim 160$ GeV and decreases afterwards. Around the Z peak some mis-modeling is observed, which is most likely originating from missing contributions of the Z+jets MC sample. The Feynman diagram, in which the radiated gluon decays into a $b\bar{b}$ pair is a higher order process and not included in the generation. Outside of this region the ratio of data and background

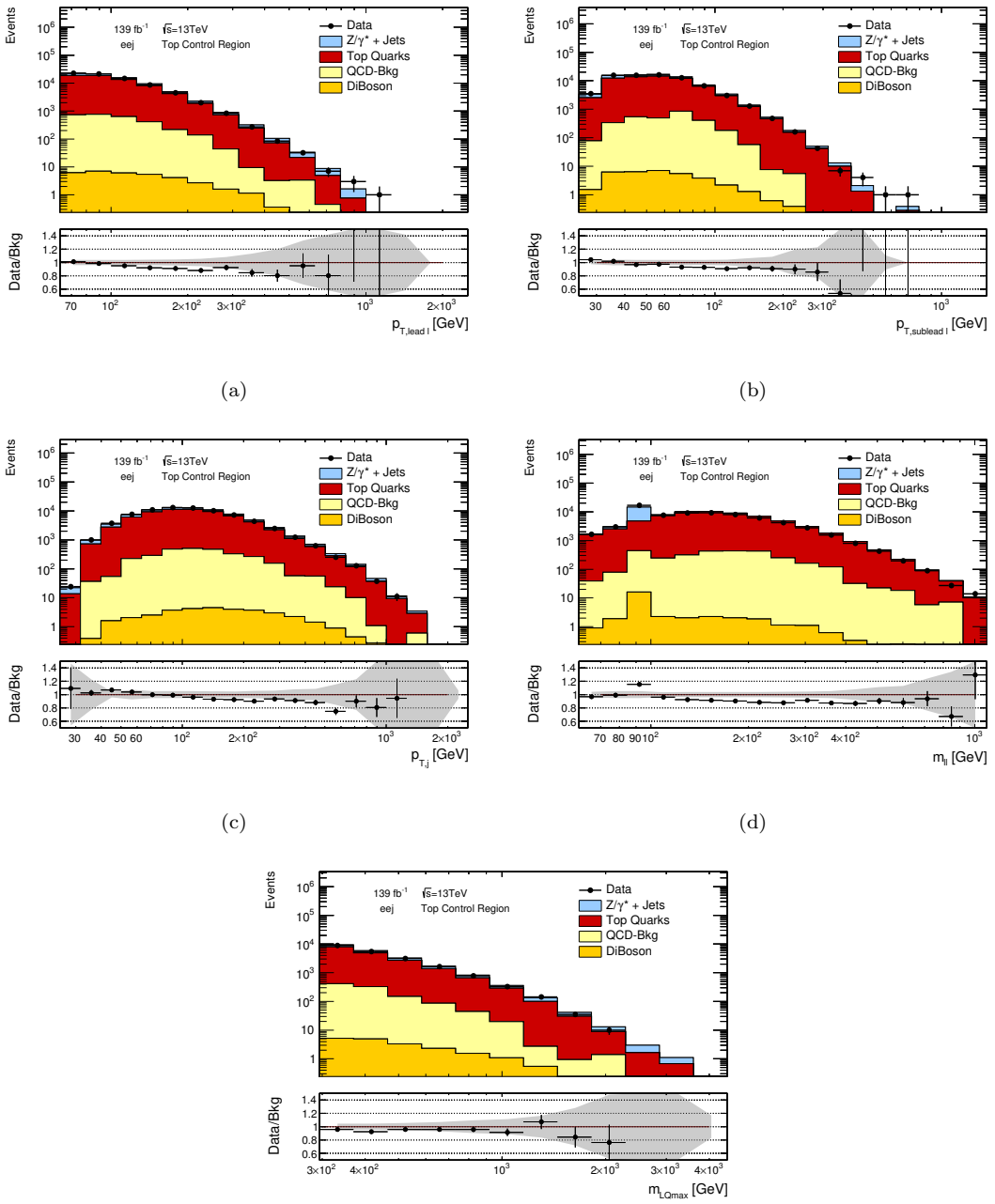

(a) (b) (c) (d) (e)

FIGURE 11.28: Electron channel distributions of the lepton candidates' p_T (a)(b) and the leading jet's p_T (c) in the top control region. Additionally, the invariant mass of the electron candidate pairs and the LQmax pairs are shown in (d) and (e). The upper panel shows the data points as well as the background prediction, with its contributing fractions drawn stacked. In the lower panel the ratio of the data and the total background estimate is displayed. The gray band indicates the impact of experimental uncertainties and limited MC statistics.

prediction is flat and slightly below one. (e) shows the falling m_{LQmax} distribution. The data to background ratio is very close to one. The deviations in the tail are covered by uncertainties.

11.7.3 Validation Region

The validation regions are designed to have a more signal region like event topology while expecting negligible signal contributions. This is the reason why the m_{ll} interval studied in this selection is higher compared to the control regions with 250 GeV $< m_{ll} <$ 400 GeV. This leads to less statistics in the investigated distributions.

Fig. 11.29 shows muon channel distributions that are obtained in the *b*-veto region in the left column and in the *b*-tag region in the right column. In (a) and (b) the leading jet's and in (c) and (d) the leading muon candidates' p_T distributions are displayed. (e) and (f) illustrate the m_{LQmax} spectra. The shapes of most distributions and the background compositions are very similar to the ones discussed in the Z/γ^* control regions. The minimal invariant mass of lepton pairs selected is higher at 250 GeV in this region. This is the reason why most events that are selected have a lepton candidate pair with invariant mass in a small window starting at 250 GeV. This leads to a shift of the maximum observed in (c) and (d) to higher momenta of around $p_T \sim 125$ GeV compared to the Z/γ^* control region distributions.

The jet's p_T distribution in the *b*-veto region, that is displayed in (a), shows reasonable data to background agreement. The modeling problems of this variable in the Z/γ^*+jets MC is present in on-shell Z events and becomes less pronounced in the high m_{ll} range. Deviations between data and background expectation that are observed in the other diagrams are covered by the large statistical uncertainties of the data and the MC.

In summary the modeling in all regions is found to be reasonable. Uncertainties that are considered are sufficiently large to account for observed differences between the data and the background expectation.

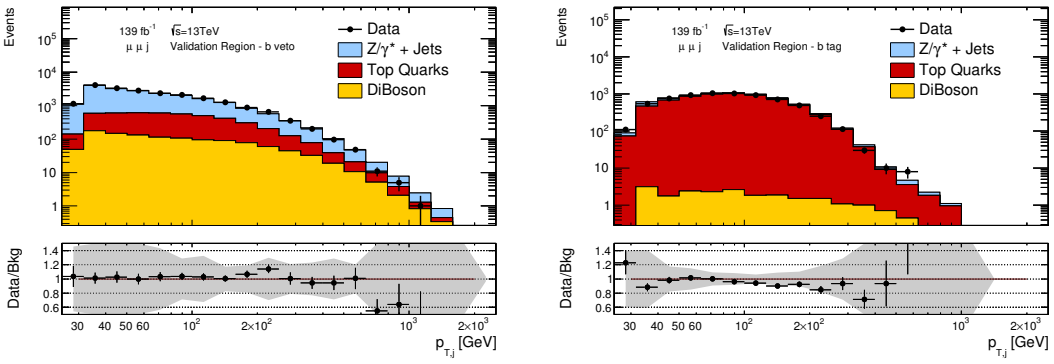

(a)

(b)

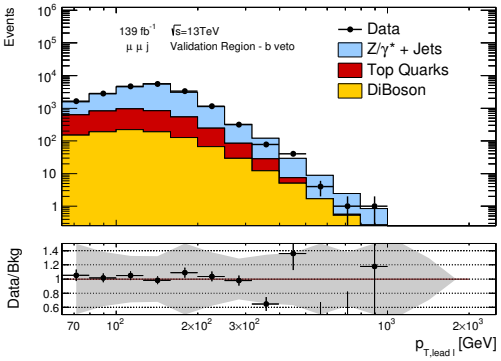

(c)

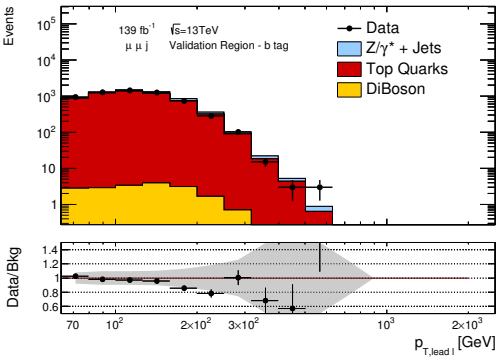

(d)

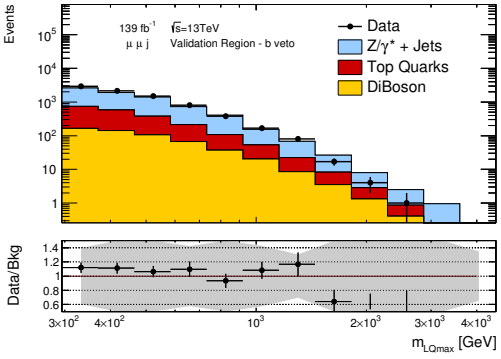

(e)

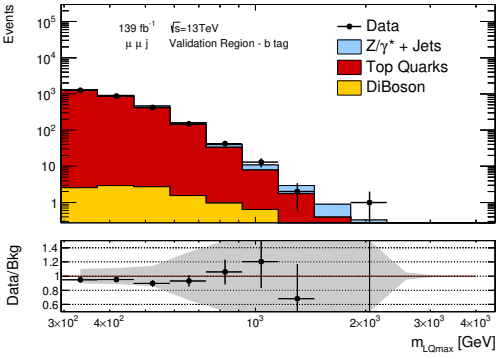

(f)

FIGURE 11.29: Jet's p_T (a)-(b), leading muon candidates' p_T (c)-(d) and m_{LQmax} distributions in the muon channel validation region - for the b-veto and b-tag category in the left and right column. The upper panel shows the data points as well as the background prediction, with its contributing fractions drawn stacked. In the lower panel the ratio of the data and the total background estimate is displayed. The gray band indicates the impact of experimental uncertainties and limited MC statistics.

Chapter 12

Results and Statistical Interpretation

This chapter discusses statistical methods, that are used to optimize the signal region probed for each mass hypothesis as well as the interpretation of the results. First the general methodology and definitions are introduced in Sec. 12.1. Afterwards, in Sec. 12.2 the procedure to determine exclusion limits in the frequentist approach is discussed. A signal region m_{LQmax} cut optimization is conducted with this technique and described in Sec. 12.3. In Sec. 12.4 observed event yields in all signal regions are shown and compared to the background expectation. Finally, observations are interpreted utilizing a likelihood ratio test to assess and quantify deviations from the background-only hypothesis in Sec. 12.5. In case no significant deviation is observed, upper exclusion limits on the cross-section times branching ratio and the LQ mass are presented in Sec. 12.6. The statistical analysis package TRexFitter [173] is used for the following statistical tests.

12.1 Methodology and Likelihood Function

Event yields in each region are considered in a single m_{LQmax} interval due to limited MC statistics. The generation of the Z/γ^*+jets MC is divided into sub-samples covering a distinct phase space region each (see Sec. 11.2.5). Migration effects in combination with large differences of the cross-section event weights between those sub-samples create structures in the tail of the m_{LQmax} background distribution. The utilization of a single-bin approach counteracts convergence problems. These might occur when non-smooth background estimates with highly varying statistical uncertainties in different m_{LQmax} intervals are used.

A detailed description of the methods is given in [150][152]. In each region r the number of events follows a Poisson distribution with the expectation value λ_r. λ_r is given by the sum of expected signal and background events in each region - s_r and b_r. Uncertainties are included by a set of gaussian distributed nuisance parameters (NP) $\vec{\theta}$. NP of the same uncertainty are treated as correlated across all regions in a given channel. The propagation of these uncertainties to the expected number of signal and background events has been discussed in Sec. 8.1. An additional NP is introduced in each region to account for limited MC statistics. s_r depends on the parameter of interest - the product of signal cross-section and branching ratio σB. In the following discussions of test-statistic distributions - instead of σB - the signal strength parameter μ is used to be more demonstrative. These two quantities are related by the expression

$$\mu = \frac{\sigma\mathrm{B}}{(\sigma\mathrm{B})_{\mathrm{LQ}}}. \tag{12.1}$$

$(\sigma\mathrm{B})_{\mathrm{LQ}}$ is the expected signal cross-section for fixed input parameters of the probed model.

Eq. 12.2 illustrates the decomposition of the expectation value λ_r in each region and its dependencies. The likelihood function for each channel in the statistical analysis is shown in Eq. 12.3.

$$\lambda_r(\sigma\mathrm{B}, \vec{\theta}) = s_r(\sigma\mathrm{B}, \vec{\theta}) + b_r(\vec{\theta}) \tag{12.2}$$

$$L(\sigma\mathrm{B}, \vec{\theta}) = \prod_r L_r = \prod_r \frac{\lambda_r^{n_r} \cdot e^{-\lambda_r}}{\lambda_r!} \tag{12.3}$$

n_r is the observed number of events in region r.

The background expectation is corrected first for the following statistical analysis . This is done by a maximum likelihood fit in the control regions for each channel separately. The normalization of the dominant background contributions (Z/γ^*+jets and $t\bar{t}$) are varied by the inclusion of normalization factors - μ_Z and $\mu_{t\bar{t}}$. Additionally nuisance parameter (NP), which propagate the effect of systematic uncertainties to the expected number of background events, are estimated within their constraints. The largest and therefore most relevant uncertainties considered are the ones introduced by the theoretical predictions discussed in Sec. 11.6.2. In the b-tagged channels the uncertainty of the background extrapolation method plays a major role as well.

Tab. 12.1 shows the normalization coefficients and their uncertainties determined in each channel. Values determined for $\mu_{t\bar{t}}$ are consistently close to one. The same can be observed for μ_Z in channels in which b-jets are vetoed. This is compatible with the good background modelling

	electron b-veto	electron b-tag	muon b-veto	muon b-tag
μ_Z	1.01 ± 0.18	1.32 ± 0.81	1.05 ± 0.20	1.26 ± 0.73
$\mu_{t\bar{t}}$	0.98 ± 0.27	0.97 ± 0.28	1.02 ± 0.28	1.00 ± 0.30

TABLE 12.1: Normalization coefficients applied to the expected number of events of the dominant background processes Z/γ^*+jets and $t\bar{t}$. These are determined by a fit of data to the background-only hypotheses in the control regions.

observed in the corresponding regions shown in Sec. 11.7. In the b-tag regions, the coefficient for the Z/γ^*+jets background is large at 1.32 in the electron and 1.26 in the muon channel. The single-bin approach introduces high correlations of NPs and the normalization coefficients. This leads to large uncertainties on the coefficients themselves. Additionally, the uncertainty of μ_Z in the b-tag channels is increased by the low contributions of the corresponding process to the b-tag Z/γ^* control regions. Uncertainties for μ_{top} are approximately 0.3, while the uncertainties on μ_Z are around 0.2 in the b-veto channels. In both b-tag channels $\Delta\mu_Z$ is higher than 0.7.

In the following statistical analysis the corrected background estimate is used.

12.2 Frequentist Exclusion Limits

The frequentist probability interpretation is used to determine upper limits on the signal strength μ. These can be expressed as limits on σB of the signal process in each channel. In the frequentist approach probabilities are interpreted by counting certain outcomes under multiple repetitions of a measurement.

A one-sided, lower-bound likelihood ratio test statistic is used [152][150].

$$t_\mu = \begin{cases} -2\ln\frac{L(\mu,\hat{\hat{\theta}}(\mu))}{L(0,\hat{\hat{\theta}}(0))} & \hat{\mu} < 0 \\ -2\ln\frac{L(\mu,\hat{\hat{\theta}}(\mu))}{L(\hat{\mu},\hat{\theta})} & 0 \leq \hat{\mu} \leq \mu \\ 0 & \hat{\mu} > \mu \end{cases} \tag{12.4}$$

Here, L are likelihood functions defined in Eq. 12.3, and μ is the signal strength. $\hat{\mu}$ and $\hat{\theta}$ are given by the signal strength and NP values which maximize the likelihood function in an unconditional fit to data. The set of NPs, which maximizes the likelihood for a fixed signal strength value μ, is defined as $\hat{\hat{\theta}}(\mu)$. Three different cases are considered separately for the functional form of the test statistic t_μ. Scenarios with negative signal strength are not considered in this search. In case a negative signal strength maximizes the likelihood function the likelihood in the denominator of the logarithmic argument is evaluated for the background-only hypothesis. In the regime where the signal strength parameter μ is smaller than the value $\hat{\mu}$, t is set to 0.

The integral starting from a given value t_μ to infinity is defined as the p-value in each channel. This is defined separately for the background-only and signal-plus-background hypothesis and are synonymous with CL_b and CL_{s+b}, while their ratio is called CL_s. These relations are illustrated in Eq. 12.5.

$$\mathrm{CL}_s = \frac{\mathrm{p}_{s+b}}{\mathrm{p}_b} = \frac{\mathrm{CL}_{s+b}}{\mathrm{CL}_b} = \frac{\int_{t_{\mu,obs}}^{\infty} p(t|s+b)dt}{\int_{t_{\mu,obs}}^{\infty} p(t|b)dt} \tag{12.5}$$

$p(t|s+b)$ and $p(t|b)$ are the test statistic distributions under the signal-plus-background and background-only hypothesis. $t_{\mu,obs}$ is the test statistics value calculated from data. Varying the signal strength shifts the test statistic distribution under the signal-plus-background hypothesis $p(t|s+b)$ and thus changes the CL_s. The exclusion limit on μ - or alternatively σB - at a confidence level of $X\%$ is defined as the signal strength, which corresponds to the test statistic value where $\mathrm{CL}_s = 1 - X/100$. This is done in every channel for each LQ mass hypothesis. Signals were injected to verify that the setup of the tools, which is used to calculate limits, behaves as expected.

One possibility to obtain the test statistic distributions $p(t|s+b)$ and $p(t|b)$ is via toy experiments. For this, the expected number of events are statistically varied according to a Poisson distribution assuming a fixed value of μ. This is very expensive in terms of computing time which is the reason why an asymptotic procedure is utilized to obtain approximate sampling distributions of the test-statistic [152].

12.3 Signal Region Optimization

The $\mathrm{m_{LQmax}}$ cut applied in the signal region is optimized for each mass hypothesis in every channel. This is done by determining expected limits while varying the lower $\mathrm{m_{LQmax}}$ thresholds in 100 GeV steps. The starting point is 1 TeV below the LQ mass - for low masses at least 300 GeV - and goes up to $\mathrm{m_{LQ}} + 300$ GeV. The signal region definition, which leads to the strongest expected 95% CL cross-section limits per mass point, is used for further analysis.

Fig. 12.1 illustrates the threshold scan in each channel. The $\mathrm{m_{LQmax}}$ cut is shown on the y-axis against the mass of the LQ on the x-axis. On the z-axis the ratio of the expected 95% CL cross-section limit and the best limit, that has been obtained in the respective column is displayed. Red boxes indicate the threshold, which yields the best limit and which is taken for the limit setting. In most cases the optimized values are a few 100 GeV below the mass of the LQ signal hypothesis probed. For a few signal hypothesis the thresholds determined by the optimization procedure are slightly above the LQ mass. This is for example observed in the electron b-veto channel at $\mathrm{m_{LQ}} = 750$ GeV. The main cause of this is that background

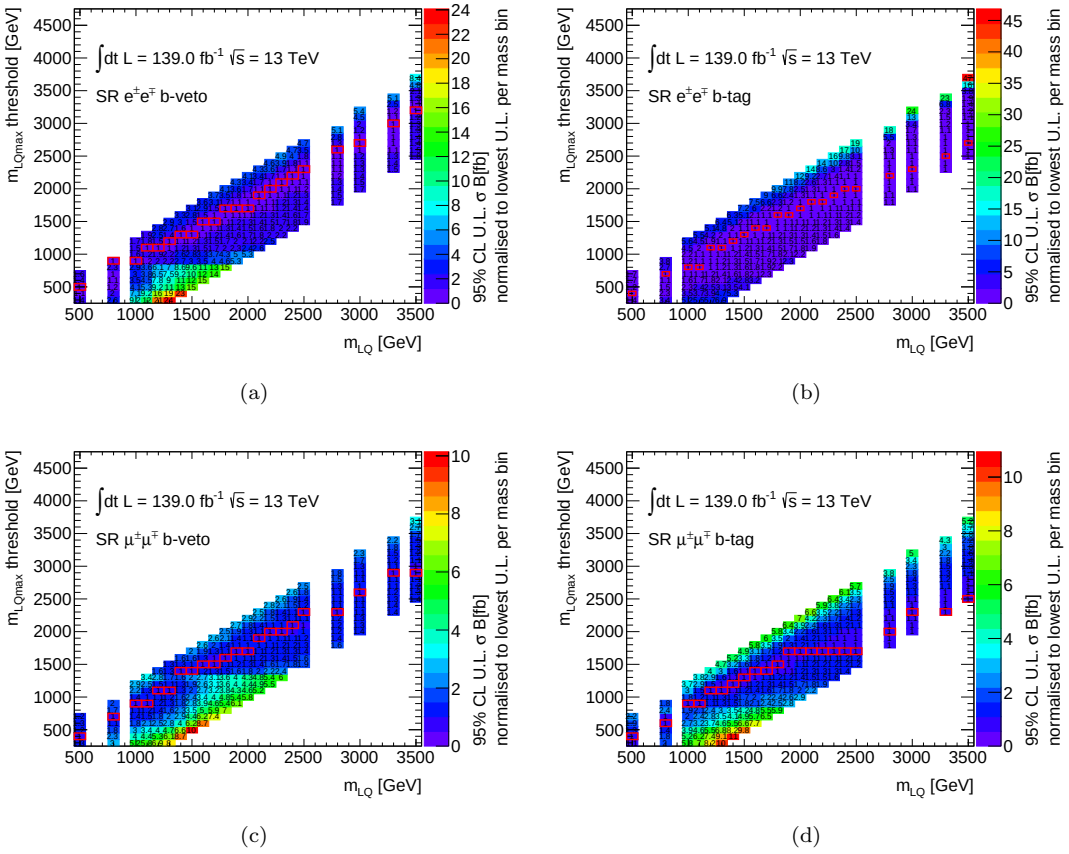

FIGURE 12.1: Threshold scan used to optimize the m_{LQmax} cut applied in each channels signal regions for each mass hypothesis. The x-axis shows the LQ mass of the signal, the y-axis the applied m_{LQmax} threshold and the z-axis the rato of the 95% CL expected cross-section limit to the best limit obtained for a given mass hypothesis. Red boxes indicate the threshold which gives the best limit and is taken for further analysis.

uncertainties vary across the mass spectrum for statistical and systematical reasons. Especially the Z/γ^*+jets background has problems in certain m_{LQmax} intervals since the sub-samples do not have sufficient phase space overlap. In combination with high cross-section weights applied, this leads to high fluctuations in statistical uncertainties of the background estimate. Additionally, the high mass tail of the signal is enhanced by the choice of m_{LQmax} as sensitive variable.

12.4 Event Yields

In this section signal region event yields are studied and compared to the corrected background estimate. Fig. 12.2 displays the observed number of data events as well as the corrected background expectation in every region per channel. In each diagram the first two bins show the top and Z/γ^* control regions (TopCR and ZCR), the third bin the validation regions (VR), which is followed by all signal regions utilized for different mass hypotheses. The x-axis label displays the m_{LQmax} cut applied. Background contributions of different processes are drawn stacked on top of each other to allow comparison to the data yields. Signal expectations for mass hypothesis where m_{LQ} is an integer multiple of 500 GeV and $\lambda_{lq} = 1$ are shown as well. Some signal regions are used to probe multiple LQ mass hypotheses. This is the reason why only a small ensemble of signal expectations is displayed. The uncertainty on the total background is illustrated by the shaded area.

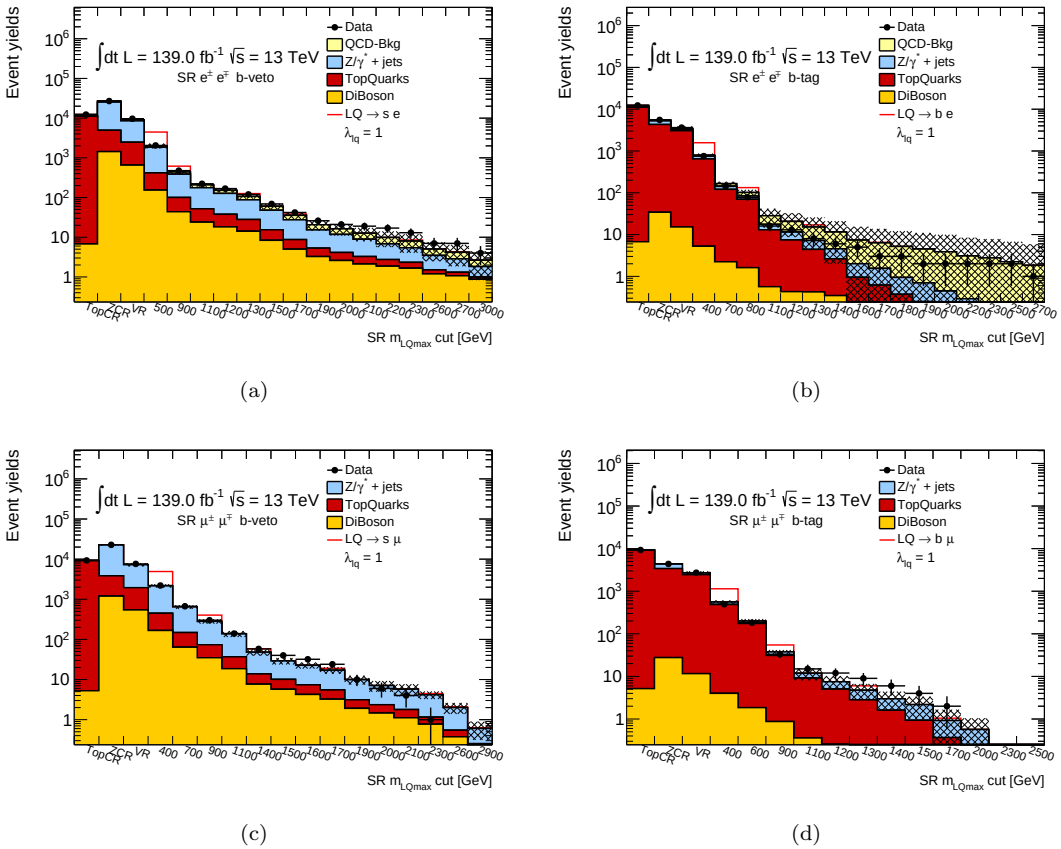

FIGURE 12.2: Data event yields and background expectation in every region per channel. Background expectations are drawn stacked. The shaded area illustrates the background uncertainty. Control regions (TopCR, ZCR) are displayed in the first two bins. The third bin shows the the validation region (VR), which is followed by the signal regions in each channel. These are defined by the m_{LQmax} cut applied. Signal hypotheses for $m_{LQ} = n \cdot 500$ GeV with $n \in 1, 2, 3, 4, 5, 6, 7$ and $\lambda_{lq} = 1$ are shown as well in the relevant signal regions.

By design the data and the varied background expectation agree very well in both control regions in each channel. In every channel the measured data events are in good agreement to the background-only prediction in the validation region. This serves as a cross-check for the background corrections, that are obtained by the maximum likelihood fit in the control region. A slight excess of data events is observed in the high mass SRs in the electron b-veto channel - displayed in (a). The fraction of each process to the total background is approximately constant over the whole mass range. This is consistent with the background expectation, that is displayed in the muon b-veto region in (c). Here, the data tends to overshoot the background-only hypotheses for m_{LQmax} cuts around 1.5 TeV. In regions with a higher thresholds a deficit of data events with respect to the background expectation is observed.

The composition of the expected background in the b-tag channels, that are shown in (b) and (d), changes significantly with the m_{LQmax} cut. For low mass thresholds the dominant background contribution comes from processes with top quarks. This holds in control and validation regions as well, which require a minimum m_{LQmax} of 300 GeV each. In regions starting at $m_{LQmax} = 1.1$ TeV the contribution of Z/γ^*+jets becomes more relevant. At this point, the QCD background takes over as the dominant background process in the electron channel. This is due to the fact that the $t\bar{t}$ process falls more steeply toward high m_{LQmax} compared to other contributions, because the jet, which is used for the mass determination originates most likely from a top quark decay. In other background processes the jet is created often times by initial state radiation and shows a more flat distributed p_T. This statement does not apply to the b-veto channels since the selected jet is not b-tagged. The uncertainty on the Z/γ^*+jets background is large when requiring a b-tag due to the high uncertainty on the normalization coefficient μ_Z. As described previously, the background-only fit gives large uncertainties due to the low Z/γ^*+jets contribution in the corresponding control regions. Additionally, the QCD-background estimate causes very large uncertainties at high masses. In the b-tag signal regions the relative uncertainty is the largest since the spectrum, that has been obtained by the Matrix Method, which is used as input of the extrapolation procedure, has the lowest statistics in this kinematic region. A deficit of data can be observed in the electron b-tag channel consistently, which is fully covered by the uncertainties shown. For mass thresholds from 1.1 TeV to 1.7 TeV a slight excess of data is measured in the muon channel.

In summary, most deviations observed lie within the uncertainty band of the background expectation. Discrepancy of the event yields measured in data to the background-only expectation are quantified for each m_{LQ} hypothesis in the next section.

12.5 Likelihood Ratio Test

A discovery test is performed to quantify significances of excesses and deficits as well as interpret the result. The likelihood ratio test conducted follows closely the one discussed in Sec. 8.2 and will be briefly outlined here again [150].

The used test statistic is the uncapped variant of the likelihood ratio evaluated at $\mu = 0$ for the background-only hypothesis as illustrated in Eq. 12.6.

$$t = \begin{cases} +2 \ln \frac{L(0,\hat{\hat{\theta}}(0))}{L(\hat{\mu},\hat{\theta})} & \hat{\mu} < 0 \\ -2 \ln \frac{L(0,\hat{\hat{\theta}}(0))}{L(\hat{\mu},\hat{\theta})} & 0 \leq \hat{\mu} \end{cases} \tag{12.6}$$

L is given by the likelihood function introduced in Sec. 12.1. $\hat{\mu}$ is the signal strength value which maximizes the likelihood function L in combination with the set of NPs $\hat{\theta}$ in an unconditional fit. $\hat{\hat{\theta}}(0)$ is the set of NPs which maximizes the likelihood under the $\mu = 0$ (background-only) assumption.

The uncapped distribution allows to quantify deficits, that are observed compared to the background-only hypothesis as well. In contrast the likelihood ratio test performed in Sec. 8.2 only probes positive significances and thus data excesses. However, when evaluating surpluses of data both test statistic definitions give the same results.

The p_0 value for each LQ mass is determined by integrating over the tail of the test statistics distribution $f(t|\mu = 0)$ to infinity. The distribution of the test statistic is obtained by the same asymptotic procedure as in Sec. 12.2 [152]. The starting point is the test statistic value observed in data t_{obs}. The significance z is defined as the inverse cumulate Gaussian probability density function Φ^{-1} of p_0. These relations are displayed in Eq. 12.7 and Eq. 12.8.

$$\mathrm{p}_0 = \int_{t_{obs}}^{\infty} f(t|\mu = 0)dt \tag{12.7}$$

$$\mathrm{z} = \Phi^{-1}(\mathrm{p}_0) \tag{12.8}$$

An approximation using Wilks' theorem [153] saves computing time. This leads to the simplified functions

$$\mathrm{p}_0 = \begin{cases} 1 - \Phi(\sqrt{t_{obs}}) \\ 1 - \Phi(-\sqrt{-t_{obs}}) \end{cases} \qquad \mathrm{z} = \begin{cases} \sqrt{t_{obs}} & 0 \leq \hat{\mu} \\ -\sqrt{-t_{obs}} & \hat{\mu} < 0 \end{cases} . \tag{12.9}$$

This setup of the tools has been validated by injecting signals, with varying signal strength. Afterwards it has been verified, that $\hat{\mu}$ corresponds to each value. The result of the discovery test is shown in Fig. 12.3. Local significances are displayed against m_{LQ} for each channel. In the following discussion, the distribution of event yields shown in Fig. 12.2 is considered. The most significant excess is observed in the muon b-veto channel for $m_{LQ} = 1.8$ TeV at $1.3\,\sigma$. Measured event yields in signal regions of the electron b-veto as well as the muon b-tag channel show a similarly large positive significance in some of them. In the former channel this is the case for a signal hypothesis with LQ mass of 2.4 TeV and in the latter one this is the case for $m_{LQ} = 1.5$ TeV. Negative significances are observed at high masses in both muon channels as a consequence of the undershooting of the data in the corresponding signal regions. Deficits of data in all electron b-tag signal regions lead to negative significances over the whole m_{LQ} range. No significant excess or deficit is identified by the discovery test.

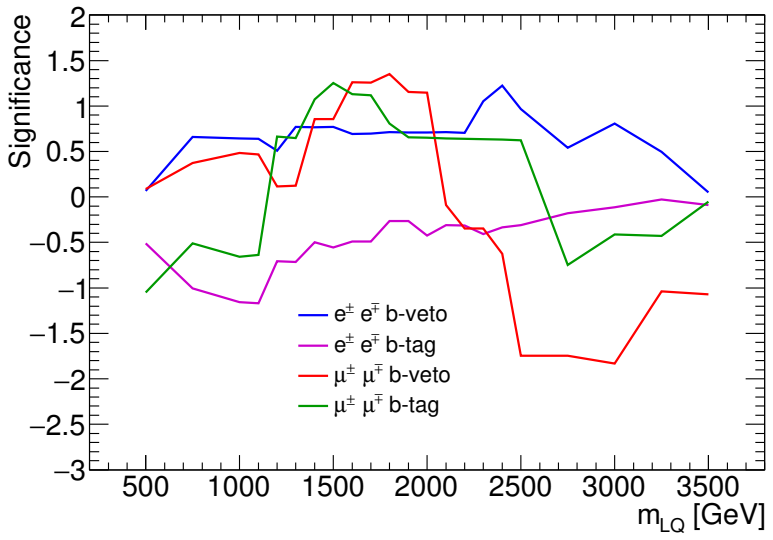

FIGURE 12.3: Result of the likelihood ratio test. The local significances are drawn against the LQ mass hypotheses for each channel.

12.6 Exclusion Limits

In this section 95% confidence level (CL) limits on the signal cross-sections are presented using the procedure discussed in Sec 12.2. The signal shape in the b-veto channels is estimated using MC simulation of the $\tilde{S}_1$ representation [59] of the decay LQ $\rightarrow sl$ at leading-order. The charge-conjugated process is included as well. When considering another light quark flavor the signal shape differs slightly. A quark of the same flavor enters the initial state of the LO signal Feynman diagram shown in Fig. 11.2. The differences between parton distribution functions for each quark introduce minor variations of kinematic distributions of decay products, which lead to acceptance differences. For the b-tag channels the signal shape is obtained utilizing the $\tilde{S}_1$ representation as well and the decay LQ$\rightarrow bl$.

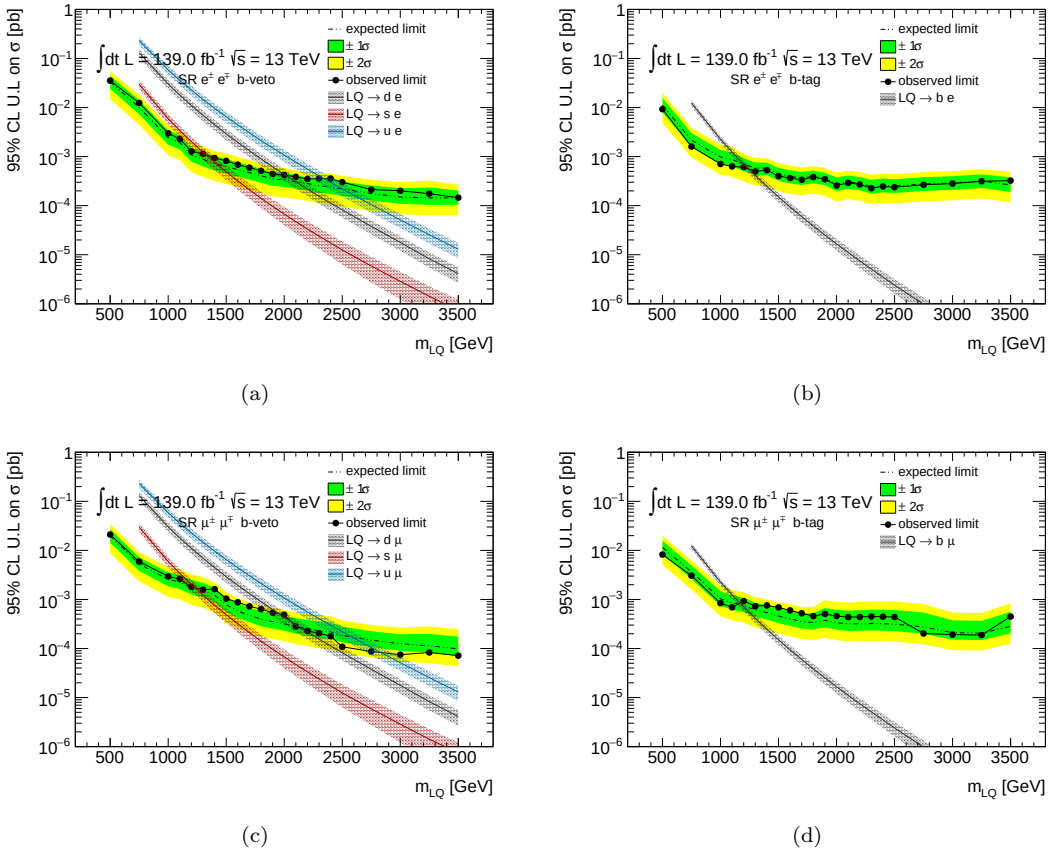

FIGURE 12.4: 95% CL upper cross-section limit for singly produced Leptoquarks (LQ) against LQ mass in each channel. (a) and (b) display results obtained in the electron channel b-veto and b-tag region while (c) and (d) show the analog ones determined in the muon channels. Expected limits are illustrated as black dashed lines with green one σ and yellow two σ uncertainty bands. The observed limit is drawn as black data points. Additionally, the LO signal cross-section for the singly produced LQ decaying into an up, down and strange quark are overlaid in the b-veto channels, while the cross-section for the decay into a bottom quark is shown in the b-tag regions. Uncertainties of these include renormalization and factorization scale variations as well as PDF uncertainties.

Fig. 12.4 shows the 95% CL cross-section limits against m_{LQ} in each channel. Expected limits are drawn as a dashed line with one σ and two σ uncertainty bands, that are drawn in green and yellow. The data points illustrate the observed limits for a given LQ mass hypothesis. Additionally, the LO signal cross-sections under the assumption of $\lambda_{lq} = 1$ for different quark types in the final state are displayed. These predictions consider the Yukawa coupling to the charged lepton and quark type probed as 1, while all other elements of the coupling matrix are set 0 (see Sec. 2.4.4). In the calculation of the uncertainty bands, PDF as well as renormalization and factorization scale variations are considered. Signal cross-sections for the process LQ $\rightarrow ul$ are using the S_1 representation of a scalar LQ [59]. The parameter space in which the signal model cross-section is higher than the observed limit can be excluded at 95% CL. Consequently the LQ masses at which the observed and expected limit intersect these curves are interpreted as lower LQ mass limits under the assumption of $\lambda_{lq} = 1$.

For low pole masses up to 1.5 TeV the expected and observed cross-section limits get stronger with increasing m_{LQ} in all channels. This is due to the high number of background events that are expected and the low signal acceptance for low mass points. At high masses these curves flatten. Here, statistical uncertainties become dominant. In the b-tag channels shown in (b) and (d) this effect is more pronounced due to the large uncertainties at high masses introduced by the normalization coefficient of the $Z/\gamma*$+jets background. The incorporation of the QCD-background in the electron channels introduces additional large uncertainties, which flattens the cross-section limits even further in (a) and (b). Steps and spikes in the limit curves are connected to changes in signal region definitions between mass points and the composition variations of considered uncertainties.

In the electron b-veto channels shown in Fig. 12.4 (a), the observed limit lies on the upper edge of the one σ uncertainty band of the expected limit. This is consistent with a small excess of data events in the signal region yields. Event yields in the electron b-tag signal regions consistently undershoot the background expectation, which is the reason why the observed limit lies one σ below the expected limit in the diagram in (b). Background expectation uncertainties become very large around 1.3 TeV. Therefore the observed limit approaches the expected limit at m_{LQ} values above.

In the muon b-tag channel - in Fig. 12.4 (c) - the observed limit is very close to the expected limit for low LQ masses. At 1.4 TeV it moves to the upper edge of the one σ band. For masses higher than 2 TeV it lies on top of the expected limit again before shifting to the lower border of the green band at 2.5 TeV. This is consistent with the excess in the event yield in Fig. 12.2 (c) in the signal regions with mass thresholds between 1.4 TeV and 1.7 TeV. The drop in the data events for m_{LQmax} cuts above 2 TeV explains the strong observed limits for the highest mass hypotheses. Trends displayed in the muon b-tag channel limit curves in (d) are similar to the b-veto channel. In the medium mass range of $m_{LQ} \in \{1200, 2500\}$ GeV the observed limit lies

process ($\lambda_{lq} = 1$)	expected limit [TeV]	observed limit [TeV]
$LQ(S_1) \to ue$	2.5	2.3
$LQ(\tilde{S}_1) \to de$	2.0	1.9
$LQ(\tilde{S}_1) \to se$	1.4	1.3
$LQ(\tilde{S}_1) \to be$	1.2	1.2
$LQ(S_1) \to u\mu$	2.6	2.8
$LQ(\tilde{S}_1) \to d\mu$	2.1	2.0
$LQ(\tilde{S}_1) \to s\mu$	1.2	1.2
$LQ(\tilde{S}_1) \to b\mu$	1.2	1.2

TABLE 12.2: 95% CL expected and observed lower mass limits on single LQ production assuming $\lambda_{lq} = 1$ for the quark and lepton type probed.

above the expected limit. The corresponding signal regions show data excesses. Consequently, the observed limits here are weaker than the expected ones. A drop of event yields at high masses leads to the fact that observed limits lie below the expected limit curve outside the one σ band. The observed limits for each mass point in every channel agree with the expected limit within the one σ and two σ band.

95% CL lower limits on the LQ mass in a given signal model are identified as the m_{LQ} value at which the signal cross-section intersects the observed and expected limit. The results for the processes LQ $\to dl$ and LQ $\to ul$ come with an additional uncertainties due to the signal shape assumed in the b-veto channels. To estimate the impact of this, the acceptance variation when exchanging the quark flavor is studied on generator level. Differences due to the quark type in the final are on a low percent level. This propagates directly to the upper cross-section limit determined in b-veto channels - in Fig. 12.4 (a) and (c). A percent level uncertainty can be neglected in comparison to the magnitude of uncertainties on the expected limit and the signal cross-sections. Generator level plots and acceptance studies for different final state quark flavors are detailed in App. B.4. Tab. 12.2 show the expected and observed 95% CL lower mass limits for a each LQ decay under the assumption of $\lambda_{lq} = 1$.

Mass limits for LQ decays into up and down quarks are the strongest. This is consistent with the fact that these quark types have larger contributions to the proton PDF, which is the reason why the corresponding signal cross-sections are larger compared to the processes with bottom and strange quarks. For the decay into first generation quarks the mass limits in the muon channel are higher compared to the electron channel. This is due to large QCD background uncertainties in the high mass signal regions of the electron channel. For the decay into down quarks observed and expected limits are around 2.0 TeV, while in the up quark case the observed limits are at 2.3 TeV in the electron channel and 2.8 TeV in the muon channel. Considering the signal process with strange quarks the observed limits are 1.3 TeV and 1.4 TeV in association with an electron or muon. This can be explained by the higher signal acceptance for low masses in the electron channel and the fact that the QCD background contribution is not dominant yet

for m_{LQmax} cuts around 1 TeV. The b-tag channels allow setting mass limits for the LQ decays into bottom quarks. In the electron channel as well as the muon channel observed and expected limits are at 1.2 TeV.

12.7 Outlook

Aspects, which might improve the sensitivity as well as the interpretation of the search results, are discussed in the following. Modeling problems in the jet p_T distributions shown in Sec. 11.7 originate most likely from the choice of the renormalization scale in the generation of the Z/γ^*+jets MC sample with SHERPA2.2.1 [143]. Corrected modelling might eliminate the necessity of the background normalization variations, that is determined by a fit in the control regions, which come with large uncertainties. Additionally, a more efficient way to generate background events in the whole phase space would allow to obtain better statistics of dominant background samples. On one hand, this would remove some large uncertainties introduced by the background extrapolation procedure. On the other hand, a background description with smaller statistical uncertainties might allow to exploit the resonant shape of the signal process. The incorporation of shape information by disregarding the single bin approach in the signal regions would increase the sensitivity of this search.

A search for pair-produced LQ [159] uses multivariate techniques to optimize selections and define kinematic regions while dealing with complex event topologies. These techniques have the power to further increase sensitivity but require thorough checks of the modeling in the MC samples.

Additional improvements can be achieved for the interpretation of the results. A larger set of signal samples in which the coupling parameter λ_{lq} is varied, would allow to probe signals and set exclusion limits in the two dimensional parameter plane ($m_{LQ} - \lambda_{lq}$). This can not be done reliable with existing signal samples that are generated with $\lambda_{lq} = 1$, due to the large impact the coupling has on the width of the signal. A change in the width leads to a in signal acceptance variation, which would require a dedicated signal region optimization for each coupling parameter and LQ mass hypothesis. Therefore the generation of additional samples is a necessity for a stronger result interpretation.

Chapter 13

Conclusion

A search for singly produced Leptoquarks (LQ) has been presented using 139 fb^{-1} of data collected by the ATLAS experiment in proton-proton collisions at a center of mass energy of $\sqrt{s} = 13$ TeV. LQ decays into electrons or muons in combination with up, down, strange or bottom quarks are investigated separately in four different channels. The scalar LQ implementation of the 'ToolBox' UFO model [59][158] serves as a signal hypothesis. For the decay into down type quarks the $\tilde{S}_1$ representation and for the decay into up quarks the S_1 representation is used. All signal hypotheses assume a LQ-lepton-quark coupling of $\lambda_{lq} = 1$ for each specific quark and lepton type, while other couplings are set to zero, as well as a branching ratio to charged leptons of $\beta = 1$.

Background expectations have been estimated with Monte Carlo simulations and data driven methods. For the search, events with high invariant masses of lepton-jet pairs are selected. Background estimates which suffer from low statistics have been extrapolated to the high mass regimes. Control region selections are defined to determine corrections on the modeling of dominant background contributions. A validation region in each channel is used to verify the background description. Systematic uncertainties in each region are studied and included in the statistical analysis. The first step of the statistical analysis consists of a likelihood ratio test, which probes deviations of the data to the background-only hypothesis. No significant excess or deficit has been observed. Consequently 95% confidence level (CL) exclusion limits have been determined on the product of signal cross-section and branching ratio in each channel. 95% CL lower mass limits are obtained by comparing these cross-section limits to theoretical predictions. The observed LQ mass limits in case of the decay of a singly produced LQ into a bottom quark is 1.2 TeV in the electron and muon channel. Considering the decay into a strange quark, the limit in the muon channel stays the same, while in the electron channel a slightly stronger result of 1.3 TeV was obtained. Determined values are strongest when considering LQs decaying into

first generation quarks. For down quarks in the final state the observed limit is 1.9(2.0) TeV in the electron(muon) channel and for the final state with an up quark the limit is 2.3(2.8) TeV.

Almost all other LQ searches performed at the LHC use the Buchmüller-Rückl-Wyler model (BRW) [174] to estimate their signal hypothesis. In this theory LQs only interact with leptons and quarks within one generation, which complicates comparisons to this result. A search on $19.6\,\text{fb}^{-1}$ of 8 TeV proton-proton data performed by CMS [66] previously gave the strongest mass limits on first and second generation LQs in the single production channel. The mass limits, which have been determined under the coupling and branching ratio assumption of $\lambda_{\text{lq}} = 1$ and $\beta = 1$, are at 1.73 TeV and 530 GeV for the first and second generation. The signal model here allows only the decay into leptons and quarks of the same generation. The analysis which obtained the strongest limits available while probing cross-generational LQ decays was performed in the pair production channel at the ATLAS experiment with the full Run 2 139 fb^{-1} proton-proton data set at $\sqrt{s} = 13$ TeV [61]. A branching ratio to charged leptons of $\beta = 1$ is assumed. No differentiation between the light-flavor quarks (u, d, s) is done, since the production cross-section for the pair production of LQs does not depend on λ_{lq}. Limits for light-flavor quarks are lower than the ones, that were obtained in the analysis presented in this thesis - with 1.8 TeV in the electron and 1.6 TeV in the muon channel. The observed limits of the LQ decay into b-quarks are stronger with 1.8 TeV and 1.7 TeV. This is due to the fact that the production cross-section does not depend on the PDF of the b-quark.

Under the assumption of a coupling of $\lambda_{\text{lq}} = 1$ and considering the caveat that a different model has been probed in contrast to other publications, the lower LQ mass limits on LQ, that decay into up and down quarks, are the strongest available to date.

Chapter 14

Summary and Outlook

In last decades the Standard Model (SM) of particle physics has been extensively probed and has successfully described a large variety of precise measurements. However, there are measurements, which are inconsistent with the prediction of the SM, and other shortcomings that indicate the necessity of further extensions to describe the whole picture. Experiments at large accelerator facilities allow to probe and extend knowledge to new energy range. During the years 2015 to 2018 the Large Hadron Collider (LHC) at CERN collided protons at the highest center of mass energies ever reached on earth based experiments - at $\sqrt{s} = 13$ TeV. The data set recorded by the ATLAS experiment during this time span gives an unprecedented opportunity to search for new physics theories and to challenge existing standards by exploring phenomena on the TeV scale. Two direct searches for new particles were presented in this thesis.

The search for new heavy charged gauge bosons is performed on 36.1 fb^{-1} of data collected in 2015 and 2016. A charged lepton[1] in combination with large missing transverse energy serves as a very clean final state allowing to probe the existence of a new heavy particle. For this search the presence of a resonant structure in the transverse mass spectrum is investigated. Background expectations are estimated with Monte Carlo simulations and a data driven technique. Spectra, which were selected by relaxed requirements, are investigated to validate the background contribution of mis-identified signatures in a phase space, in which limited sensitivity to the new physics models is predicted. The total background description is further evaluated in signal region distributions of observables in which no signal is visible even under the signal+background hypothesis. After validation of the background modeling, a likelihood ratio test is performed to investigate excesses of the data compared the background-only hypothesis in the transverse mass distribution. No globally significant excess is observed and 95% confidence level (CL) limits on the product of signal cross-section and branching ratio are obtained

[1]The terminology used does not differentiate between particle and anti-particle. This classification is done by referring to its electric charge. The term charged lepton is used for electrons and muons as well as their anti-particle.

using the Bayesian probability interpretation. These limits are converted to lower exclusion limits on the Sequential Standard Model (SSM) [52] W'_{SSM} mass. The mass limit determined in the electron channel is at 5.19 TeV and in the muon channel at 4.69 TeV. A mass below 5.42 TeV can be excluded at 95% CL when combining both channels. The strongest exclusion limit obtained by ATLAS in the same final state exploiting the full Run 1 data set of roughly 20 fb^{-1} of proton-proton collisions at a center of mass energy of 8 TeV is at 3.24 TeV [148]. This underlines the fact that an increase in $\sqrt{s}$ is very beneficial for this kind of direct searches. ATLAS published in 2019 a search [155] in the same final states using the full Run 2 139 fb^{-1} data set, which excludes W'_{SSM} masses below 6.0 TeV in the electron and 5.1 TeV in the muon channel.

The full $\sqrt{s} = 13$ TeV proton-proton data set of 139 fb^{-1} is used to search for singly produced Leptoquarks (LQ) in the second part of this thesis. SM extensions, which introduce the possibility for lepton flavor universality violations, gained large traction in recent years due to the observations of so-called flavour anomalies [49][51]. Some of these new models introduce LQs, which decay into a lepton and a quark. In Part II final states with an oppositely charged electron or muon pair in combination with jets are investigated. Channels in which the selected high energy jet is b-tagged and explicitly not b-tagged are studied separately. Most previous searches at large high energy particle physics experiments exploited the LQ pair production channel. Predictions of these processes require fewer model assumptions compared to the single production. However, no evidence of the LQ existence has been found when examining their production in pairs. The single production channel on the other hand allows to probe higher mass ranges under specific model assumptions. Due to the challenging background modelling in the complicated final state, signal regions are defined in a single bin. The estimates of the dominant background sources are probed and corrected in dedicated control regions. For the statistical interpretation of the result the significance of disagreements between the data and the background expectation in four different channels are probed with a likelihood ratio test. No significant excess and thus no evidence for the existence of a LQ is observed. Consequently limits are set on the signal cross-section in each of the four channels using a frequentist approach. The 95% CL lower mass limits obtained for the LQ decaying into quarks of the first generation are the strongest available to date under the assumption of a branching fraction to charged leptons of $\beta = 1$ and a LQ-lepton-quark coupling of $\lambda_{\text{lq}} = 1$. It has to be noted that the presented analysis utilizes a different signal model [59] compared to other publications. LQ mass limits obtained with an up(down) and strange(bottom) quark in the final state are at 2.3(1.9) TeV and 1.3(1.2) TeV in the electron channel. The ones determined in the muon channel final states are stronger with 2.8(2.0) TeV for up(down) quarks and 1.2(1.2) TeV for strange(bottom) quarks, with the exception of the strange quark. Limits with quarks of the second and third generation are approximately 600 GeV weaker compared to results obtained by ATLAS in the pair production channel [61]. This is due to the fact that all LO Feynman

diagrams of the single LQ production have a quark in the initial state. Therefore their production is suppressed by PDF effects compared to the LQ pair production, which is taking place via the strong interaction circumventing this limitation.

During the next two Runs of the LHC a significantly larger proton-proton collision data set of $3\,\mathrm{ab}^{-1}$ is expected to be collected by ATLAS at a similar center of mass energy. At first order cross-section exclusion limits scale inversely linear with the integrated luminosity while $\sqrt{s}$ is kept constant. The expected lower mass exclusion limits for W'_{SSM} with $300\,\mathrm{fb}^{-1}$ was estimated to be at 6.7 TeV and with $3\,\mathrm{ab}^{-1}$ at 7.9 TeV [156]. For this analysis the assumption was made that the LHC is operating at a center of mass energy of 14 TeV in Run 3 and Run 4. The higher value of $\sqrt{s}$ improves the sensitivity significantly. Similar sensitivity improvements are expected for the search for singly produced LQ when exploring this data set. Additionally, MC modeling and more efficient event generation give an opportunity to gain additional sensitivity compared to the analysis presented in Part II. A good background description would reduce uncertainties introduced by the control region fit, which is conducted to correct the background normalization. An efficient generation of $t\bar{t}$ events in the high mass tail would render the extrapolation methods obsolete for this background contribution and remove one dominant source of uncertainties. Furthermore, reduced statistical uncertainties of the background description in the signal regions would allow to exploit the resonant shape of the signal. In combination these points yield a expansion of the sensitive mass range. Additionally due to the complex event topology of the selection, the exploration of multivariate techniques might be beneficial for optimization. These methods have been successfully used by a search for pair produced LQs by the ATLAS collaboration [159]. However, a good MC modeling is crucial for the training step. Furthermore, there is room for improvement in the interpretation of the results. A larger set of signal samples gives the opportunity to probe signals and set exclusion limits in a two-dimensional parameter-plane $(\mathrm{m_{LQ}} - \lambda_{\mathrm{lq}})$.

Appendix A

Search for New Physics in Final States with One Lepton Plus Missing Transverse Energy

A.1 Monte Carlo Samples

The following tables list information of all MC simulations used in Part. I. This includes a process description, the number of generated events, the product of cross-section and branching ratio on generator level times the filter-efficiency as well as the integrated luminosity the generated amount of data correspond to.

process	$N_{\text{evt}}/10^3$	generator σB [nb]
$W' \to e\nu$ (Flat)	998	$2.50 \cdot 10^{-2}$
$W' \to \mu\nu$ (Flat)	1000	$2.49 \cdot 10^{-2}$
$W' \to e\nu$ (4 TeV)	20	$1.79 \cdot 10^{-6}$
$W' \to e\nu$ (5 TeV)	20	$4.01 \cdot 10^{-7}$
$W' \to \mu\nu$ (4 TeV)	20	$1.78 \cdot 10^{-6}$
$W' \to \mu\nu$ (5 TeV)	20	$4.09 \cdot 10^{-7}$

TABLE A.1: MC W' signal samples. For each data set, the following is listed: the physics process (including the pole mass in TeV), the number of generated events and cross-section times branching ratio

process	$N_{\mathrm{evt}}/10^3$	generator σB [pb]	$\mathrm{L_{int}}$ [fb^{-1}]
$W^+ \to e\nu$	41415	$11.3 \cdot 10^3$	3.60
$W^- \to e\nu$	49904	$8.28 \cdot 10^3$	5.82
$W^+(120, 180) \to e\nu$	500	32.1	$1.56 \cdot 10^1$
$W^+(180, 250) \to e\nu$	250	5.00	$5.00 \cdot 10^1$
$W^+(250, 400) \to e\nu$	140	1.75	$7.98 \cdot 10^1$
$W^+(400, 600) \to e\nu$	100	$3.12 \cdot 10^{-1}$	$3.20 \cdot 10^2$
$W^+(600, 800) \to e\nu$	50	$6.08 \cdot 10^{-2}$	$8.22 \cdot 10^2$
$W^+(800, 1000) \to e\nu$	50	$1.77 \cdot 10^{-2}$	$2.83 \cdot 10^3$
$W^+(1000, 1250) \to e\nu$	50	$7.29 \cdot 10^{-3}$	$6.86 \cdot 10^3$
$W^+(1250, 1500) \to e\nu$	50	$2.51 \cdot 10^{-3}$	$1.99 \cdot 10^4$
$W^+(1500, 1750) \to e\nu$	50	$9.86 \cdot 10^{-4}$	$5.07 \cdot 10^4$
$W^+(1750, 2000) \to e\nu$	40	$4.25 \cdot 10^{-4}$	$9.42 \cdot 10^4$
$W^+(2000, 2250) \to e\nu$	47	$1.95 \cdot 10^{-4}$	$2.41 \cdot 10^5$
$W^+(2250, 2500) \to e\nu$	50	$9.33 \cdot 10^{-5}$	$5.36 \cdot 10^5$
$W^+(2500, 2750) \to e\nu$	50	$4.63 \cdot 10^{-5}$	$1.08 \cdot 10^6$
$W^+(2750, 3000) \to e\nu$	50	$2.35 \cdot 10^{-5}$	$2.13 \cdot 10^6$
$W^+(3000, 3500) \to e\nu$	50	$1.85 \cdot 10^{-5}$	$2.71 \cdot 10^6$
$W^+(3500, 4000) \to e\nu$	50	$5.10 \cdot 10^{-6}$	$9.81 \cdot 10^6$
$W^+(4000, 4500) \to e\nu$	50	$1.43 \cdot 10^{-6}$	$3.49 \cdot 10^7$
$W^+(4500, 5000) \to e\nu$	50	$4.01 \cdot 10^{-7}$	$1.25 \cdot 10^8$
$W^+(> 5000) \to e\nu$	50	$1.53 \cdot 10^{-7}$	$3.26 \cdot 10^8$
$W^-(120, 180) \to e\nu$	500	22.2	$2.25 \cdot 10^1$
$W^-(180, 250) \to e\nu$	250	3.29	$7.61 \cdot 10^1$
$W^-(250, 400) \to e\nu$	150	1.08	$1.38 \cdot 10^2$
$W^-(400, 600) \to e\nu$	100	$1.75 \cdot 10^{-1}$	$5.70 \cdot 10^2$
$W^-(600, 800) \to e\nu$	50	$3.10 \cdot 10^{-2}$	$1.61 \cdot 10^3$
$W^-(800, 1000) \to e\nu$	50	$8.29 \cdot 10^{-3}$	$6.03 \cdot 10^3$
$W^-(1000, 1250) \to e\nu$	50	$3.16 \cdot 10^{-3}$	$1.58 \cdot 10^4$
$W^-(1250, 1500) \to e\nu$	50	$1.00 \cdot 10^{-3}$	$4.99 \cdot 10^4$
$W^-(1500, 1750) \to e\nu$	50	$3.68 \cdot 10^{-4}$	$1.36 \cdot 10^5$
$W^-(1750, 2000) \to e\nu$	50	$1.49 \cdot 10^{-4}$	$3.35 \cdot 10^5$
$W^-(2000, 2250) \to e\nu$	50	$6.53 \cdot 10^{-5}$	$7.66 \cdot 10^5$
$W^-(2250, 2500) \to e\nu$	50	$3.02 \cdot 10^{-5}$	$1.66 \cdot 10^6$
$W^-(2500, 2750) \to e\nu$	50	$1.45 \cdot 10^{-5}$	$3.44 \cdot 10^6$
$W^-(2750, 3000) \to e\nu$	50	$7.26 \cdot 10^{-6}$	$6.89 \cdot 10^6$
$W^-(3000, 3500) \to e\nu$	50	$5.67 \cdot 10^{-6}$	$8.82 \cdot 10^6$
$W^-(3500, 4000) \to e\nu$	50	$1.60 \cdot 10^{-6}$	$3.13 \cdot 10^7$
$W^-(4000, 4500) \to e\nu$	50	$4.72 \cdot 10^{-7}$	$1.06 \cdot 10^8$
$W^-(4500, 5000) \to e\nu$	50	$1.43 \cdot 10^{-7}$	$3.50 \cdot 10^8$
$W^-(> 5000) \to e\nu$	50	$6.16 \cdot 10^{-8}$	$8.11 \cdot 10^8$

TABLE A.2: MC samples used for background determination. For each data set, the following is listed: the physics process (including the mass range $\mathrm{m}_{e\nu}$ in GeV), the number of generated events, the cross-section times branching ratio, and the equivalent integrated luminosity $\mathrm{L_{int}} = N_{\mathrm{evt}}/(\sigma\mathrm{B})$.

process	$N_{\mathrm{evt}}/10^3$	generator σB [pb]	$\mathrm{L_{int}}$ [fb^{-1}]
$W^+ \to \mu\nu$	39962	$11.3 \cdot 10^3$	3.47
$W^- \to \mu\nu$	31973	$8.28 \cdot 10^3$	3.73
$W^+(120,180) \to \mu\nu$	500	32.1	$1.56 \cdot 10^1$
$W^+(180,250) \to \mu\nu$	250	5.00	$5.00 \cdot 10^1$
$W^+(250,400) \to \mu\nu$	150	1.75	$8.55 \cdot 10^1$
$W^+(400,600) \to \mu\nu$	100	$3.12 \cdot 10^{-1}$	$3.20 \cdot 10^2$
$W^+(600,800) \to \mu\nu$	50	$6.08 \cdot 10^{-2}$	$8.22 \cdot 10^2$
$W^+(800,1000) \to \mu\nu$	50	$1.77 \cdot 10^{-2}$	$2.83 \cdot 10^3$
$W^+(1000,1250) \to \mu\nu$	50	$7.29 \cdot 10^{-3}$	$6.86 \cdot 10^3$
$W^+(1250,1500) \to \mu\nu$	50	$2.51 \cdot 10^{-3}$	$1.99 \cdot 10^4$
$W^+(1500,1750) \to \mu\nu$	50	$9.86 \cdot 10^{-4}$	$5.07 \cdot 10^4$
$W^+(1750,2000) \to \mu\nu$	50	$4.25 \cdot 10^{-4}$	$1.18 \cdot 10^5$
$W^+(2000,2250) \to \mu\nu$	50	$1.95 \cdot 10^{-4}$	$2.57 \cdot 10^5$
$W^+(2250,2500) \to \mu\nu$	50	$9.33 \cdot 10^{-5}$	$5.36 \cdot 10^5$
$W^+(2500,2750) \to \mu\nu$	50	$4.63 \cdot 10^{-5}$	$1.08 \cdot 10^6$
$W^+(2750,3000) \to \mu\nu$	50	$2.35 \cdot 10^{-5}$	$2.13 \cdot 10^6$
$W^+(3000,3500) \to \mu\nu$	50	$1.85 \cdot 10^{-5}$	$2.71 \cdot 10^6$
$W^+(3500,4000) \to \mu\nu$	50	$5.10 \cdot 10^{-6}$	$9.81 \cdot 10^6$
$W^+(4000,4500) \to \mu\nu$	50	$1.43 \cdot 10^{-6}$	$3.49 \cdot 10^7$
$W^+(4500,5000) \to \mu\nu$	50	$4.01 \cdot 10^{-7}$	$1.25 \cdot 10^8$
$W^+(> 5000) \to \mu\nu$	50	$1.53 \cdot 10^{-7}$	$3.26 \cdot 10^8$
$W^-(120,180) \to \mu\nu$	500	22.2	$2.25 \cdot 10^1$
$W^-(180,250) \to \mu\nu$	250	3.29	$7.61 \cdot 10^1$
$W^-(250,400) \to \mu\nu$	150	1.08	$1.38 \cdot 10^2$
$W^-(400,600) \to \mu\nu$	100	$1.75 \cdot 10^{-1}$	$5.70 \cdot 10^2$
$W^-(600,800) \to \mu\nu$	50	$3.10 \cdot 10^{-2}$	$1.61 \cdot 10^3$
$W^-(800,1000) \to \mu\nu$	50	$8.29 \cdot 10^{-3}$	$6.03 \cdot 10^3$
$W^-(1000,1250) \to \mu\nu$	50	$3.16 \cdot 10^{-3}$	$1.58 \cdot 10^4$
$W^-(1250,1500) \to \mu\nu$	50	$1.00 \cdot 10^{-3}$	$4.99 \cdot 10^4$
$W^-(1500,1750) \to \mu\nu$	50	$3.68 \cdot 10^{-4}$	$1.36 \cdot 10^5$
$W^-(1750,2000) \to \mu\nu$	50	$1.49 \cdot 10^{-4}$	$3.35 \cdot 10^5$
$W^-(2000,2250) \to \mu\nu$	50	$6.53 \cdot 10^{-5}$	$7.66 \cdot 10^5$
$W^-(2250,2500) \to \mu\nu$	50	$3.02 \cdot 10^{-5}$	$1.66 \cdot 10^6$
$W^-(2500,2750) \to \mu\nu$	50	$1.45 \cdot 10^{-5}$	$3.44 \cdot 10^6$
$W^-(2750,3000) \to \mu\nu$	50	$7.26 \cdot 10^{-6}$	$6.89 \cdot 10^6$
$W^-(3000,3500) \to \mu\nu$	50	$5.67 \cdot 10^{-6}$	$8.82 \cdot 10^6$
$W^-(3500,4000) \to \mu\nu$	50	$1.60 \cdot 10^{-6}$	$3.13 \cdot 10^7$
$W^-(4000,4500) \to \mu\nu$	50	$4.72 \cdot 10^{-7}$	$1.06 \cdot 10^8$
$W^-(4500,5000) \to \mu\nu$	50	$1.43 \cdot 10^{-7}$	$3.50 \cdot 10^8$
$W^-(> 5000) \to \mu\nu$	50	$6.16 \cdot 10^{-8}$	$8.11 \cdot 10^8$

TABLE A.3: MC samples used for background determination. For each data set, the following is listed: the physics process (including the mass range $\mathrm{m}_{\mu\nu}$ in GeV), the number of generated events, the cross-section times branching ratio, and the equivalent integrated luminosity $\mathrm{L_{int}} = N_{\mathrm{evt}}/(\sigma\mathrm{B})$.

process	$N_{evt}/10^3$	generator σB [pb]	L_{int} [fb^{-1}]
$W^+ \to \tau\nu$	29982	$11.3 \cdot 10^3$	2.61
$W^- \to \tau\nu$	19955	$8.28 \cdot 10^3$	2.33
$W^+(120, 180) \to \tau\nu$	500	32.1	$1.56 \cdot 10^1$
$W^+(180, 250) \to \tau\nu$	250	5.00	$5.00 \cdot 10^1$
$W^+(250, 400) \to \tau\nu$	150	1.75	$8.55 \cdot 10^1$
$W^+(400, 600) \to \tau\nu$	100	$3.12 \cdot 10^{-1}$	$3.20 \cdot 10^2$
$W^+(600, 800) \to \tau\nu$	50	$6.08 \cdot 10^{-2}$	$8.23 \cdot 10^2$
$W^+(800, 1000) \to \tau\nu$	50	$1.77 \cdot 10^{-2}$	$2.83 \cdot 10^3$
$W^+(1000, 1250) \to \tau\nu$	50	$7.29 \cdot 10^{-3}$	$6.86 \cdot 10^3$
$W^+(1250, 1500) \to \tau\nu$	50	$2.51 \cdot 10^{-3}$	$1.99 \cdot 10^4$
$W^+(1500, 1750) \to \tau\nu$	50	$9.86 \cdot 10^{-4}$	$5.07 \cdot 10^4$
$W^+(1750, 2000) \to \tau\nu$	50	$4.25 \cdot 10^{-4}$	$1.18 \cdot 10^5$
$W^+(2000, 2250) \to \tau\nu$	50	$1.95 \cdot 10^{-4}$	$2.57 \cdot 10^5$
$W^+(2250, 2500) \to \tau\nu$	50	$9.33 \cdot 10^{-5}$	$5.36 \cdot 10^5$
$W^+(2500, 2750) \to \tau\nu$	50	$4.63 \cdot 10^{-5}$	$1.08 \cdot 10^6$
$W^+(2750, 3000) \to \tau\nu$	50	$2.35 \cdot 10^{-5}$	$2.13 \cdot 10^6$
$W^+(3000, 3500) \to \tau\nu$	50	$1.85 \cdot 10^{-5}$	$2.71 \cdot 10^6$
$W^+(3500, 4000) \to \tau\nu$	50	$5.10 \cdot 10^{-6}$	$9.81 \cdot 10^6$
$W^+(4000, 4500) \to \tau\nu$	50	$1.43 \cdot 10^{-6}$	$3.50 \cdot 10^7$
$W^+(4500, 5000) \to \tau\nu$	50	$4.01 \cdot 10^{-7}$	$1.25 \cdot 10^8$
$W^+(> 5000) \to \tau\nu$	50	$1.53 \cdot 10^{-7}$	$3.26 \cdot 10^8$
$W^-(120, 180) \to \tau\nu$	470	22.2	$2.12 \cdot 10^1$
$W^-(180, 250) \to \tau\nu$	250	3.29	$7.61 \cdot 10^1$
$W^-(250, 400) \to \tau\nu$	150	1.08	$1.39 \cdot 10^2$
$W^-(400, 600) \to \tau\nu$	100	$1.75 \cdot 10^{-1}$	$5.70 \cdot 10^2$
$W^-(600, 800) \to \tau\nu$	50	$3.10 \cdot 10^{-2}$	$1.61 \cdot 10^3$
$W^-(800, 1000) \to \tau\nu$	50	$8.29 \cdot 10^{-3}$	$6.03 \cdot 10^3$
$W^-(1000, 1250) \to \tau\nu$	46	$3.16 \cdot 10^{-3}$	$1.46 \cdot 10^4$
$W^-(1250, 1500) \to \tau\nu$	50	$1.00 \cdot 10^{-3}$	$4.99 \cdot 10^4$
$W^-(1500, 1750) \to \tau\nu$	50	$3.68 \cdot 10^{-4}$	$1.36 \cdot 10^5$
$W^-(1750, 2000) \to \tau\nu$	50	$1.49 \cdot 10^{-4}$	$3.35 \cdot 10^5$
$W^-(2000, 2250) \to \tau\nu$	50	$6.53 \cdot 10^{-5}$	$7.66 \cdot 10^5$
$W^-(2250, 2500) \to \tau\nu$	50	$3.02 \cdot 10^{-5}$	$1.66 \cdot 10^6$
$W^-(2500, 2750) \to \tau\nu$	50	$1.45 \cdot 10^{-5}$	$3.44 \cdot 10^6$
$W^-(2750, 3000) \to \tau\nu$	50	$7.26 \cdot 10^{-6}$	$6.89 \cdot 10^6$
$W^-(3000, 3500) \to \tau\nu$	50	$5.67 \cdot 10^{-6}$	$8.82 \cdot 10^6$
$W^-(3500, 4000) \to \tau\nu$	50	$1.60 \cdot 10^{-6}$	$3.13 \cdot 10^7$
$W^-(4000, 4500) \to \tau\nu$	50	$4.72 \cdot 10^{-7}$	$1.06 \cdot 10^8$
$W^-(4500, 5000) \to \tau\nu$	50	$1.43 \cdot 10^{-7}$	$3.50 \cdot 10^8$
$W^-(> 5000) \to \tau\nu$	50	$6.16 \cdot 10^{-8}$	$8.11 \cdot 10^8$

TABLE A.4: MC samples used for background determination. For each data set, the following is listed: the physics process (including the mass range $m_{\tau\nu}$ in GeV), the number of generated events, the cross-section times branching ratio, and the equivalent integrated luminosity $L_{int} = N_{evt}/(\sigma B)$.

process	$N_{\mathrm{evt}}/10^3$	generator σB [pb]	$\mathrm{L_{int}}$ [fb^{-1}]
$Z \to ee$	79942	$1.90 \cdot 10^{3}$	$4.15 \cdot 10^{1}$
$Z(120,180) \to ee$	1249	17.5	$7.15 \cdot 10^{1}$
$Z(180,250) \to ee$	900	2.92	$3.08 \cdot 10^{2}$
$Z(250,400) \to ee$	1200	1.08	$1.11 \cdot 10^{3}$
$Z(400,600) \to ee$	900	$1.96 \cdot 10^{-1}$	$4.60 \cdot 10^{3}$
$Z(600,800) \to ee$	510	$3.74 \cdot 10^{-2}$	$1.36 \cdot 10^{4}$
$Z(800,1000) \to ee$	250	$1.06 \cdot 10^{-2}$	$2.36 \cdot 10^{4}$
$Z(1000,1250) \to ee$	100	$4.26 \cdot 10^{-3}$	$2.35 \cdot 10^{4}$
$Z(1250,1500) \to ee$	50	$1.42 \cdot 10^{-3}$	$3.52 \cdot 10^{4}$
$Z(1500,1750) \to ee$	50	$5.45 \cdot 10^{-4}$	$9.17 \cdot 10^{4}$
$Z(1750,2000) \to ee$	100	$2.30 \cdot 10^{-4}$	$4.35 \cdot 10^{5}$
$Z(2000,2250) \to ee$	50	$1.04 \cdot 10^{-4}$	$4.81 \cdot 10^{5}$
$Z(2250,2500) \to ee$	50	$4.94 \cdot 10^{-5}$	$1.01 \cdot 10^{6}$
$Z(2500,2750) \to ee$	50	$2.45 \cdot 10^{-5}$	$2.04 \cdot 10^{6}$
$Z(2750,3000) \to ee$	50	$1.25 \cdot 10^{-5}$	$4.00 \cdot 10^{6}$
$Z(3000,3500) \to ee$	50	$1.00 \cdot 10^{-5}$	$4.99 \cdot 10^{6}$
$Z(3500,4000) \to ee$	50	$2.93 \cdot 10^{-6}$	$1.70 \cdot 10^{7}$
$Z(4000,4500) \to ee$	50	$8.98 \cdot 10^{-7}$	$5.57 \cdot 10^{7}$
$Z(4500,5000) \to ee$	50	$2.81 \cdot 10^{-7}$	$1.78 \cdot 10^{8}$
$Z(> 5000) \to ee$	50	$1.26 \cdot 10^{-7}$	$3.95 \cdot 10^{8}$

TABLE A.5: MC samples used for background determination. For each data set, the following is listed: the physics process (including the mass range m_{ee} in GeV), the number of generated events, the cross-section times branching ratio, and the equivalent integrated luminosity $\mathrm{L_{int}} = N_{\mathrm{evt}}/(\sigma\mathrm{B})$.

process	$N_{\mathrm{evt}}/10^3$	generator σB [pb]	$\mathrm{L_{int}}$ [fb^{-1}]
$Z \to \mu\mu$	79874	$1.90 \cdot 10^{3}$	$4.15 \cdot 10^{1}$
$Z(120,180) \to \mu\mu$	2000	17.5	$1.14 \cdot 10^{2}$
$Z(180,250) \to \mu\mu$	1150	2.92	$3.94 \cdot 10^{2}$
$Z(250,400) \to \mu\mu$	1345	1.08	$1.24 \cdot 10^{3}$
$Z(400,600) \to \mu\mu$	1000	$1.96 \cdot 10^{-1}$	$5.11 \cdot 10^{3}$
$Z(600,800) \to \mu\mu$	600	$3.74 \cdot 10^{-2}$	$1.60 \cdot 10^{4}$
$Z(800,1000) \to \mu\mu$	300	$1.06 \cdot 10^{-2}$	$2.83 \cdot 10^{4}$
$Z(1000,1250) \to \mu\mu$	150	$4.26 \cdot 10^{-3}$	$3.52 \cdot 10^{4}$
$Z(1250,1500) \to \mu\mu$	100	$1.42 \cdot 10^{-3}$	$7.03 \cdot 10^{4}$
$Z(1500,1750) \to \mu\mu$	100	$5.45 \cdot 10^{-4}$	$1.83 \cdot 10^{5}$
$Z(1750,2000) \to \mu\mu$	100	$2.30 \cdot 10^{-4}$	$4.35 \cdot 10^{5}$
$Z(2000,2250) \to \mu\mu$	100	$1.04 \cdot 10^{-4}$	$9.63 \cdot 10^{5}$
$Z(2250,2500) \to \mu\mu$	100	$4.94 \cdot 10^{-5}$	$2.02 \cdot 10^{6}$
$Z(2500,2750) \to \mu\mu$	100	$2.46 \cdot 10^{-5}$	$4.09 \cdot 10^{6}$
$Z(2750,3000) \to \mu\mu$	100	$1.25 \cdot 10^{-5}$	$8.01 \cdot 10^{6}$
$Z(3000,3500) \to \mu\mu$	100	$1.00 \cdot 10^{-5}$	$9.97 \cdot 10^{6}$
$Z(3500,4000) \to \mu\mu$	100	$2.93 \cdot 10^{-6}$	$3.41 \cdot 10^{7}$
$Z(4000,4500) \to \mu\mu$	100	$8.98 \cdot 10^{-7}$	$1.11 \cdot 10^{8}$
$Z(4500,5000) \to \mu\mu$	100	$2.81 \cdot 10^{-7}$	$3.56 \cdot 10^{8}$
$Z(> 5000) \to \mu\mu$	100	$1.26 \cdot 10^{-7}$	$7.91 \cdot 10^{8}$

TABLE A.6: MC samples used for background determination. For each data set, the following is listed: the physics process (including the mass range $\mathrm{m}_{\mu\mu}$ in GeV), the number of generated events, the cross-section times branching ratio, and the equivalent integrated luminosity $\mathrm{L_{int}} = N_{\mathrm{evt}}/(\sigma\mathrm{B})$.

process	$N_{\text{evt}}/10^3$	generator σB [pb]	L_{int} [fb^{-1}]
$Z \to \tau\tau$	39495	$1.90 \cdot 10^{3}$	$2.08\text{e} \cdot 10^{1}$
$Z(120, 180) \to \tau\tau$	450	1.75	$2.57 \cdot 10^{1}$
$Z(180, 250) \to \tau\tau$	423	2.92	$1.45 \cdot 10^{2}$
$Z(250, 400) \to \tau\tau$	444	1.08	$4.10 \cdot 10^{2}$
$Z(400, 600) \to \tau\tau$	599	$1.96 \cdot 10^{-1}$	$3.07 \cdot 10^{3}$
$Z(600, 800) \to \tau\tau$	450	$3.74 \cdot 10^{-2}$	$1.20 \cdot 10^{4}$
$Z(800, 1000) \to \tau\tau$	450	$1.06 \cdot 10^{-2}$	$4.24 \cdot 10^{4}$
$Z(1000, 1250) \to \tau\tau$	450	$4.26 \cdot 10^{-3}$	$1.06 \cdot 10^{5}$
$Z(1250, 1500) \to \tau\tau$	450	$1.42 \cdot 10^{-3}$	$3.16 \cdot 10^{5}$
$Z(1500, 1750) \to \tau\tau$	350	$5.45 \cdot 10^{-4}$	$6.42 \cdot 10^{5}$
$Z(1750, 2000) \to \tau\tau$	235	$2.30 \cdot 10^{-4}$	$1.02 \cdot 10^{6}$
$Z(2000, 2250) \to \tau\tau$	450	$1.04 \cdot 10^{-4}$	$4.33 \cdot 10^{6}$
$Z(2250, 2500) \to \tau\tau$	350	$4.94 \cdot 10^{-5}$	$7.08 \cdot 10^{6}$
$Z(2500, 2750) \to \tau\tau$	350	$2.45 \cdot 10^{-5}$	$1.43 \cdot 10^{7}$
$Z(2750, 3000) \to \tau\tau$	350	$1.25 \cdot 10^{-5}$	$2.80 \cdot 10^{7}$
$Z(3000, 3500) \to \tau\tau$	350	$1.00 \cdot 10^{-5}$	$3.49 \cdot 10^{7}$
$Z(3500, 4000) \to \tau\tau$	400	$2.93 \cdot 10^{-6}$	$1.36 \cdot 10^{8}$
$Z(4000, 4500) \to \tau\tau$	315	$8.98 \cdot 10^{-7}$	$3.51 \cdot 10^{8}$
$Z(4500, 5000) \to \tau\tau$	350	$2.81 \cdot 10^{-7}$	$1.25 \cdot 10^{9}$
$Z(> 5000) \to \tau\tau$	350	$1.26 \cdot 10^{-7}$	$2.77 \cdot 10^{9}$

TABLE A.7: MC samples used for background determination. For each data set, the following is listed: the physics process (including the mass range $\text{m}_{\tau\tau}$ in GeV), the number of generated events, the cross-section times branching ratio, and the equivalent integrated luminosity $\text{L}_{\text{int}} = N_{\text{evt}}/(\sigma\text{B})$.

process	$N_{\text{evt}}/10^3$	generator $\sigma\text{B} \cdot \varepsilon_{\text{filt}}$ [pb]	L_{int} [fb^{-1}]
$ZZ \to llll$	17842	$1.28 \cdot 1.0$	$1.43 \cdot 10^{4}$
$WZ \to lll\nu$	15537	$4.58 \cdot 1.0$	$3.40 \cdot 10^{3}$
$VV \to ll\nu\nu$	14996	$12.5 \cdot 1.0$	$1.20 \cdot 10^{3}$
$WZ \to l\nu\nu\nu$	5999	$3.23 \cdot 1.0$	$1.85 \cdot 10^{3}$
$W^+W^- \to l\nu qq$	7188	$24.7 \cdot 1.0$	$2.91 \cdot 10^{2}$
$W^+W^- \to qql\nu$	7194	$24.7 \cdot 1.0$	$2.91 \cdot 10^{2}$
$WZ \to l\nu qq$	7180	$11.4 \cdot 1.0$	$6.29 \cdot 10^{2}$
$WZ \to qqll$	5400	$3.43 \cdot 1.0$	$1.57 \cdot 10^{3}$
$ZZ \to qqll$	5400	$15.6 \cdot 0.141$	$2.45 \cdot 10^{3}$

TABLE A.8: MC samples used for background determination. For each data set, the following is listed: the physics process, the number of generated events, the cross-section times branching ratio times the generator filter-efficiency $\varepsilon_{\text{filt}}$ and the equivalent integrated luminosity $\text{L}_{\text{int}} = N_{\text{evt}}/(\sigma\text{B} \cdot \varepsilon_{\text{filt}})$

process	$N_{\text{evt}}/10^3$	generator $\sigma\text{B} \cdot \varepsilon_{\text{filt}}$ [pb]	k-factor	L_{int} [fb^{-1}]
$t\bar{t} \to lX$	119432	$730 \cdot 0.544$	1.140	$2.64 \cdot 10^{2}$
s-channel $t \to lX$	2000	$2.03 \cdot 1.0$	1.017	$9.70 \cdot 10^{2}$
s-channel $\bar{t} \to lX$	2000	$1.27 \cdot 1.0$	1.017	$1.55 \cdot 10^{3}$
t-channel $t \to lX$	4790	$37.0 \cdot 1.0$	1.194	$1.08 \cdot 10^{2}$
t-channel $\bar{t} \to lX$	4761	$22.2 \cdot 1.0$	1.185	$1.81 \cdot 10^{2}$
s-channel Wt	4996	$38.0 \cdot 1.0$	0.945	$1.39 \cdot 10^{2}$
s-channel $W\bar{t}$	4999	$37.9 \cdot 1.0$	0.946	$1.39 \cdot 10^{2}$

TABLE A.9: MC samples used for background determination. For each data set, the following is listed: the physics process, the number of generated events, the product of cross-section and branching ratio times the generator filter-efficiency $\varepsilon_{\text{filt}}$, the higher order correction factor k and the equivalent integrated luminosity $\text{L}_{\text{int}} = N_{\text{evt}}/(\sigma\text{B}k \cdot \varepsilon_{\text{filt}})$

Appendix B

Search for Singly Produced Leptoquarks

B.1 Monte Carlo Samples

This section gives an overview over simulated samples used as signal hypotheses and for background determination in Part II. Each signal sample used for the LQ search contains 10000 events.

The following tables list information on MC simulations used for background estimation. A process description, the number of generated events, the product of generator level cross-section and branching ratio, the generator filter-efficiency, the higher order theoretical correction factor k as well as the integrated luminosity the generated amount of events correspond to is given. For each year of data taking the run conditions are modeled in a different simulation setup. Between those the amount of generated events differs. These numbers are separated within one cell by a horizontal bar (''|''). The first entry corresponds to the data taking conditions in the years 2015 and 2016, the middle one to 2017 and the last one to 2018 (2015+2016|2017|2018).

process	$N_{\text{evt}}/10^3$	generator σB [pb]	$\varepsilon_{\text{filt}}$	k-factor	L_{int} [fb^{-1}]
$\bar{t}tW$	7497|7497|11922	5.48 $\cdot 10^{-1}$	1.00	1.10	(1.2|1.2|2.0) $\cdot 10^4$
$\bar{t}tZ(\to \nu\nu)$	1500|1500|2001	1.55 $\cdot 10^{-1}$	1.00	1.11	(8.7|8.7|12) $\cdot 10^3$
$\bar{t}tZ(\to qq)$	3000|3000|3587	5.28 $\cdot 10^{-1}$	1.00	1.11	(5.1|5.1|6.1) $\cdot 10^3$
$\bar{t}tZ(\to ee)$	1410|1337|2168	3.69 $\cdot 10^{-2}$	1.00	1.12	(3.4|3.2|5.3) $\cdot 10^4$
$\bar{t}tZ(\to \mu\mu)$	1410|1339|2173	3.69 $\cdot 10^{-2}$	1.00	1.12	(3.4|3.2|5.3) $\cdot 10^4$
$\bar{t}tZ(\to \tau\tau)$	935|900|958	3.66 $\cdot 10^{-2}$	1.00	1.12	(2.3|2.2|2.3) $\cdot 10^4$
$\bar{t}t$	39974|44876|33102	730	0.11	1.14	(4.6|5.1|3.8) $\cdot 10^2$
tW	4996|6243|8300	37.9	1.00	0.95	(1.4|1.7|2.3) $\cdot 10^2$
$\bar{t}W$	4999|6240|8272	37.9	1.00	0.95	(1.4|1.7|2.3) $\cdot 10^2$

TABLE B.1: MC samples used for background determination. For each data set, the following is listed: the physics process, the number of generated events, the product of cross-section and branching ratio, the generator filter-efficiency $\varepsilon_{\text{filt}}$, the higher order correction factor k and the equivalent integrated luminosity $L_{\text{int}} = N_{\text{evt}}/(\sigma B k \cdot \varepsilon_{\text{filt}})$. Variations between different simulation setups used to model differences in the data taking conditions are divided by '|' within one cell (2015+2016|2017|2018).

process	$N_{\text{evt}}/10^3$	generator σB [pb]	$\varepsilon_{\text{filt}}$	k-factor	L_{int} [fb^{-1}]
$ZZ \to qqll$	5400|11161|9315	15.6	0.14	1.00	(2.45|5.06|4.22) $\cdot 10^3$
$WZ \to qqll$	5400|11160|9310	3.43	1.00	1.00	(1.57|3.24|2.71) $\cdot 10^3$
$ZZ \to llll$	17843|35996|25684	1.25	1.00	1.00	(1.4|2.9|2.1) $\cdot 10^4$
$WZ \to lll\nu$	15538|32114|26790	4.58	1.00	1.00	(3.4|7.0|5.9) $\cdot 10^3$
$VV \to ll\nu\nu$	14996|29975|24889	12.5	1.00	1.00	(1.2|2.4|2.0) $\cdot 10^3$

TABLE B.2: MC samples used for background determination. For each data set, the following is listed: the physics process, the number of generated events, the product of cross-section and branching ratio, the generator filter-efficiency $\varepsilon_{\text{filt}}$, the higher order correction factor k and the equivalent integrated luminosity $L_{\text{int}} = N_{\text{evt}}/(\sigma B k \cdot \varepsilon_{\text{filt}})$. Variations between different simulation setups used to model differences in the data taking conditions are divided by ''|'' within one cell (2015+2016|2017|2018).

process	$N_{\text{evt}}/10^3$	generator σB [pb]	$\varepsilon_{\text{filt}}$	k-factor	L_{int} [fb^{-1}]
$Z \to \mu\mu(< 70)$ light-jet	7970|9909|13263	$1.98 \cdot 10^3$	0.82	0.98	5.0|6.2|8.3
$Z \to \mu\mu(< 70)$ c-jet	4982|6199|8283	$1.98 \cdot 10^3$	0.11	0.98	23|28|38
$Z \to \mu\mu(< 70)$ b-jet	7983|9621|13240	$1.98 \cdot 10^3$	0.06	0.98	$(6.3\|7.6\|10) \cdot 10^1$
$Z \to \mu\mu(70, 140)$ light-jet	5983|7478|9943	109	0.69	0.98	$(8.1\|10\|14) \cdot 10^1$
$Z \to \mu\mu(70, 140)$ c-jet	1997|2495|3312	109	0.19	0.98	$(9.6\|12\|16) \cdot 10^1$
$Z \to \mu\mu(70, 140)$ b-jet	5982|7469|9941	109	0.11	0.98	$(4.8\|6.0\|8.0) \cdot 10^2$
$Z \to \mu\mu(140, 280)$ light-jet	5000|6244|8286	39.9	0.61	0.98	$(2.1\|2.7\|3.6) \cdot 10^2$
$Z \to \mu\mu(140, 280)$ c-jet	3000|3750|4987	39.9	0.23	0.98	$(3.3\|4.1\|5.5) \cdot 10^2$
$Z \to \mu\mu(140, 280)$ b-jet	12459|15629|20743	39.9	0.15	0.98	$(2.1\|2.6\|3.4) \cdot 10^3$
$Z \to \mu\mu(280, 500)$ light-jet	2000|2460|3321	8.53	0.56	0.98	$(4.3\|5.3\|7.1) \cdot 10^2$
$Z \to \mu\mu(280, 500)$ c-jet	1000|1249|1669	8.53	0.27	0.98	$(4.5\|5.6\|7.5) \cdot 10^2$
$Z \to \mu\mu(280, 500)$ b-jet	1999|2498|3327	8.53	0.18	0.98	$(1.4\|1.7\|2.3) \cdot 10^3$
$Z \to \mu\mu(500, 1000)$	2997|3747|5095	1.79	1.00	0.98	$(1.7\|2.1\|2.9) \cdot 10^3$
$Z \to \mu\mu(> 1000)$	997|1250|1667	$1.48 \cdot 10^{-1}$	1.00	0.98	$(6.9\|8.7\|12) \cdot 10^3$
$Z \to ee(< 70)$ light-jet	8000|9998|13267	$1.98 \cdot 10^3$	0.82	0.98	5.0|6.3|8.4
$Z \to ee(< 70)$ c-jet	4999|6241|8308	$1.98 \cdot 10^3$	0.11	0.98	23|28|38
$Z \to ee(< 70)$ b-jet	7996|9993|13277	$1.98 \cdot 10^3$	0.06	0.98	$(6.3\|7.9\|10) \cdot 10^1$
$Z \to ee(70, 140)$ light-jet	5956|7385|9952	111	0.69	0.98	$(8.0\|9.9\|13) \cdot 10^1$
$Z \to ee(70, 140)$ c-jet	1999|2495|3328	111	0.18	0.98	$(9.8\|12\|16) \cdot 10^1$
$Z \to ee(70, 140)$ b-jet	5970|7493|9910	110	0.11	0.98	$(4.7\|5.9\|7.8) \cdot 10^2$
$Z \to ee(140, 280)$ light-jet	5000|6250|8356	40.6	0.61	0.98	$(2.0\|2.6\|3.4) \cdot 10^2$
$Z \to ee(140, 280)$ c-jet	3000|3748|4986	40.7	0.23	0.98	$(3.2\|4.1\|5.4) \cdot 10^2$
$Z \to ee(140, 280)$ b-jet	12440|15662|20737	40.7	0.15	0.98	$(2.0\|2.6\|3.4) \cdot 10^3$
$Z \to ee(280, 500)$ light-jet	2000|2500|3424	8.67	0.56	0.98	$(4.2\|5.2\|7.1) \cdot 10^2$
$Z \to ee(280, 500)$ c-jet	1000|1250|1737	8.67	0.26	0.98	$(4.4\|5.6\|7.7) \cdot 10^2$
$Z \to ee(280, 500)$ b-jet	2000|2500|3328	8.67	0.17	0.98	$(1.3\|1.7\|2.2) \cdot 10^3$
$Z \to ee(500, 1000)$	2999|3712|4983	1.81	1.00	0.98	$(1.7\|2.1\|2.8) \cdot 10^3$
$Z \to ee(> 1000)$	1000|1250|1669	$1.49 \cdot 10^{-1}$	1.00	0.98	$(6.9\|8.6\|12) \cdot 10^3$
$Z \to \tau\tau(< 70)$ light-jet	7986|9998|13274	$1.98 \cdot 10^3$	0.82	0.98	5.0|6.2|8.2
$Z \to \tau\tau(< 70)$ c-jet	4979|6138|8274	$1.98 \cdot 10^3$	0.11	0.98	24|29|39
$Z \to \tau\tau(< 70)$ b-jet	7886|9994|13278	$1.98 \cdot 10^3$	0.06	0.98	$(6.3\|7.9\|10) \cdot 10^1$
$Z \to \tau\tau(70, 140)$ light-jet	5998|7499|9974	111	0.69	0.98	$(8.0\|10\|13) \cdot 10^1$
$Z \to \tau\tau(70, 140)$ c-jet	1999|2499|3328	110	0.18	0.98	$(9.7\|12\|16) \cdot 10^1$
$Z \to \tau\tau(70, 140)$ b-jet	5810|7499|9963	111	0.11	0.98	$(4.9\|6.3\|8.2) \cdot 10^2$
$Z \to \tau\tau(140, 280)$ light-jet	4940|6228|8297	40.8	0.61	0.98	$(2.0\|2.5\|3.4) \cdot 10^2$
$Z \to \tau\tau(140, 280)$ c-jet	3000|3750|4987	40.7	0.23	0.98	$(3.2\|4.0\|5.4) \cdot 10^2$
$Z \to \tau\tau(140, 280)$ b-jet	4993|6213|8285	40.7	0.13	0.98	$(8.1\|10\|13) \cdot 10^2$
$Z \to \tau\tau(280, 500)$ light-jet	2000|2499|3318	8.66	0.56	0.98	$(4.2\|5.3\|7.0) \cdot 10^2$
$Z \to \tau\tau(280, 500)$ c-jet	1000|1234|1668	8.68	0.26	0.98	$(4.5\|5.5\|7.5) \cdot 10^2$
$Z \to \tau\tau(280, 500)$ b-jet	1984|2497|3324	8.68	0.17	0.98	$(1.3\|1.7\|2.2) \cdot 10^3$
$Z \to \tau\tau(500, 1000)$	3000|3750|4961	1.81	1.00	0.98	$(1.7\|2.1\|2.8) \cdot 10^3$
$Z \to \tau\tau(> 1000)$	1000|1250|1667	$1.48 \cdot 10^{-1}$	1.00	0.98	$(6.9\|8.6\|12) \cdot 10^3$

TABLE B.3: MC samples used for background determination. For each data set, the following is listed: the physics process (including the $\max(H_T, p_{T,V})$ range in GeV and the jet filter), the number of generated events, the cross-section times branching ratio, the generator filter-efficiency $\varepsilon_{\text{filt}}$, the higher order correction factor k and the equivalent integrated luminosity $L_{\text{int}} = N_{\text{evt}}/(\sigma B)$. Variations between different simulation setups used to model differences in the data taking conditions are divided by '|' within one cell (2015+2016|2017|2018).

B.2 High Mass Top Structures

Structures in the highest populated m_{LQmax} intervals in the m_{LQmax} distribution of background contributions from processes with top quarks are observed. These are introduced by the large amounts of $t\bar{t}$ events selected. This observation is investigated by decomposing the $t\bar{t}$ background by the number of bottom-quarks entering the fiducial region on generator level. There are contributions from events with zero, one and two b quarks to all regions convoluted with the corresponding b-tagging efficiency or inefficiency. The underlying distributions run out of statistics at different points in the mass spectrum. This is the reason why there are edges at which the migration from one sample to the selected background per region is not possible anymore. When doing the extrapolations (in Sec. 11.5.2) it is ensure that these effects are covered by the extrapolation uncertainty.

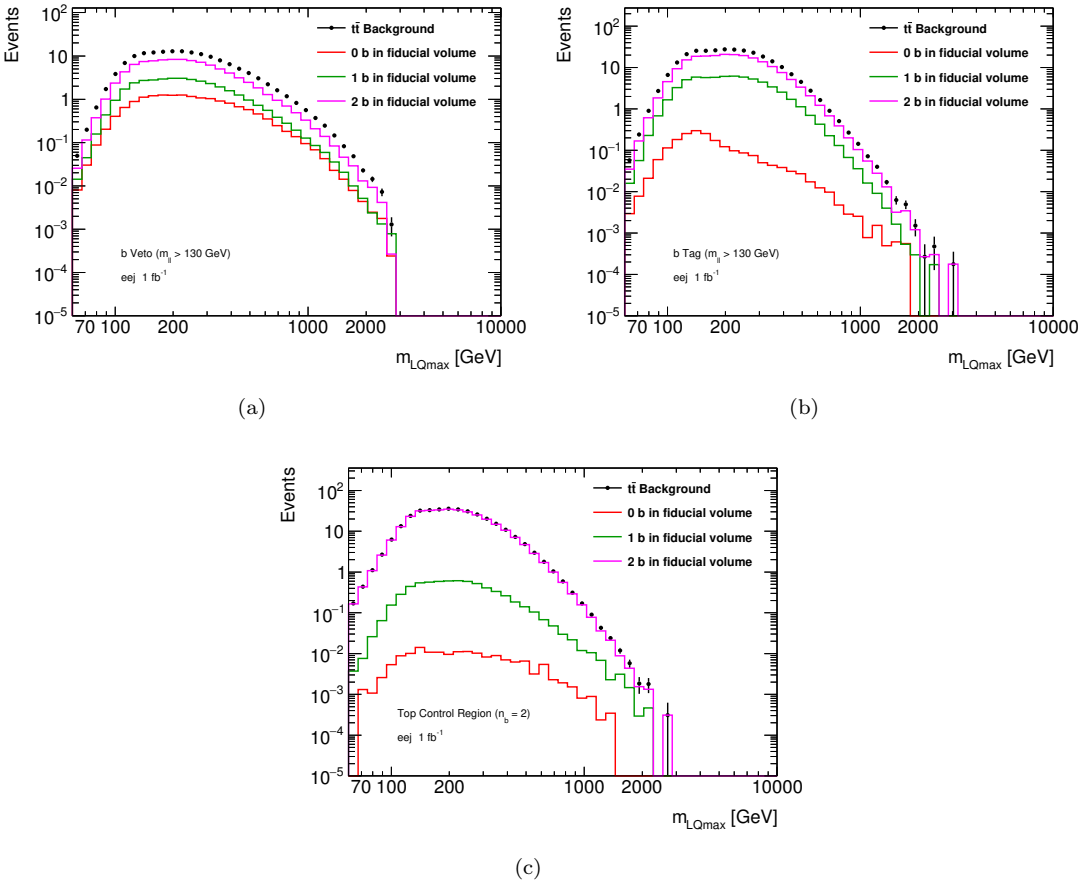

FIGURE B.1: $t\bar{t}$ background m_{LQmax} distributions in the b-veto (a) and b-tag (b) combined region ($m_{ll} > 130\,\text{GeV}$) as well as the Top control region (c). The total background is illustrated by the black data points. Different contributions classified by the number of b quarks in the fiducial region are given by the purple, green and red line.

Fig. B.1 shows the electron channel m_{LQmax} distributions in the combined b-tag and b-veto region as well as the top control region as an example. Similar observations are made in the muon channel. Illustrated distributions are decomposed into samples of events with zero, one

and two b quarks within the fiducial volume on generator level. The invariant mass of the lepton pair is required to be larger than 130 GeV to obtain the combination of the signal, Z/γ^* control and validation region. In the top control region no m_{ll} cut is applied as described in Sec. 11.4.4. The sum of each contributions is drawn as black data points, while each single are displayed in colors. Contributions of events with two b quarks are the dominant ones, even in the region where events with b-tagged jets are neglected. By far most events have two b quarks in the fiducial volume. The b-tagging efficiency is only 77%. The relative contribution of the ensembles of events shown in red and green is enhanced in the regions with less than two b-tagged jets. All distributions have similar shapes and the hypotheses, that each contribution runs out of statistics at different m_{LQmax} values in the tail, is confirmed.

B.3 Leptoquark Kinematic Distributions

Angular distributions of the sub-leading lepton are shown exemplarily for the Z/γ^*+jets control region exemplarily in Fig. B.2. ϕ and pseudorapidity distributions are shown in the top row for the electron channel and in the bottom row for the muon channel. The shape of the drawn spectra as well as the data to background agreement is in line to the leading lepton diagrams. Shape discussions are given in Sec. 11.7.1.1.

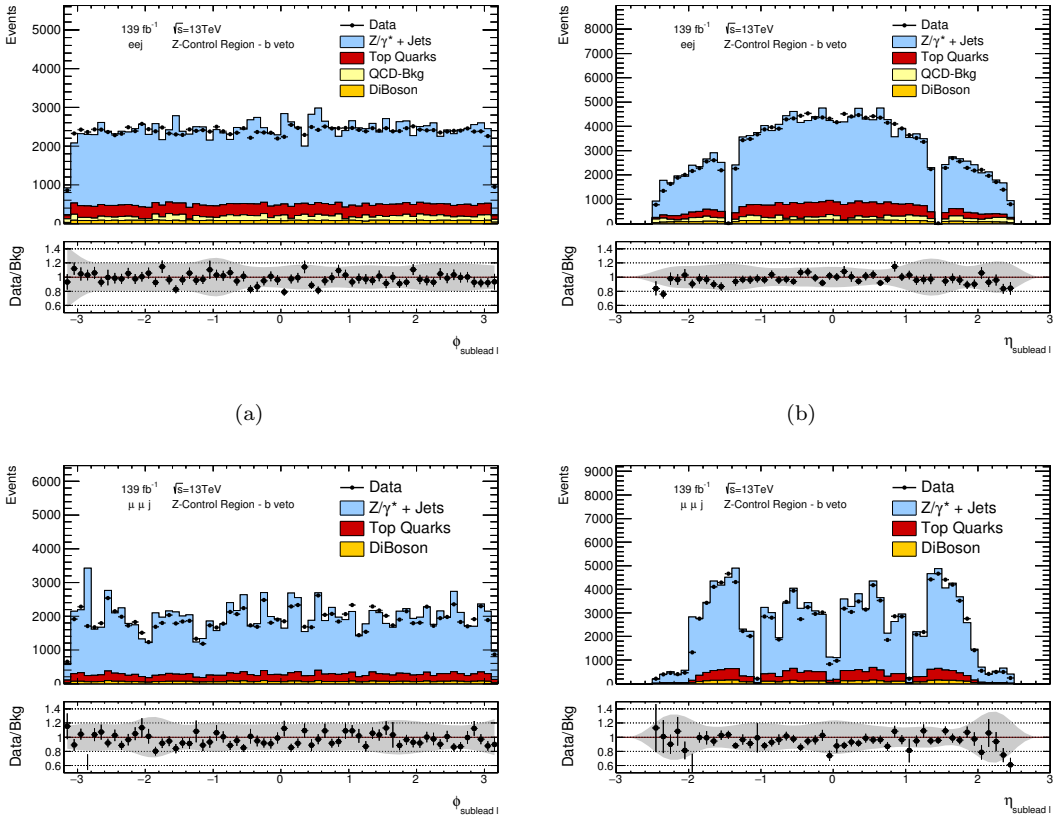

(a) (b)

(c) (d)

FIGURE B.2: Angular distributions ϕ and η shown for sub-leading electron candidates (a)-(b) and muon candidates (c)-(d). The upper panel shows the data points as well as the background prediction, with its contributing fractions drawn separately but stacked. The lower panel displays the ratio of data and total background estimate. The gray band indicates the impact of uncertainties originating from experimental uncertainties and limited MC statistics.

B.4 Leptoquark Signal Shape and Acceptance Studies

The impact of the quark flavor in the final state of the Leptoquark (LQ) decay on the shape of kinematic distributions is studied. This is relevant for the result interpretation in the b-veto channels in which light-flavor jets are selected (veto events with b-tagged jets). In the statistical analysis the kinematic distribution of the process $pp \to l\mathrm{LQ} \to lls$ is used as a substitute for the decay into up and down quarks. The signal cross-section has no influence on the determined cross-section exclusion limit in Sec. 12.6. However, acceptance differences of the signal will have an impact.

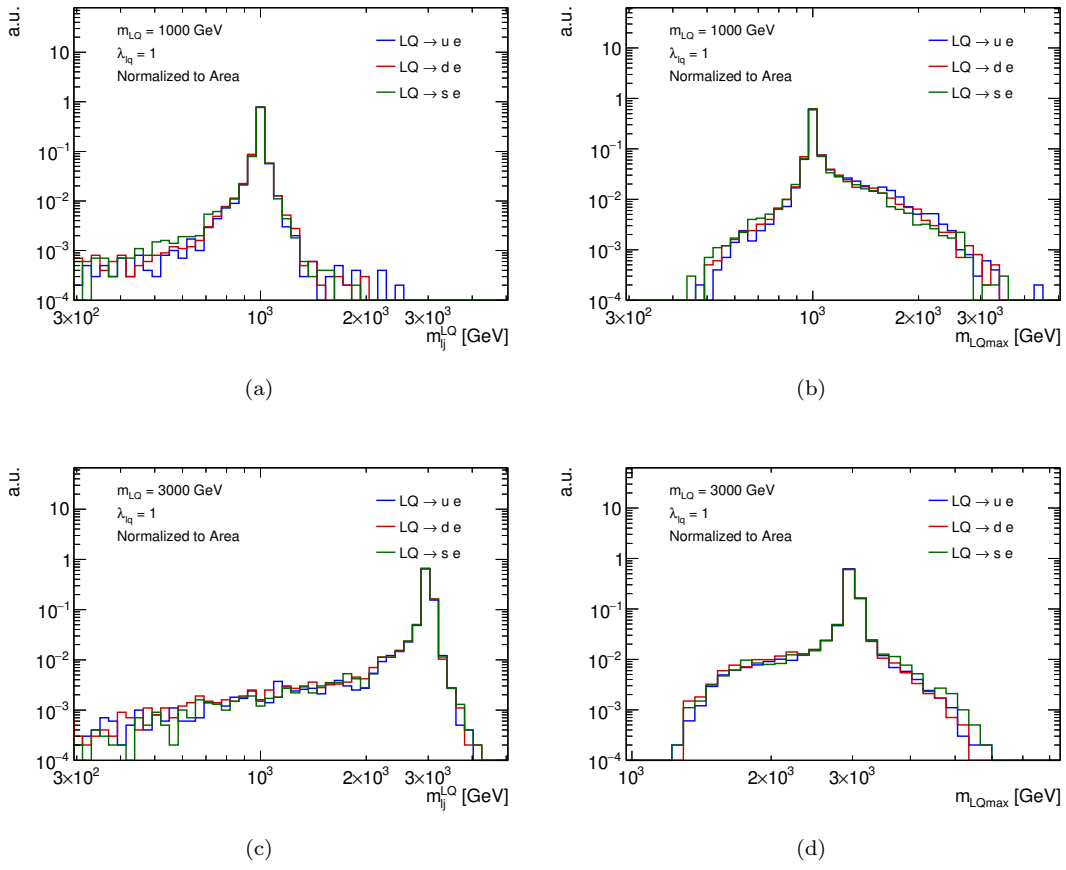

FIGURE B.3: Generator level m_{lj}^{LQ} and m_{LQmax} distributions for signal processes including different quark types. Each spectrum is normalized to its area. In the top row the signal process $pp \to l\mathrm{LQ} \to lls$ with a LQ mass hypothesis of 1 TeV and in the bottom row for 3 TeV were generated. The LQ-lepton-quark coupling is assumed to be $\lambda_{lq} = 1$.

Fig. B.3 and Fig. B.4 compares generator level kinematic distributions of signal hypotheses with different quark flavors in the final state for LQ masses of 1 TeV and 3 TeV with $\lambda_{lq} = 1$. No detector response is simulated which is the reason why the shape of the distribution is independent of the lepton flavor in the mass range investigated. Processes with an electron in the final state are shown exemplarily.

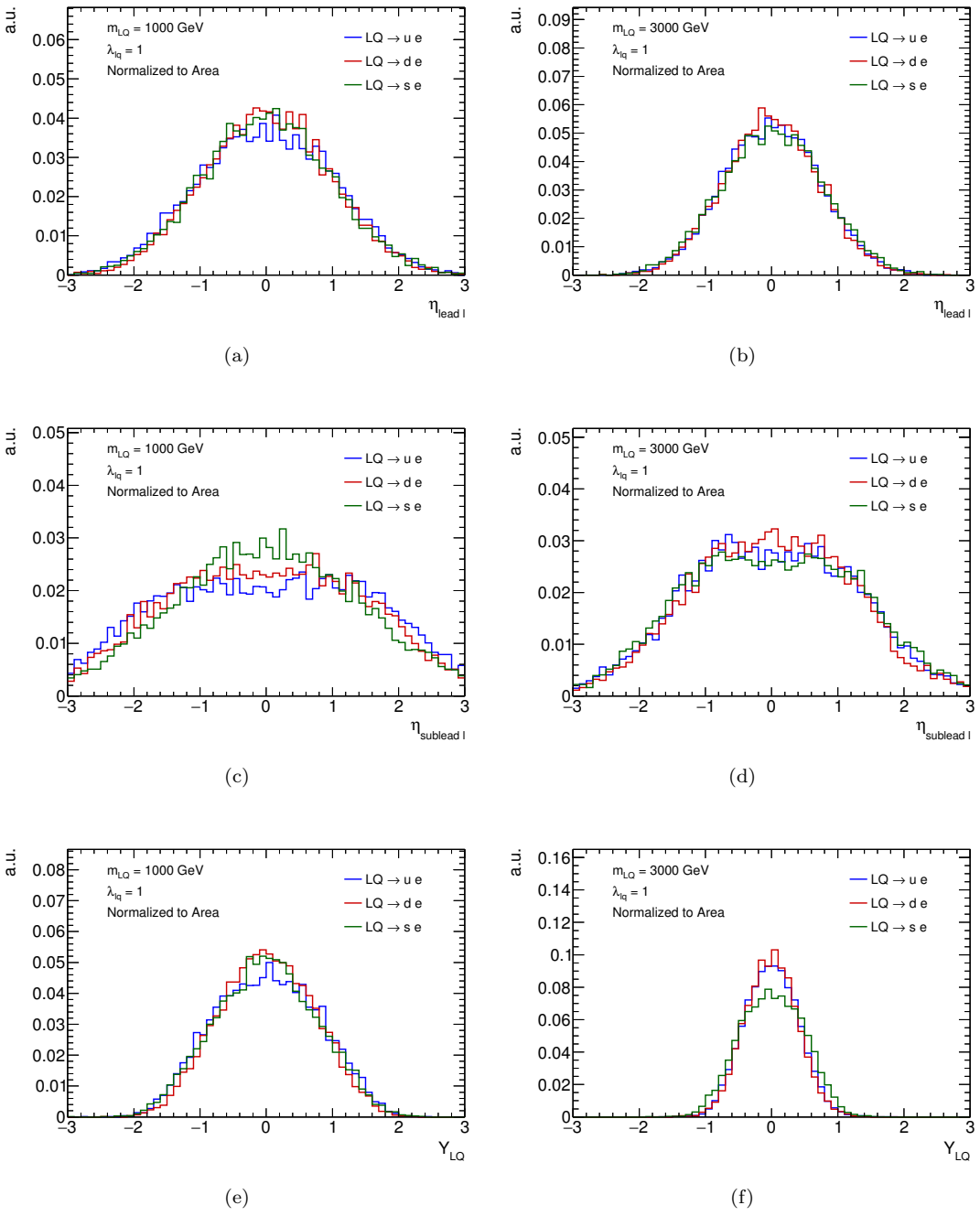

FIGURE B.4: Generator level lepton pseudorapidity η and LQ rapidity distributions for signal processes including different quark types. Each spectrum is normalized to its area. In the first column the signal process $pp \to l\mathrm{LQ} \to lls$ (+ c.c.) with a LQ mass hypothesis of $m_{LQ} = 1$ TeV and in the second column for $m_{LQ}3$ TeV were generated. A LQ-lepton-quark coupling of $\lambda_{lq} = 1$ is assumed.

The m_{lj}^{LQ} and m_{LQmax} distributions are displayed in Fig. B.3 for a m_{LQ} hypothesis of 1 TeV in the top row and 3 TeV in the bottom row. Each spectrum is normalized to its area to allow shape comparisons. All mass distributions shown do not depend on the quark flavor in first order. Each spectrum has a resonant structure at the mass of the LQ. For the mass hypothesis

of 1 TeV - (a) and (b) - kinematic distributions of the process with a strange quark in the final state is slightly shifted toward the lower end of the range compared to the others. The opposite can be observed in the bottom row in which a LQ with $m_{LQ} = 3$ TeV has been simulated. To come to this conclusion the tail above and below the resonance is examined. This effect is explained by considering the product of Bjorken x values of initial state particles. Valence quark contributions are higher for the initial state up and down quarks at low LQ mass hypotheses. For high masses the initial state quark originates in most cases from the sea of the proton. The case of high m_{LQ} in combination with a valence quark in the initial state leads to an enhancement of the low mass tail and increases the fraction of off-shell produced LQ.

Pseudorapidity distributions of the leading and sub-leading electron as well as the rapidity spectrum of the LQ are shown in Fig. B.3 for a LQ mass hypothesis of 1 TeV in the first column and 3 TeV in the second one. The distributions of the leading lepton pseudorapidities shown in (a) and (b) is not influenced by the quark flavor. Leading leptons are produced more centrally in case of the higher LQ mass of 3 TeV. These are almost all the time produced in the LQ decay vertex. In case of a LQ mass of 3 TeV, the quark flavor is not impacting the sub-leading lepton pseudorapidity distribution displayed in (d). For $m_{LQ} = 1$ TeV the sub-leading lepton is produced more central, if the LQ in the signal process comes from initial state strange quarks. The rapidity spectra shown in (e) ar more flat for up quarks if LQ simulated has a mass of 1 TeV. In case of a mass of 3 TeV, LQs are produced more central in processes with up and down quarks in the initial state.

Finally, the impact on the acceptance of minor shape variations in kinematic distributions introduced by the quark flavor are quantified. For this a fixed number of events is generated for every mass hypothesis with each (anti-)quark (u, d, s) and lepton (e, μ) flavor. The acceptance variation is estimated by comparing the number of events entering the fiducial volume of each signal region (defined in Sec. 11.4.3 and Sec. 12.3). In the statistical analysis the signal process with a (anti-)strange quark is considered. This is the reason why the variation of the (anti-)up quark and (anti-)down quark process is evaluated relative to the LQ decay into a (anti-)strange quark. Fig. B.5 displays these relative acceptance differences for up and down quarks - drawn in blue and red - against the LQ mass. (a) shows the curve in case of electrons in the final state and (b) the one determined with muons. Variations observed are on percent level. This is negligible in comparison to the large uncertainties on the expected limit and the signal cross-section curves presented in Sec. 12.6.

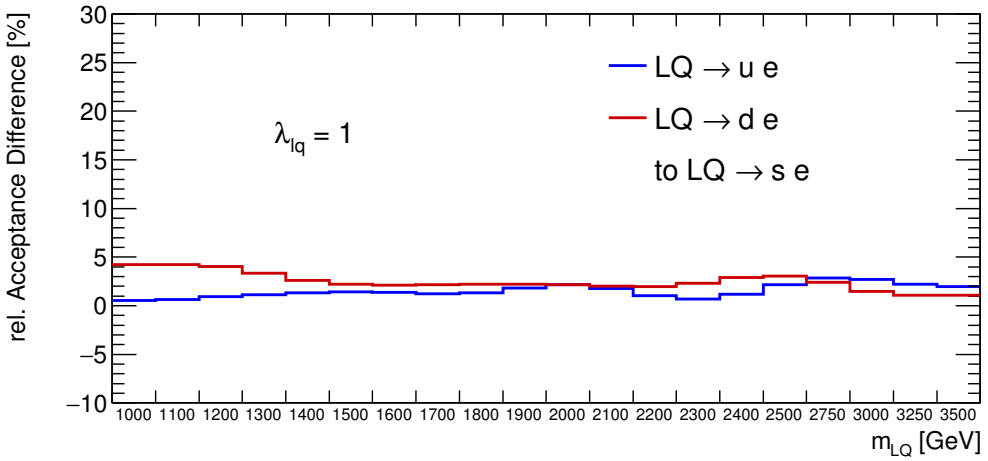

(a)

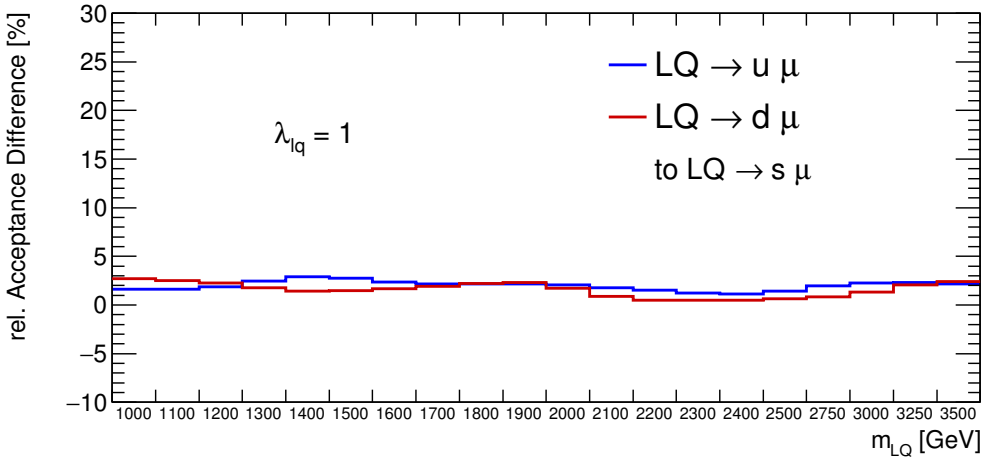

(b)

FIGURE B.5: Acceptance variations when exchanging the quark flavor in the LQ decay vs the mass hypothesis. A fixed number of events has been generated for each process and the ratio of event yields in the fiducial volume of the signal regions are compared. Signal processes with (anti-)up and (anti-)down quarks are set in relation to the (anti-)strange quark process, which is used in the statistical analysis.

Bibliography

[1] J. J. Thomson. 'Cathode rays'. In: *Phil. Mag.* 44 (1897), pp. 293–316. DOI: 10.1080/14786449708621070.

[2] E. Rutherford. 'The scattering of alpha and beta particles by matter and the structure of the atom'. In: *Phil. Mag.* 21 (1911), pp. 669–688. DOI: 10.1080/14786440508637080.

[3] J. Chadwick. 'Possible Existence of a Neutron'. In: *Nature* 129 (1932), p. 312. DOI: 10.1038/129312a0.

[4] Murray Gell-Mann. 'A Schematic Model of Baryons and Mesons'. In: *Phys. Lett.* 8 (1964), pp. 214–215. DOI: 10.1016/S0031-9163(64)92001-3.

[5] G. Zweig. 'An SU(3) model for strong interaction symmetry and its breaking. Version 2'. In: *Developments in the quark theory of hadrons. Vol. 1. 1964 - 1978.* Ed. by D.B. Lichtenberg and Simon Peter Rosen. 1964, pp. 22–101. URL: http://inspirehep.net/record/4674/files/cern-th-412.pdf.

[6] Martin Breidenbach et al. 'Observed Behavior of Highly Inelastic electron-Proton Scattering'. In: *Phys. Rev. Lett.* 23 (1969), pp. 935–939. DOI: 10.1103/PhysRevLett.23.935.

[7] Elliott D. Bloom et al. 'High-Energy Inelastic e p Scattering at 6-Degrees and 10-Degrees'. In: *Phys. Rev. Lett.* 23 (1969), pp. 930–934. DOI: 10.1103/PhysRevLett.23.930.

[8] M. Banner et al. 'Observation of Single Isolated Electrons of High Transverse Momentum in Events with Missing Transverse Energy at the CERN anti-p p Collider'. In: *Phys. Lett.* B122 (1983), pp. 476–485. DOI: 10.1016/0370-2693(83)91605-2.

[9] G. Arnison et al. 'Experimental observation of isolated large transverse energy electrons with associated missing energy at sqrt(s)=540 GeV'. In: *Physics Letters B* 122 (Feb. 1983), pp. 103–116. DOI: 10.1016/0370-2693(83)91177-2.

[10] F. Halzen and A. D. Martin.
'Quarks and Leptons: An Introductory Course in Modern Particle Physics'.
In: *New York, Usa: Wiley (1984) 396p* (1984).

[11] Lisa Randall and Raman Sundrum.
'A Large mass hierarchy from a small extra dimension'.
In: *Phys. Rev. Lett.* 83 (1999), pp. 3370–3373. DOI: 10.1103/PhysRevLett.83.3370.
arXiv: hep-ph/9905221 [hep-ph].

[12] H. Georgi and S. L. Glashow. 'Unity of All Elementary Particle Forces'.
In: *Phys. Rev. Lett.* 32 (1974), pp. 438–441. DOI: 10.1103/PhysRevLett.32.438.

[13] Lyndon Evans and Philip Bryant. 'LHC Machine'. In: *JINST* 3 (2008), S08001.
DOI: 10.1088/1748-0221/3/08/S08001.

[14] G. Aad et al. 'The ATLAS Experiment at the CERN Large Hadron Collider'.
In: *JINST* 3 (2008), S08003. DOI: 10.1088/1748-0221/3/08/S08003.

[15] Stephen P. Martin. 'A Supersymmetry primer'.
In: (1997). [Adv. Ser. Direct. High Energy Phys.18,1(1998)].
DOI: 10.1142/9789812839657_0001,10.1142/9789814307505_0001.
arXiv: hep-ph/9709356 [hep-ph].

[16] Jogesh C. Pati and Abdus Salam.
'Unified Lepton-Hadron Symmetry and a Gauge Theory of the Basic Interactions'.
In: *Phys. Rev.* D8 (1973), pp. 1240–1251. DOI: 10.1103/PhysRevD.8.1240.

[17] Holger Herr. 'Search for High-Mass Resonances of Electron-Positron Pairs in Proton-Proton Collisions at 13 TeV with the ATLAS experiment'.
Presented Nov. 2015.

[18] M. Tanabashi et al. 'Review of Particle Physics'.
In: *Phys. Rev.* D98.3 (2018), p. 030001. DOI: 10.1103/PhysRevD.98.030001.

[19] Michael E. Peskin and Daniel V. Schroeder.
An Introduction To Quantum Field Theory.
Addison-Wesley Publishing Company, 1995. ISBN: 978-0-201-50397-5.

[20] R. P. Feynman. 'The Theory of Positrons'. In: *Phys. Rev.* 76 (1949).
DOI: 10.1103/PhysRev.76.749.

[21] Orear, J. and Fermi, E.
'Nuclear Physics: A Course Given by Enrico Fermi at the University of Chicago'.
In: *University of Chicago Press* (1950).

[22] Raymond Brock et al. 'Handbook of perturbative QCD; Version 1.1: September 1994'.
In: *Rev. Mod. Phys.* (1994).

[23] Steven Weinberg. 'A Model of Leptons'. In: *Phys.Rev.Lett.* 19 (1967), pp. 1264–1266. DOI: 10.1103/PhysRevLett.19.1264.

[24] S.L. Glashow. 'Partial Symmetries of Weak Interactions'. In: *Nucl.Phys.* 22 (1961), pp. 579–588. DOI: 10.1016/0029-5582(61)90469-2.

[25] Abdus Salam. 'Weak and Electromagnetic Interactions'. In: *Conf.Proc.* C680519 (1968), pp. 367–377.

[26] Nicola Cabibbo. 'Unitary Symmetry and Leptonic Decays'. In: *Phys. Rev. Lett.* 10 (1963), pp. 531–533. DOI: 10.1103/PhysRevLett.10.531.

[27] Makoto Kobayashi and Toshihide Maskawa. 'CP Violation in the Renormalizable Theory of Weak Interaction'. In: *Prog. Theor. Phys.* 49 (1973), pp. 652–657. DOI: 10.1143/PTP.49.652.

[28] Ling-Lie Chau and Wai-Yee Keung. 'Comments on the Parametrization of the Kobayashi-Maskawa Matrix'. In: *Phys. Rev. Lett.* 53 (1984), p. 1802. DOI: 10.1103/PhysRevLett.53.1802.

[29] B. Pontecorvo. 'Inverse beta processes and nonconservation of lepton charge'. In: *Sov. Phys. JETP* 7 (1958), pp. 172–173.

[30] Ziro Maki, Masami Nakagawa and Shoichi Sakata. 'Remarks on the unified model of elementary particles'. In: *Prog. Theor. Phys.* 28 (1962), pp. 870–880. DOI: 10.1143/PTP.28.870.

[31] Peter W. Higgs. 'Broken symmetries, massless particles and gauge fields'. In: *Phys.Lett.* 12 (1964), pp. 132–133. DOI: 10.1016/0031-9163(64)91136-9.

[32] R. P. Feynman. 'The behavior of hadron collisions at extreme energies'. In: *Conf. Proc.* C690905 (1969), pp. 237–258.

[33] S. Chekanov et al. 'Measurement of the neutral current cross-section and F(2) structure function for deep inelastic e + p scattering at HERA'. In: *Eur.Phys.J.* C21 (2001), pp. 443–471. DOI: 10.1007/s100520100749. arXiv: hep-ex/0105090 [hep-ex].

[34] C. Adloff et al. 'Measurement of neutral and charged current cross-sections in positron proton collisions at large momentum transfer'. In: *Eur.Phys.J.* C13 (2000), pp. 609–639. DOI: 10.1007/s100520050721. arXiv: hep-ex/9908059 [hep-ex].

[35] R.S. Towell et al. 'Improved measurement of the anti-d / anti-u asymmetry in the nucleon sea'. In: *Phys.Rev.* D64 (2001), p. 052002. DOI: 10.1103/PhysRevD.64.052002. arXiv: hep-ex/0103030 [hep-ex].

[36] R. D. Ball et al. 'Parton distributions for the LHC Run II'. In: *JHEP* 04 (2015), p. 040. DOI: 10.1007/JHEP04(2015)040. arXiv: 1410.8849 [hep-ph].

[37] Y. L. Dokshitzer. 'Calculation of the Structure Functions for Deep Inelastic Scattering and e+ e- Annihilation by Perturbation Theory in Quantum Chromodynamics.' In: *Sov. Phys. JETP* 46 (1977). [Zh. Eksp. Teor. Fiz.73,1216(1977)], pp. 641–653.

[38] V. N. Gribov and L. N. Lipatov. 'e+ e- pair annihilation and deep inelastic e p scattering in perturbation theory'. In: *Sov. J. Nucl. Phys.* 15 (1972). [Yad. Fiz.15,1218(1972)], pp. 675–684.

[39] G. Altarelli and G. Parisi. 'Asymptotic Freedom in Parton Language'. In: *Nucl. Phys.* B126 (1977), p. 298.

[40] Guido Altarelli and G. Parisi. 'Asymptotic Freedom in Parton Language'. In: *Nucl.Phys.* B126 (1977), p. 298. DOI: 10.1016/0550-3213(77)90384-4.

[41] A. Vogt, S. Moch and J.A.M. Vermaseren. 'The Three-loop splitting functions in QCD: The Singlet case'. In: *Nucl.Phys.* B691 (2004), pp. 129–181. DOI: 10.1016/j.nuclphysb.2004.04.024. arXiv: hep-ph/0404111 [hep-ph].

[42] Richard D. Ball et al. 'Parton distributions from high-precision collider data'. In: *Eur. Phys. J.* C77.10 (2017), p. 663. DOI: 10.1140/epjc/s10052-017-5199-5. arXiv: 1706.00428 [hep-ph].

[43] J. Pumplin et al. 'Uncertainties of predictions from parton distribution functions. 2. The Hessian method'. In: *Phys.Rev.* D65 (2001), p. 014013. DOI: 10.1103/PhysRevD.65.014013. arXiv: hep-ph/0101032 [hep-ph].

[44] S.D. Drell and Tung-Mow Yan. 'Partons and their Applications at High-Energies'. In: *Annals Phys.* 66 (1971), p. 578. DOI: 10.1016/0003-4916(71)90071-6.

[45] Vera C. Rubin and W. Kent Ford Jr. 'Rotation of the Andromeda Nebula from a Spectroscopic Survey of Emission Regions'. In: *Astrophys. J.* 159 (1970), pp. 379–403. DOI: 10.1086/150317.

[46] G. Hinshaw et al. 'Five-Year Wilkinson Microwave Anisotropy Probe (WMAP) Observations: Data Processing, Sky Maps, and Basic Results'. In: *Astrophys. J. Suppl.* 180 (2009), pp. 225–245. DOI: 10.1088/0067-0049/180/2/225. arXiv: 0803.0732 [astro-ph].

[47] A. Augusto Alves Jr. et al. 'The LHCb Detector at the LHC'. In: *JINST* 3 (2008), S08005.

[48] Roel Aaij et al. 'Test of lepton universality using $B^+ \to K^+\ell^+\ell^-$ decays'. In: *Phys. Rev. Lett.* 113 (2014), p. 151601. DOI: 10.1103/PhysRevLett.113.151601. arXiv: 1406.6482 [hep-ex].

[49] R. Aaij et al. 'Test of lepton universality with $B^0 \to K^{*0}\ell^+\ell^-$ decays'.
In: *JHEP* 08 (2017), p. 055. DOI: 10.1007/JHEP08(2017)055.
arXiv: 1705.05802 [hep-ex].

[50] J. T. Wei et al. 'Measurement of the Differential Branching Fraction and Forward-Backword Asymmetry for $B \to K^{(*)}\ell^+\ell^-$'.
In: *Phys. Rev. Lett.* 103 (2009), p. 171801. DOI: 10.1103/PhysRevLett.103.171801.
arXiv: 0904.0770 [hep-ex].

[51] Roel Aaij et al. 'Search for lepton-universality violation in $B^+ \to K^+\ell^+\ell^-$ decays'.
In: *Phys. Rev. Lett.* 122.19 (2019), p. 191801. DOI: 10.1103/PhysRevLett.122.191801.
arXiv: 1903.09252 [hep-ex].

[52] Guido Altarelli, B. Mele and M. Ruiz-Altaba.
'Searching for New Heavy Vector Bosons in $p\bar{p}$ Colliders'.
In: *Z. Phys.* C45 (1989). [Erratum: Z. Phys.C47,676(1990)], p. 109.
DOI: 10.1007/BF01552335,10.1007/BF01556677.

[53] Chiara Arina et al. 'Constraints on sneutrino dark matter from LHC Run 1'.
In: *JHEP* 05 (2015), p. 142. DOI: 10.1007/JHEP05(2015)142.
arXiv: 1503.02960 [hep-ph].

[54] G. Senjanovic and Rabindra N. Mohapatra.
'Exact Left-Right Symmetry and Spontaneous Violation of Parity'.
In: *Phys. Rev.* D12 (1975), p. 1502. DOI: 10.1103/PhysRevD.12.1502.

[55] Alessio Maiezza et al. 'Left-Right Symmetry at LHC'.
In: *Phys. Rev.* D82 (2010), p. 055022. DOI: 10.1103/PhysRevD.82.055022.
arXiv: 1005.5160 [hep-ph].

[56] Rabindra N. Mohapatra and Goran Senjanovic.
'Neutrino Mass and Spontaneous Parity Violation'.
In: *Phys. Rev. Lett.* 44 (1980), p. 912. DOI: 10.1103/PhysRevLett.44.912.

[57] Howard Georgi and S. L. Glashow. 'Unity of All Elementary-Particle Forces'.
In: *Phys. Rev. Lett.* 32 (8 1974), pp. 438–441. DOI: 10.1103/PhysRevLett.32.438.
URL: https://link.aps.org/doi/10.1103/PhysRevLett.32.438.

[58] Paul H. Frampton and Bum-Hoon Lee. 'SU(15) grand unification'.
In: *Phys. Rev. Lett.* 64 (6 1990), pp. 619–621. DOI: 10.1103/PhysRevLett.64.619.
URL: https://link.aps.org/doi/10.1103/PhysRevLett.64.619.

[59] Ilja Doršner and Admir Greljo. 'Leptoquark toolbox for precision collider studies'.
In: *JHEP* 05 (2018), p. 126. DOI: 10.1007/JHEP05(2018)126.
arXiv: 1801.07641 [hep-ph].

[60] Gudrun Hiller, Dennis Loose. 'Flavorful leptoquarks at hadron colliders'. In: *Phys. Rev. D* 97 (7 2018), p. 075004. DOI: 10.1103/PhysRevD.97.075004. URL: https://link.aps.org/doi/10.1103/PhysRevD.97.075004.

[61] Georges Aad et al. 'Search for pairs of scalar leptoquarks decaying into quarks and electrons or muons in $\sqrt{s} = 13$ TeV pp collisions with the ATLAS detector'. In: (June 2020). arXiv: 2006.05872 [hep-ex].

[62] Morad Aaboud et al. 'Searches for scalar leptoquarks and differential cross-section measurements in dilepton-dijet events in proton-proton collisions at a centre-of-mass energy of $\sqrt{s} = 13$ TeV with the ATLAS experiment'. In: *Eur. Phys. J.* C79.9 (2019), p. 733. DOI: 10.1140/epjc/s10052-019-7181-x. arXiv: 1902.00377 [hep-ex].

[63] Morad Aaboud et al. 'Searches for third-generation scalar leptoquarks in $\sqrt{s} = 13$ TeV pp collisions with the ATLAS detector'. In: *JHEP* 06 (2019), p. 144. DOI: 10.1007/JHEP06(2019)144. arXiv: 1902.08103 [hep-ex].

[64] Albert M Sirunyan et al. 'Search for pair production of first-generation scalar leptoquarks at $\sqrt{s} = 13$ TeV'. In: *Phys. Rev.* D99.5 (2019), p. 052002. DOI: 10.1103/PhysRevD.99.052002. arXiv: 1811.01197 [hep-ex].

[65] Albert M Sirunyan et al. 'Search for heavy neutrinos and third-generation leptoquarks in hadronic states of two τ leptons and two jets in proton-proton collisions at $\sqrt{s} = 13$ TeV'. In: *JHEP* 03 (2019), p. 170. DOI: 10.1007/JHEP03(2019)170. arXiv: 1811.00806 [hep-ex].

[66] Vardan Khachatryan et al. 'Search for single production of scalar leptoquarks in proton-proton collisions at $\sqrt{s} = 8\ TeV$'. In: *Phys. Rev.* D93.3 (2016). [Erratum: Phys. Rev.D95,no.3,039906(2017)], p. 032005. DOI: 10.1103/PhysRevD.95.039906,10.1103/PhysRevD.93.032005. arXiv: 1509.03750 [hep-ex].

[67] A. M. Sirunyan et al. 'Search for a singly produced third-generation scalar leptoquark decaying to a τ lepton and a bottom quark in proton-proton collisions at $\sqrt{s} = 13$ TeV'. In: *JHEP* 07 (2018), p. 115. DOI: 10.1007/JHEP07(2018)115. arXiv: 1806.03472 [hep-ex].

[68] S. Chatrchyan et al. 'The CMS experiment at the CERN LHC'. In: *JINST* 3 (2008), S08004. DOI: 10.1088/1748-0221/3/08/S08004.

[69] A. Augusto Alves Jr. et al. 'The LHCb Detector at the LHC'. In: *JINST* 3 (2008), S08005. DOI: 10.1088/1748-0221/3/08/S08005.

[70] K. Aamodt et al. 'The ALICE experiment at the CERN LHC'. In: *JINST* 3 (2008), S08002. DOI: 10.1088/1748-0221/3/08/S08002.

[71] Esma Mobs. 'The CERN accelerator complex. Complexe des accélérateurs du CERN'. In: (2016). General Photo. URL: https://cds.cern.ch/record/2197559.

[72] Joao Pequenao. 'Computer generated image of the whole ATLAS detector'. 2008. URL: https://cds.cern.ch/record/1095924.

[73] S Haywood et al. *ATLAS inner detector: Technical Design Report, 2*. Technical Design Report ATLAS. Geneva: CERN, 1997.

[74] *ATLAS central solenoid: Technical Design Report*. Technical Design Report ATLAS. Electronic version not available. Geneva: CERN, 1997.

[75] Joao Pequenao. 'Computer generated image of the ATLAS inner detector'. 2008. URL: https://cds.cern.ch/record/1095926.

[76] Norbert Wermes and G Hallewel. *ATLAS pixel detector: Technical Design Report*. Technical Design Report ATLAS. Geneva: CERN, 1998.

[77] M Capeans et al. *ATLAS Insertable B-Layer Technical Design Report*. Tech. rep. CERN-LHCC-2010-013. ATLAS-TDR-19. Geneva: CERN, 2010. URL: https://cds.cern.ch/record/1291633.

[78] Joao Pequenao. 'Computer Generated image of the ATLAS calorimeter'. 2008. URL: https://cds.cern.ch/record/1095927.

[79] *ATLAS liquid-argon calorimeter: Technical Design Report*. Technical Design Report ATLAS. Geneva: CERN, 1996.

[80] *ATLAS calorimeter performance: Technical Design Report*. Technical Design Report ATLAS. Geneva: CERN, 1996.

[81] *ATLAS tile calorimeter: Technical Design Report*. Technical Design Report ATLAS. Geneva: CERN, 1996.

[82] A. Artamonov et al. 'The ATLAS forward calorimeters'. In: *JINST* 3 (2008), P02010. DOI: 10.1088/1748-0221/3/02/P02010.

[83] *ATLAS muon spectrometer: Technical Design Report*. Technical Design Report ATLAS. distribution. Geneva: CERN, 1997.

[84] Georges Aad et al. 'Muon reconstruction performance of the ATLAS detector in proton–proton collision data at $\sqrt{s}$ =13 TeV'. In: *Eur. Phys. J.* C76.5 (2016), p. 292. DOI: 10.1140/epjc/s10052-016-4120-y. arXiv: 1603.05598 [hep-ex].

[85] Joao Pequenao. 'Computer generated image of the ATLAS Muons subsystem'. 2008. URL: https://cds.cern.ch/record/1095929.

[86] J P Badiou et al. *ATLAS barrel toroid: Technical Design Report.* Technical Design Report ATLAS. Electronic version not available. Geneva: CERN, 1997.

[87] *ATLAS end-cap toroids: Technical Design Report.* Technical Design Report ATLAS. Electronic version not available. Geneva: CERN, 1997.

[88] *ATLAS level-1 trigger: Technical Design Report.* Technical Design Report ATLAS. Geneva: CERN, 1998.

[89] Peter Jenni et al. *ATLAS high-level trigger, data-acquisition and controls: Technical Design Report.* Technical Design Report ATLAS. Geneva: CERN, 2003.

[90] G Avoni et al. 'The new LUCID-2 detector for luminosity measurement and monitoring in ATLAS'. In: *JINST* 13.07 (2018), P07017. 33 p. DOI: 10.1088/1748-0221/13/07/P07017. URL: http://cds.cern.ch/record/2633501.

[91] V. Cindro et al. 'The ATLAS beam conditions monitor'. In: *JINST* 3 (2008), P02004. DOI: 10.1088/1748-0221/3/02/P02004.

[92] L Adamczyk et al. *Technical Design Report for the ATLAS Forward Proton Detector.* Tech. rep. CERN-LHCC-2015-009. ATLAS-TDR-024. 2015. URL: https://cds.cern.ch/record/2017378.

[93] Vladislav Balagura. 'Notes on van der Meer Scan for Absolute Luminosity Measurement'. In: *Nucl.Instrum.Meth.* A654 (2011), pp. 634–638. DOI: 10.1016/j.nima.2011.06.007. arXiv: 1103.1129 [physics.ins-det].

[94] Giovanna Lehmann Miotto et al. 'Configuration and control of the ATLAS trigger and data acquisition'. In: *Nucl. Instrum. Meth.* A623 (2010), pp. 549–551. DOI: 10.1016/j.nima.2010.03.066.

[95] Christoph Eck et al. *LHC computing Grid: Technical Design Report. Version 1.06 (20 Jun 2005).* Technical Design Report LCG. Geneva: CERN, 2005. URL: https://cds.cern.ch/record/840543.

[96] R.W.L. Jones. 'ATLAS computing and the GRID'. In: *Nucl. Instrum. Meth. A* 502 (2003). Ed. by V.A. Ilyin, V.V. Korenkov and D. Perret-Gallix, pp. 372–375. DOI: 10.1016/S0168-9002(03)00446-7.

[97] R. Brun and F. Rademakers. 'ROOT: An object oriented data analysis framework'. In: *Nucl.Instrum.Meth.* A389 (1997), pp. 81–86. DOI: 10.1016/S0168-9002(97)00048-X.

[98] High Performance Computing Group, University of Mainz. https://hpc.uni-mainz.de.

[99] M. Aaboud et al. 'Performance of the ATLAS Track Reconstruction Algorithms in Dense Environments in LHC Run 2'. In: *Eur. Phys. J.* C77.10 (2017), p. 673. DOI: 10.1140/epjc/s10052-017-5225-7. arXiv: 1704.07983 [hep-ex].

[100] R. Fruhwirth. 'Application of Kalman filtering to track and vertex fitting'. In: *Nucl. Instrum. Meth.* A262 (1987), pp. 444–450. DOI: 10.1016/0168-9002(87)90887-4.

[101] Morad Aaboud et al. 'Reconstruction of primary vertices at the ATLAS experiment in Run 1 proton–proton collisions at the LHC'. In: *Eur. Phys. J.* C77.5 (2017), p. 332. DOI: 10.1140/epjc/s10052-017-4887-5. arXiv: 1611.10235 [physics.ins-det].

[102] Morad Aaboud et al. 'Electron and photon energy calibration with the ATLAS detector using 2015–2016 LHC proton-proton collision data'. In: *JINST* 14.03 (2019), P03017. DOI: 10.1088/1748-0221/14/03/P03017. arXiv: 1812.03848 [hep-ex].

[103] Georges Aad et al. 'Electron and photon performance measurements with the ATLAS detector using the 2015–2017 LHC proton-proton collision data'. In: *JINST* 14.12 (2019), P12006. DOI: 10.1088/1748-0221/14/12/P12006. arXiv: 1908.00005 [hep-ex].

[104] Morad Aaboud et al. 'Electron reconstruction and identification in the ATLAS experiment using the 2015 and 2016 LHC proton-proton collision data at $\sqrt{s} = 13$ TeV'. In: *Eur. Phys. J. C* 79.8 (2019), p. 639. DOI: 10.1140/epjc/s10052-019-7140-6. arXiv: 1902.04655 [physics.ins-det].

[105] ATLAS Isolation Forum. https://twiki.cern.ch/twiki/bin/view/AtlasProtected/IsolationForum (Internal documentation).

[106] Georges Aad et al. 'Measurement of the muon reconstruction performance of the ATLAS detector using 2011 and 2012 LHC proton–proton collision data'. In: *Eur. Phys. J.* C74.11 (2014), p. 3130. DOI: 10.1140/epjc/s10052-014-3130-x. arXiv: 1407.3935 [hep-ex].

[107] G. Aad et al. 'Expected Performance of the ATLAS Experiment - Detector, Trigger and Physics'. In: (2009). arXiv: 0901.0512 [hep-ex].

[108] G. Aad et al. 'The ATLAS Simulation Infrastructure'.
In: *Eur.Phys.J.* C70 (2010), pp. 823–874. DOI: 10.1140/epjc/s10052-010-1429-9.
arXiv: 1005.4568 [physics.ins-det].

[109] G. Aad et al. 'Topological cell clustering in the ATLAS calorimeters and its performance in LHC Run 1'. In: *The European Physical Journal C* 77.7 (2017).
ISSN: 1434-6052. DOI: 10.1140/epjc/s10052-017-5004-5.
URL: http://dx.doi.org/10.1140/epjc/s10052-017-5004-5.

[110] Morad Aaboud et al.
'Jet reconstruction and performance using particle flow with the ATLAS Detector'.
In: *Eur. Phys. J. C* 77.7 (2017), p. 466. DOI: 10.1140/epjc/s10052-017-5031-2.
arXiv: 1703.10485 [hep-ex].

[111] M. Aaboud et al. 'Jet energy scale measurements and their systematic uncertainties in proton-proton collisions at $\sqrt{s} = 13$ TeV with the ATLAS detector'.
In: *Phys. Rev.* D96.7 (2017), p. 072002. DOI: 10.1103/PhysRevD.96.072002.
arXiv: 1703.09665 [hep-ex].

[112] Matteo Cacciari, Gavin P Salam and Gregory Soyez.
'The anti-ktjet clustering algorithm'.
In: *Journal of High Energy Physics* 2008.04 (2008), 063–063. ISSN: 1029-8479.
DOI: 10.1088/1126-6708/2008/04/063.
URL: http://dx.doi.org/10.1088/1126-6708/2008/04/063.

[113] *Tagging and suppression of pileup jets with the ATLAS detector.*
Tech. rep. ATLAS-CONF-2014-018. Geneva: CERN, 2014.
URL: https://cds.cern.ch/record/1700870.

[114] *Selection of jets produced in 13TeV proton-proton collisions with the ATLAS detector.*
Tech. rep. ATLAS-CONF-2015-029. Geneva: CERN, 2015.
URL: https://cds.cern.ch/record/2037702.

[115] Matteo Cacciari and Gavin P. Salam. 'Pileup subtraction using jet areas'.
In: *Phys. Lett.* B659 (2008), pp. 119–126. DOI: 10.1016/j.physletb.2007.09.077.
arXiv: 0707.1378 [hep-ph].

[116] Georges Aad et al. 'ATLAS b-jet identification performance and efficiency measurement with $t\bar{t}$ events in pp collisions at $\sqrt{s} = 13$ TeV'.
In: *Eur. Phys. J. C* 79.11 (2019), p. 970. DOI: 10.1140/epjc/s10052-019-7450-8.
arXiv: 1907.05120 [hep-ex].

[117] Morad Aaboud et al. 'Performance of missing transverse momentum reconstruction with the ATLAS detector using proton-proton collisions at $\sqrt{s} = 13$ TeV'.
In: *Eur. Phys. J. C* 78.11 (2018), p. 903. DOI: 10.1140/epjc/s10052-018-6288-9.
arXiv: 1802.08168 [hep-ex].

[118] M. Aaboud et al. 'Measurement of the photon identification efficiencies with the ATLAS detector using LHC Run-1 data'.
In: *The European Physical Journal C* 76.12 (2016). ISSN: 1434-6052.
DOI: 10.1140/epjc/s10052-016-4507-9.
URL: http://dx.doi.org/10.1140/epjc/s10052-016-4507-9.

[119] Georges Aad et al. 'Identification and energy calibration of hadronically decaying tau leptons with the ATLAS experiment in *pp* collisions at $\sqrt{s}$=8 TeV'.
In: *Eur. Phys. J.* C75.7 (2015), p. 303. DOI: 10.1140/epjc/s10052-015-3500-z.
arXiv: 1412.7086 [hep-ex].

[120] 'Reconstruction, Energy Calibration, and Identification of Hadronically Decaying Tau Leptons in the ATLAS Experiment for Run-2 of the LHC'. In: (2015).

[121] 'Measurement of the tau lepton reconstruction and identification performance in the ATLAS experiment using *pp* collisions at $\sqrt{s} = 13$ TeV'. In: (May 2017).

[122] Michael H. Seymour and Marilyn Marx. 'Monte Carlo Event Generators'.
In: *Proceedings, 69th Scottish Universities Summer School in Physics : LHC Phenomenology (SUSSP69): St.Andrews, Scotland, August 19-September 1, 2012*. 2013, pp. 287–319. DOI: 10.1007/978-3-319-05362-2_8. arXiv: 1304.6677 [hep-ph].

[123] Stefan Höche. 'Introduction to parton-shower event generators'.
In: *Proceedings, Theoretical Advanced Study Institute in Elementary Particle Physics: Journeys Through the Precision Frontier: Amplitudes for Colliders (TASI 2014): Boulder, Colorado, June 2-27, 2014*. 2015, pp. 235–295.
DOI: 10.1142/9789814678766_0005. arXiv: 1411.4085 [hep-ph].

[124] Michael H. Seymour and Marilyn Marx. 'Monte Carlo Event Generators'. In: (2013).
arXiv: 1304.6677 [hep-ph].

[125] S. Catani et al. 'QCD matrix elements + parton showers'. In: *JHEP* 11 (2001), p. 063.
DOI: 10.1088/1126-6708/2001/11/063. arXiv: hep-ph/0109231 [hep-ph].

[126] Bo Andersson et al. 'Parton Fragmentation and String Dynamics'.
In: *Phys. Rept.* 97 (1983), pp. 31–145. DOI: 10.1016/0370-1573(83)90080-7.

[127] Geoffrey C. Fox and Stephen Wolfram. 'A Model for Parton Showers in QCD'.
In: *Nucl. Phys.* B168 (1980), pp. 285–295. DOI: 10.1016/0550-3213(80)90111-X.

[128] S. Agostinelli et al. 'GEANT4: A Simulation toolkit'.
In: *Nucl.Instrum.Meth.* A506 (2003), pp. 250–303.
DOI: 10.1016/S0168-9002(03)01368-8.

[129] ATLAS Luminosity Working Group. https://twiki.cern.ch/twiki/bin/view/AtlasPublic/LuminosityPublicResultsRun2.

[130] Physics Analysis Tools. 'Pileup Reweighting'. https://twiki.cern.ch/twiki/bin/viewauth/~AtlasProtected/ExtendedPileupReweighting (Internal documentation).

[131] T. Sjöstrand, S. Mrenna, and P. Z. Skands. 'A Brief Introduction to PYTHIA 8.1'. In: *Comput. Phys. Commun.* 178 (2008), p. 852. DOI: 10.1016/j.cpc.2008.01.036. arXiv: 0710.3820 [hep-ph].

[132] R. D. Ball et al. 'Parton distributions with LHC data'. In: *Nucl. Phys.* B867 (2013), pp. 244–289. DOI: 10.1016/j.nuclphysb.2012.10.003. arXiv: 1207.1303 [hep-ph].

[133] P. Golonka and Z. Was. 'PHOTOS Monte Carlo: a precision tool for QED corrections in Z and W decays'. In: *Eur. Phys. J.* C45 (2006), p. 97. DOI: 10.1140/epjc/s2005-02396-4. arXiv: hep-ph/0506026.

[134] Elena Accomando et al. 'Interference effects in heavy W'-boson searches at the LHC'. In: *Phys. Rev.* D85 (2012), p. 115017. DOI: 10.1103/PhysRevD.85.115017. arXiv: 1110.0713 [hep-ph].

[135] Paul Gessinger-Befurt. 'Search for new heavy charged gauge bosons with the ATLAS detector'. Presented 15 May 2017. 2017. URL: https://cds.cern.ch/record/2276657.

[136] S. Alioli, P. Nason, C. Oleari, and E. Re. 'A general framework for implementing NLO calculations in shower Monte Carlo programs: the POWHEG BOX'. In: *JHEP* 06 (2010), p. 043. DOI: 10.1007/JHEP06(2010)043. arXiv: 1002.2581 [hep-ph].

[137] H.-L. Lai et al. 'New parton distributions for collider physics'. In: *Phys. Rev.* D82 (2010), p. 074024. DOI: 10.1103/PhysRevD.82.074024. arXiv: 1007.2241 [hep-ph].

[138] C. Anastasiou, L. Dixon, K. Melnikov, and F. Petriello. 'High precision QCD at hadron colliders: Electroweak gauge boson rapidity distributions at NNLO'. In: *Phys. Rev.* D69 (2004), p. 094008. DOI: 10.1103/PhysRevD.69.094008. arXiv: hep-ph/0312266 [hep-ph].

[139] Uta Klein. https://twiki.cern.ch/twiki/bin/view/AtlasProtected/HigherOrderCorrections2015 (Internal documentation).

[140] D. Bardin et al. 'SANC integrator in the progress: QCD and EW contributions'. In: *JETP Lett.* 96 (2012), pp. 285–289. DOI: 10.1134/S002136401217002X. arXiv: 1207.4400 [hep-ph].

[141] S. G. Bondarenko and A. A. Sapronov.
'NLO EW and QCD proton-proton cross section
calculations with mcsanc-v1.01'.
In: *Comput. Phys. Commun.* 184 (2013), pp. 2343–2350.
DOI: 10.1016/j.cpc.2013.05.010. arXiv: 1301.3687 [hep-ph].

[142] Torbjorn Sjostrand, Stephen Mrenna and Peter Z. Skands.
'PYTHIA 6.4 Physics and Manual'. In: *JHEP* 05 (2006), p. 026.
DOI: 10.1088/1126-6708/2006/05/026. arXiv: hep-ph/0603175 [hep-ph].

[143] T. Gleisberg et al. 'Event generation with SHERPA 1.1'. In: *JHEP* 02 (2009), p. 007.
DOI: 10.1088/1126-6708/2009/02/007. arXiv: 0811.4622 [hep-ph].

[144] Georges Aad et al. 'Search for new phenomena in the dijet mass distribution using $p-p$ collision data at $\sqrt{s} = 8$ TeV with the ATLAS detector'.
In: *Phys. Rev.* D91.5 (2015), p. 052007. DOI: 10.1103/PhysRevD.91.052007.
arXiv: 1407.1376 [hep-ex].

[145] ATLAS Physics Modeling Group.
https://twiki.cern.ch/twiki/bin/view/Atlas/LuminosityForPhysics (Internal documentation).

[146] Sayipjamal Dulat et al.
'New parton distribution functions from a global analysis of quantum chromodynamics'.
In: *Phys. Rev.* D93.3 (2016), p. 033006. DOI: 10.1103/PhysRevD.93.033006.
arXiv: 1506.07443 [hep-ph].

[147] Jon Butterworth et al. 'PDF4LHC recommendations for LHC Run II'.
In: *J. Phys.* G43 (2016), p. 023001. DOI: 10.1088/0954-3899/43/2/023001.
arXiv: 1510.03865 [hep-ph].

[148] Georges Aad et al. 'Search for new particles in events with one lepton and missing transverse momentum in pp collisions at $\sqrt{s} = 8$ TeV with the ATLAS detector'.
In: *JHEP* 09 (2014), p. 037. DOI: 10.1007/JHEP09(2014)037.
arXiv: 1407.7494 [hep-ex].

[149] Vardan Khachatryan et al.
'Search for physics beyond the standard model in final states with a lepton and missing transverse energy in proton-proton collisions at sqrt(s) = 8 TeV'.
In: *Phys. Rev.* D91.9 (2015), p. 092005. DOI: 10.1103/PhysRevD.91.092005.
arXiv: 1408.2745 [hep-ex].

[150] Glen Cowan. *Statistical Data Analysis*. Oxford University Press, Oxford, 1998.

[151] L. Moneta et al. *The RooStats Project*. PoS(ACAT2010)057. 2010.
URL: http://pos.sissa.it/archive/conferences/093/057/ACAT2010_057.pdf.

[152] Glen Cowan et al. 'Asymptotic formulae for likelihood-based tests of new physics'. In: *Eur. Phys. J.* C71 (2011). [Erratum: Eur. Phys. J.C73,2501(2013)], p. 1554. DOI: 10.1140/epjc/s10052-011-1554-0,10.1140/epjc/s10052-013-2501-z. arXiv: 1007.1727 [physics.data-an].

[153] S. S. Wilks. 'The Large-Sample Distribution of the Likelihood Ratio for Testing Composite Hypotheses'. In: *Annals Math. Statist.* 9.1 (1938), pp. 60–62. DOI: 10.1214/aoms/1177732360.

[154] A. Caldwell, D. Kollar, and K. Kroninger. 'BAT: The Bayesian Analysis Toolkit'. In: *Comput. Phys. Commun.* 180 (2009), pp. 2197–2209. DOI: 10.1016/j.cpc.2009.06.026. arXiv: 0808.2552 [physics.data-an].

[155] Georges Aad et al. 'Search for a heavy charged boson in events with a charged lepton and missing transverse momentum from pp collisions at $\sqrt{s} = 13$ TeV with the ATLAS detector'. In: *Phys. Rev. D* 100.5 (2019), p. 052013. DOI: 10.1103/PhysRevD.100.052013. arXiv: 1906.05609 [hep-ex].

[156] 'Prospects for searches for heavy Z' and W' bosons in fermionic final states with the ATLAS experiment at the HL-LHC'. In: (2018).

[157] In: *Physics Reports* 427.5-6 (2006), 257–454. ISSN: 0370-1573. DOI: 10.1016/j.physrep.2005.12.006. URL: http://dx.doi.org/10.1016/j.physrep.2005.12.006.

[158] I. Doršner et al. 'Physics of leptoquarks in precision experiments and at particle colliders'. In: *Phys. Rept.* 641 (2016), pp. 1–68. DOI: 10.1016/j.physrep.2016.06.001. arXiv: 1603.04993 [hep-ph].

[159] Morad Aaboud et al. 'Searches for scalar leptoquarks and differential cross-section measurements in dilepton-dijet events in proton-proton collisions at a centre-of-mass energy of $\sqrt{s} = 13$ TeV with the ATLAS experiment'. In: *Eur. Phys. J.* C79.9 (2019), p. 733. DOI: 10.1140/epjc/s10052-019-7181-x. arXiv: 1902.00377 [hep-ex].

[160] Johan Alwall et al. 'MadGraph 5 : Going Beyond'. In: *JHEP* 06 (2011), p. 128. DOI: 10.1007/JHEP06(2011)128. arXiv: 1106.0522 [hep-ph].

[161] Y. Li and F. Petriello. 'Combining QCD and electroweak corrections to dilepton production in the framework of the FEWZ simulation code'. In: *Phys. Rev.* D86 (2012), p. 094034. DOI: 10.1103/PhysRevD.86.094034. arXiv: 1208.5967 [hep-ph].

[162] Kirill Melnikov and Frank Petriello.
'Electroweak gauge boson production at hadron colliders through $\mathcal{O}(\alpha_s^2)$'.
In: *Phys. Rev. D* 74 (2006), p. 114017. DOI: 10.1103/PhysRevD.74.114017.
arXiv: hep-ph/0609070 [hep-ph].

[163] Ryan Gavin et al.
'FEWZ 2.0: A code for hadronic Z production at next-to-next-to-leading order'.
In: *Comput. Phys. Commun.* 182 (2011), p. 2388. DOI: 10.1016/j.cpc.2011.06.008.
arXiv: 1011.3540 [hep-ph].

[164] A. D. Martin et al. 'Parton distributions for the LHC'.
In: *Eur. Phys. J.* C 63 (2009), p. 189. DOI: 10.1140/epjc/s10052-009-1072-5.
arXiv: 0901.0002 [hep-ph].

[165] Peter Zeiler Skands. 'Tuning Monte Carlo Generators: The Perugia Tunes'.
In: *Phys. Rev. D* 82 (2010), p. 074018. DOI: 10.1103/PhysRevD.82.074018.
arXiv: 1005.3457 [hep-ph].

[166] Tanju Gleisberg and Stefan Hoeche. 'Comix, a new matrix element generator'.
In: *JHEP* 12 (2008), p. 039. DOI: 10.1088/1126-6708/2008/12/039.
arXiv: 0808.3674 [hep-ph].

[167] Federico Buccioni et al. 'OpenLoops 2'. In: *Eur. Phys. J. C* 79.10 (2019), p. 866.
DOI: 10.1140/epjc/s10052-019-7306-2. arXiv: 1907.13071 [hep-ph].

[168] Matteo Cacciari, Gavin P. Salam and Gregory Soyez.
'The Anti-k(t) jet clustering algorithm'. In: *JHEP* 04 (2008), p. 063.
DOI: 10.1088/1126-6708/2008/04/063. arXiv: 0802.1189 [hep-ph].

[169] Y. Afik. *private communication.*

[170] L. A. Harland-Lang et al. 'Parton distributions in the LHC era: MMHT 2014 PDFs'.
In: *Eur. Phys. J.* C75.5 (2015), p. 204. DOI: 10.1140/epjc/s10052-015-3397-6.
arXiv: 1412.3989 [hep-ph].

[171] ATLAS Physics Modeling Group.
https://twiki.cern.ch/twiki/bin/view/AtlasProtected/PhysicsModellingGroup
(Internal documentation).

[172] ATLAS Physics Modeling Group.
https://twiki.cern.ch/twiki/bin/view/LHCPhysics/TtbarNNLO (Internal
documentation).

[173] M. Pinamonti, L. Valery, A. Held and T. Dado.
https://trexfitter-docs.web.cern.ch/trexfitter-docs/.

[174] W. Buchmuller, R. Ruckl and D. Wyler. 'Leptoquarks in Lepton - Quark Collisions'. In: *Phys. Lett. B* 191 (1987). [Erratum: Phys.Lett.B 448, 320–320 (1999)], pp. 442–448. DOI: 10.1016/0370-2693(87)90637-X.